Design analysis and performance evaluation of fiberoptic pressure sensors based on Fabry-Perot interferometer

By

SHIVAM MISHRA

ENGG01201204012

Bhabha Atomic Research Centre, Mumbai

A thesis submitted to the
Board of Studies in Engineering Sciences

In partial fulfilment of requirements
for the degree of

DOCTOR OF PHILOSOPHY

of

HOMI BHABHA NATIONAL INSTITUTE

September, 2020

STATEMENT BY AUTHOR

This dissertation has been submitted in partial fulfillment of requirements for an advanced degree at Homi Bhabha National Institute (HBNI) and is deposited in the Library to be made available to borrowers under rules of the HBNI.

Brief quotations from this dissertation are allowable without special permission, provided that accurate acknowledgement of source is made. Requests for permission for extended quotation from or reproduction of this manuscript in whole or in part may be granted by the Competent Authority of HBNI when in his or her judgment the proposed use of the material is in the interests of scholarship. In all other instances, however, permission must be obtained from the author.

Shivam Mishra

(Shivam Mishra)

DECLARATION

I, hereby declare that the investigation presented in the thesis has been carried out by me. The work is original and has not been submitted earlier as a whole or in part for a degree / diploma at this or any other Institution / University.

Shivam Mishra

(Shivam Mishra)

List of Publications arising from the thesis

Journals

1. **Mishra S.**, Balasubramaniam R., Chandra S., *Suppression of span in sealed microcavity Fabry–Perot pressure sensors*, **Optical Engineering** (2017), 56(1), 016105, 1–9.

2. **Mishra S.**, Balasubramaniam R., Chandra S., *Finite element analysis and experimental validation of suppression of span in optical MEMS pressure sensors*, **Microsystems Technologies** (2019), 25(10), 3691-3701

Conferences

1. **Mishra S.**, Balasubramaniam R., Chandra S., *Temperature effects of gas in sealed microcavity Fabry-Perot pressure sensors*, **National Laser Symposium** (NLS-27), RRCAT, Indore, 03-06 Dec, 2018.

2. **Mishra S.**, Balasubramaniam R., Chandra S., *A Technique for Noncontact Measurement of Cavity Lengths and Deflection Shape in Optical MEMS Pressure Transducers*, **Design, Test, Integration & Packaging of MEMS and MOEMS** (**DTIP 2019**),Paris - France, May 12th - May 15th, 2019.

Shivam Mishra

(Shivam Mishra)

Dedicated to My Parents, Teachers, Family and Friends

Acknowledgements

I would like to express my deepest and heartfelt gratitude to my supervisor and guide Dr. R. Balasubramaniam (Bala sir). He has always pressed me hard to pursue the work and keep achieving the milestones towards completion of the PhD. He always supported and helped in materializing the research. He had given guidance to help me perform even under constraints, commitments and other workloads. He emphasized on continuous sustained endeavour. He helped me accomplish the milestones to reach this point of writing acknowledgement today.

I would like to express my sincere gratitude to my co-supervisor, Dr. Sudhir Chandra, who retired as Professor from CARE, IIT Delhi and is presently associated with Bennett University, Greater Noida. He helped me at technical as well as at philosophical levels where I had to take a call at important junctures. I learn from his commitments towards his work.

I thank my former division head and mentor Dr. V K Suri, who encouraged me to register for PhD. He always gave enormous freedom to pursue the ideas. I take opportunity to thank my present division head Shri A K Wankhede for his support in concluding the research. I further thank Shri Veerendra Dhyani, Research Fellow at IIT Delhi during 2014-15. He fabricated the devices at Mircoelectronics Lab, CARE, IIT Delhi as per my design. I Thank Professor Ramesh Singh, of IIT Bombay and his students who helped me in characterization of the micromachined silicon cavities using their optical instruments. I also thank Shri Ajit K Pappu, of Reactor Engineering Division, BARC for his cordial support for pressure testing of sensors. I thank the technical team of the CPIU lab under him for their support in testing. I further thank my colleagues Ms. Shrinkhla Ghildiyal (SG) and Dr. Prabhat Ranjan (PR), who have been absolutely unconditional in helping me during this research work. While SG helped me in voluminous signal processing, referencing etc.; PR helped me in mechanical conceptions, fixture designs and simulations. I thank my colleague Mr. Ashwin Rathod whose software was useful in data logging and some of the studies. I thank my other technical support staff, Shri N V Surendran for doing fine machining, fittings and other technical helps. I am thankful to my friends and well-wishers who were always there to talk, share information and knowledge, and give encouragement and guidance.

I greatly acknowledge the contributions of my doctoral committee chairperson Dr. (Smt.) Archana Sharma and members Dr. V H Patankar, Dr. (Smt.) Gopika Vinod, Dr. Biswaranjan Dikshit who spared their valuable time for periodical critical assessment of my work. Incorporation of their suggestions has greatly enhanced the level of my research work. I am also thankful to Dr. P D Naik (Dean HBNI), Dr. A K Bhattacharjee (Academic Dean, HBNI), Dr. D K Maity (Associate Dean HBNI), Board of Studies (Engg. Sciences, HBNI). I also thank members of administrative staff for their constant support during my PhD research work.

I am always thankful, whether mentioned or not, to my parents Mr. U C Mishra and Late Mrs Saroj Mishra and my elder sister Mrs. Garima. I am grateful to my family: my wife Hem Lata Mishra and children Master Siddharth Mishra and Ms. Parnika Mishra, for their support and sacrifices.

Synopsis

The broader field of present research is Fabry-Perot interferometer based fiberoptic pressure sensors. The optical pressure sensors based on MEMS fabrication technology in particular have been investigated. It is found that the optical sensors have a sealed cavity to prevent the ingress of foreign material. The sealing method used in any fabrication technology leaves behind some residual gas in the cavity unless special measures are taken. In the literature, effect of the trapped gas has been studied only from the perspective of its temperature behaviour. Calibration with temperature and pressure is carried out to achieve active temperature compensation of the pressure sensor. However, an effect which has been largely ignored in the literature, is the central idea of this research work, as outlined further.

The trapped gas pressure in the sealed cavity is effectively the ‘reference’ pressure for the pressure sensor. The reference pressure must be firm in all the operating conditions of the sensor. However, in microcavity sensors, it is anticipated that the movement of diaphragm would result in change of reference pressure. Thus there is a mutual dependency; the deflection (under a given applied pressure) depends on reference pressure and the reference pressure depends on deflection. Therefore, the diaphragm would not take the position it is supposed to take; as the reference pressure varies with deflection. It was found very interesting to develop the insight into the phenomenon and have quantification of the extent of the underlined effect.

In the present work, the optical pressure sensors having MEMS design have been investigated. The fabrication involves anodic bonding of glass and structured silicon wafers. An analytical model is developed and a characteristic equation is derived for finding the deflection of diaphragm in a sealed microcavity sensor. It emerges that there is a phenomenon of "suppression of span" in the sealed microcavity pressure sensors. The effect is more for low range pressure sensors such as 1 bar than that for high range sensor such as 10 bar. Further analysis is focussed on a 1 bar (absolute) pressure sensor which is very useful in various vacuum systems in measuring the rough vacuum. The suppression is stronger for sealed cavities of small lengths such as up to 30 μm. The achievable span in sealed cavity system depends nonlinearly on the cavity length design parameter of a sensor. The achievable span is very sensitive to cavity length value in the regime of small cavity lengths. The achievable span is also dependent on the pressure of the trapped gas; higher the pressure of the trapped gas, more is the suppression of span and smaller span is achieved. The temperature effects due to the gas alone are studied based on the derived characteristic equation. It is found that the large cavity lengths give more controlled characteristics of the sensor and have various other advantages.

Numerical modelling and finite element based analysis are carried out using fluid-structure interaction to solve this coupled-physics problem. The results of the FE analysis match closely with the results of the analytical model. Thus the analytical model gets validated through the FE based analysis.

When the sensors are fabricated in batches, different cavities are likely to have different residual pressure. The achievable span is dependent on the pressure of the trapped gas. It is seen that the larger cavity lengths are beneficial as those would bring all the batch fabricated sensors at par. However, by optical design small cavity length Fabry-Perot sensors are preferred. In order to accommodate these two contradictory requirements, inclusion of a "buffer cavity" is suggested. This cavity would be coupled to the main (Fabry-Peort) cavity and would provide extra volume to circumvent the problem of suppression of span. The buffer cavity is designed to provide same overall volume to the device as would have been there for buffer-less large cavity of desired cavity length. Finite element analysis is carried out to validate the efficacy of the buffer cavity.

Pressure sensors of 1 bar range having different cavity lengths have been designed and fabricated. The sensors have been packaged in prototype test packaging and tested for pressure response. The Fabry-Perot (FP) cavity length is noted with applied pressure and diaphragm deflection is found. Further, the pressure of the trapped gas in various sensors is estimated from the experimentally found deflection characteristics. The experimentally found trapped gas pressures along with the actual cavity lengths are used to fit analytical model to experimental data. The suppression of span is estimated for sensors of various cavity lengths.

In a batch of fabricated sensor 2.0 mm thick glass was used. It was found very difficult to acquire optical signal from the sensor, as the signal was weak, the devices had bow and stray reflections were stronger. A technique is developed to obtain the desired interferometric signal by deploying “angle-cut” multimode optical fiber. The technique enables noncontact measurement of cavity length of the interferometer in the fabricated device. The developed technique is used to characterize the devices post-fabrication for fabricated depths of front (FP) cavity. Further, the entire interferometer is scanned in “noncontact” manner and deflection shape of anisotropic square silicon diaphragm is measured. The technique is validated by fitting the deflection shape function from literature on experimental data.

At the end, the conclusions of the research work are given and future scope of research is mentioned.

Contents

List of Figures

List of tables

Nomenclatures

Symbol	**Description**
A	Area of diaphragm times normalized average deflection
B	Deflection sensitivity of diaphragm (µm/MPa)
C	Constant C' multiplied by initial volume (V_0) of the cavity
C'	Value of 'ambient pressure divided by bonding temperature' (MPa/K) during anodic bonding
D_a	Anisotropic flexural rigidity of silicon
F	Reflectivity dependent 'Finesse' of FPI
h	Thickness of diaphragm
I, I_1, I_2	Intensity of interfering light beams
I_0	Resultant intensity from two beam interference
L	Edge length of square diaphragm
l	Cavity length of Fabry-Perot interferometer in general
l_0	Initial cavity length (corresponds to null-deflection of diaphragm) of Fabry-Perot cavity in the sensor
$n, n1, n2$	Refractive index of medium of light travel
P, P_a	Applied pressure
P_c	Cavity pressure in general operating condition
P_{c0}	Pressure of gas in sealed cavity at null-deflection of diaphragm
R	Reflectivity due to Fresnel reflection at the interface of two media of light
R_{FP}	Resultant (phase dependent) reflectivity of FPI
R_S	Reflectivity of each mirror in FPI

S	Span or full scale deflection of diaphragm
T	Absolute temperature
V	Visibility (or contrast) of interference fringes
ν *(nu)*	Average normalized deflection over area of diaphragm
V_0	Initial volume of the cavity
V_C	Cavity volume in general case
w	Deflection (μm) of diaphragm at any point
w_0 , x	Deflection (μm) of diaphragm at centre
Y_{max}	Maximum Y-value of a fringe in spectral signal
Y_{min}	Minimum Y-value of a fringe in spectral signal
β	Constant governing the deflection shape of anisotropic silicon diaphragm
δ	Phase change of light over round trip in Fabry-Perot interferometer (FPI)
θ	Half-cone angle of acceptance cone of a multimode optical fiber
λ	Wavelength of light
μl	Micro litre
φ	Phase difference between two interfering light beams

Abbreviations

Abbreviation	Full form
Abs.	Absolute
ADC	Analog to Digital Converter
AND	Average Normalized Deflection
Atm.	Atmosphere
BCS	Buffer Cavity Sensor
CCD	Charge Coupled Devices
CL	Cavity Length
DSF	Deflection Shape Function
EFPI	Extrinsic Fabry-Perot Interferometer
FBG	Fiber Bragg Grating
FE	Finite Element
FEA	Finite Element Analysis
FOS	Fiber Optic Sensors
FP	Fabry-Perot
FPI	Fabry-Perot Interferometer
FSD	Full Scale Deflection
FSR	Free Spectral Range
LCI	Low Coherence Interferometry

MEMS	Micro Electro Mechanical Systems
MI	Michelson Interferometer
MOEMS	Micro Opto Electro Mechanical Systems
MZI	Mach-Zehnder Interferometer
OPD	Optical Path Difference
OSA	Optical Spectrum Analyzer
TCO	Temperature Coefficient of Offset
TCS	Temperature Coefficient of Span
SCIIB	Self Calibrated Interferometric Intensity Based (sensors)
THL	Tungsten Halogen Lamp
WLI	White Light Interferometry

Chapter 1

INTRODUCTION

1.1. Relevance and Motivation

The field of sensors is very extensive encompassing variety of sensors for measuring various parameters such as pressure, temperature, level, flow, speed, rpm, load, displacement, position, strain, magnetic field, current, pH and so on [1,2]. There can be more than one technique or principle of measurement of a parameter of interest. For example, a displacement can be measured in a noncontact manner using capacitive, inductive or optical principles. In optical, there are multiple techniques such as laser triangulation, time-of-flight, total reflected power and confocal which is wavelength selective. Similarly, pressure which is a very important parameter in industry and biomedical, can be measured in several possible ways. The pressure is indirectly measured by converting it to strain or displacement. Thus the pressure can be measured by strain gauges, piezoresistors, piezoelectric crystal (through strain) or by capacitance, inductance, interference and other optical principles (through displacement) [1,3].

In nutshell, there are varieties of parameters for which sensors are required and variety of technologies are there on which the sensors are based. Every technology has some advantage over other. Also, sensor based on one technology may not be able to cover the entire range of the parameter and may not be suitable in certain environments. That is why there are sensors based on different technologies to suit different requirements of cost, size, working environment etc.

With the advents in the field of "microsystems", MEMS (Micro Electro Mechanical Systems) based sensors and actuators are entering the market place [4]. These systems, as the name implies, are very tiny which can be integrated to some larger systems in very effective manner. MEMS micro-pump actuators are used in inkjet printers. Other very successful MEMS sensors are the inertial and pressure sensors. The inertial sensors are found in accelerometers, mobile phones and digital cameras. MEMS pressure sensors are commonly based on capacitive or piezoresistive principles. The MEMS pressure sensors are also used as SMD (Surface Mount Devices) component on electronic printed circuit boards (PCB). An extension of the MEMS is MOEMS (Micro Opto Electro Mechanical Systems) where the optical parts are also there in the MEMS. Example of MOEMS are DMD (digital micro-mirror device) which is a chip used in modern picture projectors. MOEMS based optical switches are used in high speed optical communication networks [4,5].

The information technology is the backbone of present time. The "fiberoptic communication" has evolved tremendously in last three decades with high speed networks, links and components such as low loss optical fibers, laser diodes, modulators and detectors. Though this progress was fuelled by the demands of communication networks, great amount of interest was seen in "fiberoptic sensing". The reasons for this inclination towards sensing by light were small size, light weight, inherent immunity of light from electromagnetic or radio frequency interference (EMI/RFI). One technology that was matured early was "fiberoptic gyro" for defence navigation applications. Of late, the Fiber Bragg Grating (FBG) based strain sensors have gained attention for Structural Health Monitoring (SHM) applications of large civil structures such as bridges, damns, pipelines, fencing etc. Other fiberoptic sensors have been explored widely for biomedical, oil & gas, energy and other sectors.

A Fabry-Perot Interferometer (FPI) is a type interferometer in optics which has very high wavelength (or frequency) selectivity. It typically has two plane, parallel, high-reflectivity partial mirrors, wherein light undergoes multiple reflections in the cavity between the two mirrors and acts as an optical resonator. The wavelengths transmitted through the interferometer are a function of the cavity length (gap between the mirrors) and the refractive index of cavity media. The FPI are used in spectral analysis of materials and as laser cavities.

As the fusion of technologies continued and evolved, miniature pressure sensors have been developed on the tip of optical fiber using MEMS fabrication techniques. Such sensors are also referred to as optical or optically interrogated MEMS pressure sensors or fiber FPI pressure sensors. The low reflectivity mirrors are common in these sensors unlike classical interferometer, yet they have been referred to as ‘FPI sensors’ for the mirrors being parallel. These sensors have been made for different pressure ranges such as absolute, low, medium or high; and demonstrated for various applications such as biomedical, IC engine and turbine research, oil & gas well etc.

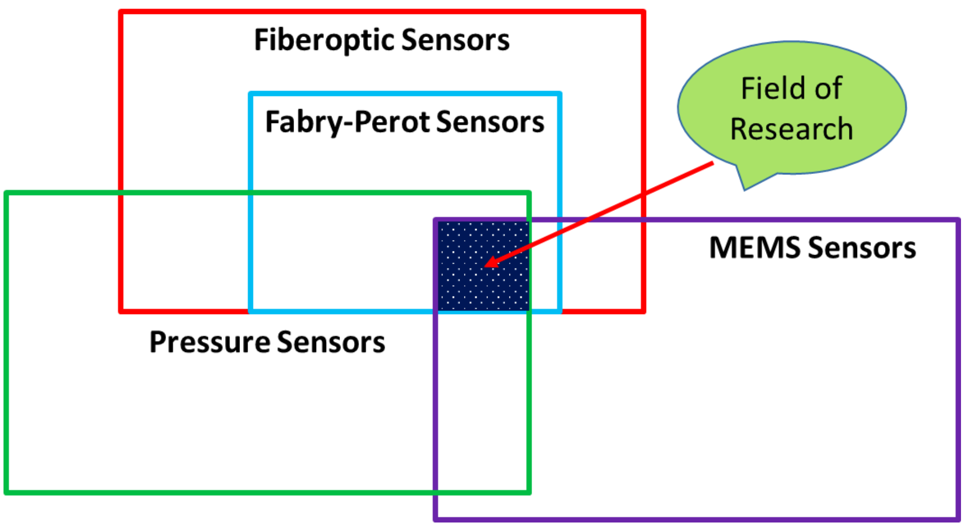

Fig. 1.1 The field of research

Different designs, materials (polymer, silicon, glass, sapphire, metal etc.) and fabrication techniques (moulding, lithography, chemical etching, focussed ion beam and laser beam based fusion or joining etc.) are used. The present research is focussed on optical MEMS pressure sensors working on the principle of FP interferometer, as shown highlighted in Fig. 1.1.

1.1.1. Motivation of research

The Optical MEMS Pressure Sensors with bonded glass wafer involve “Anodic Bonding”. It is understood when the latter is performed under ambient pressure, the sealed cavity has trapped gases with sub-atmospheric pressures. The sealed cavity pressure in effect becomes the ‘reference’ pressure for the pressure sensor. Reference pressure must remain constant in all operating conditions of the pressure sensor. In literature, the researchers have considered only the temperature effects of the gas from the objective of active temperature compensation of the pressure sensor. However, the effect of changing reference pressure arising from the movement of diaphragm in sealed microcavity sensors and its effect on sensor performance have not been studied.

As depicted in Fig. 1.2, the sensor can be treated as a system with applied pressure as input and the measured deflection (of diaphragm) at any given applied pressure as output. In case of sealed cavity sensors of small cavity lengths, such as FPI based sensors, the deflection of diaphragm may change the cavity volume considerably. The change of cavity volume would accordingly change the cavity pressure, **thus making the ‘reference’ pressure dependent on the deflection**. Thus, it is found interesting to derive the closed loop solution for diaphragm deflection and the equilibrium position that the diaphragm would take. The quantification of the effect of trapped gas on sensor characteristics (offset, span, linearity) was largely unattended in the literature.

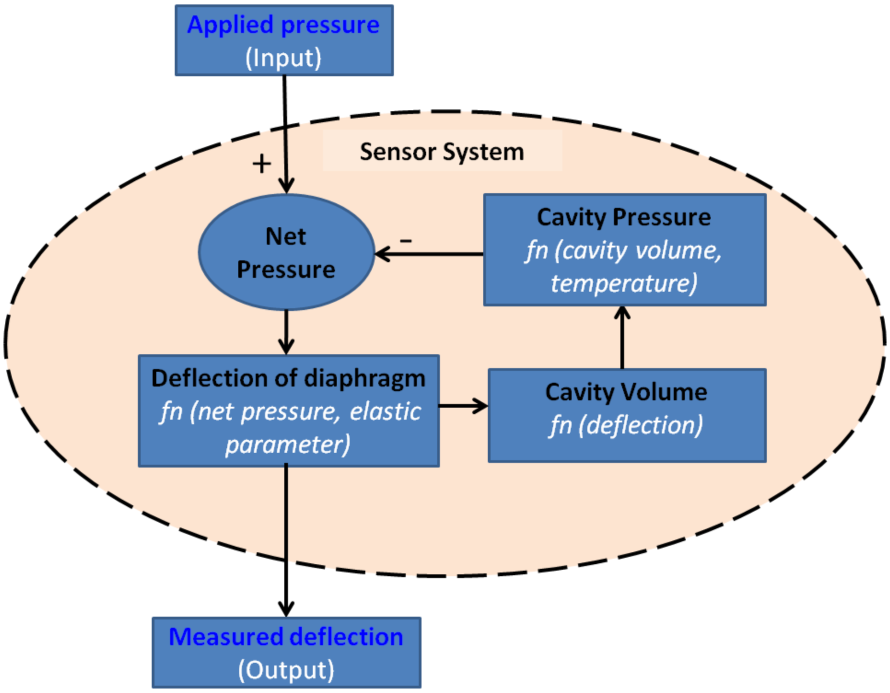

Fig. 1.2 Interdependency of various parameters in a sealed microcavity pressure sensor

Therefore, this effect should be analysed with respect to design parameters of sensor such as FP cavity length, sensitivity of diaphragm and pressure of the trapped gas. In the present work this effect has been investigated theoretically and experimentally.

1.2. Objectives

The objectives of the present research work are enumerated below:

1) Design of the silicon diaphragm and sensor for 0-1 bar and 0-10 bar pressure ranges
2) Development of Analytical model (a closed loop solution) for deflection of diaphragm while the cavity pressure changes in response to diaphragm movement
3) Derivation of deflection characteristics (comprising span and offset of sensor) from the developed analytical model for various cavity length values
4) Study of offset and span of diaphragm with cavity length as design parameter

5) The temperature effects of trapped gas on offset and span

6) Study of suppression of span at various trapped gas pressures

7) Finite Element Study of 0-1 bar sensors of different cavity lengths

8) FE analysis to validate the efficacy of proposed ‘Buffer cavity’ to circumvent suppression of span

9) Fabrication, packaging and testing of sensors of different FP cavity lengths and validation of the results of analytical and numerical models

10) Development of a noncontact measurement and characterization technique for sensors with thick glass

1.3. Organisation of the Chapters

In **Chapter 1**, relevance and motivations are reported with objectives of present research work. The objectives of the research have been listed encompassing the design, analysis, buffer cavity, fabrication, packaging, testing and a characterization technique.

Chapter 2 gives general background knowledge of the field of research. It has been tried to be comprehensive and lucid enough so that the reader zeroes down very conveniently to the problem statement of research. The brief is given about the pressures sensors and various popular technologies. Thereafter, the optical pressure sensors including the fiberoptic versions have been introduced. The working principle of present design of sensor is given followed by a comprehensive literature survey. The gap area is identified and highlighted.

Chapter 3 describes an **analytical model** of the pressure sensor where a closed loop solution has been derived for the deflection of diaphragm, when the reference pressure is not constant but responsive to deflection itself. A characteristic equation is obtained on which various interpretations are based. A phenomenon of "suppression of span" is highlighted.

Chapter 4 describes a **numerical model** and finite element based analysis of the pressure sensors of various cavity lengths. The phenomenon underlined in the previous chapter is also validated by the numerical model.

Chapter 5 briefly explains the fabrication of MEMS based optical pressure sensors. A technique is developed to overcome the problem of capturing the weak optical signal from thick glass devices by using an angle-cut multimode fiber as probe. This technique is used to characterize the cavity lengths in various fabricated sensor. The technique is conveniently used for characterization of deflection shape of square silicon diaphragm and validated using shape function from literature.

Chapter 6 describes the experimental work for functional testing of the pressure sensors and validation of the results of the analytical model.

Chapter 7 introduces the idea of a buffer cavity to provide extra volume to the main cavity and circumvent the unfavourable aspects arising from the small length cavities. The design of the size of buffer cavity is carried out. Finite element simulations are also carried out to validate the efficacy of the buffer cavity in eliminating the adverse effects of trapped gas in sensors of small FP cavity lengths.

Chapter 8 gives conclusions on the work carried out under the scope of present research. Also, the future directions are suggested for investigation of some of the aspects from present research.

Chapter 2

LITERATURE SURVEY

2.1. Introduction

This chapter starts with a brief introduction of pressure sensors based on various technologies. A relatively new genre of sensors based on fiberoptics and optical principles is then introduced mentioning their advantages over conventional technologies. A brief section is dedicated to the working principle of a Fabry-Perot Interferometer (FPI). This is among the most prominent principles on which fiberoptic pressure sensors are developed and researched worldwide. Thereafter, a brief overview is given on major ‘optical demodulation’ methods with a simple schematic of the FPI sensor. The sensor design is directly related to the selected method of demodulation. Various implementations of fiber FPI pressure sensors have been studied in detail. It is found that certain phenomenon which may lead to a compromised design were overlooked. The gap area has been highlighted and scope of the research work is formulated.

2.2. Pressure Sensors

The pressure is defined as force per unit area. A pressure sensor is one of the most common sensors in scientific, industrial and other applications. In day-to-day applications, pressure sensors are found in tyre inflators, blood pressure monitor, water pipelines, industrial gas cylinders (oxygen, nitrogen, argon etc.), air compressors, pneumatic and hydraulic machines, vacuum systems etc. The pressure sensors are also used in flow rate measurement (in AC ducts, gas or liquid pipelines) and level liquid sensing. Miniature pressure sensors fabricated using MEMS technologies are deployed in various advance systems (intraocular pressure sensing, bed inflator, automobiles etc.) are often unnoticeable to the user.

2.2.1. Types of pressure measurements

The pressure measurement is of three kind gauge, absolute and differential as shown in Fig. 2.1. [6]

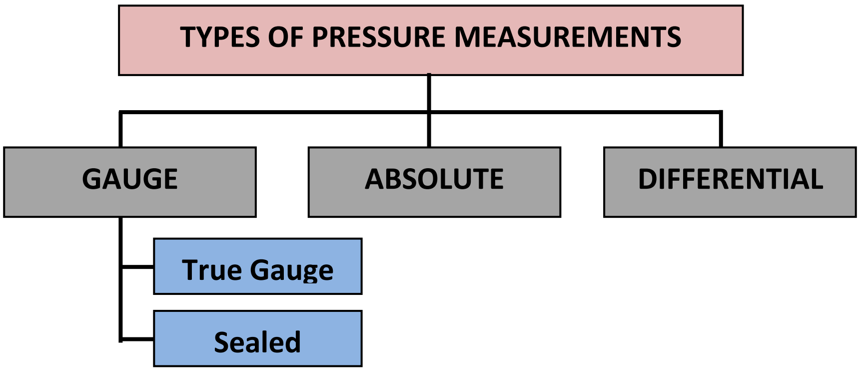

Fig. 2.1 Types of pressure measurement [6]

Gauge pressure is measured relative to atmospheric pressure. The 'gauge' type measurement has great relevance for the systems which are normally exposed to atmosphere. The measurement of tyre pressure, blood pressure and liquid levels are common examples.

However, the atmospheric pressure is not constant. It varies with temperature, altitude, and from place-to-place on the land. A 'true gauge' sensor has an opening to allow atmospheric pressure reach the reference side of the pressure sensing element for accurate measurements. The true gauge type measurement might be necessary for moderate pressure ranges (e.g. 10 bar or lesser) depending upon the accuracy demanded. However, in certain working environments, such as those with slurry, mud, dust or water jet, it is not favourable to provide a vent (access) to the sensing element (e.g. diaphragm) because any possible ingress may mar the functionality of the sensor. Therefore, some sensors have a reference cavity sealed under atmospheric pressure to circumvent the abovementioned issues. Such ruggedness is achieved at the cost of accuracy. The inaccuracy of measurement is same as difference of atmospheric pressures at the place of measurement and place of sensor calibration (not necessarily the place of fabrication). The sealed gauge pressure sensors are acceptable where the pressure range is high or geographical change of place or altitude is not there.

The absolute pressure is measured with respect to vacuum. The absolute pressure measurement is required for knowing the true (absolute) value of any pressure, and achieved by disallowing the atmospheric pressure in to the sensor. The absolute pressure measurement has significance for vacuum systems, gas flow at sub-atmospheric pressure as well as for quantification of atmospheric pressure itself.

Low (rough) vacuum (1 mbar to 10^3 mbar) can be measured with gauges employing mechanical sensing elements. These pressure sensors have an evacuated reference cavity for absolute measurement and the output is independent of the type of gas. For higher vacuum, Pirani (thermal conductivity), Penning (cold cathode ionization) and hot cathode ionization gauges are used.

Differential pressure is the measurement of 'difference' between two pressures. Generally, the differential is a small value compared to two pressures. The individual pressure values are independent and can be below, above or at par to atm. pressure. In fact, the gauge pressure is also a differential pressure wherein one of the pressures is atm. pressure. Similarly, an absolute pressure is a differential pressure where reference pressure is high vacuum. The differential pressure measurement is generally used for indirect measurement of flow velocity. In Fig. 2.2 [6], implementation of absolute, true gauge and differential measurements in diaphragm based pressure sensors is shown. In Fig. 2.2 (a), the reference side of the diaphragm is vacuum, hence this is an absolute type pressure sensor. In Fig. 2.2 (b), the reference side of the diaphragm is open to atmosphere; therefore such a sensor measures the applied pressure with respect to the actual or true pressure present at the place of measurement. In part Fig. 2.2 (c), the difference of any two pressures is measured by deflection of diaphragm.

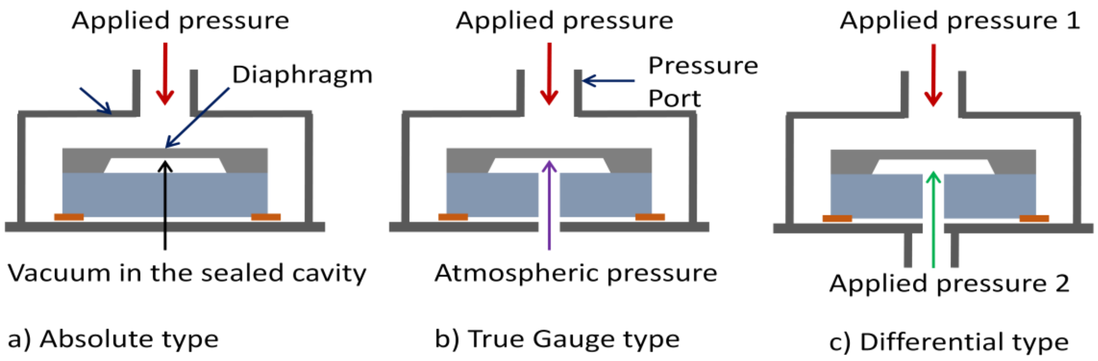

Fig. 2.2 Configurations for diaphragm based absolute, true gauge and differential pressure sensors [6]

2.2.2. Pressure sensor technologies

The effect of pressure can be seen in the form of deformation, deflection or movement of a flexible mechanical element. Such a mechanical flexible element is thus called 'sensing element' for pressure. Most common pressure sensing elements are diaphragms, bourdon tubes, capsules and bellows. It is worth mentioning, that any deflection of sensing element also accompanies strain in the element. Therefore, physical movement or strain in the sensing element can be 'related' to the applied pressure. The 'effect' of pressure shall be measured with a suitable transduction mechanism to give useful output (Fig.2.3) [7].

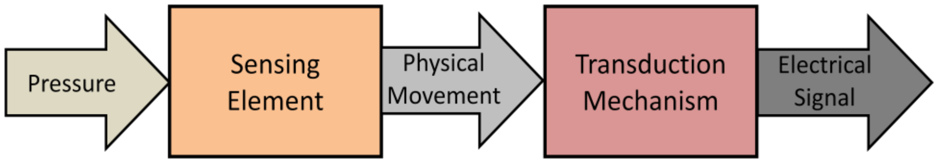

Fig. 2.3 Basic building blocks of a pressure sensor [7]

The physical movement can be read in contact (such as connected dial indicator or an LVDT) or noncontact fashions (such as capacitive or optical). The pressure can also be related to the developed strain in the sensing element. This forms the basis of transduction in the pressure sensors using strain gauges of various types. The sensing elements can be designed as per pressure range and the desired movement or strain.

There are numerous transduction principles such as pure mechanical, electromechanical (strain gauge, piezo-resistive, capacitance, inductance, variable reluctance, piezoelectric etc.) and opto-mechanical (Fig. 2.4) [7-8]. However, for technological reasons a few transduction principles have larger prominence than all others.

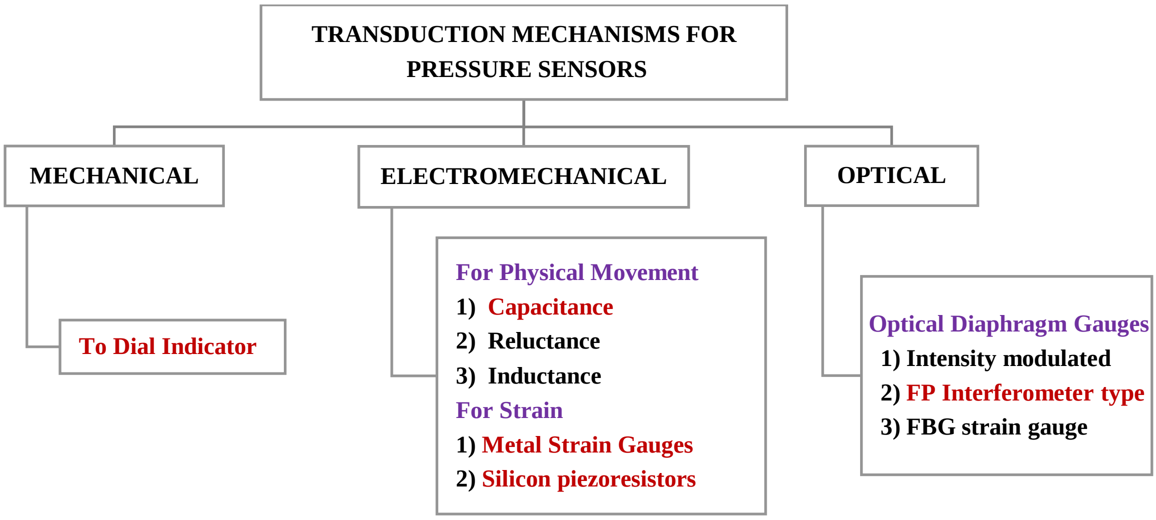

Fig. 2.4 Important transduction principles for pressure sensor [7-8]

MEMS is a cutting edge technology through which many types of microsystems including sensors and actuators are fabricated. An overview of MEMS pressure sensors can be found in the books by Beeby [8] and Alvi [9]. Topical review of MEMS piezoresistive pressure sensors is given by Shwetha [10] and Kumar [11]. A Critical review of MEMS capacitive pressure sensors is given by Kirankumar [12] and Eswaran [13]. The piezoelectric and piezoresistive pressure sensors are described in book by Wilson [14].

2.3. Optical Pressure Sensors

The optical sensors are based on changing an attribute of light by the measurand [15]. The light is an electromagnetic wave; hence it has associated amplitude (intensity), wavelength (frequency), phase, polarization and linear propagation property. Among these, intensity and phase are the most explored attributes for pressure sensing purpose. All interferometric sensors are based on change of phase as interference is a phase dependent phenomenon [15-16].

2.3.1. Intensity modulated optical pressure sensors

The optical pressure sensors can be based on numerous concepts and designs. The most straight forward designs are based of connecting a measurand to **change the intensity** of light. These sensors use simple low cost optoelectronic components (LED, photodiode) and therefore are **less expensive** in comparison of more sophisticated sensors based on phase or polarization (which require one or more of stabilized laser, tuneable laser, special fibers, polarisers, rotators, spectrometers etc.) [15-16].

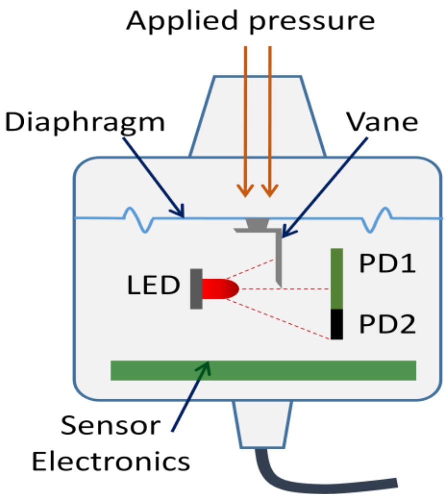

Fig. 2.5 Schematic of an optical pressure sensor with on gauge LED light source and photo diodes [17-18]

Schematic of a simple opto-mechanical diaphragm based pressure gauge is shown in Fig. 2.5 [17-18]. A vane connected to diaphragm blocks the light and moves in response to applied pressure. The amount of light received at measuring diode is related to the position of the vane and hence to the pressure. Only small deflections of diaphragm such as up to 0.5 mm are sufficient to cover full operational range. There is a reference photo diode for ratio-metric measurement of optical power and compensation of temperature drifts (of source and detectors both) as well as aging of LED. These optical pressure transducers do not require much maintenance. They have excellent stability and are designed for long-duration measurements. They are available with ranges from 5 psig to 60,000 psig (35 kPa to 413 MPa) and with 0.1% full scale accuracy.

2.3.1.1 Fiberoptic versions of intensity modulated pressure sensors

In some optical pressure sensors, light is carried to and from the sensor head by optical fibers; hence such sensors are also called **fiberoptic pressure sensors**. Another simple configuration based on ‘intensity’ of light is shown in Fig. 2.6 [15].

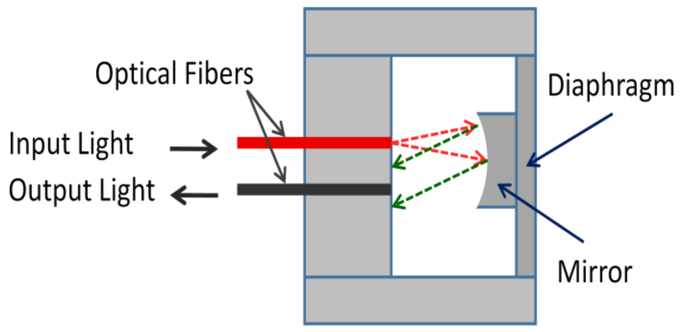

Fig. 2.6 An intensity based fiberoptic pressure sensor [15]

There are two fibers one input fiber carrying light from a light source and other collection fiber taking light to a photodiode. As the electronics is away from the sensor head or transducer, such sensors can withstand **electromagnetic /RF interference** and **higher temperatures**. The amount of light collected by latter is dependent on the position of reflecting diaphragm, which in turn depends on the applied pressure. Deflections of several tens to hundreds of microns are suitable for this type of transduction. A reference collection fiber can enhance the performance of sensor against factors such as aging of light source and losses over fibers and connectors. Such sensors can also be made using **fiberoptic bundles** of suitable configuration such as concentric, random or hemispherical. The receiving bundle is generally bifurcated in two parts, one for signal and other for reference.

Other intensity modulated pressure sensors are based on **micro-bending** of optical fibers [15]. A part of multimode fiber is sandwiched in saw-tooth or similar kind of structure causing micro-bending over the pressed length, as shown in Fig. 2.7 .

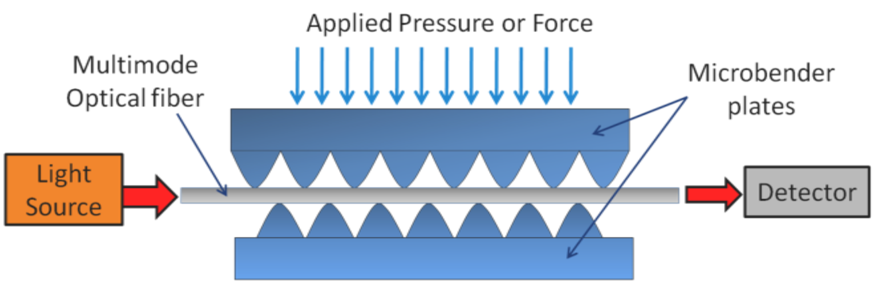

Fig. 2.7 A set-up for providing microbending to a multimode optical fiber [15]

The micro-bending results in leakage of light from the sides of an optical fiber. The loss of light increases with applied pressure, and this forms another basis of pressure sensing based on light intensity. A reference fiber is generally used which is not subjected to the micro-bending. It helps in ratio-metric measurement of signal and reference to eliminate common mode variability such as light source aging and bending losses.

2.3.2. Phase modulated fiberoptic sensors

The phase modulated optical sensors are based on principle of **interference**; hence they are very sensitive to the measurand and even a very small change is detectable. There are various types of interferometers in the field of optics such as Michelson, Fizeau, Twyman-Green, Mach-Zehnder, Sagnac and Fabry-Perot interferometer [19-21]. These classical **bulk-optics** based interferometers have little different physical implementations from one another, and hence suited for different kinds of applications.

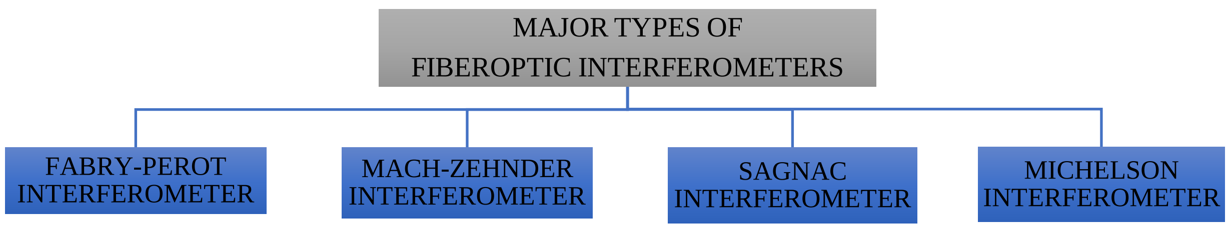

Fig. 2.8 Major types of fiberoptics interferometers used in phase modulated optical fiber sensors [22-24]

Many of these classical interferometers have been **implemented using fiberoptics** [16, 22-24]. Applications of Fiber-Optic interferometry technology in sensor fields, is given in [24]. Popular fiberoptic interferometers are given in Fig. 2.8 and their schematics are given in Fig. 2.9.

In the fiberoptic interferometers, fused fiber splitter (coupler) is used instead of cubic (or plate based) beam splitter. The cleaved ends of optical fiber act as reference mirror in FP and Michelson interferometers. In the fiberoptic interferometers, as the light is guided in optical fibers, extra mirrors for bending or changing the direction of beam are not required. Thus fiberoptics based interferometers are **light weight, portable, compact, robust and less expensive**. Therefore, fiberoptic interferometers are more apt choice for sensing application as compared to their bulk optics counterparts.

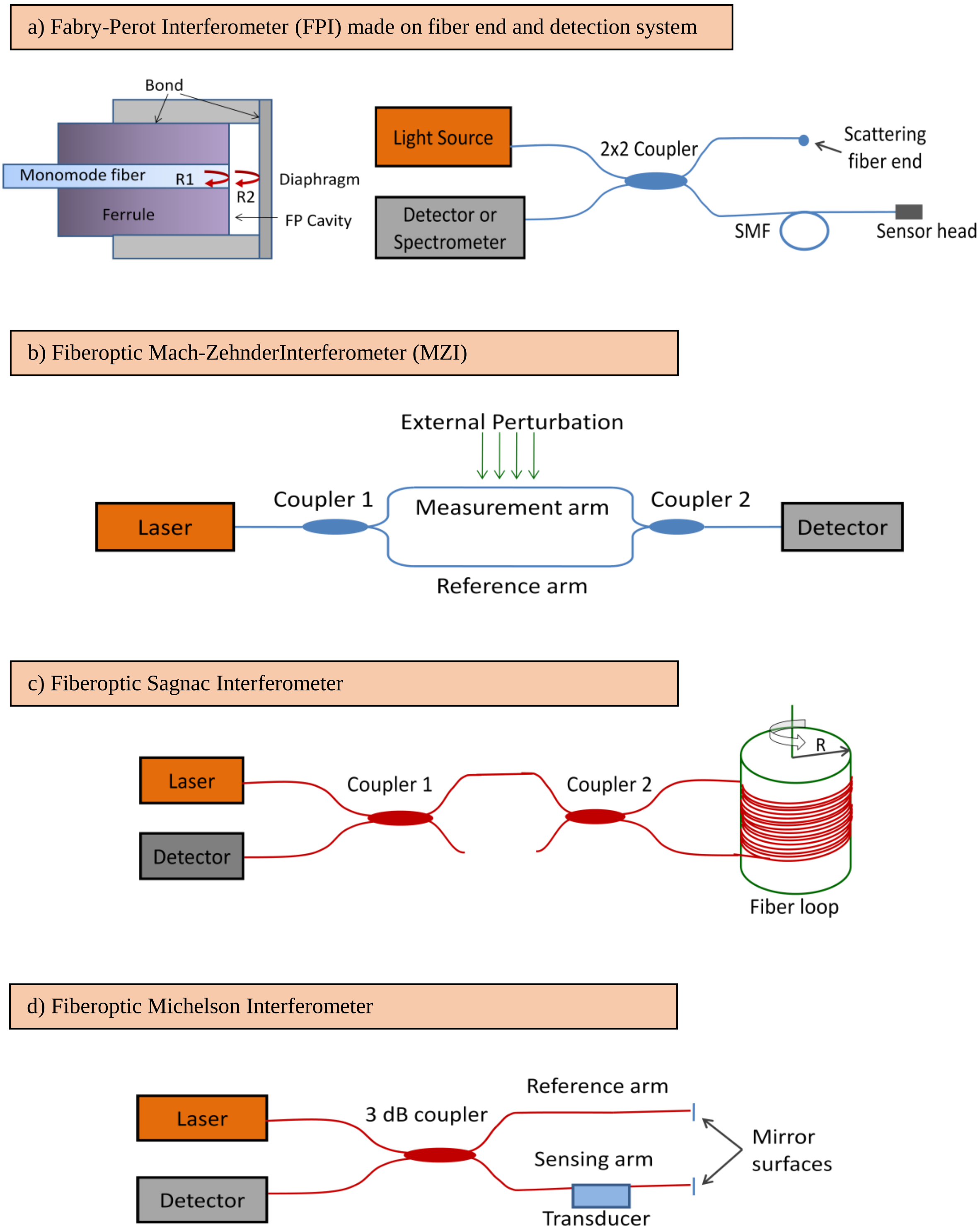

Fig. 2.9 Popular fiberoptic versions of the interferometers [15-16, 22-24]

The **FP interferometer** [20-21] has two partial reflectors (or mirrors) parallel to each other. The classical FPIs use very high reflectivity (> 99%) mirrors which result in '**multi beam interference**' and high finesse of interferometer. However, in the domain of fiber optic FP sensors, low-finesse interferometers are also widely accepted. A cleaved end of an optical fiber itself can act a partial mirror due to Fresnel reflection from the glass-air interface. The surface can be coated with thin films or metallic layer to enhance the reflectivity and control the properties of the interferometer.

A simple schematic of a FO FPI pressure sensor is given in Fig. 2.9 (a). The first reflection of light takes place at the cleaved end of the optical fiber. The second reflection is at the diaphragm surface. The gap between the two mirrors is called '**FP cavity length'.** On application of pressure, the diaphragm deflects and changes the cavity length and thus the 'optical path difference (OPD)' in the interferometer. The OPD is detected (or sensor demodulated) using one of several techniques (section2.5). The OPD can be **calibrated** against the known applied pressure. The FP interferometers fabricated partially or fully outside on the optical fiber end are called External or **Extrinsic FPI** (**EFPI**) sensor. Such a pressure sensor can be packaged in the form of sensor probe with pressure port for connection. Chronology of Fabry-Perot interferometer based fiber-optic sensors and their applications, is given by Islam *et al.* [25] in 2016.

The fiberoptic **Mach-Zehnder Interferometer (MZI)** uses a first fiberoptic splitter (coupler) to split the light power in two parts (Fig. 2.9 b). One part goes into '**reference arm**' optical fiber which is shielded from exposure to measurand (or perturbation). Other part goes in '**sensing arm**' (or measurement arm) optical fiber. When the measurement arm is subjected to the external strain or temperature, its optical path length (OPL) is changed accordingly. This creates an optical path difference (OPD) between the two arms. A second fiber optic coupler **combines** the two light beams in the output fiber. The change in measurand changes of output optical power in sinusoidal fashion. The two arms are coated to enhance and reduce the individual sensitivity towards measurand, and enhance the differential sensitivity. This interferometer is more suitable for strain measurement such as intrusion detection, but can also be designed to sense pressure through proper sensing element. Simultaneous measurement of refractive index and temperature using a Mach-Zehnder interferometer is presented by Tao Jiao [26] in 2019.

The fiberoptic **Sagnac interferometer** (Fig. 2.9 c) uses a loop of optical fiber with light propagating in both, clockwise as well as anti-clockwise directions. The rotation gives a phase difference between two components. This interferometer was very successfully used in fiberoptic gyros for navigation control of aircrafts. This gyro has the advantage of no mechanical moving part (hence no wear or hysteresis), light weight, compact and high sensitivity [27]. Overview of principle and applications of Sagnac fiber interferometer is given by Brian Culshaw [28]. Its application in temperature measurement is given in [29].

A classical **Michelson Interferometer (MI)** has one moving (sensing) reflector (mirror) and one reference reflector. The fiberoptic version of the interferometer can be implemented with cleaved fiber ends of splitter acting as two reflectors (Fig. 2.9 d). The transducer can be designed to convert the measurand such as pressure into strain in the sensing arm using suitable design of sensing element. MI gives “two-beam interference” as other interferometers (excluding high Finesse FPI which essentially has high reflectivity mirrors). They are used in acoustic [30] and ultrasonic sensing [31] among others.

2.4. Theory of Fabry-Perot Interferometer

The theory of FP interferometer is given in detail with derivations in books by Born and Wolf [20] and Ghatak and Thyagarajan [21]. A classical FP interferometer consists of two plane partial mirrors of very high reflectivity arranged parallel to each other at certain gap, as shown in the figure drawn (Fig. 2.10).

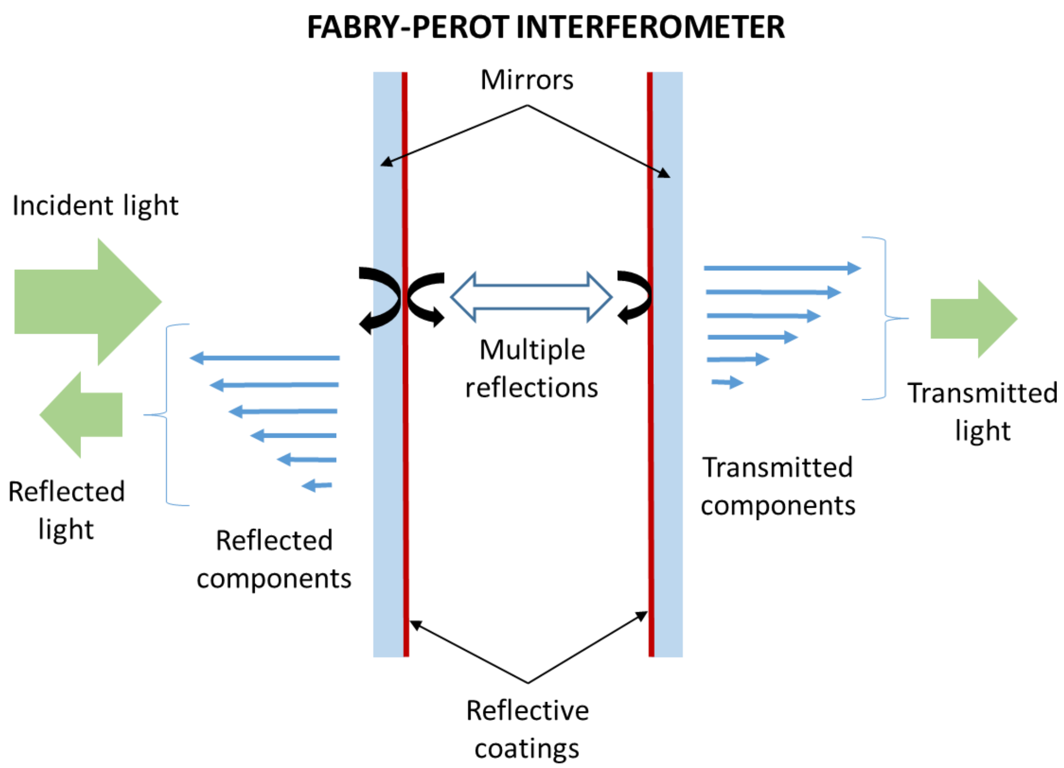

Fig. 2.10 A Fabry-Perot Interferometer (FPI) [20-21]

The light beam incident on the first mirror undergoes a reflection there and remaining part enters the FP cavity. Then the remaining part of the light beam undergoes reflection and transmission at the second mirror. The second transmission component comes out of the cavity, but the second reflected component undergoes multiple reflections between the two mirrors. On each reflection from the mirrors of FP cavity, there is some component of light that leaks (transmitted) out of the cavity. The amplitude of each successive reflected and transmitted beam reduces after each incidence. Also there is some phase retardation while the beam travels between the two mirrors. Thus, at both the side of FP cavity, there is a set of beams with relative change in amplitude and frequency that “**interfere**” to yield resultant intensity. The detailed derivation of expression for the reflected and transmitted power from FPI can be found in the book by Ghatak and Thyagarajan [21]. The reflected and transmitted optical intensities (power) are complementary to each other for any wavelength.

The reflectivity R_{FP} of an FPI is given by following equation

$$\boldsymbol{R_{FP} = \frac{F.sin^2\left(\frac{\delta}{2}\right)}{1 + F.sin^2\left(\frac{\delta}{2}\right)}} \qquad \textbf{Eq. 2-1}$$

Where the ‘F’ is called the “**Reflectivity Finesse**” of the FPI and ‘δ’ is the phase change (or phase retardation) underwent by the light in completing one close loop in the FP cavity, as given below

$$\boldsymbol{F = \frac{4R_s}{(1 - R_s)^2}} \qquad \textbf{Eq. 2-1}$$

$$\boldsymbol{\delta = \frac{4\pi nl}{\lambda}} \qquad \textbf{Eq. 2-2}$$

Where ‘R_s’ is the “**surface reflectivity**” of each mirror, ‘l’ is “**cavity length**” (that is gap between the two mirrors) and ‘n’ is the **refractive index** of medium in FPI. The ‘λ’ is the “**wavelength**” of light.

Fig. 2.11 Plotted 'Reflectivity Finesse' of FPI with normalized reflectivity of mirrors

The **finesse** of FPI increases rapidly (for any wavelength) when the reflectivity of mirrors is high, as plotted in Fig. 2.11 using Eq. 2-2. In the figure, the normalized reflectivity is plotted on x-axis. It basically signifies the selectivity of the FPI for a wavelength. **High finesse FPI** are used to separate very close spectral lines (example sodium lamp), as tuneable filter and in laser cavities.

The phase retardation (δ) is dependent on both, the length (l) of FP cavity as well as the wavelength (λ) under consideration (Eq. 2-3). Typical overall reflectivity characteristics of FPI as a device are plotted in Fig. 2.12 using Eq.2-1. The reflectivity of FPI is a function of phase retardation which in turn is a function of optical path length and wavelength. The phase can be changed by changing cavity length or the wavelength of operation. The phase change of light is presented in terms of angle. Therefore, the reflection characteristics are periodic with change of phase. The shape of reflectivity curve of the FPI is dependent on the finesse of the interferometer. As the finesse of the FPI increases, the top becomes flatter and the notches become sharper in the reflection characteristics.

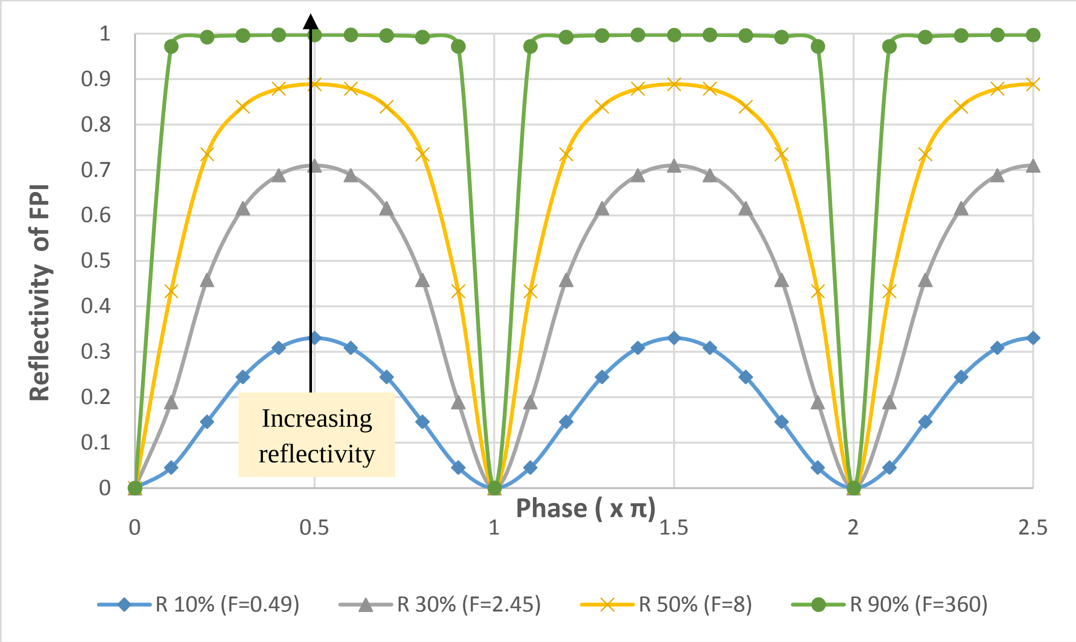

Fig. 2.12 The reflection characteristics of a Fabry-Perot Interferometer

The reflection and transmission characteristics are complementary to each other, assuming that there is no absorption (or other losses) of light in the cavity. In the transmission, there would be sharp peaks for high finesse FPI, which are used as wavelength filter.

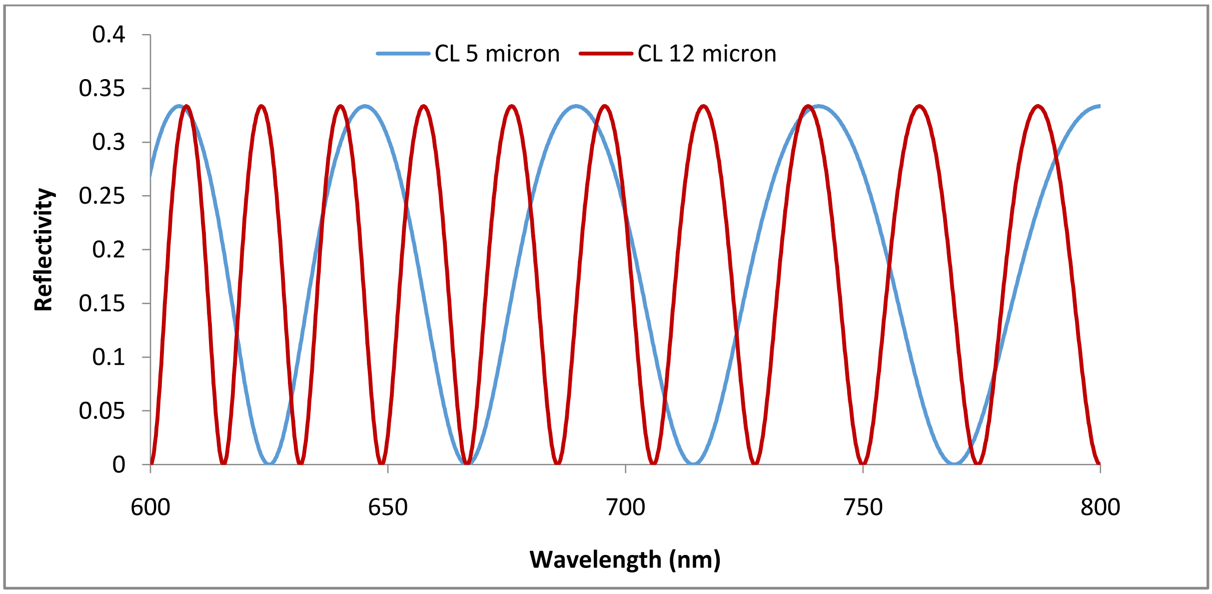

Fig. 2.13 Plotted reflectivity of FPI with wavelength

The reflection characteristics of an FPI are shown **with wavelength** in Fig. 2.13 for two FP cavity lengths with finesse value 0.5 (both mirrors with 10% reflectivity). The small cavity length gives lesser number of fringes in a given wavelength window and vice-versa. The periodicity decreases with increasing wavelength. For low finesse FPI, the reflection curves are near sinusoidal. As the finesse increases, more number of beams participate in the interference and result in more skewed characteristics.

It is clear from Fig. 2.12 that the output of an FPI varies with the phase(δ) of light which in turn depends on the cavity length and refractive index between the two mirrors and the wavelength of light used. Therefore, if a measurand is connected to an FPI in such a way that its variation varies either the cavity length or the refractive index (RI) or both in a defined manner, then it would form a basis of sensing the measurand.

The fiberoptic FPI pressure sensors are generally designed in such a way that pressure changes the cavity length through deflection of a diaphragm in a hollow cavity (Fig. 2.9 a). However, for temperature sensor, a solid optical cavity is used. The RI and the cavity length both vary with temperature.

2.4.1. FPI based fiberoptic pressure sensors

A review of fiberoptic sensors is given by Kersey [32]. High performance fiberoptic sensing is described by Kirkendall [33]. Various fiber-optic pressure sensors for biomedical and biomechanical applications is given by Roriz Paulo [34]. The technological advances and industrial state-of-the-art of fiberoptic sensors is given by Tucker [35]. Wild et al. [36] have given overview and state-of-the art of various optical fiber sensors including fiber interferometers for detection of dynamic strain and acoustic waves. The literature discloses various fiberoptic sensors for different scientific and engineering applications.

Fabry-Perot Interferometer (FPI) based fiberoptic sensors are the most popular phase modulated (interference based) pressure sensors. Very small deflections of diaphragm can be measured with high accuracy. A review of fiberoptic extrinsic FPI sensors is given by Rao [37] and that of **fiberoptic Fabry-Perot interferometer based pressure sensors** is given by Yu [38]. The full scale deflections of diaphragms are generally within several micrometres only. One of the physical implementation is shown in Fig. 2.14. There is a reference reflective surface (such as end face of fiber) and a reflecting diaphragm. They are spaced at very small cavity gaps from a fraction of micrometre to several tens of micrometres, based on the pressure range and optical demodulation method. The two reflected beams interfere and demodulated by an optoelectronic analyser at the distal end of fiber. These sensors have advantage of small size and high sensitivity among others.

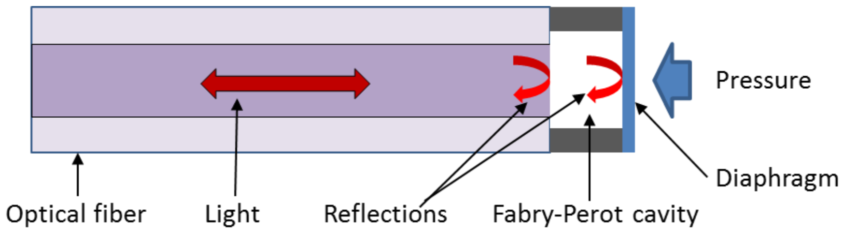

Fig. 2.14 A Fabry-Perot pressure sensor made on optical fiber end [38]

2.5. Demodulation methods and design of FP sensors

The pressure sensor design relates the pressure range to the measurable deflection (or strain) range. The pressure range is governed by the application for which the sensor is to be developed. The measurable deflection is governed by the underlying technology or method of detection. Therefore, the diaphragm as a sensing element is designed to “map” the full scale pressure to a full scale deflection.

More sensitive detection techniques such as interferometry require very small deflection. Accordingly, the lateral dimensions of the diaphragm can also be reduced while keeping other parameters (thickness, maximum stress) same. This opens the avenues for miniaturization of sensors.

The FPI based interferometers can be “demodulated” in various ways. Some popular methods of demodulation are classified and represented in Fig. 2.15. These methods or techniques can be broadly divided in two categories: a) Laser based demodulation and b) Low Coherence (or White Light) based demodulation [38].

The laser based demodulation systems have lesser complexity of hardware. The detection is based on the measurement of optical power through photodetector(s). The resolution of movement is governed by the detector noise as well as the stability of laser in terms of power output and wavelength.

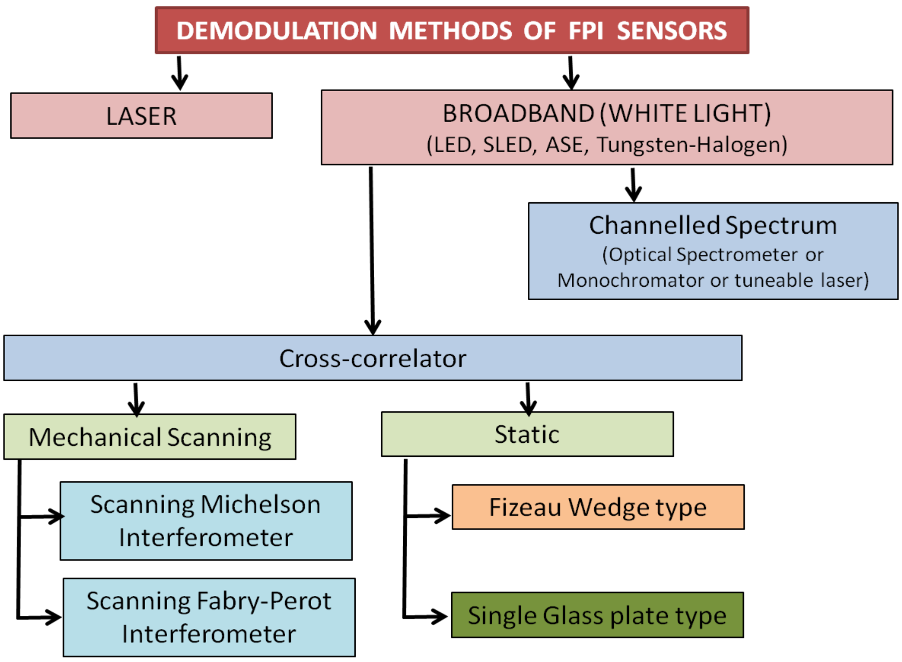

Fig. 2.15 Various popular demodulation techniques for FPI based sensors [38-52]

The maximum movement of diaphragm is limited to within a quarter wavelength, else there would be phase ambiguity in detection. For example, if a 1550 nm laser is used for the sensing, the diaphragm movement should be less than 387 nm (less than 0.4 μm). As the measurements are based on power, random losses by fiber bending or connector also affect the measurement accuracy. Jun Wang et al. [39] have implemented a new technique named SCIIB to overcome the losses on the optical path and drift of power of light source. SCIIB (Self Calibrated Interferometry Intensity Based) uses a broadband light source and the part of the broadband signal from the FPI sensor is channelled through a narrowband filter. The OPD in FPI sensor is so designed that the narrowband signal gives interference like laser and broadband does not. The ratio of first (narrow) to second compensates for any losses of optical power over the optical circuit. However, this technique has similar limitation of movement of diaphragm, as in other laser based system. The absolute cavity length cannot be measured.

The low coherence (or white light) based demodulation techniques use a broadband light source such as a LED (light emitting diode), ASE (amplified spontaneous emission), SLED (super-luminescent LED), THL (tungsten halogen lamp) or tuneable laser.

These Low Coherence Interferometry (LCI) also known as White Light Interferometry (WLI) based techniques are at large immune to variations (losses) in optical power levels. They do not suffer from phase ambiguity in detection, therefore, allow for larger movement of diaphragm compared to those by lasers. Rao and Jackson [40] have given a comprehensive insight into fibre optic low-coherence interferometry. The LCI or WLI technique was widely preferred and implemented by various researchers in demodulation of FPI based sensors of different designs [41-43]. As given in Fig. 2.15, cross-correlator and channelled spectrum are two popular types of LCI or WLI.

2.5.1. Cross-correlator based demodulation

A cross-correlator uses a second interferometer for the demodulation (finding OPD) of the sensing interferometer. The second interferometer gives high optical output when its OPD matches exactly with that of sensing interferometer. Conventionally, the second interferometer's path length is varied with mechanical sweep. It involves time of scan and mechanical wear, thus are not amenable for field instrumentation.

The static correlators do not need mechanical tuning to match the OPD with the sensing interferometer. A popular and simple cross-correlator is based on a Fizeau wedge interferometer as demonstrated by Belleville and Duplain [44] for WLI based fiber-optic strain sensors. The Fizeau wedge essentially has a gradually varying OPD (due to air wedge between two glass plates). The incoming light is expanded to fall over the length of the Fizeau interferometer. The cross-correlation pattern is captured using CCD linear array detector. The pattern moves on the CCD when the OPD in sensing interferometer changes. The demodulator is simple, static and fast. However, the maximum change of OPD is limited to under 10 µm, which is yet good for many sensor designs. A recent (2019) paper by Zilong describes the optimization of the wedge to select a single cavity length signal from the compound signal [45].

A recent (2019) paper by Ke Chen reports an even simpler correlator where just a small piece of glass wafer is used along with CCD array detector [46]. There are other types of correlators also which use fiberoptic versions of interferometers or other advance techniques for detection of OPD of sensing interferometer [47].

2.5.2. The Channelled spectrum technique

This technique is based on analysis of modulation in spectral domain. Monochromators, tuneable or sweeping lasers or linear array based spectrometers are used. The spectrometer is most common for its fast electronic scan and read time. The spectrometer is used in two ways:

2.5.2.1 Fringe tracking

A peak or valley is tracked with change of OPD in sensing interferometer [48-49]. The method allows for simple algorithm for detection, as the measurand is directly related to the position of peak or valley on a linear array detector. The sensor design is considered accordingly. The FPI sensor should have sharp valleys, thus high Finesse and highly reflective coatings are desired. Also, the **cavity lengths should be small** to give a large FSR (Free Spectral Range) in the signal which means that the valleys will have large gap in wavelength domain. This will increase the movement of diaphragm of sensor.

2.5.2.2 Absolute cavity length

More than one value of peaks or valleys of the spectral signal can be used to calculated the cavity length in FP sensor. This technique allows for very large movement of diaphragm as it can measure wide range of cavity lengths. Shrinkhla Ghildiyal *et al.* [50] and Rathod *et al.* [51] used diffraction grating and linear CCD based optical spectrometer for FPI measurement. Ma Cheng [52] analysed the spectrum for low finesse EFPI.

The **sensor design parameters** such as cavity length, range of deflection, reflectivity of mirrors, natural frequency of diaphragm, multiplexing of sensors; all are **dependent on the demodulation method** selected.

2.6. EFPI sensor materials, fabrication techniques and applications

The EFPI fiberoptic pressure sensors have various physical designs and materials such as silica [53-56], sapphire [57-58], polymer [59-63], metal [50, 64-66], composite [67] and silicon [68-69]. These materials are suited for different applications; such as polymer for low cost biomedical, sapphire for very high temperature and reactive environment etc.

Various micro-fabrication techniques are used for making FPI sensors. These are fusion splicing [54], joining by CO_2 laser [68, 70], femtosecond laser machining [71], UV molding [72], Focussed Ion Beam (FIB) [73] and Diamond Turn Machining [64, 74]. There are varieties of applications such as biomedical, acoustics, ultrasonic, partial discharge, high temperature application in the sensing of pressure, strain, temperature etc.

In the present work the focus is on MEMS based designs of EFPI pressure sensors as discussed in the next section.

2.7. MEMS based EFPI pressure sensors

The MEMS stands for *Micro Electro Mechanical Systems*. The technology is also referred to as the *Microsystems Technology* in some parts of the world. MEMS, as the name indicates are basically the sensors & actuators with size of functional elements in the range of sub millimeter to a few millimeters. MEMS technology generally harnesses the electrical, mechanical and crystallographic properties of silicon. Functional elements like diaphragms, cantilevers, beams and proof mass etc. can be fabricated by (Bulk and Surface) Micromachining techniques developed for silicon [4-5]. The electronics can also be fabricated on the same chip. MEMS sensors are very high accuracy, small size and light weight and find applications in the fields of space, communications, defense, automobiles, biomedical and many others. The popular commercial available MEMS are pressure sensors (capacitive or piezoresistive), accelerometer, micro-pumps, optical communication switches etc. In the field of optical pressure sensors, the micro fabrication technologies have been used and demonstrated in the literature [75-77]. Such sensors have been referred to as optically interrogated or optical MEMS pressure sensors [76]. Some relevant examples are given here.

Abeysinghe *et al.* [78] describes **optically interrogated MEMS pressure sensor** fabricated directly on an optical fiber. The fabrication includes photolithographic patterning, wet etching of a cavity on glass ferrule, and **anodic bonding** of a silicon diaphragm. This employed both 200 and 400 µm-diameter multimode optical fibers. The sensor showed a linear response over 0–80 psi static pressure. This sensor is expected to find application in situations where small size is advantageous and where dense arrays may be useful (Fig. 2.16).

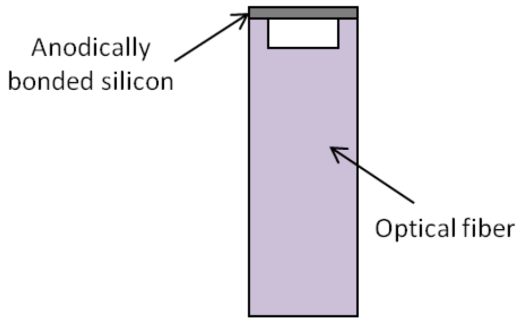

Fig. 2.16 Configuration of a fiber optically interrogated MEMS pressure sensor [78]

The Fig. 2.16 shows the usual configuration, which consists of a glass plate with a shallow cylindrical cavity etched into one surface with the cavity covered by a thin silicon diaphragm that has been anodic bonded to the patterned glass wafer. In the second configuration, the cavity is formed on the end of the optical fiber and a silicon diaphragm is bonded by anodic bonding. The linear pressure range here is approximately 5.44 Atmosphere. This was beginning of such sensors thus the issues like **"Entrapped Gas in Sealed FP Cavity"** have not been given any consideration.

Xiaodong Wang *et al.* [79] described a very sensitive acoustic sensor for partial discharge. This sensor is meant to work in oil media with some static pressure. The side hole drilled in the glass substrate is meant for providing the same static pressure at the reference side of the diaphragm also. The centre hole is 40 µm deep and the main cavity is 50 µm deep. There is no entrapped gas as the cavity is open. Also, the deflection is limited to 4.73 µm (Fig. 2.17).

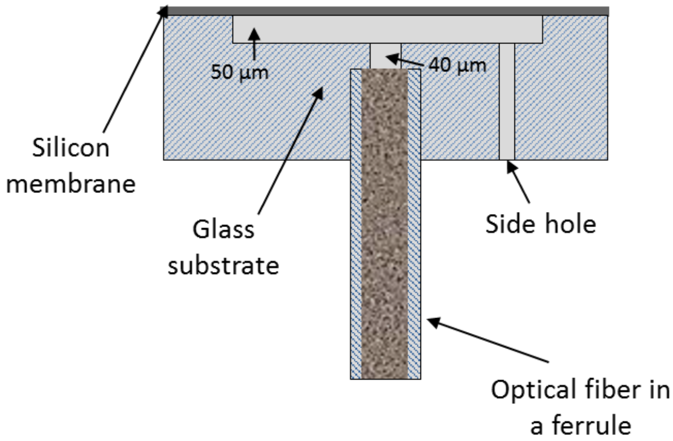

Fig. 2.17 Pressure sensor based on MEMS technology [79]

Ni xiao-qi *et al.* [80] demonstrated a pressure sensor based on FPI and MEMS technology. Light is coupled into the sensor through a fiber. **Dual-wavelength** demodulation method is used to analyze the reflected optical signals and compensate the errors. Experimental results for pressure measurements ranging from 0 to **3 MPa (30 bar)** demonstrate reasonable linearity and sensitivity (Fig. 2.18).

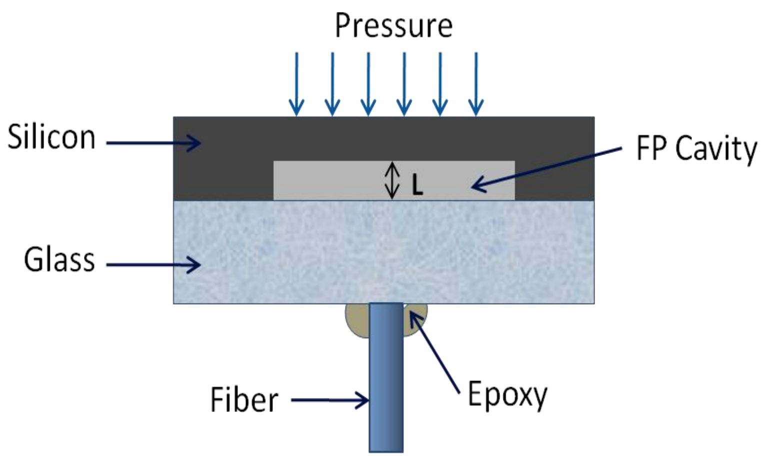

Fig. 2.18 Optical MEMS Pressure Sensor [80]

In this **Anodic Bonding** is used to bond silicon to glass. However, it is **not mentioned** if the same is performed under vacuum or atmosphere. It seems to have been performed under atmosphere. The cavity length is 4.1 µm only and full scale deflection is yet smaller, a mere 0.38 µm over 30 bar pressure. Though the **trapped gas is there**, the effect of it would be ignorable, so it was not reported in this work.

Jinde Yin *et al.* [81-82] have fabricated **MEMS-based fiberoptic pressure sensor** with **anodic bonding**. The vacuum-sealed microcavity with a thin silicon diaphragm is used as sensing element and its deformation characteristics determine the pressure measurement performance. Considering **residual gas** inside Fabry-Perot cavity and the thermal properties of material, they have established a **mathematical model** for sensor's **temperature response** based on **ideal gas equation** and elastic theory. Temperature experiment of this sensor was carried out under vacuum. This work provides a guideline for temperature compensation process for achieving high precision pressure measurement (Fig. 2.19).

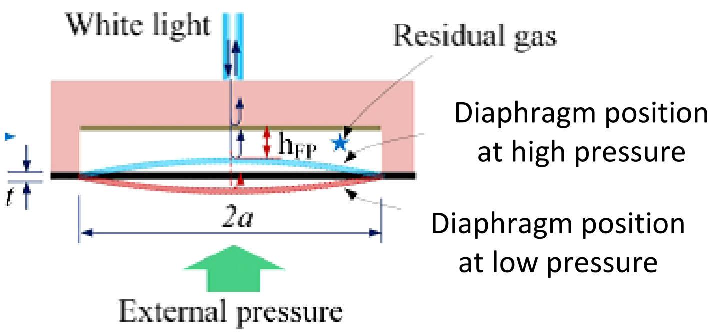

Fig. 2.19 MEMS based FP pressure sensor [81-82]

The residual pressure of about 250 to 400 mbar indicates that the anodic bonding is done under ambient pressure. This paper is majorly concerned about the temperature response of the EFPI sensor. The cavity length is 27.3 μm, circular diaphragm's diameter is 1.86 mm. Temperature range is 230 K to 370 K and pressure range is 0 to 2 bar (absolute). The deflection range simulated is only 0.8 μm whereas experimentally verified one is only 0.08 μm. Here, the maximum deflection (0.8 μm) is about 2.9 % of the cavity length (27.3 μm). **However, in this paper a) deflections are too small compared to cavity length b) characteristic equation is not derived c) Span and offset are not considered with pressure range and cavity length as design parameters.**

2.8. Summary of literature survey

The fiberoptic sensors offer special advantages such as immunity to EMI/RFI, miniature size, light weight, high temperature capacity and intrinsically safe. These sensors can be the only choice for doing measurements in high voltage, hostile or RF environments. A sensor of range 1 bar absolute is very useful for measuring rough vacuum in systems such Chemical Vapour Deposition (CVD), sputtering, ion implantation, e-beam welding and other vacuum systems.

The pressure sensors based on the principle of a Fabry-Perot interferometer (FPI) are being very widely pursued by researchers in the domain of fiberoptic sensors. These sensors are fabricated using MEMS technologies and appropriately named as optical MEMS pressure sensors or so.

It is seen that many implementations of these sensors used some kind of bonding to create the FPI cavity. There would be some amount of residual air or gas left in the cavity after the sealing process. The adverse effect of this has been explored by the researchers from the perspective of its temperature effects. However, an effect that was ignored is related to the change of cavity pressure by movement of the diaphragm itself in the sealed micro cavity sensors. It is found interesting as well as worthy to investigate and understand the behaviour of pressure sensor having trapped gas in sealed cavity. The same is the subject matter of this research work.

2.9. Gap areas

Sensors fabricated using silicon & allied technologies are widely known as MEMS sensors. Also, fiberoptic pressure sensors based on principle of Fabry-Perot Interferometer (FPI) are known in literature. These have been realized in various forms and for different applications as discussed earlier in this chapter. FPI sensors those based on MEMS technology are also referred to as Optical MEMS Pressure Sensors [47, 79-80].

In literature, wherever Anodic Bonding is applied for fabrication of such sensors; it is done either under "vacuum" environment for low pressure sensors for the best results; or the same is done under atmospheric pressure, when the pressure range is high and the diaphragm deflections are small compared to cavity length. It is intuitive that any resultant gas captured in the sealed cavity (when the same is done under atmospheric pressure) will resist the inside deflection of the diaphragm of pressure sensor. The gas will also respond to temperature. Thus the reference pressure itself is not constant. This will affect the offset, span, linearity and temperature behaviour of the pressure sensor. The following gap areas have been identified in literature.

1) The deflection range of pressure sensing diaphragm is underutilized for compactness of the sensors. This leads to more sophisticated and costly detection systems [78, 80].
2) The sensor designs leading to low cost, compact and field deployable systems have not been fully explored
3) Multiplexing of EFPI pressure sensors is not much explored
4) The EFPI pressure sensors based on metallic construction have not been explored widely
5) Combination of different types of fiberoptic interferometers for simultaneous measurement of pressure and temperature have not been explored
6) Other principles of temperature measurements such as black body radiation, spectral absorption or standard electrical sensors wherever possible have not been explored for combining with FP pressure sensors
7) Any other effect of trapped gas, different than that arising from change of temperature, is not considered in the literature
8) The deflection-dependent reference pressure as well as deflection of diaphragm in such case are not modeled
9) The analysis of sensor’s performance with cavity length parameter is not carried
10) The FE analysis of pressure sensor comprising trapped gas is lacking
11) Technique for non-contact measurement and characterization of cavity length in the Fabry-Perot sensor is not found

2.10. Scope of the research work

The deflection of diaphragm depends on reference pressure, which depends on cavity volume and that depends on deflection itself. Thus, it is found interesting to derive the closed loop solution for deflection of the diaphragm given the cyclic nature of dependency.

Further, the extent and severity of effects of trapped gas on sensor characteristics (viz. offset, span, linearity, and temperature effects) were largely unattended. Also, how these effects depend on different design parameters such as FP cavity length, pressure of the trapped gas and the deflection sensitivity of diaphragm, are not known. While the 1 bar absolute pressure sensor is very useful for vacuum systems, the 10 bar sensor is useful in process instrumentation [83-85]. Two ranges have been chosen to see the extent of effect of the trapped gas on pressure sensors having diaphragms of different rigidities. A difference of an order of magnitude is deemed appropriate for comprehensive study. Thus, the following is the scope of research in the present work.

1) Design of the silicon diaphragm based sensor (0-1bar and 0-10 bar pressure ranges)
2) Modelling of closed loop solution for deflection of diaphragm of sealed cavity sensor
3) Modelling of deflection characteristics (comprising span and offset) with cavity length as design parameter
4) Study of the temperature effects of the trapped gas on sensor characteristics and the effect of cavity size
5) Numerical modelling of the sealed cavity pressure sensor
6) Fabrication, testing and experimental validation

Chapter 3

ANALYTICAL MODELLING OF SEALED MICROCAVITY FABRY-PEROT PRESSURE SENSORS

3.1. Introduction

The residual gas in the sealed cavity has largely been neglected in previously published literature. In this chapter, the effect of varying reference cavity pressure on the sensor characteristics has been investigated and modelled. The developed model is not limited to anodic bonding only and can be used for sensors fabricated using any other sealing method. Sensors of two pressure ranges namely 0-10 bar and 0-1 bar (absolute) have been designed. They are referred to as 10 bar sensor and 1 bar sensor respectively, for brevity in further discussions. In the following sections design of the sensors, derivation of governing equations, deflection characteristics including offset and span of sensor are presented. It is followed by discussions and conclusion.

3.2. Design of EFPI pressure sensor for analysis

For the present analysis, the MEMS based design of the pressure sensor as shown in Fig. 3.1 is considered. The desired deflection of diaphragm has been set about 15 µm in order to have moderate change in the FP cavity length. This large deflection can easily be handled with WLI based optical interrogation method. As a rule of thumb for linear mechanical behaviour of square diaphragm, the full scale deflection should be less than 25% of the thickness of diaphragm [86]. For 1 bar pressure sensor, the diaphragm thickness of around 130 µm is chosen so that the full scale deflection is less than 12% of the thickness. This requires square diaphragm to have side length of about 8 mm. Thicker and larger diaphragms with same deflection could have been designed as well, thus producing sensors of different lateral sizes but same cavity length. However, these sensors would perform in the same manner due to same volumetric changes on application of external pressure. Sensors of different FP cavity lengths such as 7, 15, 30, 60, 100 μm and more have been investigated. As the design of the sensor is based on MEMS, the following major fabrication steps are involved. The front cavity, which defines the length of Fabry-Perot Interferometer (FPI), is created by anisotropic wet etching after photolithography. The silicon wafer comprising front cavity is joined to suitable glass wafer by anodic bonding process [87]. The backside cavity, which determines the thickness of the diaphragm, is formed after the bonding using reactive ion etching. The FPI gets formed between the inner surfaces of glass wafer and the silicon diaphragm. The optical fiber is connected on the glass surface.

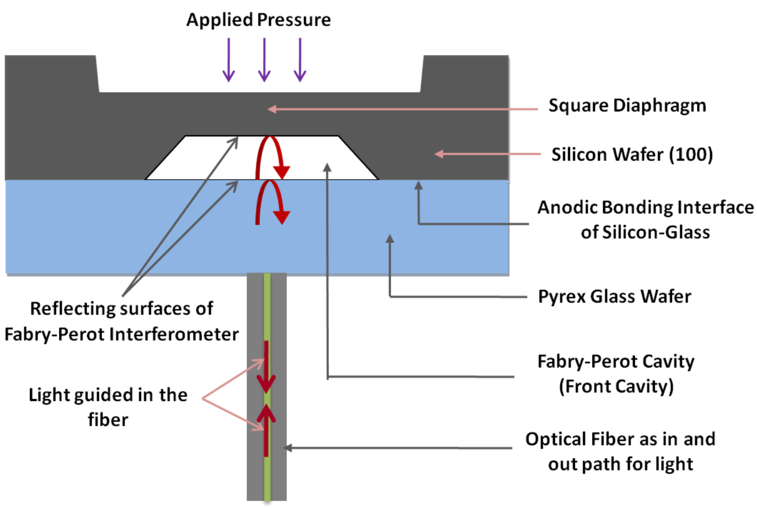

Fig. 3.1 FPI based pressure sensor with MEMS construction

3.3. Analysis of the sealed micro cavity pressure sensor

The deflection of diaphragm is shown in the schematic of pressure sensor (Fig. 3.2). As there is finite pressure of trapped gas in the sealed cavity, the deflection is inward (positive) when the applied pressure (P_a) exceeds the pressure of trapped gas (P_c). The deflection is outward (negative) when the applied pressure is less than the pressure of trapped gas. The pressure and volume of the cavity change in response to the applied pressure. The cavity pressure increases with increasing applied pressure and increasing inward deflection of diaphragm; and vice-versa.

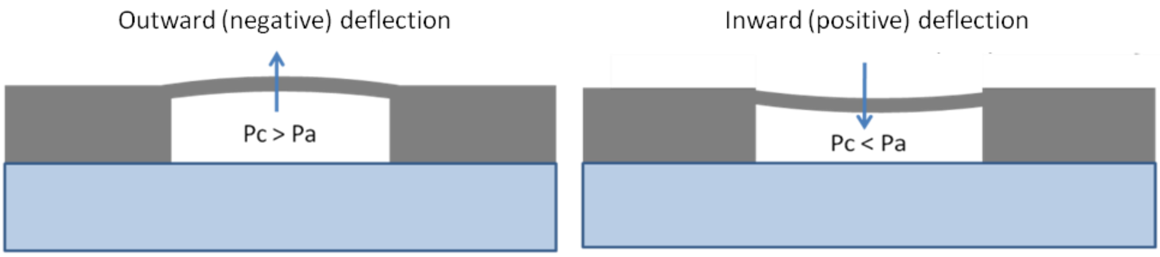

Fig. 3.2 Negative and positive deflections of diaphragm

The deflection is 'zero' (null-deflection) when both the pressures are equal (Fig. 3.3). Therefore, irrespective of pressure range of the sensor, the zero deflection occurs when the applied pressure is same as pressure in the cavity. The pressure (P_c) and volume (V_c) in this case are referred to as 'initial' cavity pressure (P_{c0}) and 'initial' volume (V_0) respectively.

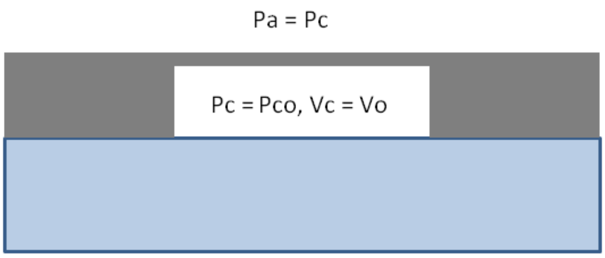

Fig. 3.3 The null-deflection condition of diaphragm

The analysis is carried out to understand the effect of trapped air on span and offset of the pressure sensor. The assumptions in this analysis are listed below. A closed loop solution is derived for diaphragm deflection as a function of applied pressure and sensor parameters. In the following subsections, estimation of residual pressure, deflection shape of diaphragm, volume change and derivation of sensor characteristics are presented.

3.3.1. Assumptions in the analysis

Following assumptions have been included in the derivation of the model for deflection of diaphragm in the sealed cavity sensor.

a) The aspect ratio (edge length /thickness) of the diaphragm is appropriate to classify it as "**thin plates with small deflections**" [88]

b) The deflection of diaphragm is a small fraction of its thickness; therefore the deflection is entirely due to the **bending** based on theory of plates. [88-90]

c) As the deflection is entirely due to bending and there is no stretching of the diaphragm, the deflection will be **linear** with applied net (or differential) pressure [86].

d) The deflection sensitivity (B) of diaphragm is **constant** as the deflection is in the linear regime. The same is validated through FE analysis in Chapter 4 [91-92].

e) The **dimensionless shape function** derived by La Cour *et al.* [89] is **applicable** irrespective of dimensions of diaphragm. The same is validated through FE analysis for the size of diaphragm considered in the thesis and over the entire range of deflection.

f) The anodic bonding is carried out under atmospheric pressure. No gaseous components are significantly consumed or released in the process of anodic bonding [93-94].

g) The pressure of the trapped gas after anodic bonding can be determined based on simple formula [93].

h) As the pressure of the trapped gas is sub-atmospheric (not high pressure) and temperature of normal operation of sensor is not low (negative) , the **ideal gas law** is applicable [95-96]

3.3.2. Pressure inside the cavity sealed using anodic bonding process

The residual cavity pressure after bonding under atmospheric pressure is given by Eq. 3-1 as following [93]

$$\boldsymbol{P_c = P_{atm}\,(T/T_{bonding}).(V_0\,/V_c\,)} \qquad \textbf{Eq. 3-1}$$

Where P_c , P_{atm} , V_0, V_c, T, $T_{bonding}$ denote pressure inside the sealed cavity, ambient (atmospheric) pressure, initial (no-deflection) cavity volume, cavity volume in general, cavity air temperature and bonding temperature respectively. For theoretical study of sensor behaviour, it is assumed that molecules are not significantly consumed or released due to chemical reactions during anodic bonding. At atmospheric pressure and temperature of 1013.25 mbar and 300 K respectively and the bonding temperature of 750 K (i.e. 477°C), the residual pressure in the cavity will be 405.3 mbar. The calculations are shown in Appendix A.1. Similar pressures can be expected in the sealed cavities of the sensors.

3.3.3. Deflection and the shape function of square anisotropic silicon diaphragm

The standard deflection formula for an edge-clamped isotropic square diaphragm is discussed in Appendix A.2 and compared with derived expression of this section. Deflection shape functions for square diaphragm of Capacitive Micromachined Ultrasonic Transducers (CMUT) are derived by Rahman *et al*. [88] and La Cour *et al*. [89]. Rahman *et al.* have considered isotropic polysilicon square diaphragm. On the other hand, Cour *et al.* have derived deflection shape function for a square diaphragm of single crystal silicon in (100) plane with edges aligned to <100> directions. The same analysis has been utilized for calculation of the diaphragm deflection, its shape and subsequently, the change in cavity volume. The values of effective stiffness C_{11}^{eff} and constant k_2 jointly govern maximum deflection w_0 of the diaphragm. Another constant β which depends only on k_2 governs the shape function of diaphragm. The maximum deflection (w_0) occurs at the centre of diaphragm. The same for a square shaped single crystal silicon diaphragm of edge length L, is given by Eq.3-2 [89]

$$\boldsymbol{w_0} = \frac{\mathbf{77(1432+91}\,\boldsymbol{k_2})}{\mathbf{256(16220+11}\,\boldsymbol{k_2}\,\mathbf{(329+13}\,\boldsymbol{k_2}))}\,.\boldsymbol{P(L/2)^4/D_a} \qquad \textbf{Eq. 3-2}$$

The simplification steps of above equation are given in Appendix A.3. The values of constant k_2 = 1.41 and $D_a = C_{11}^{eff}.h^3/12$ (anisotropic flexural rigidity) are also taken from the same reference [89]. The maximum deflection is given in Eq.3-3 after adjusting for units of pressure P in MPa and deflection w_0 , edge-length L and thickness h in micrometers;

$$\boldsymbol{w_0} = \mathbf{8.386}\,\boldsymbol{X}\,\mathbf{10^{-8}}.(\boldsymbol{PL^4/h^3}) \qquad \textbf{Eq. 3-3}$$

Further, Galerkin method is utilized to reach to following shape function (Eq.3-4) where $w\,(X,Y)$ is the deflection at position (X,Y) measured from centre of the diaphragm taken as origin;

$$\boldsymbol{w}\,(\boldsymbol{X},\boldsymbol{Y}) = \boldsymbol{w_0}\left[\mathbf{1}-\left(\frac{\boldsymbol{X}}{\boldsymbol{L/2}}\right)^{2}\right]^{\mathbf{2}}\left[\mathbf{1}-\left(\frac{\boldsymbol{Y}}{\boldsymbol{L/2}}\right)^{2}\right]^{\mathbf{2}}\left[\mathbf{1}+\boldsymbol{\beta}\left(\frac{\boldsymbol{X}}{\boldsymbol{L/2}}\right)^{\mathbf{2}}+\boldsymbol{\beta}\left(\frac{\boldsymbol{Y}}{\boldsymbol{L/2}}\right)^{\mathbf{2}}\right] \qquad \textbf{Eq. 3-4}$$

The normalized deflection shape of anisotropic square silicon diaphragm is drawn using the above equation and shown in Fig. 3.4. in 3D and 2D.

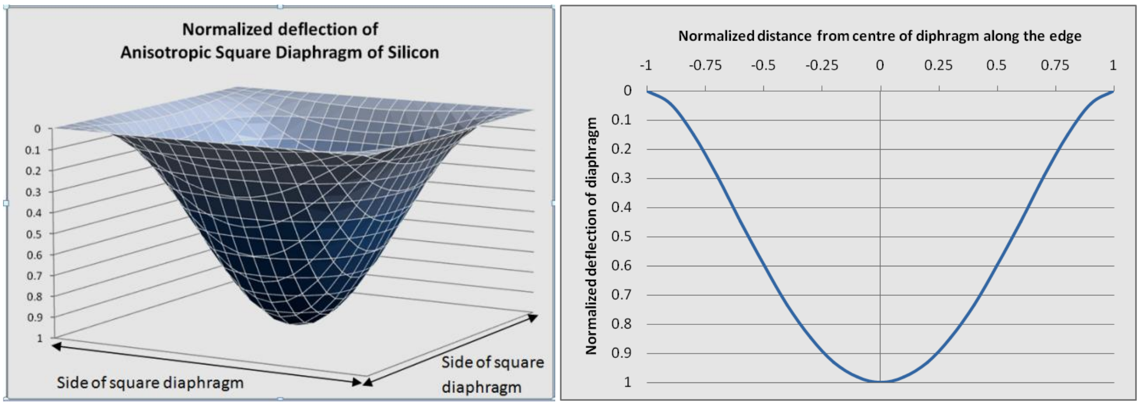

Fig. 3.4 Deflection shape for a single crystal silicon square diaphragm in (100) plane

3.3.4. Volume change by the deflected diaphragm

The volume change of the cavity due to deflected diaphragm can be calculated as

$$\boldsymbol{\Delta V = \int_{-\frac{L}{2}}^{+\frac{L}{2}} \int_{-\frac{L}{2}}^{+\frac{L}{2}} w\,(X, Y)\; dX\, dY} \qquad \textbf{Eq. 3-5}$$

As the deflection shape remains same, the change in volume will be proportional to deflection w_0 of the diaphragm. Substituting Eq. 3-4 in Eq. 3-5, the latter takes the following form,

$$\boldsymbol{\Delta V = A.w_0 = A.x} \qquad \textbf{Eq. 3-5}$$

Here onwards x will be used in place of w_0 to denote the deflection at centre of the diaphragm. From Eq. 3-5 and Eq. 3-6, the constant $'A'$ is

$$\boldsymbol{A = \frac{64\,(\,147 + 42\,\beta)}{33075} L^2 \; = \; v.L^2} \qquad \textbf{Eq. 3-6}$$

where L^2 is the area of square diaphragm and v signifies the average normalized deflection over it. With β = 0.24587, the average normalized deflection $\mathrm{v} = 0.304426$ as per Eq. 3-7; and the cavity volume V_c after diaphragm deflection is

$$V_c = V_0 - A.x = V_0 - 0.304426\, L^2 x \quad \textbf{Eq. 3-7}$$

The constant $\nu = 0.304426$ has been derived from the theory of normalized deflection of dimensionless (size independent) anisotropic silicon diaphragm (La Cour *et al.*). In the reference, the model is validated for diaphragm of size 65 µm x 65 µm and thickness 2.37 µm. It is assumed that the model will also be applicable to the size of diaphragm (8 mm x 8 mm x 0.13 mm) considered in this thesis.

3.3.5. Deflection of the diaphragm in sealed micro cavity pressure sensor

Deflection of a diaphragm is a function of differential of applied and reference pressures. The reference pressure is function of cavity volume which in turn is a function of deflection. Due to this cyclic dependency, the relationship between the deflection and applied pressure of a sealed micro cavity pressure sensor will not be straight forward as depicted by Eq. 3-2. Following are the three governing equations which should be solved to yield relationship deflection with applied pressure in this case.

$$x = fn1\,(P - P_c) \quad \textbf{Eq. 3-8}$$

$$P_c = fn2\,(V_c, T) \quad \textbf{Eq. 3-9}$$

$$V_c = fn3\,(x) \quad \textbf{Eq. 3-10}$$

where x, P, P_c, V_c, T are the diaphragm deflection, applied pressure, cavity (reference) pressure, cavity volume and temperature respectively. The functions $fn1(\;), fn2(\;)$and $fn3(\;)$ denote suitable functions defining the relationship.

The deflection x equals to deflection sensitivity Btimes the net applied pressure as per the following equation,

$$\boldsymbol{x = B.(P - P_c)} \qquad \textbf{Eq. 3-11}$$

It is also assumed that the diaphragm’s deflection characteristics are linear with respect to the net acting pressure. It is ensured by restricting the deflection well within 25% of the diaphragm thickness [86]. From Eq.3-3, the sensitivity ‘B' in linear deflection region depends on the edge length and thickness of the diaphragm as

$$\boldsymbol{B = 8.386\, X10^{-8}.(L^4/h^3)} \qquad \textbf{Eq. 3-12}$$

The temperature dependence of the sensitivity is ignored for simplicity over the temperature range of interest for this analysis. Pressure P_c of the gas trapped in sealed cavity is inversely proportional to the cavity volume V_c and proportional to temperature T, as per Eq. 3-1. In concise form,

$$\boldsymbol{P_c = C.T/V_c} \qquad \textbf{Eq. 3-13}$$

Where C for anodic bonding carried out under atmospheric pressure conditions is

$$\boldsymbol{C = \frac{P_{atm}.V_0}{T_{bonding}} = C'.V_0} \qquad \textbf{Eq. 3-14}$$

Where C' is another constant whose value depends on the cavity sealing process. Putting V_c from Eq. 3-7 into Eq. 3-14 defining P_c, and then putting P_c into Eq. 3-12 defining x gives

$$\boldsymbol{x = B.(P - \frac{C.T}{(V_0 - A.x)})} \qquad \textbf{Eq. 3-15}$$

The steps of solving the Eq.3-16 are given in Appendix A.4.; which gives deflection as:

$$\boldsymbol{x = \left(\frac{V_0}{2A} + \frac{BP}{2}\right) - \sqrt{\left(\frac{V_0}{2A} - \frac{BP}{2}\right)^2 + \frac{BCT}{A}}} \qquad \textbf{Eq. 3-16}$$

This is the **characteristic equation** for deflection of diaphragm of a sealed cavity pressure sensor. The term $'BCT/A'$ in Eq. 3-17 is due to gas entrapment in the sealed cavity and it is responsible for non-zero offset, its temperature dependence, nonlinearity and reduced full scale deflection. Had this term been zero (that is, the reference cavity has no entrapped gas and is under vacuum), the equation would have reduced to simplest form (Eq.3-18) where deflection is directly proportional to the applied pressure, offset is zero, span is full, and no temperature effects (ignoring that on B) on offset and span are there.

$$\boldsymbol{x = B.P} \qquad \textbf{Eq. 3-17}$$

3.3.6. Offset and span of the pressure sensor

In terms of deflection, offset of the pressure sensor is the deflection (at the centre of diaphragm) when applied pressure is zero. In the characteristic Eq.3-17, when the applied pressure value is put as zero, value of C is put from Eq. 3-15 and factor of 2 is put in numerator and denominator of second term in the root sign, the offset is given as

$$\boldsymbol{x_0 = \left(\frac{V_0}{2A}\right) - \sqrt{\left(\frac{V_0}{2A}\right)^2 + \left(\frac{V_0}{2A}\right).2BC'T}} \qquad \textbf{Eq. 3-18}$$

In case there is vacuum in the cavity, the offset (and its temperature dependence) reduces to zero. For large cavity volumes, Eq. 3-19 can be expanded as

$$\boldsymbol{x_0 = -BC'T\left[1 - \left(\frac{ABC'T}{V_0}\right) + 2\left(\frac{ABC'T}{V_0}\right)^2 - 5\left(\frac{ABC'T}{V_0}\right)^3 + \dots\dots\dots..\right]} \qquad \textbf{Eq. 3-19}$$

For very large cavity volumes, the offset is given by Eq. 3-21 and it is no more dependent on cavity volume.

$$x_0 = -BC'T \qquad \text{Eq. 3-20}$$

Span S is the full scale deflection of the diaphragm. It is the distance between two positions of the centre of diaphragm for full scale (P_{FS}) and zero applied pressures. For vacuum at reference (sealed cavity) side, the span is given by Eq. 3-22, with no dependence of span on cavity volume.

$$S = BP_{FS} \qquad \text{Eq. 3-21}$$

These sensor characteristics namely offset and span are studied with cavity length as a design parameter.

3.4. Deflection characteristics of 10 bar sensor

It is understood that generally the pressure of the trapped gas in the sealed cavity is 1 atmosphere or below depending on the method of sealing. In the present study, a pressure value of 405.3 mbar has been worked out and used for analysis of the behaviour of pressure sensor. It is intuitive to select one more pressure range (in addition to 1bar) that is at least 10 times higher than the pressure of the trapped gas to see the effect of latter. Therefore, a 10 bar pressure sensor has been considered in the present section to develop complete understanding.

The lateral size and the full scale deflection of both the sensors are chosen to be the same. The diaphragm has size of 8 mm x 8 mm. The full scale deflection value of about 15 µm is targeted from the perspective of optical demodulation. Only the diaphragm thickness is changed to obtain the desired deflection value. Therefore, for the 10 bar sensor, a thickness value 280.08 µm would yield a deflection of 15.63 µm. The same full scale deflection is achieved in 1 bar sensor by having a thickness value of 130 µm. Thus the 10 bar diaphragm is more stiff than the 1 bar diaphragm. The design parameters of the sensor are given in Table 3.1 (Refer Appendix A.5 for calculations).

Table 3.1 Parameters for a 10 bar pressure sensor with 8 mm x 8 mm x 0.28 mm square diaphragm

Parameter	Physical Significance	Value	Remarks
A (µm^2)	Average normalized deflection times diaphragm area	194.83 x 10^5	Gives volume change when multiplied by deflection as per Eq.3-7
B (µm/MPa)	Deflection sensitivity	15.634	15.634 µm deflection for 10 bar
C' (MPa/K)	Parameter defining the cavity pressure at given temperature	1.351 x 10^{-4}	405.3 mbar pressure at 300 K temperature as per Eq.3-15

A program is made based on developed model (Eq. 3-17) in spreadsheet to see the effects of various design parameters on the sensor characteristics.

3.4.1. Analysis of 10 bar sensor with cavity length parameter

The cavity length is directly related to cavity volume. For any given deflection of the diaphragm, a larger cavity would see lesser relative change of volume compared to what is seen by a smaller cavity. Hence, the "reference pressure" of the pressure sensor would change by different extents for cavities of different lengths. It is intuitive that the smaller cavities will suffer larger change in reference pressure. Also, in order to reach the same deflection value, the smaller cavity needs higher amount of externally applied pressure.

Minimum cavity length: At full scale applied pressure, the diaphragm has maximum inward deflection. As the value of initial (null deflection) cavity length is taken smaller, the gap between diaphragm and the bottom of the cavity decreases (Fig. 3.5). The minimum cavity length is the value of cavity length at which the diaphragm just touches the bottom of the cavity. In other words, the cavity just collapses. The minimum cavity length is dependent on the deflection sensitivity of diaphragm and on the pressure of the trapped gas. The method of finding the minimum cavity length for is given for 1 bar and 10 bar pressure sensors in Appendix A.6.

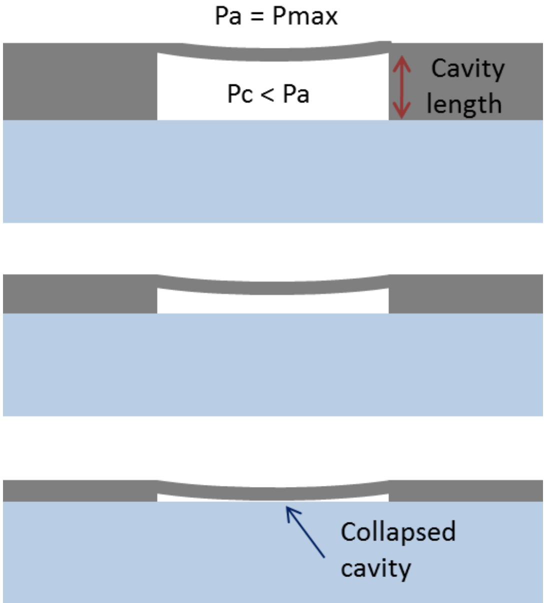

Fig. 3.5 Criterion of minimum allowed cavity length

It emerges from the analysis given in Appendix A.6 that the minimum cavity length for the full range operation of a 10 bar sensor is around 14.75 µm. If the cavity length is kept lesser than this value, the cavity will collapse at under the 10 bar pressure or lesser. It is so, because the reference pressure is quite low compared to the full scale pressure and would not be able to resist the collapse of the cavity.

The 10,000 µm cavity length is taken as the upper extreme value. This much deep cavity may not be feasible for the design shown in Fig. 3.1 due to thickness limitation of commonly used silicon wafer. Nevertheless, such a study would cover full spectrum of the design and give complete insight into the problem.

The deflection characteristics have been plotted in Fig. 3.6 for the two extreme cavity lengths to see the effect of trapped gas. It is seen that both the characteristics are linear and very close to each other. However, the one for 15 µm cavity length has slightly lesser slope and hence smaller span (numerical values). It is because of the increasing reference pressure in response to increasing applied pressure. The span is getting slightly suppressed for the 10 bar sensor of small cavity length (numerical values).

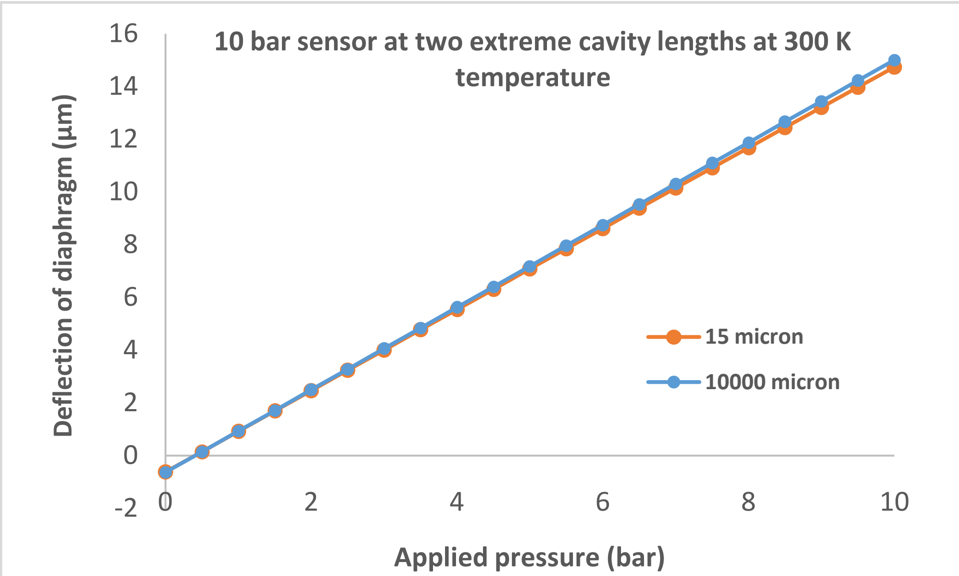

Fig. 3.6 Deflection characteristics of 10 bar sensor at 300 K for two extreme cavity lengths

The span reduces because the cavity pressure increases with inward deflection of diaphragm. The pressure increase is small compared to the applied (high) pressure. Therefore, the increased pressure is not able to offer greater resistance towards inward movement of diaphragm with increasing applied pressure. Hence, the span is not much reduced for high pressure sensor **even with smallest allowed cavity length**. For large cavity lengths, the pressure increase would be insignificant; hence full span can be achieved.

The offset of the sensor is defined as the deflection value at zero mbar absolute applied pressure. It can be seen in Fig. 3.6 that the deflection at zero applied pressure is small and negative (numerical values). It means that the trapped gas pushes the diaphragm outside by some amount till the point where all the forces are balanced.

The pressure present in the reference cavity would not be able to push the stiffer diaphragm significantly. Therefore, the offset would be smaller for stiffer diaphragm (of higher range pressure sensors).

3.4.2. Temperature effects of the gas for 10 bar sensor

There are various ways through which the temperature affects the behaviour of a pressure sensor. The sensor is analysed for limited range of temperature, from 27 °C to 77 °C (300 K to 350 K). The change of Young Modulus and the cavity volume are insignificant for this much change of temperature (numerical values). Only the increase of gas pressure with increasing temperature would be significant. Here, residual stresses and packaging stress have not been considered to see the effect of the trapped gas alone. The developed analytical model and corresponding characteristic equation includes a temperature term. The equation has been used to derive the characteristics at two temperatures.

In principle, the increase of temperature would tend to increase the cavity pressure, which would tend to push the diaphragm outward and reduce the inward deflection. The offset shall increase and the span shall reduce. The characteristics at two temperatures are shown in Fig. 3.7 for 10 bar sensor of 15 µm cavity length. The lower characteristic belongs to higher temperature value. The two characteristics are almost overlapping. Thus it is concluded that there is not any significant effect of change of temperature of the gas on a 10 bar pressure sensor for small cavity length.

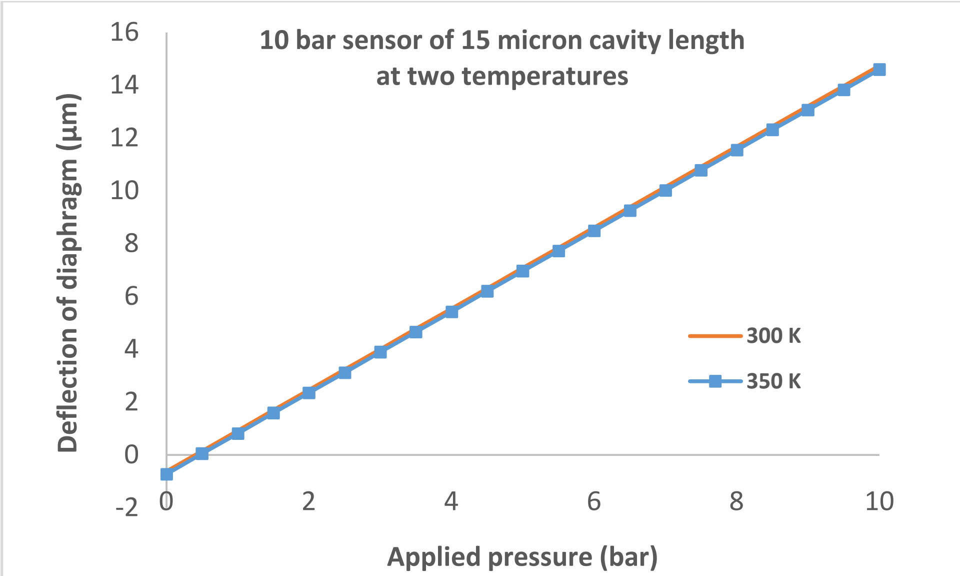

Fig. 3.7 Deflection characteristics of 10 bar sensor of 15 micron cavity length at different temperatures

When the cavity size is large, there is larger volume of gas trapped inside. Any increase of temperature would tend to increase the pressure proportionately if the volume is not allowed to change. However, in the present enclosed cavity, there is a flexible diaphragm. Hence, there would of course be a pressure increase, but not proportional to the increase of temperature, as the increase of volume is also there. The diaphragm would have to sweep more volume in larger cavity to reach its final equilibrium position. It is because the relative change of volume matters. In order to have a quantitative estimation of the temperature effects in larger cavities, characteristics are generated for a 10 bar sensor of 10000 µm cavity length, as shown in Fig. 3.8.

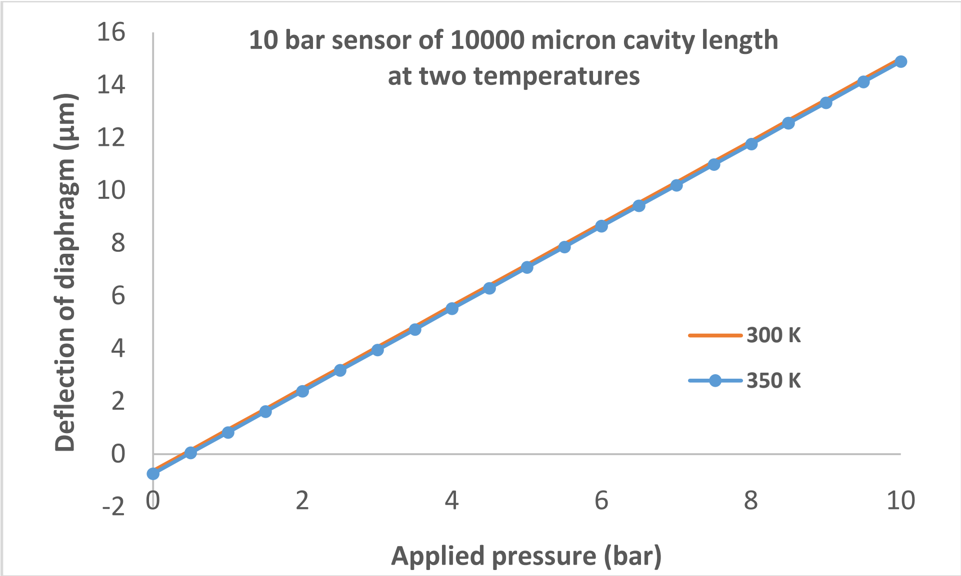

Fig. 3.8 Deflection characteristics of 10 bar sensor of 10000 micron cavity length at different temperatures

It is seen that here also there is not any significant shift in the characteristic when the temperature of the gas is changed.

3.4.3. Conclusion on 10 bar sensor

It is seen in the analysis that the sensor characteristics are not significantly dependent on the cavity length parameter for this sensor. Also, the change of gas temperature by 50 K did not affect the characteristic significantly for both small and large cavities. It is because the pressure range is almost 20 times higher than the pressure of the trapped gas. A high pressure sensor accordingly needs a high stiffness diaphragm, when the full scale deflection is same. The cavity pressure cannot move the diaphragm much and hence the cavity size and change of gas temperature don't matter much.

The effect of trapped gas would be even more insignificant for yet higher pressure ranges such as 20 bar, 50 bar, 100 bar and so on. Conversely, the gas effects are believed to be considerable high as one goes for design of lower pressure range sensors. A 1 atmosphere or 1 bar pressure sensor is very relevant in various vacuum and gas flow applications. It is apt to analyse this sensor for the expected adverse effects of the trapped gas. In the next section (3.5) a detailed analysis of a 1 bar sensor is presented.

3.5. Deflection characteristics of 1 bar sensor

Various design parameters are given in Table 3.2 for a 1 bar sensor. The designed diaphragm deflects by 15.64 µm under 1 bar pressure. The pressure of trapped gas in the sealed cavity is taken to be 405.3 mbar as per calculations presented in Section 3.3.2. The front cavity in silicon is considered trapezoidal and the effect of cavity length (essentially volume) is studied in this subsection.

Table 3.2 Parameters for 1 bar pressure sensor with 8 mm x 8 mm x 0.13 mm square diaphragm

Parameter	**Physical Significance**	**Value**	**Remarks**
A (µm^2)	Average normalized deflection times diaphragm area	194.83×10^5	Gives volume change when multiplied by deflection as per Eq.3-7
B (µm/MPa)	Deflection sensitivity	156.34	15.634 µm deflection for 1 bar
C' (MPa/K)	Parameter defining the cavity pressure at given temperature	1.351×10^{-4}	405.3 mbar pressure at 300 K temperature as per Eq.3-15

The deflection characteristics (diaphragm deflection versus applied pressure) are plotted in Fig. 3.9 for a 1 bar pressure sensor for various cavity lengths such as 7, 15, 100 and 10,000 µm. The characteristics are plotted for different cavity lengths as it is more comprehensible parameter compared to cavity volume. The front cavity is considered trapezoidal and the diaphragm dimensions are taken to be 8 mm x 8 mm for fixed deflection sensitivity, independent of cavity length. However, during sensor fabrication, a fixed size window of 8 mm x 8 mm is formed by photolithography process. The resultant scaling of deflection sensitivity of diaphragm is duly considered in analysis of results.

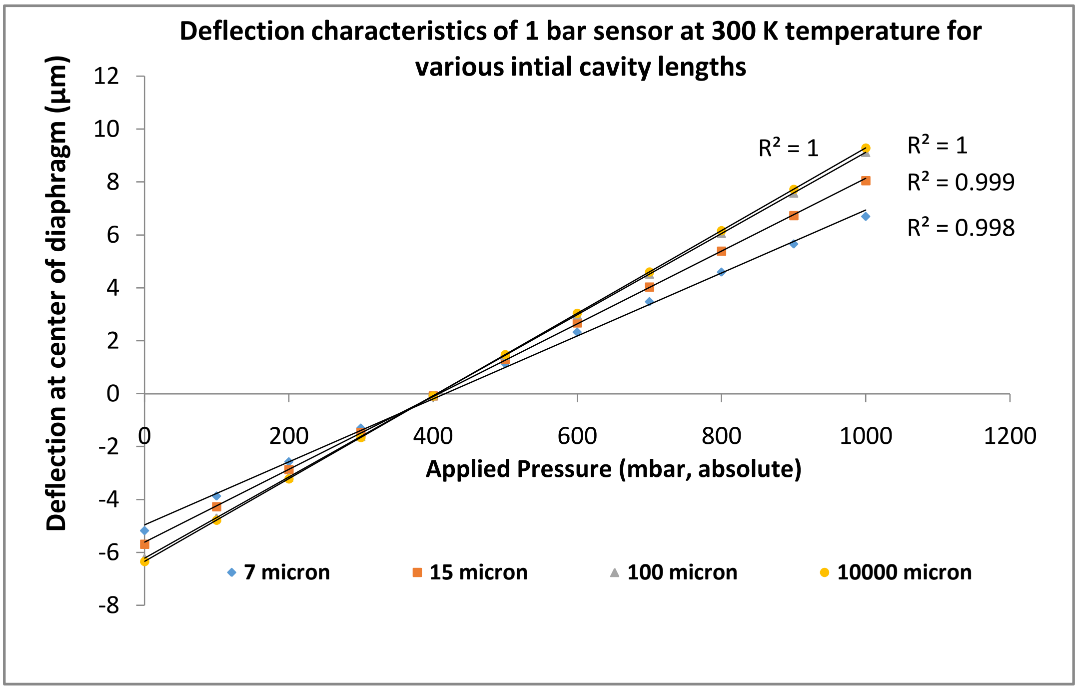

Fig. 3.9 Deflection characteristics at various cavity lengths of a 1 bar pressure sensor

As per the calculations, 7 µm is almost the minimum possible cavity length for no-collapse condition of the cavity for this sensor (specified in Table 3.2 by trapped gas pressure $C'T$ and deflection sensitivity B of the diaphragm). The 10,000 µm cavity length may not be as such practically possible, yet it is included to have complete understanding of the phenomenon. In Fig. 3.9, it is seen that the slope of the characteristics (and hence span of the sensor) is highly sensitive to cavity length parameter at small cavity lengths. For small cavity lengths, the characteristics are slightly nonlinear with applied pressure and the slope of a curve reduces with increasing pressure, which may not be so evident in Fig. 3.9. The R-square value of linear fit is given for all the curves. It is seen that the R-square value for 7 µm cavity is 0.9987 which is very close to 1, but slight nonlinearity is there. As the cavity length is taken higher, the linearity is gets improved. The R-square value of linear fit for 15 µm cavity length is 0.9999, thus it can be stated that the sensor characteristic is linear. It is because the compression of trapped gas is more for small cavities giving increased resistance on inward deflection and hence reduced span. The apparent deflection sensitivity of the pressure sensor is thus smaller than the deflection sensitivity of diaphragm. The dependence becomes weaker and the final characteristic is approached as the cavity length increases. The offset and span both increase in magnitude with cavity length. Similarly, based on characteristic Eq.3-17, effects of individual parameters can be studied. A sensor's behaviour can be seen for different pressures of the trapped gas. The suppression of span would be stronger for higher pressures.

3.5.1. Offset of 1 bar pressure sensor

In Fig. 3.10, offset is plotted with respect to cavity length as design parameter. The cavity length is plotted in logarithmic scale (of base 10) to cover wider range. The magnitude of the offset increases with cavity length Eq. 3-19 and the curve saturates to a final value given by Eq.3-21. Sensors with large cavity lengths experience lesser volumetric change and lesser drop in cavity pressure in response to any outward deflection of diaphragm. Thus, the pressure of the trapped gas on the diaphragm is higher and the diaphragm tends to stop at a position where the outward deflection (the offset) and total change of cavity volume is higher.

3.5.2. Span of the 1 bar pressure sensor

In Fig. 3.11, Span of a 1 bar sensor is plotted with cavity length as design parameter. The cavity length is plotted in logarithmic scale to cover wider range. The span is considerably lesser than the design value for small cavity lengths. The suppressed version of design span is referred to as 'achievable span' at appropriate places. For small cavities, the cavity pressure changes by larger amount with same movement of diaphragm, than in larger cavities. As the inward deflection increases, there is further rise in reference pressure (more so in small cavities), and hence span is suppressed. For very large cavities, the inward deflection reduces the cavity volume by a very small fraction and the increase in cavity pressure is very small and full designated span is attained.

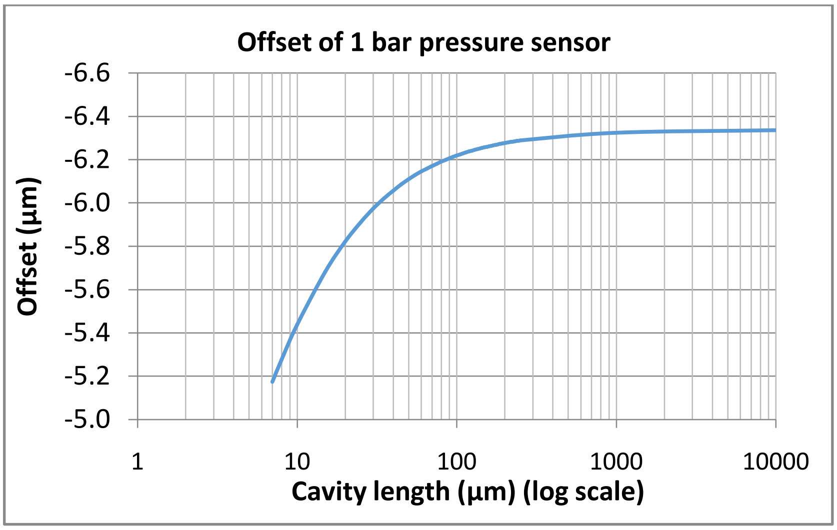

Fig. 3.10 Offset of a 1 bar pressure sensor with cavity length parameter

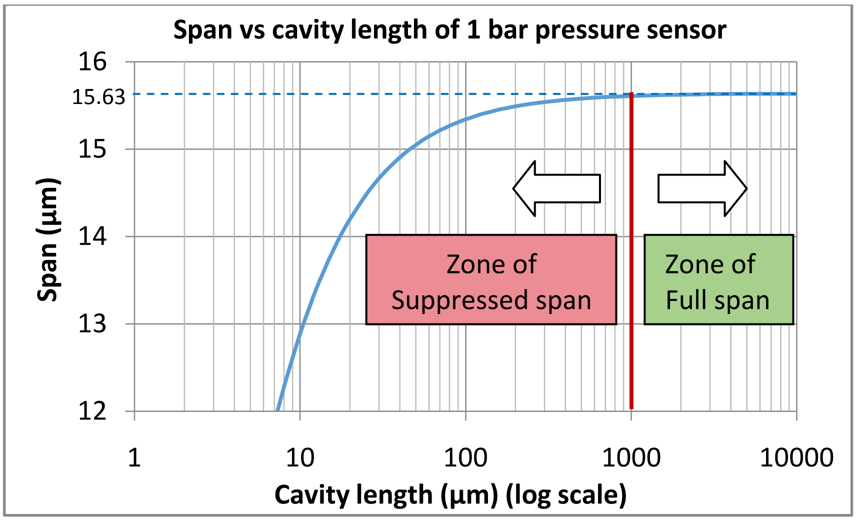

Fig. 3.11 Dependency of span on cavity length for 1 bar sensor

The span values of more than the cavity length is possible, as a part of the deflection is outward of the cavity (Fig. 3.2). In the Fig. 3.11, for example, the achievable spans are 12 µm and 13 µm, respectively at cavity lengths of 7 µm and 10 µm. In the present case (Fig. 3.11), the span is unsuppressed at cavity lengths greater than 1000 µm. The span is lesser for cavity length values less than 1000 µm. The graph has been marked with two zones, one at the right of cavity length value 1000 µm (indicated with red vertical line), where there is full span and suppression is almost nil. The second zone is at the left of the cavity length value 1000 µm, where the span is lesser than the designed value. This zone is marked as ‘zone of suppressed span.

Following are the salient observations from the analysis and the derived characteristics for 1 bar sensor:

a) For very small cavity lengths, the span is lesser due to increase in reference side (cavity) pressure caused by gas compression. The suppression of span will be much stronger for sensors having higher trapped gas pressure and/or higher deflection sensitivity of the diaphragm.

b) The span and offset curves plotted against the cavity length have rapid changes in the regime of smaller cavity lengths and saturate to a final value in the regime of large cavity lengths. It is basically the cavity volume which is important, not necessarily the cavity length. With large cavity volumes the sensors characteristics become more controllable.

c) This analysis is also helpful for estimation of minimum permissible cavity length (based on criteria of no collapse of the cavity or the optical measurability) for given deflection sensitivity and trapped gas pressure of the sensor.

3.5.3. Comparison of 1 bar and 10 bar sensors of same full scale deflection, trapped gas pressure and lateral size

The two sensors by design have same lateral size and full scale deflection of diaphragms. The diaphragms are designed to deflect 15.63 µm for net applied pressures of 1 bar and 10 bar respectively. This is achieved by changing the thickness of diaphragm. Initial (at null deflection) cavity pressure due to trapped gas is also considered same to compare two sensors. The only difference is that 10 bar sensor is 10 times stiffer than the 1 bar sensor to map the pressure range to same full scale deflection. It is to be seen if these two sensors have same offset and span values.

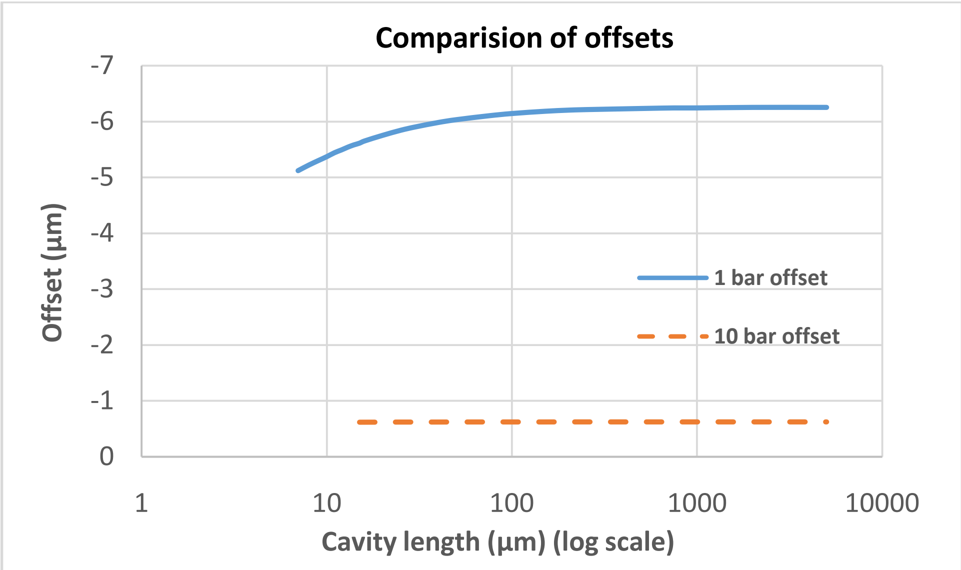

Fig. 3.12 Dependency of offset on cavity length for 1 bar and 10 bar pressure sensors

The two sensors behave differently. The offset is the deflection when external applied pressure is zero (<< 1 mbar). The offsets for two sensors are plotted in Fig. 3.12. The cavity length is in logarithmic scale on x-axis to cover wider range of values. The offset value will be smaller for 10 bar sensor because the trapped gas will not be able to push the diaphragm outside as much as for a 1 bar sensor. Also, as per Eq. 3-19, the offset value will be high for a sensor of higher sensitivity (B). Therefore, the offset value is larger for a 1 bar pressure sensor. The offset of 10 bar sensor is almost independent of the cavity length, because the factor $BC'T$ is 10 times smaller. Whereas, the offset is dependent on the cavity length, and becomes independent of it only for large values of the cavity length, such as 200 µm

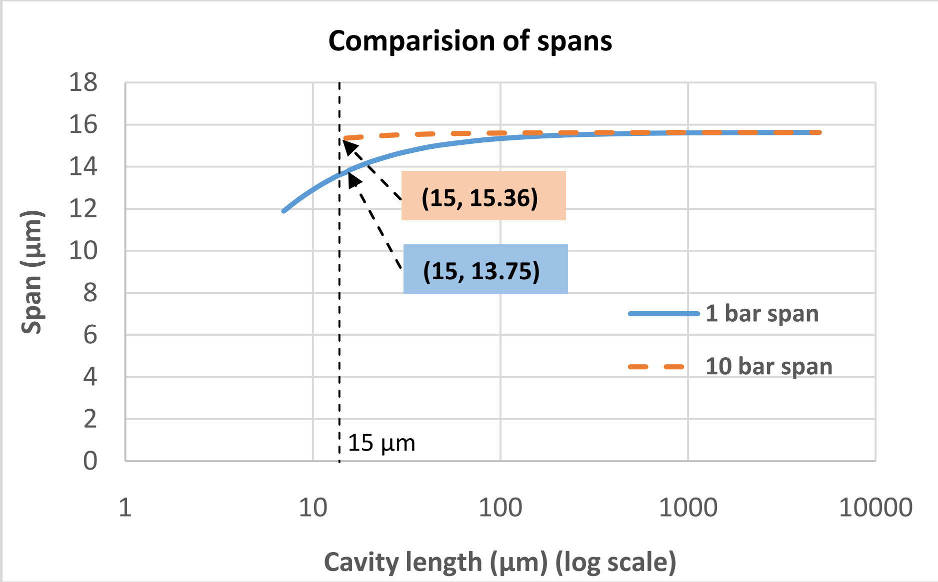

Fig. 3.13 Dependency of span on cavity length for 1 bar and 10 bar pressure sensors

The spans for two sensors are plotted in Fig. 3.13. The cavity length is in logarithmic scale on x-axis to cover wider range of values. If the spans of two sensors are compared at 15 µm cavity lengths, it is larger (15.36 µm, 98.3 % of design value 15.63 µm) for a 10 bar sensor. The span is smaller (13.75 µm, 88% of design value 15.63 µm) for the 1 bar sensor of 15 µm cavity length. This means the spans at 15 µm cavity length are suppressed by 0.7% and 12% respectively for 10 bar and 1 bar sensors. The span is almost independent of cavity length for 10 bar sensor, whereas it is dependent on cavity length for 1 bar sensor. For very large cavity lengths, the 1 bar sensor attained the design span value.

3.6. Sensor behaviour at various pressures of trapped gas

The analysis of sensor characteristics has been carried out for one example pressure (405.3 mbar) which is supposed to appear from anodic bonding in ideal situations. However, the large deviations in the pressure of the trapped gas cannot be ruled out. Moreover, the developed characteristic equation will also be applicable for the sensors bonded by other methods. Therefore, it is necessary to extend the interpretation of other gas pressures as well and compare them.

The designed full scale deflection (span) of 1 bar pressure sensor is 15.63 µm. However, due to the presence of gas in sealed microcavity of the pressure sensor, the full scale deflection is not achieved. The span undergoes some suppression and the achieved span is lesser than the designed value. The suppression is higher when the cavity is smaller and the gas pressure is higher. To study the dependence of suppression on trapped gas pressure, the spans normalized with the design span (15.63 µm) are plotted in Fig. 3.14, with cavity length for 1 bar pressure sensor at different trapped gas pressures. The x-axis shows the cavity length of the sensor in logarithmic scale.

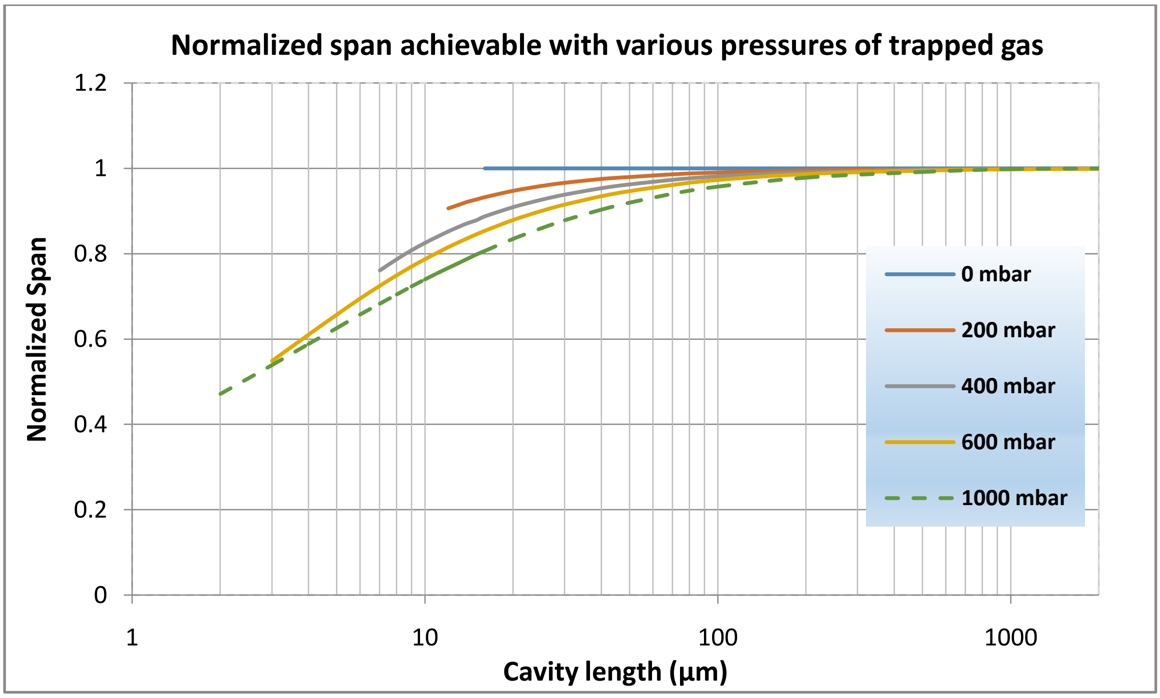

Fig. 3.14 Normalized span for 1 bar sensor at various trapped gas pressures

In case of a vacuum sealed cavity where the gas pressure is 0 mbar (or a negligibly small value compared to 1 bar), there is no suppression at all. The full span is always achievable irrespective of the cavity length. The topmost plot in Fig. 3.14 represents the case of vacuum cavity.

The minimum allowed cavity length can be decided on the criterion of ‘no collapse’ of the diaphragm of the cavity base. An additional criterion to this for an optical MEMS pressure sensor can be based on minimum readable path length in the interferometer governed by the optical demodulation method. The sensor shall be designed and fabricated to keep this much minimum cavity length. In the following description only the mechanical constraint of minimum cavity length is considered.

Here it should be noted that the minimum allowed cavity length for vacuum cavity is slightly more than the full scale deflection value. All the deflections are inward the cavity.

The minimum allowed cavity length is dependent of the gas pressure. For higher trapped gas pressure, the diaphragm is already pushed out more, so movement range of diaphragm is more towards negative side than positive side (The positive side is inward the cavity from the null deflection position of diaphragm). Therefore, shorter cavity lengths are possible when the trapped gas pressure is higher.

The minimum cavity lengths possible at 200, 400, 600 and 1000 mbar pressures are 12, 7, 3 and 2 µm respectively. The characteristics have larger deviation with decreasing length of the cavity. The suppression of span is more than 50% for sensor of 2 µm cavity length and 1000 mbar pressure of the trapped gas. The characteristics approach their common asymptotic value with increasing cavity length. The difference between the characteristics reduces rapidly with increasing cavity length. For example, at 16 µm cavity length, the spread is about 19 % whereas at 100 µm cavity length, that is about 4%. Further the spread reduces relatively at slower rate. At 200 and 500 µm cavity lengths, the spread is respectively about

2% and 1% only. With 15.63 μm full scale deflection and 200 μm cavity length, the ratio of the two is 7.8 %. Therefore, it can be concluded that deflections of less than 8 % of designed cavity length can be treated as small deflection and would not change the performance of the sensor significantly.

It is therefore beneficial to have a large cavity (or equivalent volume) to get better control on the characteristics of fabricated sensors. However, there is not much gain in going for much large cavity such as more than 500 μm of length.

3.6.1. Nonlinearity in the characteristics

When the applied pressure on the sensor is increased, the diaphragm moves inward, the trapped gas is squeezed more and the cavity pressure increases. The cavity pressure is essentially the reference pressure of the pressure sensor. Ideally the reference shall remain firm within a value for acceptable performance of the sensor. However, for a sensor with small cavity the pressure would increase considerably with the inward movement of diaphragm. The diaphragm would experience increasing resistance for further inward movement. In effect, the 'apparent' sensitivity of the diaphragm in this coupled structural-fluidic system would decrease continuously with the inward movement. To observe the extent of nonlinearity, the developed analytical model is used and deflection characteristics are plotted.

3.6.2. Summary on gas pressure dependency of sensor

This study gives a guideline on the minimum possible cavity length depending on the pressure of the trapped gas (or the method of sealing the cavity). It also suggests that there can be considerable variation in the achieved spans in a batch of fabricated sensors for small cavity lengths. It is because of high sensitivity of span on the pressure as well length of the cavity in the regime of small cavity lengths. As larger cavity lengths are taken, the variation in the span gets more reduced. Thus larger cavity lengths are beneficial in controlling the characteristics of the sensors in more deterministic way.

3.7. Temperature effects of the gas for 1 bar sensor

The characteristic equation for deflection of the diaphragm in sealed microcavity pressure sensor has been derived in section 3.3.5. The equation also comprises of a temperature term. In this section, the effects of temperature have been studied on the behaviour of a 1 bar pressure sensor. The temperature range is chosen from 300 K to 350 K (27 °C to 77 °C).

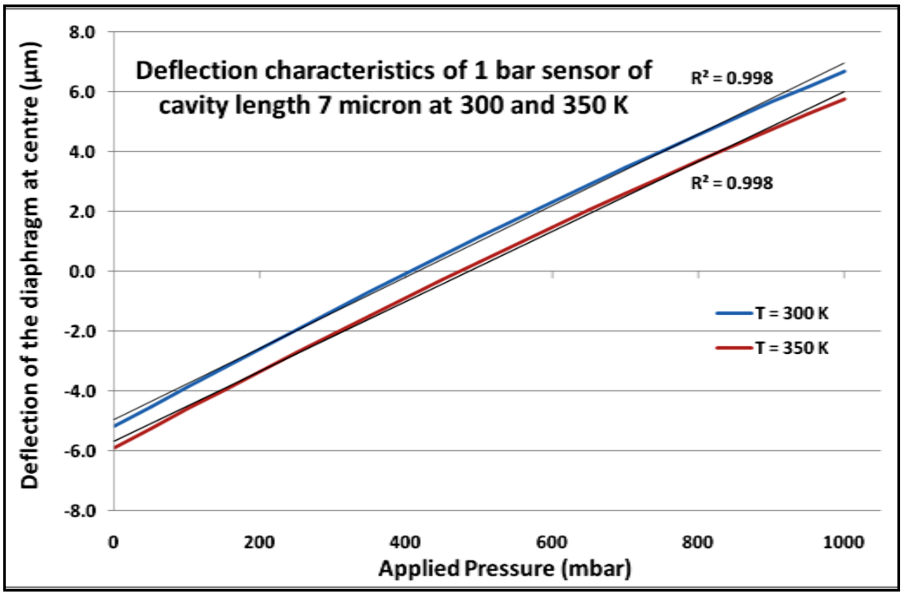

Fig. 3.15 deflection characteristics of a 1 bar sensor of minimum cavity length at two temperatures

The residual pressure is large enough to affect the characteristics of 1 bar sensor significantly. The offset is large hence minimum possible cavity length is 7 µm even though the full scale deflection is larger than the cavity length. The span gets reduced to 11.87 µm (75.9%) due to resistance from the trapped gas (Fig. 3.13, Fig. 3.14). At higher temperature, pressure of the trapped gas increases, hence gives larger offset and further reduced span. The temperature effects manifested as drift in characteristics are significant for 1 bar sensor, which is investigated further in this section.

3.7.1. Temperature dependence of span and offset

As the temperature increase, the pressure of the trapped gas tends to increase pushing the diaphragm outward and latter experiences increased resistance for inward deflection. Thus the span (or full scale deflection) is less at higher temperatures. This effect is 'suppression of span' due to increased temperature. The dependence of span on temperature is shown in Fig. 3.16 for various cavity lengths (7, 15, 100, 10000 μm). The span reduces considerably with increasing temperature for small cavity lengths (7, 15 μm). Conversely, the span is not affected by change of temperature of the gas for large cavity lengths. The plots for 100 and 10000 μm cavity lengths are almost horizontal. Therefore, large cavity size is beneficial.

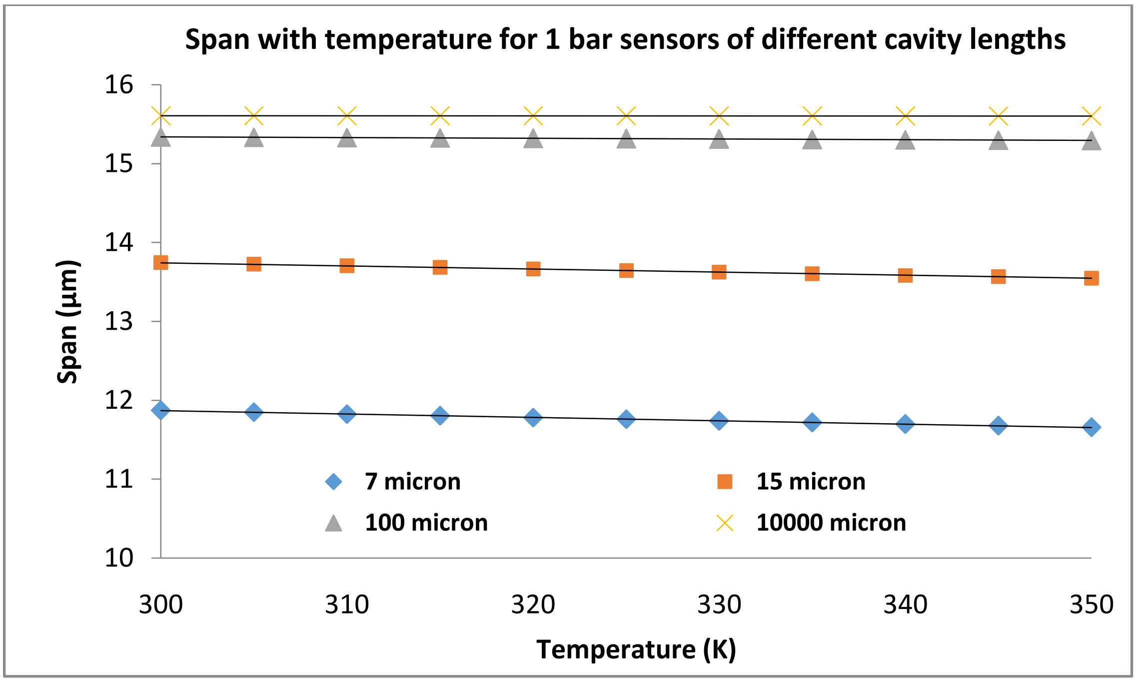

Fig. 3.16 Change of span with temperature for 1 bar sensors of different cavity lengths

The '% change of span (with respect to current span), while temperature changes from 300 K to 350 K, is plotted against cavity length in Fig. 3.17. The current span (full scale deflection, though reduced) is significant from view point of sensor's calibration. Any temperature effect (span or offset) is seen with respect to the current span in sensors' parlance. It can be observed in Fig. 3.17 that change of span (due to change of temperature) reduces fast with increasing cavity length. The y-axis value becomes 'null' (zero) for large cavity lengths (>1000 µm). It means that the **'temperature dependence of span' vanishes for large cavity lengths.**

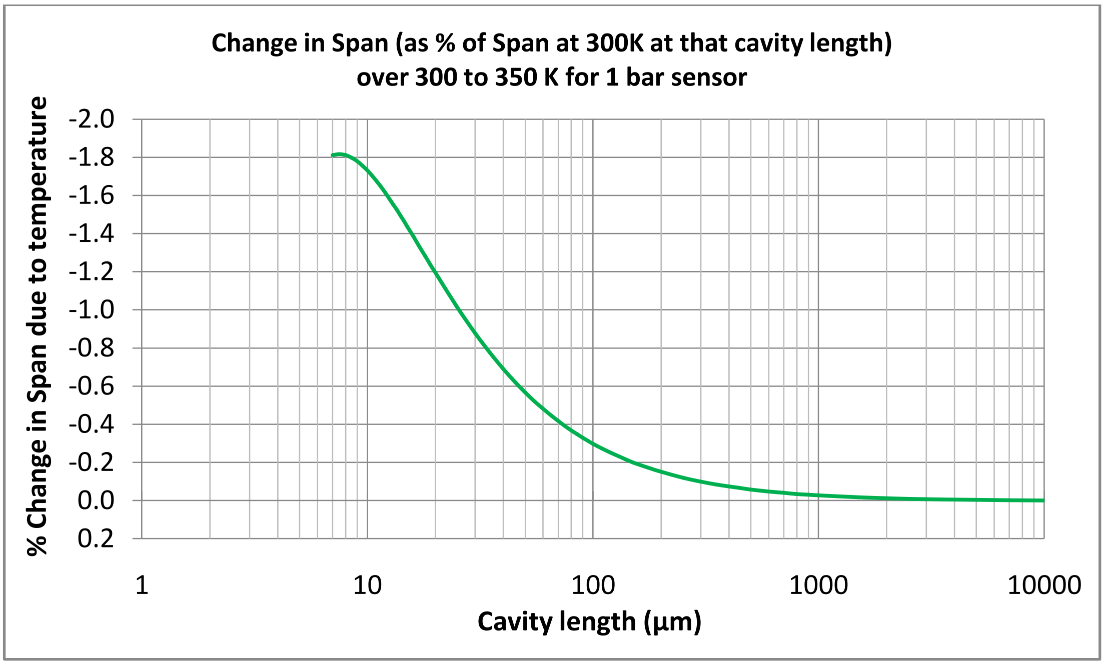

Fig. 3.17 Change in span due to temperature change (as % of current span) for 1 bar sensor

The offset for 1 bar sensors of different cavity lengths is plotted against temperature in Fig. 3.18. The magnitude of offset is larger for larger cavities and it increases with gas temperature. The offset vs. temperature characteristic are very sensitive to cavity length as a design parameter in the regime of small cavity lengths. Notice the reducing gap between the characteristics in increasing order of cavity lengths. The plots shift by large amount in y-axis from 7 to 100 µm values of cavity length; whereas the shift is comparatively very less from 100 to 10000 µm value of cavity length.

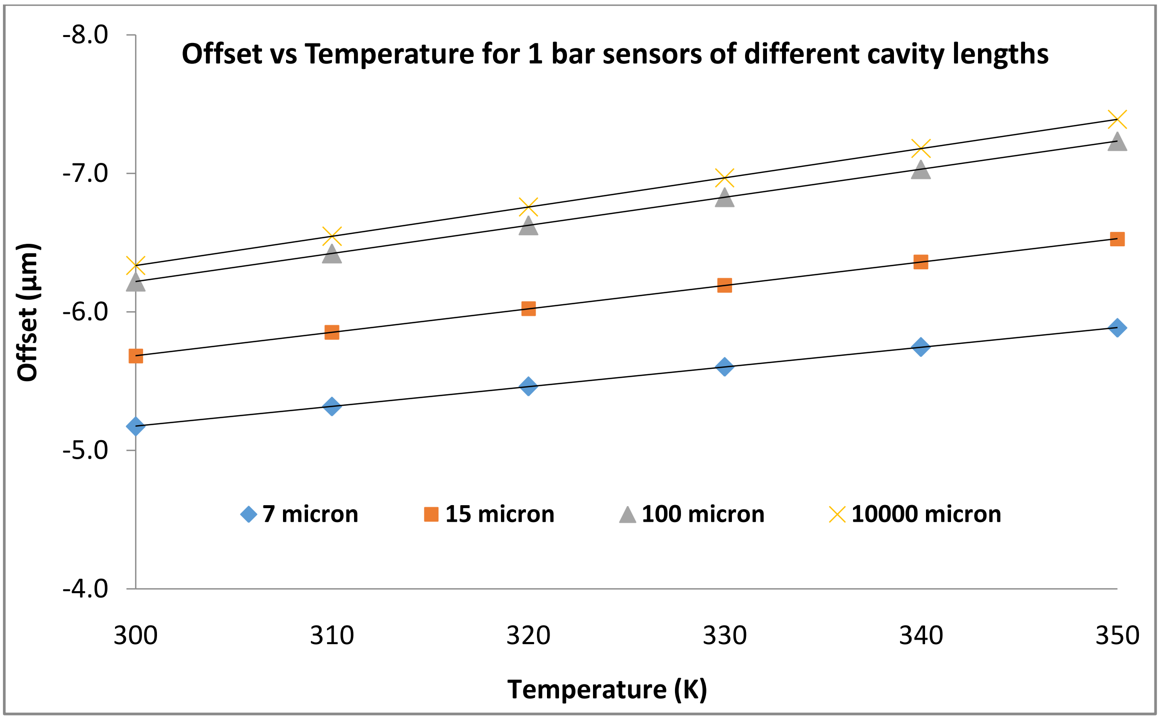

Fig. 3.18 Offset with temperature for 1 bar pressure sensors of different cavity lengths

In Fig. 3.19, change in offset (as % of current span) for ΔT = 50 K (from 300 K to 350 K) is plotted with respect to the cavity length as design parameter. The quantum of change is quite sensitive to cavity length in the regime of small cavity length values. At large cavity lengths, such as 1000 µm, the y-axis reaches saturation value. It means the temperature coefficient of offset is more deterministic. Therefore, at large cavity lengths, the offset value itself is larger, the temperature coefficient is marginally increased, but more deterministic. It will bring sensors of a batch at par performance wise, given that the cavity volume is large enough.

3.7.2. Summary of temperature effects

For small cavity lengths, the span and offset both are small in magnitude. The span reduces while offset increases with increasing temperature. Temperature sensitivity of span rolls down rapidly with cavity length and finally becomes null. Temperature sensitivity of offset increases with cavity length and attains a final value which is marginally higher than that for smallest possible cavity. The large cavity volume is beneficial towards controlling the spread of sensor characteristics as far as above effects are concerned. There are of course other factors too such as residual stresses of bonding, packaging stress, etc. which affect the response of pressure sensors, but they are kept out of scope of the present analysis.

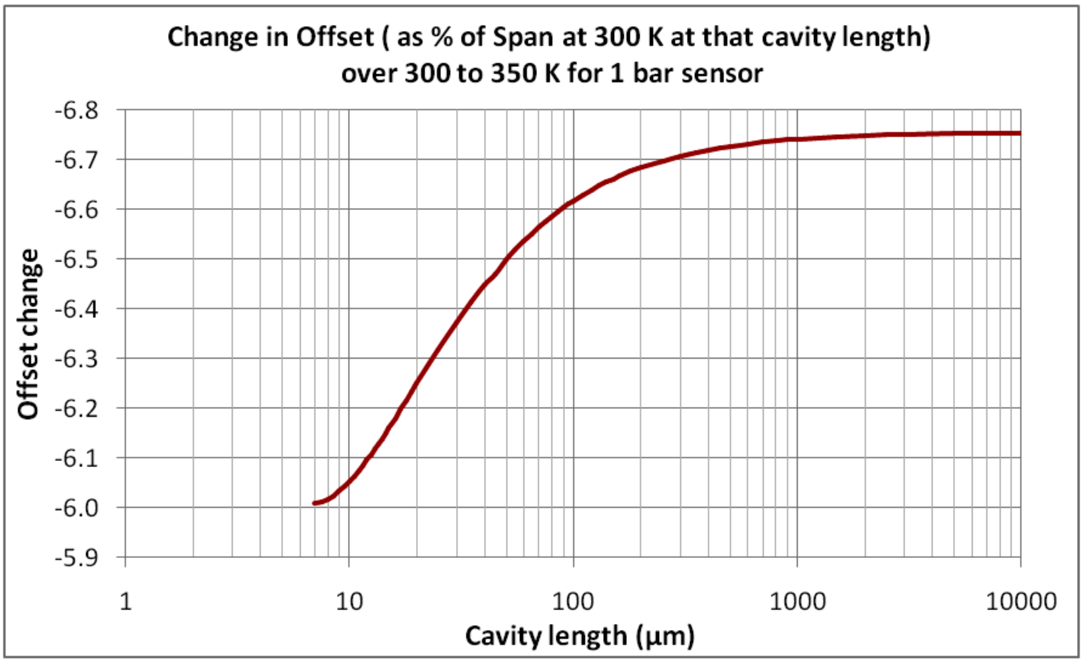

Fig. 3.19 Change in offset (% of span) due to temperature change at various cavity lengths

3.8. Summary

A closed loop solution is derived for deflection of a diaphragm in pressure sensor having trapped gas in sealed micro cavity. The variability of reference pressure (in the sealed cavity) is taken into account. The effect of trapped gas is studied on span and offset of such sensors with cavity length as a design parameter. The phenomenon of suppression of span is presented. It is also brought out that sensor span and offset is very sensitive to cavity length for short cavity lengths. This may result in considerable spread in span and offset of the fabricated sensors. It is further established that the sensor behaviour becomes more controlled and predictable for larger cavity lengths. It is shown that adverse effects of the trapped gas can be subdued by going for larger cavities. The developed theory is applicable to sealed micro cavity capacitive MEMS pressure sensors also.

Chapter 4

NUMERICAL MODELLING OF SEALED MICROCAVITY FABRY-PEROT PRESSURE SENSORS

4.1. Introduction

In the previous chapter, an analytical model for sealed microcavity Fabry-Perot pressure sensor was developed and a phenomenon named "suppression of span" was highlighted. The suppression of span was also studied with respect to the cavity length as a design parameter. It was concluded that the large size cavities are beneficial to eliminate the adverse effects of the trapped gas on the sensor performance.

Further, in order to validate the analysis carried out in previous chapter, a 'numerical model' of the sensor is developed in this chapter. The sensors of different cavity lengths are modelled and the effect of trapped gas on the span (full scale deflection) of sensors is studied. In the sensor model, there is deflection of diaphragm as well as change of volume and pressure of the trapped gas. Therefore, the model involves coupling of two physics; structural as well as fluid dynamics. Therefore, COMSOL 4.3a; a multi-physics based software package is used for the analysis. In the following sections FE modelling, simulation, results and discussions are presented.

4.2. Finite Element Model and Analysis

In the present study, a square shaped anisotropic silicon diaphragm is modelled for the required deflection under the applied pressure. The silicon structure comprising the diaphragm is considered bonded to another rigid structure (glass wafer) so that there is a sealed microcavity in between. The cavity is supposed to hold some residual air with sub-atmospheric pressure, as a result of anodic bonding under ambient pressure. The residual pressure in the sealed cavity after anodic bonding is given by Eq. 4-1 [93]

$$\boldsymbol{P_c = P_{atm}\,(T/T_{bonding}).\,(V_0\,/V_c\,)} \qquad \textbf{Eq. 4-1}$$

Where $P_c\ , P_{atm}\, , V_0, V_c, T, T_{bonding}$ represent residual pressure in sealed cavity, atmospheric pressure during bonding, initial cavity volume (without diaphragm deflection), cavity volume in general, device temperature in general and temperature during anodic bonding respectively. It is assumed that gas molecules are not significantly consumed or released in the bonding process. At atmospheric pressure and temperature of 1013.25 mbar and 300 K respectively and the bonding temperature of 750 K (i.e. 477°C), the residual pressure in the cavity is calculated to be 405.3 mbar.

The study is aimed at finding how the air trapped in the sealed cavity affects the deflection of diaphragm in such a composite structure. The following subsections present details of FE model such as governing equations, boundary conditions, initial conditions, FEA parameters, behavioural characteristics and their interpretation.

4.2.1. FE analysis of diaphragm deflection

The model geometry consists of a silicon substrate with a flexible diaphragm of parent material as shown in Fig. 4.1(a, b). The diaphragm is supposed to be realized through wet etchant based bulk micromachining technique of silicon substrate [97]. The diaphragm is made in (100) crystallographic plane of single crystal silicon, with edges aligned to <110> directions. The edge length of the square silicon diaphragm is taken as 8 mm. The silicon structure acts as a bulk material except the flexible diaphragm at centre. To find the diaphragm deflection (cavity not yet sealed) using finite element method, silicon substrate is meshed as shown in Fig. 4.2 (a, b).

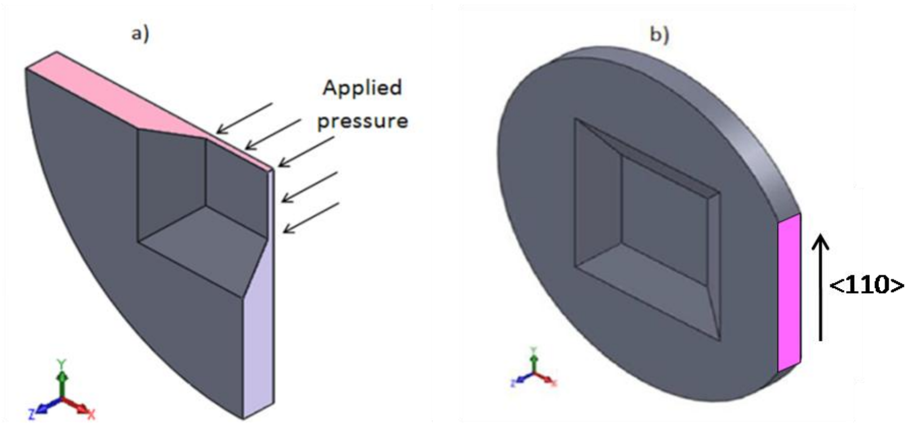

Fig. 4.1 Model of silicon substrate after chemical etching a) Quarter part and b) Full

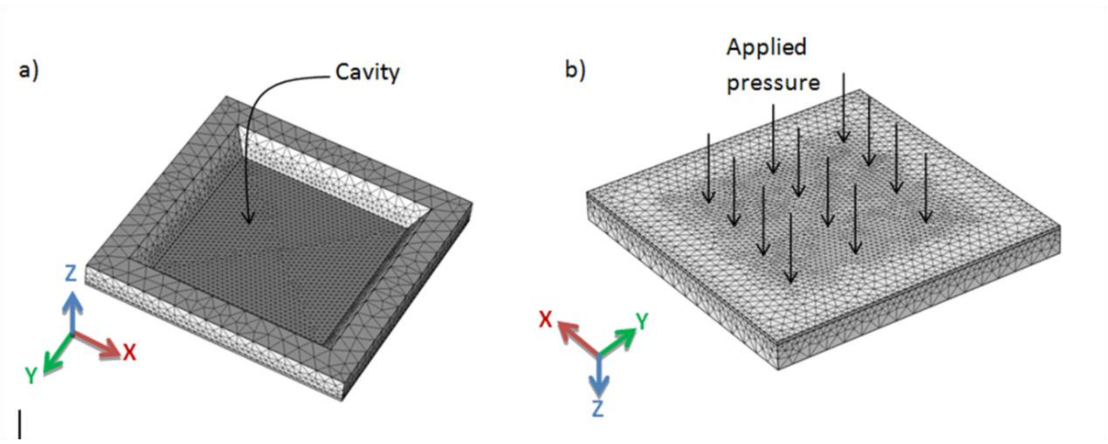

Fig. 4.2 Meshed silicon structure a) Cavity side and b) Top side

Criteria for mesh selection: A series of FE simulations are carried out with different mesh sizes. It is found that the smaller size mesh results in higher accuracy and lesser convergence error of simulation results. However, at the same time, smaller mesh increases the computation efforts and requires prolonged computation time. Hence, mesh size is optimized for convergence accuracy more than 98% and the computation time of less than an hour; which are acceptable for the present simulation work. The optimized mesh parameters are given at serial numbers 15-18 of Table 4.1. The desired full scale deflection is 15.63 μm at the centre of diaphragm for 1 bar net applied pressure. This deflection value is same as that used in analytical model described in the previous chapter. The suitable thickness of the diaphragm is found to be 139 µm for the desired full scale deflection.

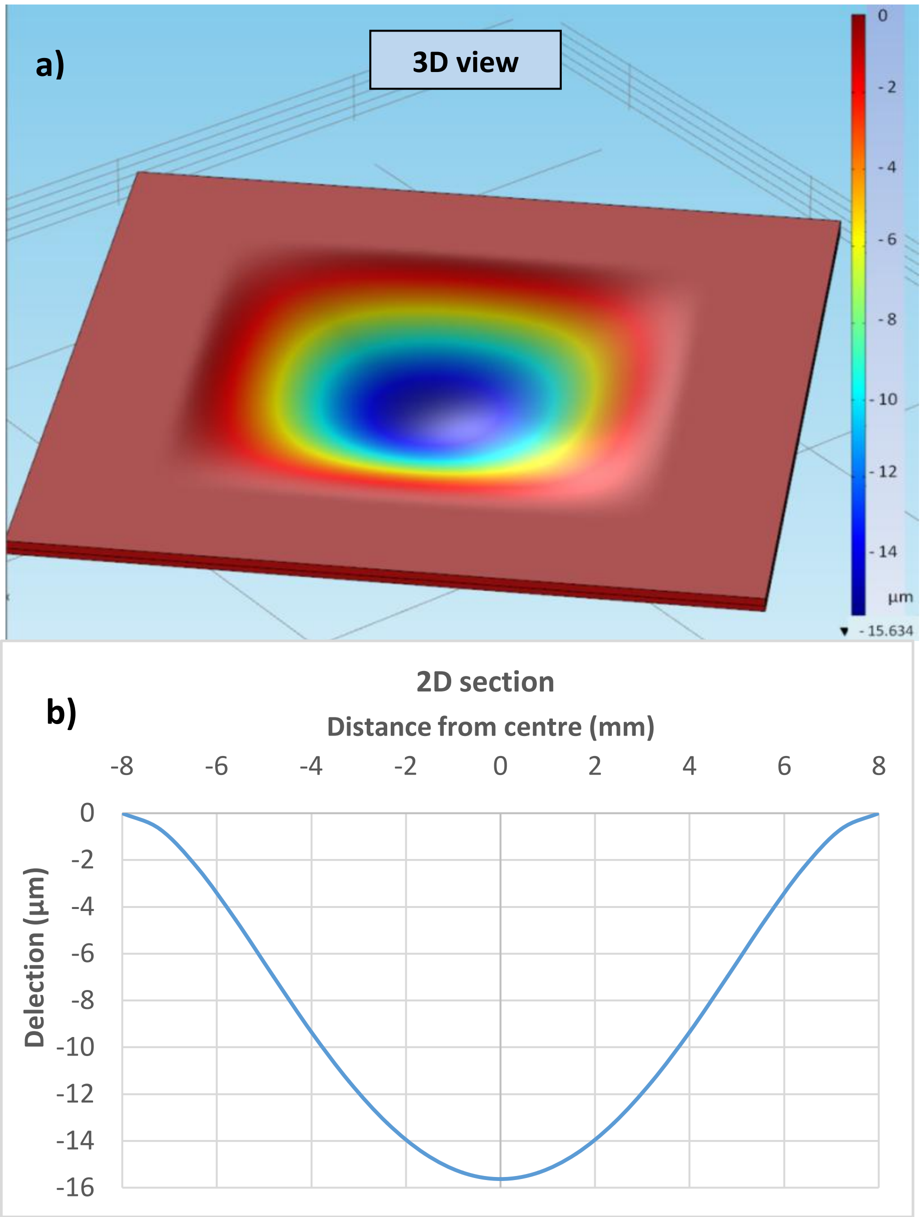

Fig. 4.3 Deflection of square shaped single crystal silicon diaphragm; a) 3D and b) 2D plots

The 3D profile and 2D section of deflection are shown in Fig. 4.3 (a, b) for net applied pressure of 1 bar. The 2D section of deflected diaphragm is taken parallel to the edge and crossing from the centre of diaphragm. The maximum deflection is 15.63 µm at the centre of diaphragm. The deflection shape of the diaphragm is important as it governs the change in volume of the cavity.

4.2.2. FE analysis of diaphragm in sealed structure

The silicon wafer is bonded to a bulk Pyrex glass wafer as shown in Fig. 4.4. There is some amount of air trapped in the cavity after sealing process takes place as also indicated in Fig. 4.4 (a).

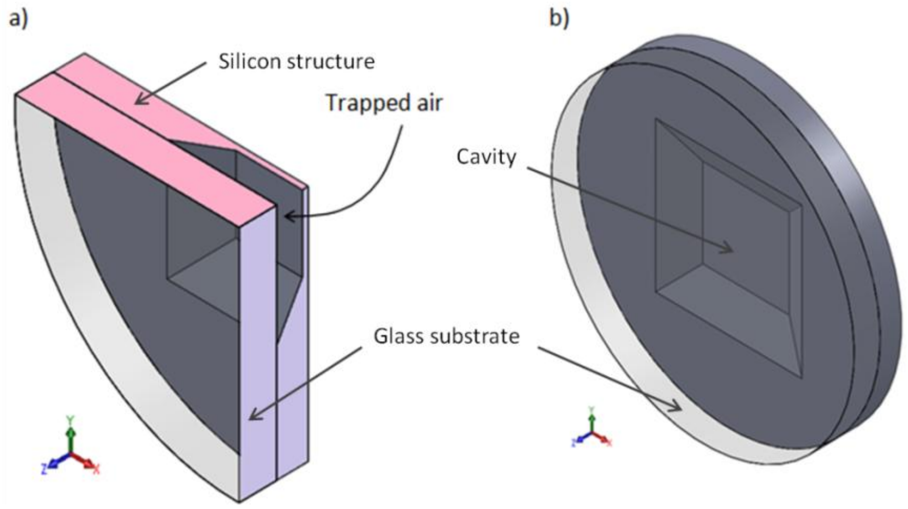

Fig. 4.4 Silicon chip bonded with glass a) Quarter part and b) Full model

During pressure testing, the test fluid applies pressure from the top surface of the silicon chip. As the applied pressure increases, the diaphragm moves inward in the cavity and compresses the trapped air which results in an increase of the cavity pressure. The increased cavity pressure puts greater resistance against any further inward deflection of diaphragm. Here, the cavity pressure is the 'reference' pressure for the pressure sensor. The reference must always be stable with environmental or operating conditions. However, in the present case reference pressure can change with applied pressure and diaphragm deflection. Therefore, the deflection behaviour of diaphragm shall be analyzed by coupling a) fluid dynamics of trapped air and b) structural mechanics of diaphragm [98]. Navier-Stokes equations are used for the fluid dynamics of trapped air. To couple the physics of fluid dynamics and structural movement, moving mesh based on ALE technique [99-100] is used in COMSOL. Details of simulation such as governing equations, boundary conditions, initial conditions etc. are described in following subsections. The mesh type, mesh size, number of elements and nodes etc. and other relevant parameters are listed in Table 4.1

4.2.2.1 Governing Equations

The governing equations for the fluid dynamics are based on Navier-Stokes relations as per Eq. (4-2 to 4-3). Governing equation for diaphragm deformation and deflection is given in Eq. 4-4.

$$\rho\frac{\partial \mathbf{u}_{\mathrm{fluid}}}{\partial t} + \rho(\mathbf{u}_{\mathrm{fluid}}.\nabla)\mathbf{u}_{\mathrm{fluid}} = \nabla.\left[-p.\mathbf{I} + \mu\left(\nabla\mathbf{u}_{\mathrm{fluid}} + (\nabla\mathbf{u}_{\mathrm{fluid}})^{T}\right) - \frac{2}{3}\mu(\nabla.\mathbf{u}_{\mathrm{fluid}})\mathbf{I}\right] \quad \textbf{Eq. 4-2}$$

$$\frac{\partial\rho}{\partial t} + \nabla.(\rho\mathbf{u}_{\mathrm{fluid}}) = 0 \quad \textbf{Eq. 4-3}$$

$$\rho\frac{\partial^2\mathbf{u}_{\mathrm{solid}}}{\partial t^2} - \nabla.\sigma = \mathbf{F}\mathrm{v} \quad \textbf{Eq. 4-4}$$

Where, $'\rho'$ is the mass density of air which is analytically correlated based on ideal gas law. The $\mathbf{u}_{\mathbf{fluid}}$ and $\mathbf{u}_{\mathrm{solid}}$ are the spatial velocity of air and structure respectively. The 'p' and 'μ' are the spatial pressure and the dynamic viscosity of air respectively. The '**I**' is unit matrix. The **F**v is the volume force in structure, which is zero in the present case. The 'σ' is stress in the structure with is expressed in Eq. 4-5.

$$\sigma = J^{-1}\mathbf{F}\mathbf{S}\mathbf{F}^{T};\ \mathbf{F} = (\mathbf{I} + \nabla\mathbf{u}_{\mathrm{solid}});\ J = \det(\mathbf{F});\ \mathbf{S} - \mathbf{S_0} = \mathbf{C}:(\varepsilon - \varepsilon_0 - \varepsilon_{\mathrm{inel}})$$

And $$\varepsilon = \frac{1}{2}\left[(\nabla \mathbf{u}_{\mathrm{solid}})^{\mathrm{T}} + \nabla \mathbf{u}_{\mathrm{solid}} + (\nabla \mathbf{u}_{\mathrm{solid}})^{\mathrm{T}} \nabla \mathbf{u}_{\mathrm{solid}} \right] \quad \textbf{Eq. 4-5}$$

Where J=determinant of deformation gradient (or Volume ratio), **F**= Deformation gradient, **S**= Second Piola Kirchhoff stress matrix, $\mathbf{S_0}$ = Initial value of the Second Piola Kirchhoff stress, σ = Cauchy stress or true stress, ***C***= Anisotropic elastic constant matrix of silicon, ε= strain vector due to the deformation of silicon structure, ε_o= pre-strain vector associated with the structure, ε_{inel}= thermal strain which is zero in present simulation.

Table 4.1 FEA parameters used to simulate diaphragm deflection

Sr. No.	FEA parameters	Value
1	Solver configuration	Coupling of structural mechanics, laminar flow, and ALE based moving mesh
2	Simulation type model	Time dependent
3	Solver type	Backwards differentiation formula (BDF) method
4	Maximum BDF order	2
5	Fraction of initial step for Backward Euler	1
6	Relative tolerance	0.001
7	Non-linear method	Constant (Newton)
8	Geometry type	3-dimenion
9	Coarse Solver	MUMS
10	Shape function for laminar flow (pressure and velocity)	Lagrange (Linear) with spatial shape frame
11	Shape function for solid mechanics (displacement in all directions)	Lagrange (Quadratic) with material shape frame
12	Shape function of deformable mesh	Lagrange (Linear)
13	Geometric shape order	Quadratic
14	Mesh smoothing type	Winslow
15	Type of mesh	Tetrahedral
16	Minimum and maximum element size on Si-structure	0.15 mm and 1.20 mm respectively, with growth rate of 1.45
17	Minimum and maximum element size on fluid	0.05 mm and 0.24 mm respectively, with growth rate of 1.25

4.2.2.2 Boundary Conditions

The side walls and bottom surface of silicon structure are set to be fixed as per the Eq. 4-6.

$$\mathbf{u}_{\mathrm{solid}} = 0 \quad \textbf{Eq. 4-6}$$

Base of the trapped air is also set as a fixed wall (Eq.4-7) because there is a glass boundary in the structure,

$$\mathbf{u}_{\mathrm{fluid}} = 0 \quad \textbf{Eq. 4-7}$$

At the interface of air and the diaphragm, a criterion of common velocity and pressure is set as expressed in Eq. 4-8 and Eq. 4-9. The displacements are represented by 'd'. Here, Eq. 4-9 shows the stress transfer from the air using force equilibrium at the interface between them.

$$\mathbf{u}_{\mathrm{solid}} = \mathbf{u}_{\mathrm{fluid}} \ ; \ \mathrm{P}_{\mathrm{solid}} = \mathrm{P}_{\mathrm{fluid}} \ ; \ \mathrm{d}_{\mathrm{solid}} = \mathrm{d}_{\mathrm{fluid}} \quad \textbf{Eq. 4-8}$$

$$\sigma.\mathbf{n} = \Gamma.\mathbf{n} \ ; \ \Gamma = [-\mathrm{p}\mathbf{I} + \mu\,(\nabla\mathbf{u}_{\mathrm{fluid}} + (\nabla\mathbf{u}_{\mathrm{fluid}})^{\mathrm{T}}) - \frac{2}{3}\,\mu\,(\nabla.\,\mathbf{u}_{\mathrm{fluid}})\mathbf{I}\,] \quad \textbf{Eq. 4-9}$$

where, **n** = the unit vector normal to the surface of silicon structure.

4.2.2.3 Initial Conditions

The initial pressure is the pressure when the silicon wafer (with front cavity) is bonded to glass wafer and there is no diaphragm in existence (The diaphragm is formed after bonding, by etching of the backside cavity on silicon wafer). Therefore, the initial pressure corresponds to 'initial volume' and the condition when there is **no deflection** (or null-deflection) of the diaphragm. During normal operation of the sensor, the null-deflection is achieved when the applied pressure is exactly equal to the initial cavity pressure (Fig. 4.5).

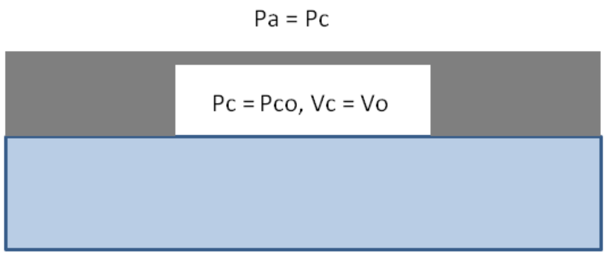

Fig. 4.5 Null-deflection condition of diaphragm

Initial values of displacement and velocity are set as zero on structure. In case of the trapped air, initial velocity is set to zero and pressure is set to 405.3 mbar (40530 Pa) which is computed from the theory of anodic bonding carried out under atmospheric pressure. The same pressure is set on structure to start with no deflection condition of diaphragm.

4.2.2.4 Application of external pressure

The external pressure is applied on the diaphragm from the top side. The pressure range to be covered is from 0 mbar (abs.) to 1000 mbar (abs.), whereas the pressure inside the cavity is 405.3 mbar (abs.) as per the initial condition. Therefore, the pressure is applied in two parts as a time based ramp function.

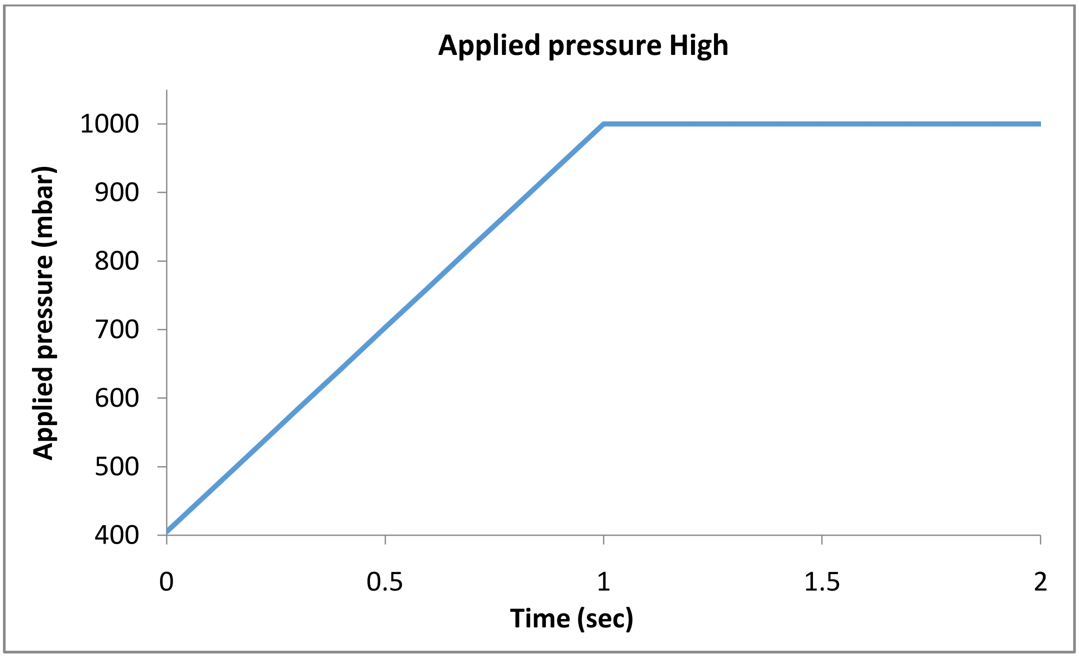

Fig. 4.6 Applied pressure as increasing ramp function

One is increasing ramp from 405.3 mbar to 1000 mbar over 1 second of time and then 1 second of dwell time (Fig. 4.6). Similarly, second part of pressure is applied as decreasing ramp from 405.3 mbar to 0 mbar over 1 second of time and then 1 second of dwell time (Fig. 4.7). The time resolution for applied pressure is 1 ms, hence the applied pressure is applied in 1000 steps for both the ramp functions.

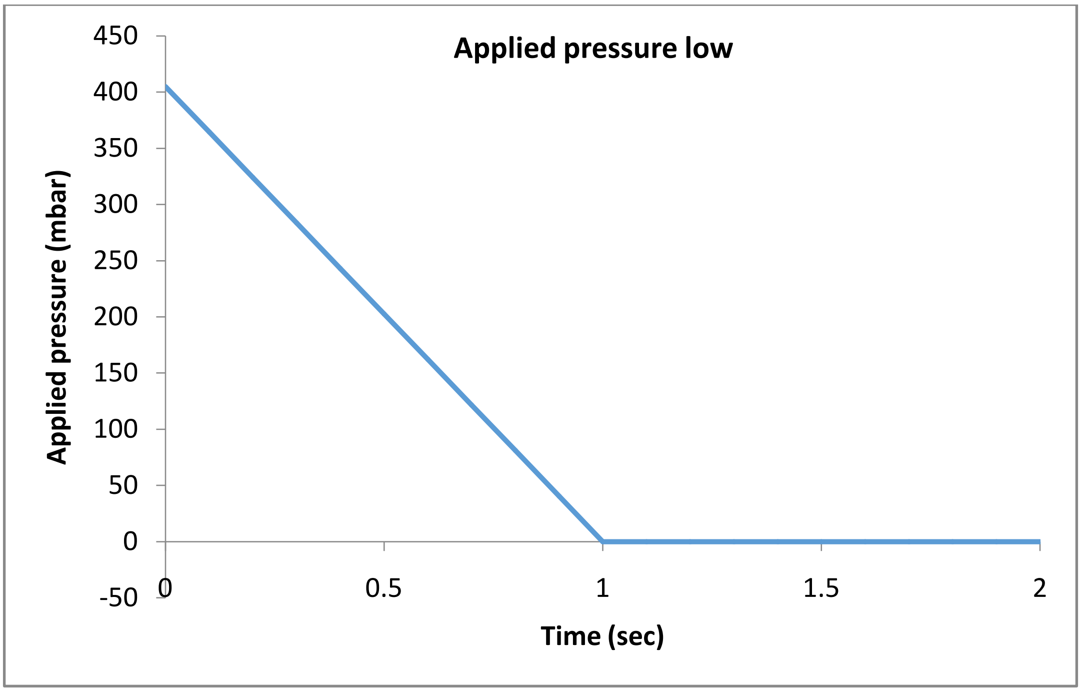

Fig. 4.7 Applied pressure as decreasing ramp function

4.2.2.5 Moving Mesh

Trapped air and diaphragm are set as deformable mesh or freely moving mesh whose movements are governed by the solution of finite element analysis. The Navier-Stokes equations are solved on a freely moving deformed mesh of the trapped air. The deformation of this mesh relative to the initial shape of the domain is computed using Winslow smoothing. Arbitrary Lagrangian-Eulerian (ALE) method is used to combine the fluid flow using Eulerian formulation and the solid mechanics using Lagrangian formulation in a spatial frame with respect to the reference frame. To solve the present problem using FEA based simulation, a list of parameters is presented in Table 4.1 for the same.

4.2.2.6 Materials Properties

A) Silicon

In the present case mono-crystalline silicon is used whose mechanical properties are listed in Eq. 4-10 [91].

$$\textbf{Elasticity matrix of silicon } (\boldsymbol{C}) = \begin{bmatrix} 165.6 & 63.9 & 63.9 & 0 & 0 & 0 \\ 63.9 & 165.6 & 63.9 & 0 & 0 & 0 \\ 63.9 & 63.9 & 165.6 & 0 & 0 & 0 \\ 0 & 0 & 0 & 79.5 & 0 & 0 \\ 0 & 0 & 0 & 0 & 79.5 & 0 \\ 0 & 0 & 0 & 0 & 0 & 79.5 \end{bmatrix} \textbf{GPa;} \quad \textbf{Eq. 4-4}$$

Mass density = 2330 kg/m^3; plane and normal of the top surface: (0 0 1) and [0 0 1].

B) Air

Dynamic viscosity = 1.825x10^{-5} Pa-s; density = 1.204 kg/m^3 at NTP

4.3. Results from FE analysis of sealed microcavity pressure sensor

The FE simulations are carried out for sensors of various cavity lengths such as 7, 15, 30, 60, 100, 200 and 500 µm. The initial pressure inside the cavity under null-deflection condition of diaphragm is taken as 405.3 mbar. The deflection x and trapped gas pressure P_c were noted against the applied pressure P_a. The results are presented in next subsections.

4.3.1. Cavity pressure P_c with applied pressure P_a

The volume of the sealed cavity changes in response to applied pressure through the deflection of diaphragm. Hence, the cavity pressure (the trapped gas pressure); which is here the ‘reference’ pressure for the pressure sensor, also changes. The cavity pressure is plotted against the applied pressure in Fig. 4.8 from the results of finite element simulations carried out for sensors of different cavity lengths. The results of 100 and 200 µm cavity are not included in this figure for sake of clarity of presentation.

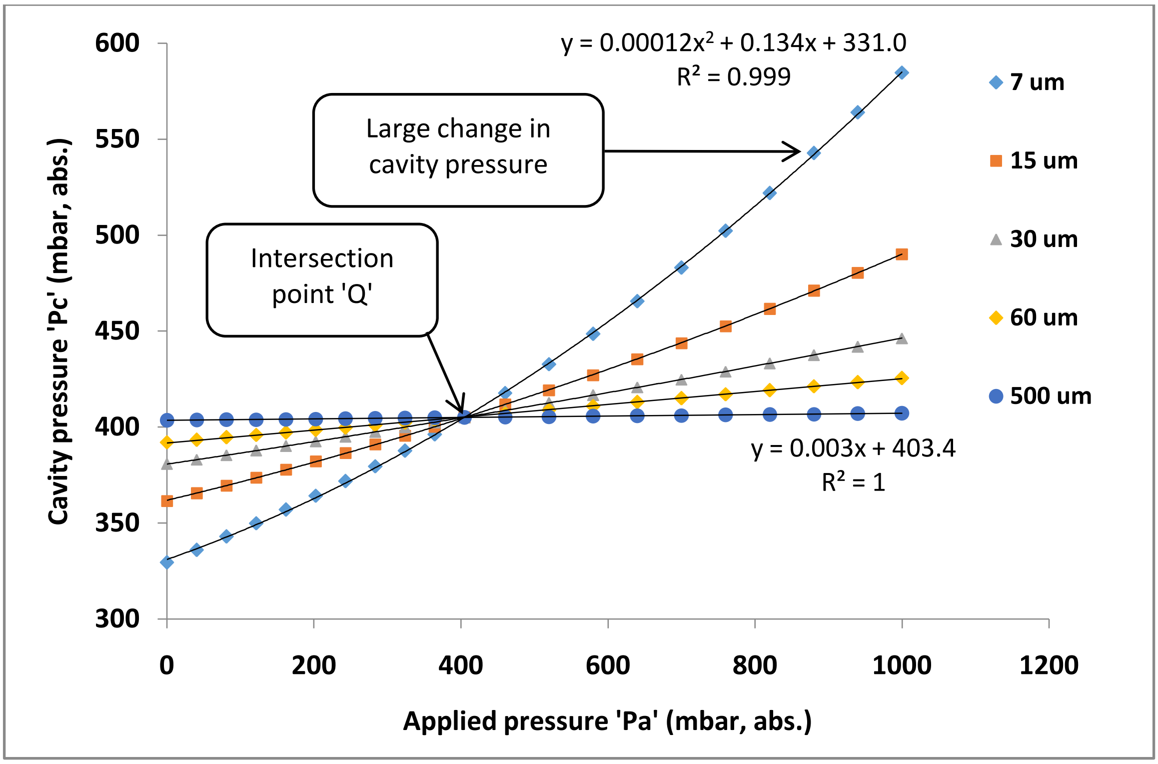

Fig. 4.8 Pressure of the trapped gas versus externally applied pressure

For all the sensors irrespective of cavity length, when the applied pressure (x-value) is 405.3 mbar, the cavity pressure (y-value) is also 405.3 mbar. Therefore, in Fig. 4.8, all the curves have common point of intersection ‘Q’.

When the applied pressure is less than the cavity pressure, the deflection is negative (outward of the cavity). In such case, the cavity volume increases and cavity pressure decreases. The same is shown towards the left side of the point ‘Q’ in Fig. 4.8. Similarly, when the pressure is more than the initial cavity pressure, the deflection is positive (inward of the cavity), the cavity volume decreases and cavity pressure increases, as shown at the right side of the point ‘Q’ in Fig. 4.8.

The curve for sensor of 7 μm cavity length is very steep (Fig. 4.8). The change in cavity (reference) pressure is from 329.4 mbar to 584.7 mbar when the applied pressure changes from minimum to maximum. The total change of cavity pressure is 255.3 mbar which is quite significant fraction (63%) of the original value of cavity pressure (405.3 mbar). The curve is nonlinear with a quadratic fit and R-square value of 0.999.

For the sensor with 15 µm cavity length, the cavity pressure varies from 361.5 mbar to 490.1 mbar (Fig. 4.8). The total change of cavity pressure is 128.6 mbar which is also considerable fraction (31.7%) of the original value of cavity pressure (405.3 mbar). However the change is almost half compared to that in sensor of 7 µm cavity length.

As the sensors of larger cavity lengths are considered, the change in cavity pressure becomes less steep with the applied pressure (Fig. 4.8). The cavity pressure becomes almost linearly dependent on the applied pressure. The change in cavity pressure is 9.9 mbar (2.4 %) and 3.7 mbar (0.9%) respectively for sensors of 200 µm and 500 µm cavity lengths.

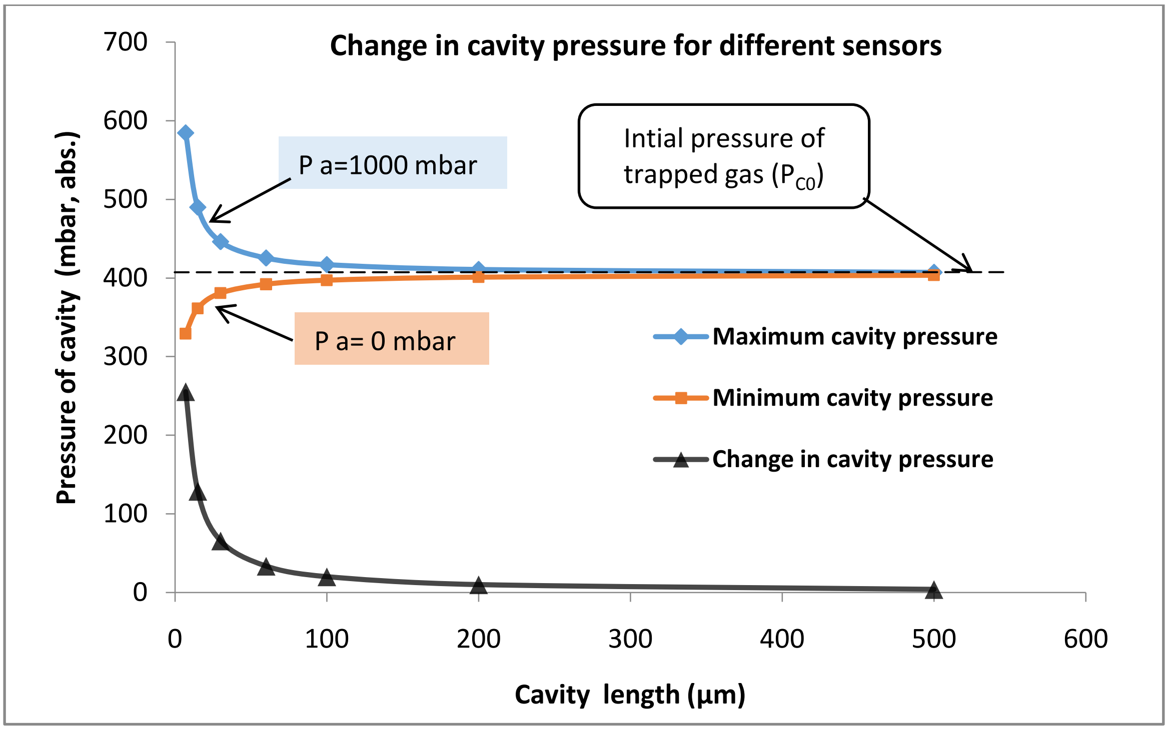

Fig. 4.9 Change in cavity pressure with cavity length for 1 bar sensor

The maximum and minimum values of cavity pressure along with total change of cavity pressure are plotted in Fig. 4.9 as a function of the cavity length of sensor. The cavity pressure is maximum when the applied pressure is 1000 mbar (abs.). It is minimum when the applied pressure is 0 mbar (abs.). The difference between the maximum pressure and minimum pressure of the cavity gives the total change of cavity pressure in the pressure range (0-1 bar) of operation of the pressure sensor.

It can be seen in Fig. 4.9 that the change in cavity pressure is dependent on the cavity length of the sensor. The change in cavity pressure is highly sensitive to the cavity length as a design parameter for the sensor. For large values of cavity lengths such as > 200 µm, the curve becomes almost flat. From the view point of sensor performance, variable reference pressure is not favourable. Hence, larger cavities (cavity lengths not less than 200 µm) shall be preferred. A 500 µm length cavity shall be a good choice as change is pressure is < 1% for this value. Nevertheless, the final decision of cavity length value is governed by the desired specifications of the sensor.

4.3.2. Diaphragm deflection x with applied pressure P_a

Deflection at the centre of square diaphragm is considered in the design of the pressure sensor. The position of null deflection of diaphragm is taken as reference for calculation of deflection. Diaphragm positions inward the cavity are denoted with positive sign and outward with negative sign.

The FE simulations are carried out for sensors of cavity lengths 7 µm, 15 µm, 30 µm, 60 µm, 100 µm, 200 µm and 500 µm. Deflection characteristics of diaphragm with applied pressure (absolute) for sensors of different cavity lengths (7 µm, 15 µm, 30 µm, 60 µm and 100 µm) are shown in Fig. 4.10. The characteristics for cavity lengths 100 µm and 200 µm have not been included in this figure for sake of clarity of presentation.

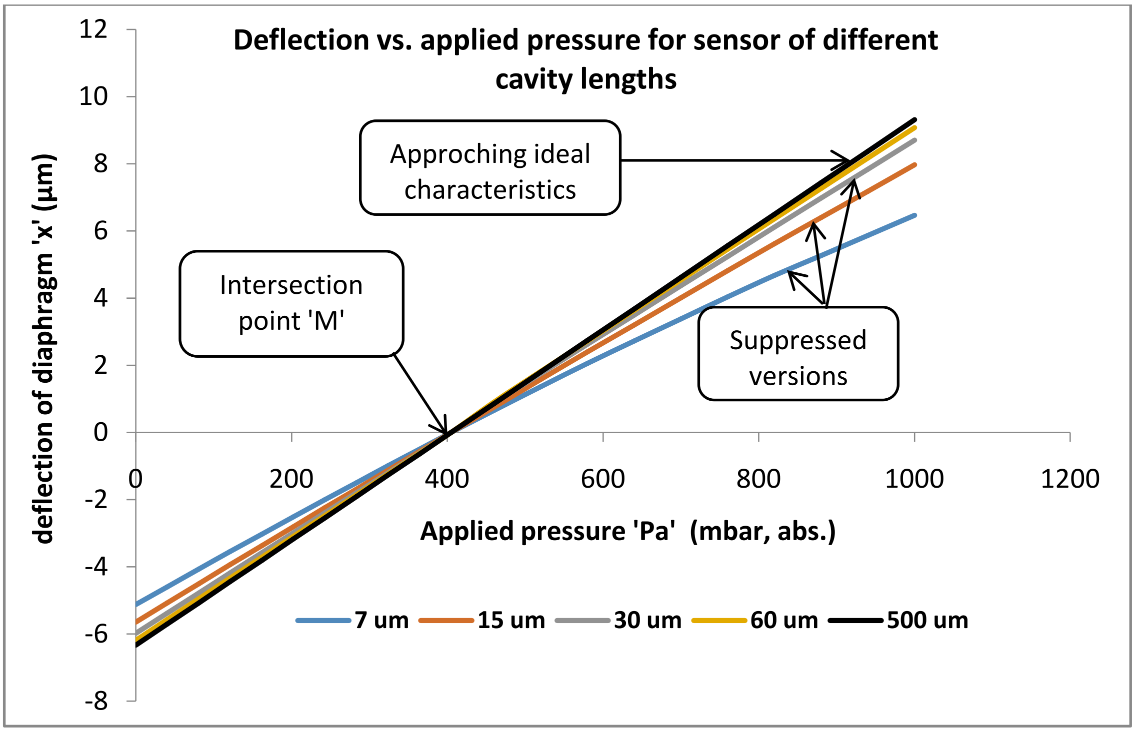

Fig. 4.10 Deflection behaviour of diaphragm in pressure sensors of different cavity lengths

The slope of characteristics increases with increasing cavity length. The characteristics for 7 µm, 15 µm, 30 µm and 60 µm cavity lengths are distinct; however, the rate of slope increase reduces with increasing cavity length. The characteristics for 60 µm and 500 µm cavity length sensors are very closely matching. The characteristic for 500 µm cavity length is almost the ideal (unsuppressed) characteristic. This indicates that for small cavity length sensors, the achievable span is a “suppressed” version of the designed span.

The span is 11.59 µm for sensor of 7 µm cavity length, which is about 74% of the design span 15.63 µm. It is due to the significant change of cavity pressure taking place in response to movement of diaphragm for small cavity length sensors. For sensor of 15 µm cavity length, the span is 13.62 µm which is about 87% of the design span. For sensor of 200 µm cavity length, the span is 15.53 µm which is more than 99% of the design span.

All the curves are intersecting at one common point ‘M’ in Fig. 4.10. This point corresponds to the null deflection condition of diaphragm, where the applied pressure is same as the pressure of trapped gas and the deflection of the diaphragm is zero.

Further, as the pressure is applied, the deflection values are different for different cavity length sensors. The characteristics are very sensitive to cavity length parameter in the regime of small cavity lengths. A small change of initial cavity length of sensor may shift the deflection behaviour considerably. Therefore, large cavity lengths are recommended to obtain more deterministic characteristics of the sensors.

4.3.3. Span S of the pressure sensor with cavity length l_0

It is shown that the span of a pressure sensor with sealed microcavity depends on the length of the cavity. For small cavity lengths, the achievable span is smaller than the designed span. In Fig. 4.11, the numerically simulated span value is plotted against the cavity length as a design parameter. In the figure, the cavity lengths up to 200 µm are taken on x-axis, to zoom in to the portion of interest where phenomenon of suppression is significant.

The dependence of achievable span on cavity length is nonlinear. In the regime of small cavity lengths, the span value is very much sensitive to the cavity length parameter. The dependence becomes weaker when the cavity length is sufficiently large such as 100 µm or more. The span reaches very close to the design value for sensors with large cavity lengths such as more than 100 µm. The achievable span is about 98.5 % at 100 µm cavity length and 99.3 % at 200 µm cavity length. This means there is very marginal gain in further increasing the cavity length.

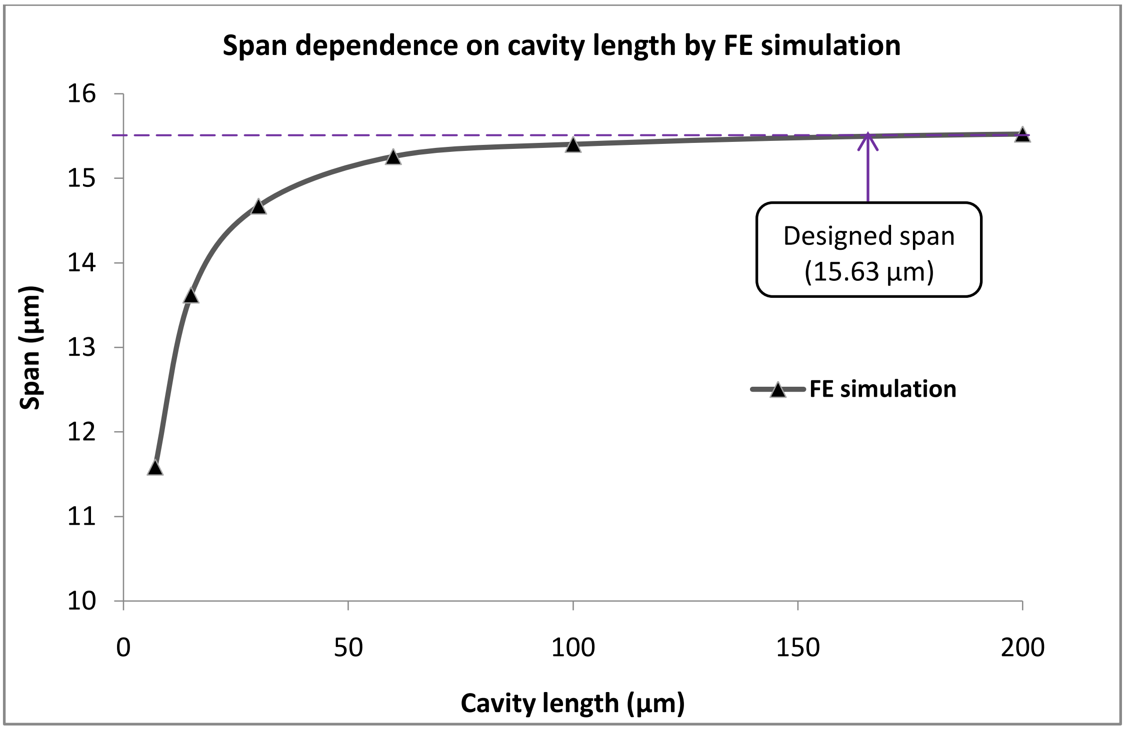

Fig. 4.11 Dependence of span on cavity length

4.4. Comparison of Analytical and Numerical Models

An analytical model is developed as presented in the previous chapter. In this chapter, the numerical model based on finite element analysis is presented. Both the models have shown similar behaviour. The phenomenon of suppression of span is exhibited by numerical model also. The achievable span is a suppressed version of designed span for small cavity lengths. As larger cavity lengths are chosen in design, the achievable span approaches the design value.

The normalized spans predicted by both the models have been plotted together in Fig. 4.12, for comparison. The x-axis is cavity length in logarithmic scale. The FE simulations show **close agreement** with the results of analytical model. The models match closely for larger cavity lengths such as more than 30 µm. However, at small cavity lengths such as those below 30 µm; there is slight deviation between the two models. The maximum disagreement between the models is **2.1 %** at the smallest cavity length value of 7 µm. The FE analysis suggests little higher suppression of span (the lower curve). As the difference between the two models is very small, the analytical model gets **validated** by the results of FE simulations.

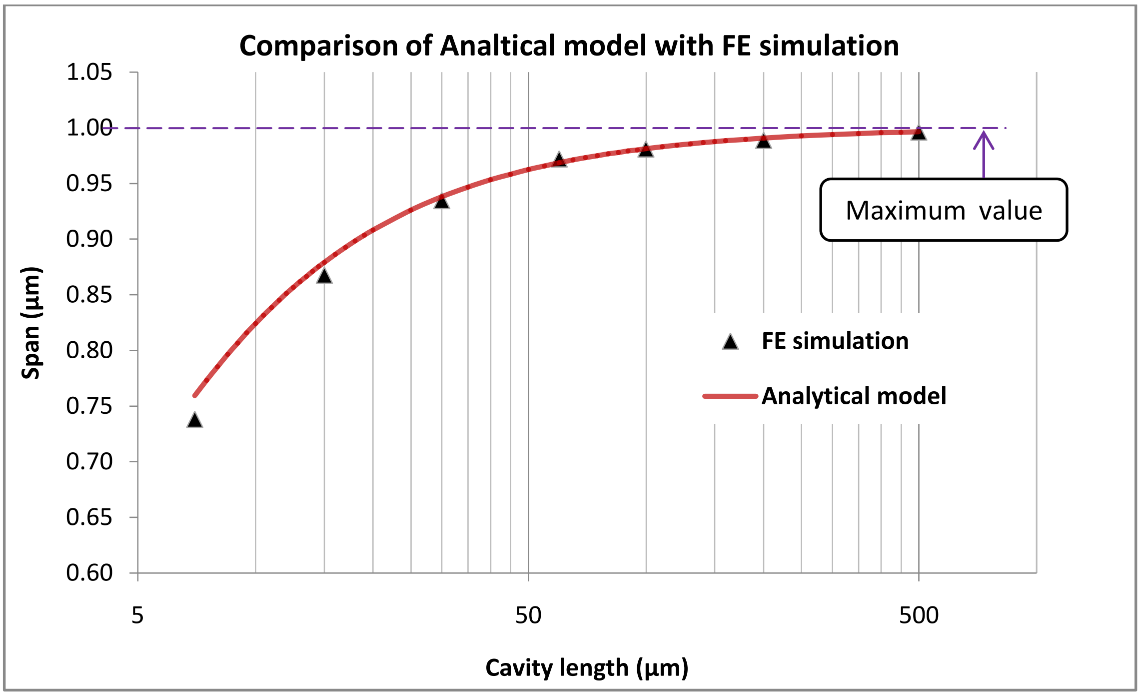

Fig. 4.12 Comparison of results of analytical and numerical models

It is found from FE simulations that there is a difference in the value of 'ν' (the average normalized deflection) between the two models. The $\nu = 0.3044$ was taken in the analytical model, whereas in the simulations the calculated value of ν is in the range of 0.319 to 0.321. This increases the total change of volume in FE analysis, which results in slightly higher cavity pressure and thus little higher suppression of span. The small difference in the volume attributing to higher value of ν is not significant for large cavities, and hence both the models show good agreement for large cavity lengths. Further in Fig. 4.13, the analytical model is plotted with results of FE simulations; after taking higher value of ν from simulations. The analytical model with higher ν, fits better on FE results, at small as well as at large cavity lengths. The maximum disagreement between the two models is **1.1%**, which is acceptable. .

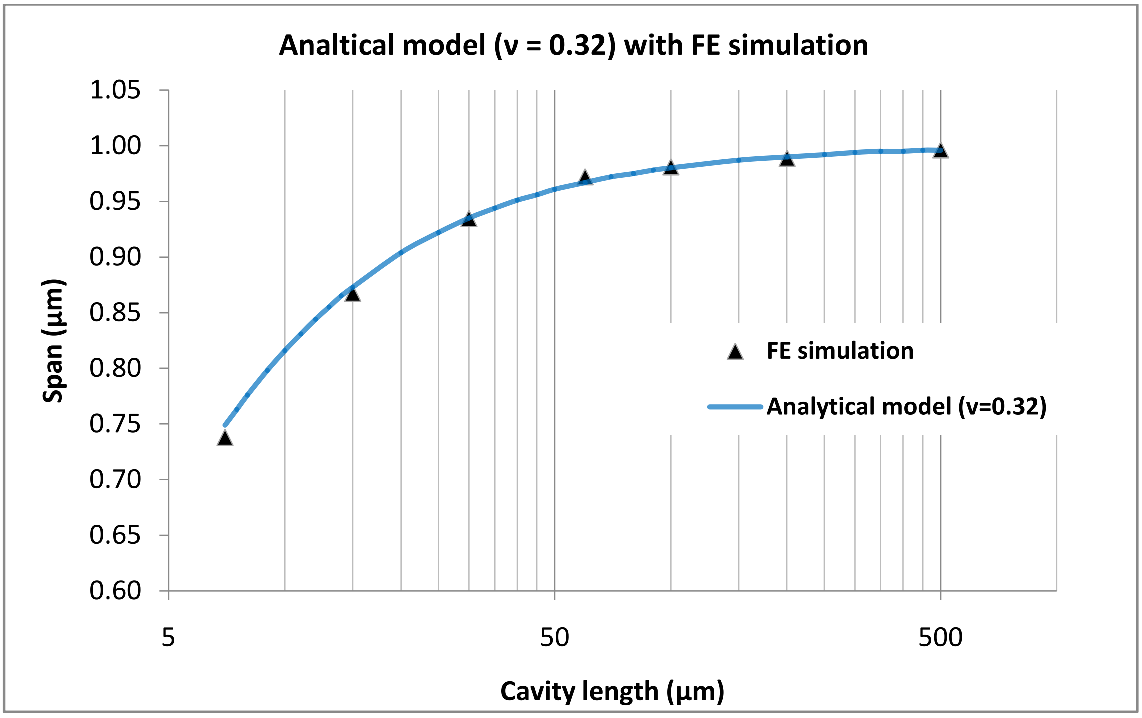

Fig. 4.13 Analytical model (with ν = 0.32) on FE simulation data

4.5. Summary

The effect of trapped gas on span of a sealed microcavity pressure sensor is studied using finite element analysis. The simulation studies clearly bring out the underlined phenomenon of 'suppression of span' in sealed microcavity pressure sensors. It is evident that the span of diaphragm is affected more severely in sensors with smaller cavity lengths due to larger change of reference pressure in the sealed cavity.

The developed numerical model is compared with the analytical model. The two models are comparable to each other with maximum error of 2.1%.. Hence, the developed **analytical model gets validated** by the FE based simulations. The design parameters of both the models are kept at par. The difference between the achievable span at small cavity lengths can be attributed to various parameters of FE simulation. It is found from FE simulations that the average normalized deflection is little higher (0.32 ± 0.001 vs. 0.3044) than what was calculated and used in developed analytical model. The value taken in the analytical model was based on the theory of dimensionless deflection shape function, which was in fact validated for small size of diaphragm in the referred literature. When the higher value of ν is taken the error reduces.

In the extrinsic Fabry-Perot pressure sensors, the cavity lengths are on smaller side, such as from about one micron to few tens of microns. The smaller cavity lengths are preferred for higher fringe contrast. Therefore, the studies carried out in previous and current chapters become more significant; as they highlight the mechanical design and performance issues associated with small cavity length sensors.

The phenomenon studied is valid regardless of the lateral size of the diaphragm. The study is relevant for capacitive MEMS pressure sensors as well and for vacuum-bonded low pressure sensors which may have trapped gas from out-gassing in long run.

Chapter 5

SENSOR FABRICATION AND DEVELOPMENT OF TECHNIQUE FOR NONCONTACT MEASUREMENT OF CAVITY LENGTH

5.1. Introduction

An analytical and a numerical model have been developed in previous chapters to understand the behaviour of sealed microcavity pressure sensors. An underlying phenomenon of suppression of span has been identified and modelled. Sensor devices are fabricated as per the design discussed earlier towards experimental study. In this chapter fabrication of the devices is explained briefly. Devices are fabricated with 0.5 mm as well as 2 mm thick glass wafers bonded to silicon wafer. It is found difficult to obtain any optical signal from devices with 2 mm thick glass due to higher glass thickness. The associated problem is identified and circumvented through a novel technique developed for measurement and testing of the devices. The developed technique is used to make the devices functional without any physical alterations such as reducing the glass thickness by grinding or chemical etching. This technique is also used for noncontact measurement and characterization of etched depth of the front cavity and deflection shape of the square silicon diaphragm. In the following sections, more details have been presented.

5.2. Fabrication of sensors

The sensors have been made using MEMS technology. The fabrication is carried out as per the design in Microelectronics lab of IIT Delhi. The flow chart comprising major steps of fabrication is shown in Fig. 5.1. The pictorial representation of fabrication steps is given in Fig. 5.2. Glasses of two different thicknesses have been used. The devices with 0.5 mm thick glass are found very easy for acquiring optical signal; however, the devices are very fragile. Therefore, a batch of sensors was fabricated using 2.0 mm thick glass as well.

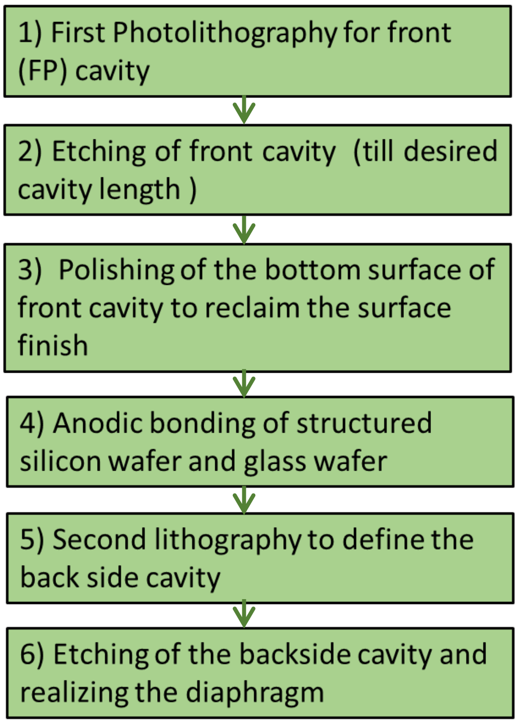

Fig. 5.1 Major steps of fabrication of the devices

The specifications of silicon wafer used are given in Appendix A.7. The front side cavity is created using photolithography and KOH based wet etching of single crystal silicon [97]. The etch rate is about 0.4 µm/min with 40% KOH solution at 65°C temperature. The depth of the etched cavity is measured on a commercial white light interferometer (Veeco NT9100). For example, the depths are found to be 14.22 µm (Fig. 5.3) and 59.64 µm, respectively for targeted values of 15 µm (sensor PS10) and 60 µm (sensor PS12). The bottom surface of the front cavity becomes poor in surface finish due to chemical etching [101-102]. Hence, the surface is polished with diamond paste to improve optical quality. Thereafter, the silicon wafer is bonded to a borosilicate glass wafer (Corning's Pyrex 7740) of 0.5 mm thickness by anodic bonding process.

The schematic and set-up of anodic bonding are shown in Appendix A.8. In another batch of sensors, the thickness of bonded glass is 2 mm.

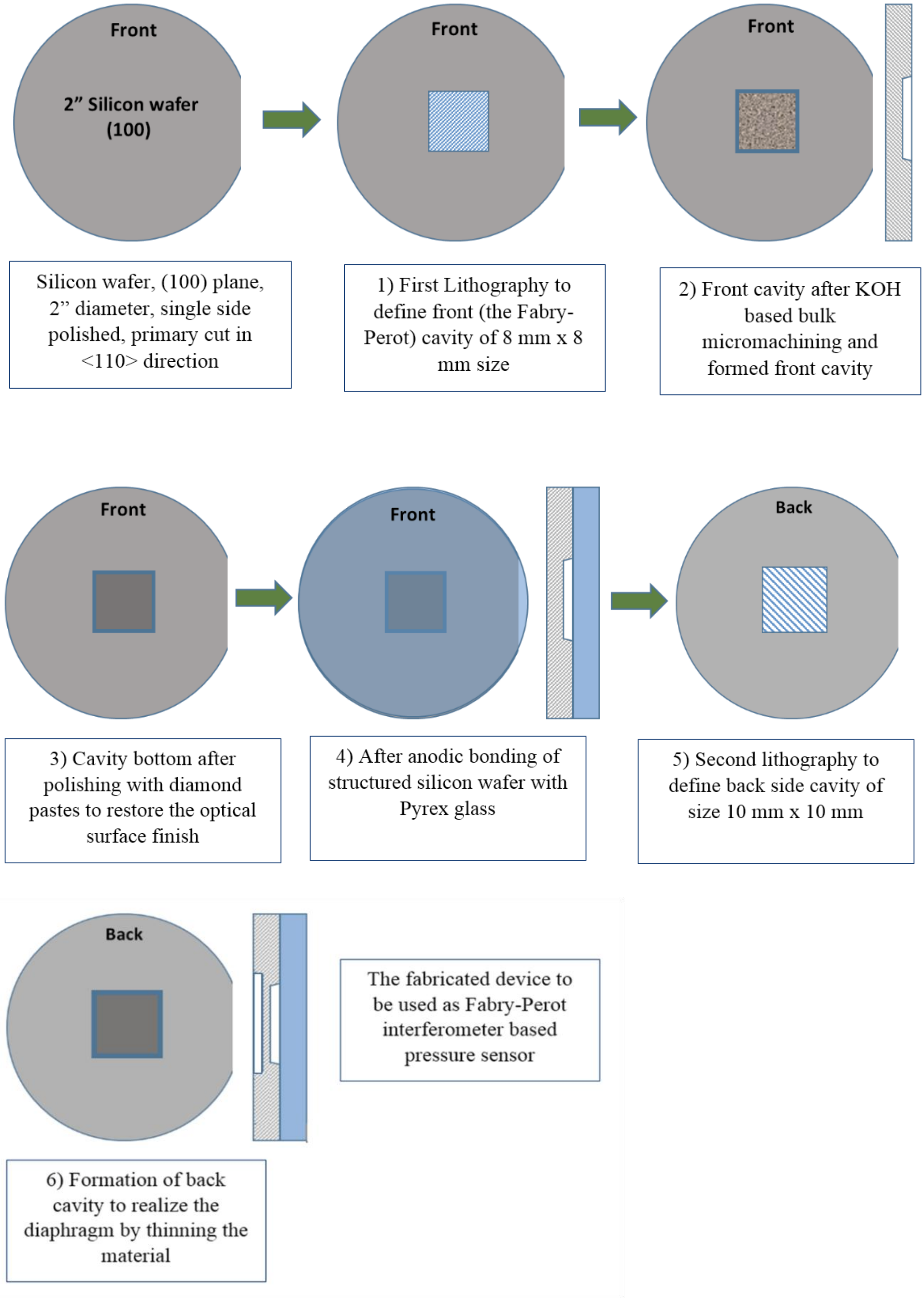

Fig. 5.2 Pictorial representation of fabrication steps of device

The bonding is performed at 450 °C temperature and 1200 V DC voltage. The atmospheric pressure was 1000 ± 8 mbar; therefore, cavity pressure is expected in the range 410-416 mbar (as per the Eq.3-1 and Appendix A.2), which is close to assumed value of 405.3 mbar. The bonding process takes about 40 minutes' time. Front-to-back alignment of second lithography window with first window is carried out [103]. After wafer bonding, etching of the back cavity was carried out on silicon using reactive ion etching (RIE) technique [104] to achieve desired diaphragm thickness. The depth of back cavity is measured using stylus-based surface profilometer (KLA Tencor's Alfastep IQ3). The dimensional measurements of front and back cavities of the devices are carried out in an optical machine vision system (Rapid-I).

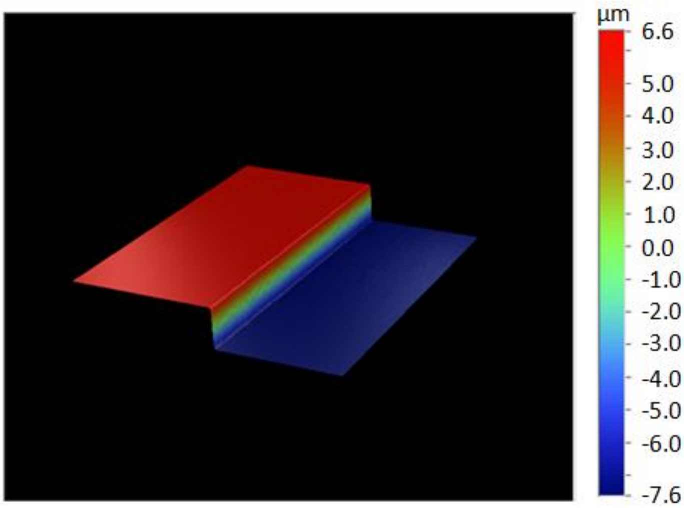

Fig. 5.3 Results of depth measurement of front cavity in silicon wafer for sensor PS10

The list of various fabricated sensors of pressure range 0-1 bar (absolute) along with their design parameters is given in Table 5.1. Photograph of a fabricated device is shown in Fig. 5.4. More photographs are given in Appendix A.9.

Table 5.1 Summary of the fabricated sensors of 0-1 bar pressure range

Sr. No.	Sensor ID	Designed Cavity length (µm)	Measured thickness of diaphragm (µm)	Bonded glass thickness (mm)
1	PS8	10	130 ± 5	0.5
2	PS9	15	132 ± 5	0.5
3	PS10	15	138 ± 5	0.5
4	PS4	30	140 ± 5	0.5
5	PS12	60	138 ± 5	0.5
6	P1	10	134 ± 5	2.0
7	P5	15	135 ± 5	2.0
8	P3	30	132 ± 5	2.0
9	P13	55	138 ± 5	2.0

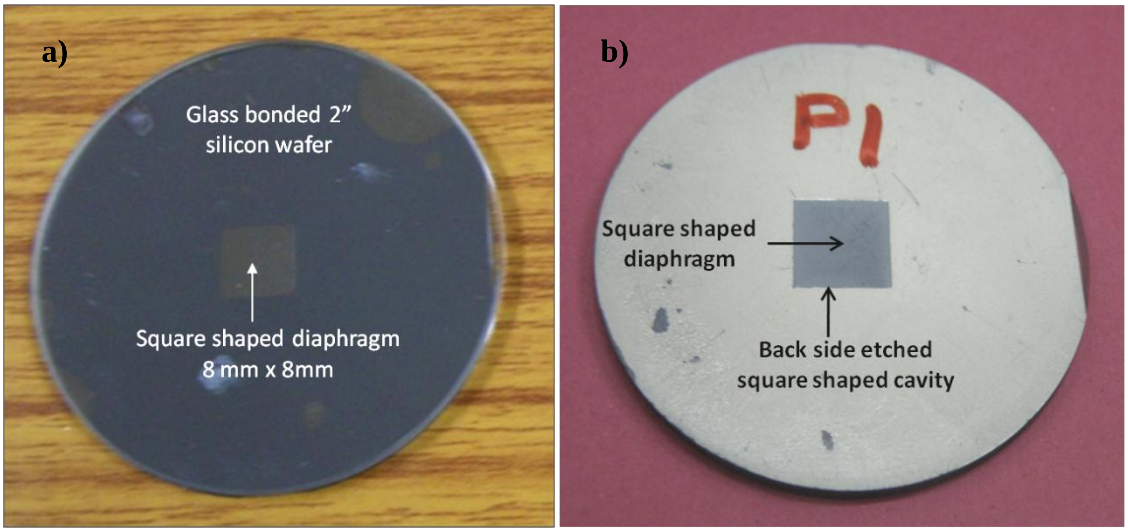

Fig. 5.4 Photograph of a fabricated device a) front b) back side

5.3. Requirement of noncontact measurement

There are two batches of devices fabricated one with 0.5 mm bonded glass and another with 2.0 mm glass. It is found very difficult to acquire any optical signal with the devices with 2 mm glass. In order to overcome this problem a noncontact technique is developed that allows for extremely easy way of sensor interrogation, characterization and measurement of deflection shape of square silicon diaphragm. The developed technique is described in detail in the following sections.

5.3.1. The Device-Under-Test

In the present work, a silicon diaphragm of size 8 mm x 8 mm square is realized after anodic bonding with Pyrex borosilicate glass (Fig. 5.5) for realising optical MEMS pressure transducer. The front cavity is first made with wet etching of silicon and the bottom surface is polished with diamond paste for improving the optical quality of the diaphragm surface. The silicon wafer with front cavity is then bonded to glass. This forms a low finesse Fabry-Perot interferometer (FPI) between glass and silicon. The silicon wafer is then etched from the other side to create cavity. As the second (backside) cavity is machined, the thickness of wafer reduced there and flexible diaphragm came into existence. The deflection sensitivity of this diaphragm is about 15 μm/bar.

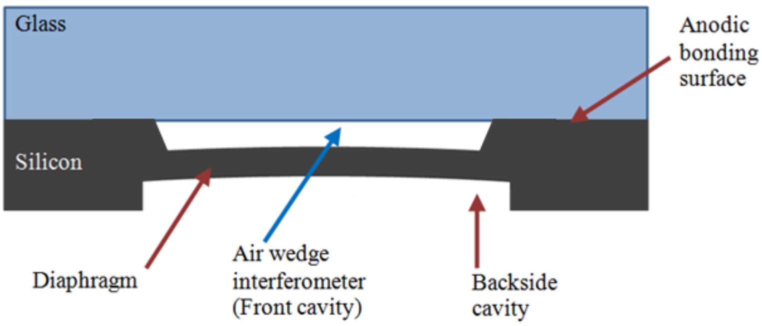

Fig. 5.5 Silicon diaphragm structure bonded to glass wafer in optical MEMS pressure transducer

The anodic bonding process is carried out at high temperature (450 °C) and under atmospheric pressure. The process results in partial vacuum in the sealed cavity. Therefore, the diaphragm is already in deflected position due to exposure to atmospheric pressure under normal conditions. The fringe contours of this air wedge interferometer could be observed with naked eyes. An example is given for device P3 (30 μm cavity length) in Fig. 5.6. The contours show the deflection of diaphragm inside the sealed cavity under atmospheric pressure.

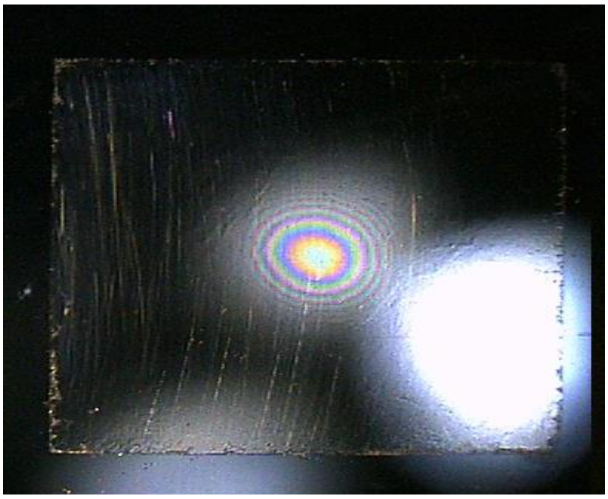

Fig. 5.6 White light fringe pattern visible on a device and captured by a CCD camera.

5.3.2. Challenges in the characterization

It is required to measure the cavity length at the centre of diaphragm as per the normal configuration of pressure sensor. Additionally, it is also desired to measure the cavity length at various points over the area of the interferometer and experimentally validate the deflection shape of the square anisotropic silicon diaphragm. However, there were few challenges in the measurement as described below.

5.3.2.1 Fiber alignment for thicker glass

Typically, a multimode fiber (MMF) of core diameter 62.5 µm or 100 µm is joined perpendicular to the glass, over the centre of diaphragm, to complete the optical pressure sensor. The multimode fibers (MMF) have larger core area than single mode fibers have (diameter less than 10 µm). Therefore, MMF can collect sufficient light from such a transducer where the interferometer is situated away from the fiber end (by the thickness of bonded glass). However, the MMF has large numerical aperture (and cone angle of light);

hence the exiting light diverges very fast, as shown in Fig. 5.7. The spot size increases and power density decreases with increasing distance.

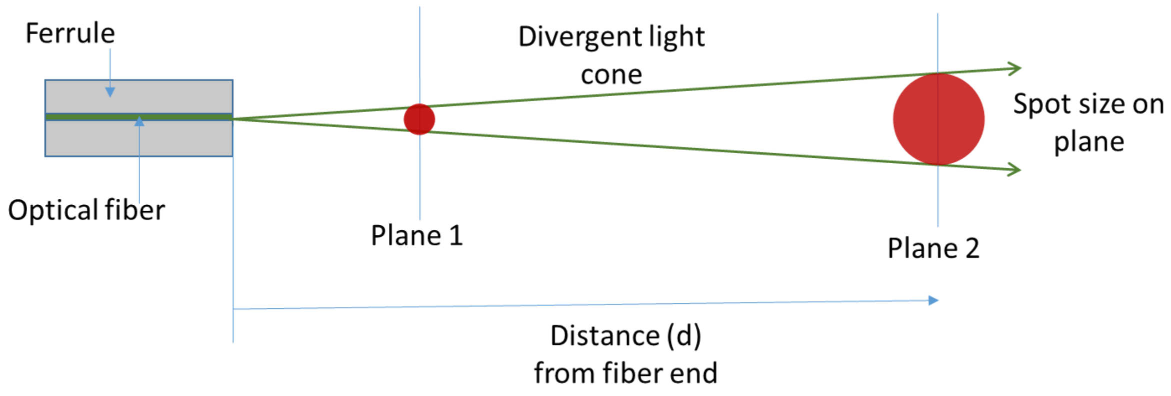

Fig. 5.7 Diverging light beam from an optical fiber

In the present work, a standard multimode optical fiber (core diameter 62.5 µm, NA 0.275, half cone angle 16°) with FC/PC type ceramic ferrule is first used to interrogate the optical signal from the air-wedge interferometer. This FC/PC ferrule has end face cut and polished perpendicular to the fiber axis. The 'PC' means 'physical contact' in this context.

In order to be able to receive the optical interferometric signal from the transducer, a) optical fiber must be normal to the glass surface at the location of interest and b) the end face of ferrule must sit flush with the glass surface. If the fiber is not normal, the reflected signal is difficult to capture due to finite thickness of the glass wafer. A small cylindrical sleeve is made to hold 2.5 mm diameter FC/PC ceramic ferrule perpendicular on the glass wafer.

In case of the sensors made with 0.5 mm thick glass, the optical signals could be obtained effortlessly with 62.5 µm PC terminated fiber in a simple flange based package. However, it is found very difficult to obtain signals from a device with 2.0 mm thick glass using the PC ferrule terminated optical fiber. In the Fig. 5.8, it a multimode optical fiber is shown which emits light in the form of a cone. The light is reflected from a plane reflecting surface.

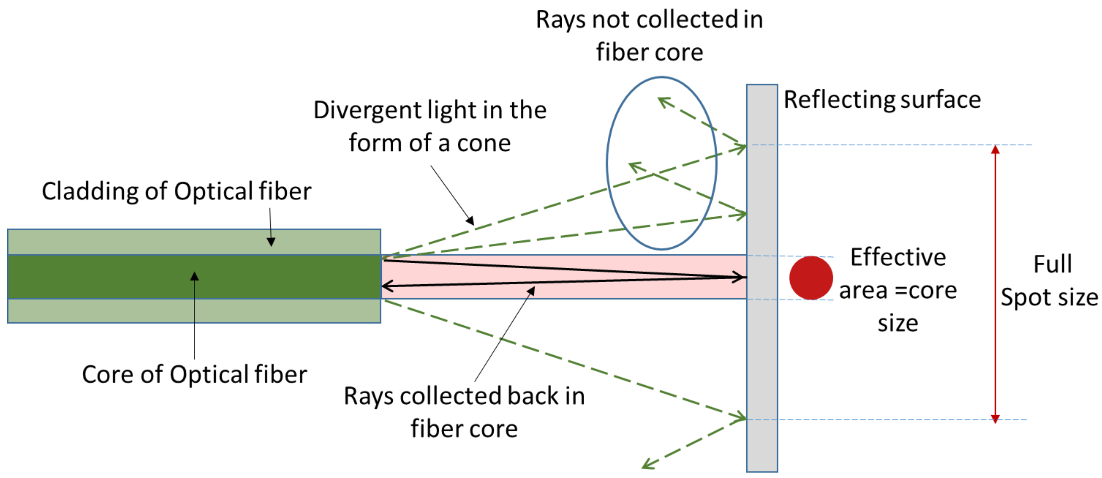

Fig. 5.8 Optical power collected in an optical fiber after reflection

It is shown that rays at larger angle are not collected back into the core of optical fiber after reflection. It is important to know that the light only from an area equal to the core can be collected back. As the distance of the reflecting surface from the end of optical fiber increases, only the rays closer to the zero angle (with respect to fiber axis) will be collected back. Therefore, the collected power decreases very fast with increasing distance. The drop in collected power follows the inverse-square-law of distance for equally illuminated spot of light [105-106]. In the present case, the spot of light has maximum intensity at centre that reduces radially outward. The spot is made with large number of modes. The modes are identified by their angle of propagation in the fiber core with respect to fiber axis. As the distance from the reflecting surface (or target) increases, the more and more higher-order modes escape collection back into the fiber core and hence the intensity of light falls (Fig. 5.8).

The light undergoes some reflection at the interface of media, such as glass-air or air-glass. This is called Fresnel reflection [21] as shown in Fig. 5.9.

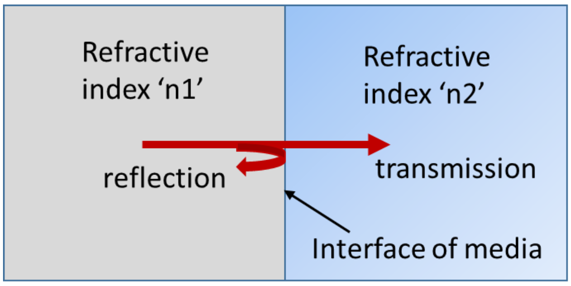

Fig. 5.9 Reflection of light at the interface of two media

The reflection coefficient (R) depends on the refractive index of the two media, as per Eq. 5-1, where ‘n1’ and ‘n2’ are the refractive indices of the media respectively and the incidence of light is considered normal to the interface. The reflection arises due to mismatch of refractive indices of the two media.

$$R = \left[\frac{\mathrm{n1} - \mathrm{n2}}{\mathrm{n1} + \mathrm{n2}}\right]^2 \qquad \textbf{Eq. 5-1}$$

Both, the glass based optical fiber and the bonded borosilicate glass, have closely matching refractive index ($\simeq$1.5). When the fiber end is in full contact with the glass surface, the Fresnel reflection is negligible (Fig. 5.10). Therefore, in this design of pressure sensor, a complete physical contact between the glass fiber and the glass wafer is necessary to ensure negligibly small reflection from the interface. In order to ensure physical contact, the flat polished fiber probe **must be preloaded** with some force and that can be detrimental to the delicate device. If the physical contact is breached, two extra partial reflectors (at fiber-air and air-glass interfaces) appear, increasing the background optical power. Considering the refractive indices of air as 1 and glass as 1.5, both the interfaces give stray reflections of about 4% of optical power, as per Eq. 5-1.

In addition, an **unintentional or stray interferometer** is formed between two reflecting interfaces (the fiber end and the glass surface) (Fig. 5.10).

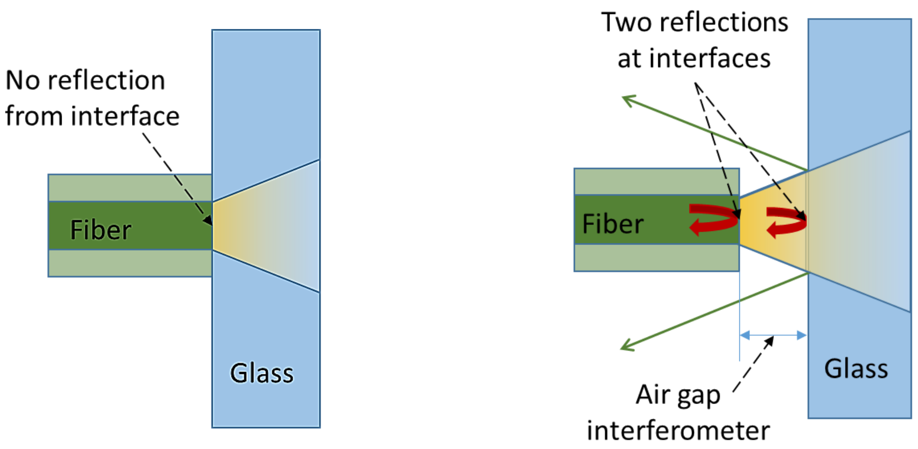

Fig. 5.10 Stray reflections due to breach of contact between the fiber end and glass

To simplify the discussions, this interferometer can be approximated to a two-beam interferometer of same beam intensities (optical power) ($I_1 = I_2 = I$). The resultant intensity $'I_0{}'$ is given by Eq.5-2 [20-21], where $\emptyset$ is the phase between the two interfering beams.

$$\boldsymbol{I_0 = I_1 + I_2 + 2.\sqrt{I_1}.\sqrt{I_2}.\cos\emptyset} \qquad \textbf{Eq. 5-2}$$

The measurement is based on white light interferometry, therefore for any given 'air gap' (of greater than half wavelength) between fiber and glass, there are wavelengths for which the interference is fully constructive. For those,$\cos\emptyset = 1$ from Eq.5.2, the resultant intensity is

$$\boldsymbol{I_0 = 4I} \qquad \textbf{Eq. 5-3}$$

The reflected power is about **4 times** the power of individual reflecting beams at the wavelengths of constructive interference. The power is minimum (near zero) at the wavelengths of destructive interference. The contrast of interference (also called fringe visibility) is given by Eq. 5-4, where I_1 and I_2 are the intensities of interfering lights.

$$\boldsymbol{v = \left(\frac{2\sqrt{I_1}\sqrt{I_2}}{I_1+I_2}\right)} \qquad \textbf{Eq. 5-4}$$

The visibility value is from 0 (no visibility) to 1 (full visibility) or 0-100 % in percentage. Here for the stray interferometer, the participating beams have almost same intensity; hence the contrast of interference is high (close to 1.0). This means the resultant intensity varies from zero to $4I$, while the average intensity is $2I$.

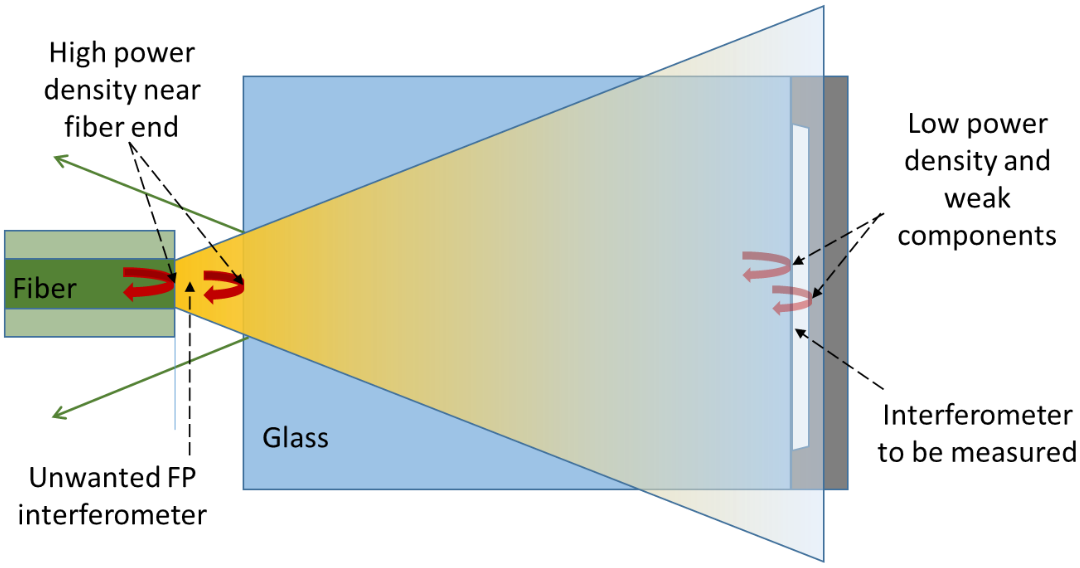

Fig. 5.11 Weaker signal due to higher thickness of bonded glass

This (unintentional) interferometer is much stronger than the one to be measured as far as reflected optical power is concerned because of very **high power density near the fiber end**. The signal is much weaker for a thick glass sensor as the power density becomes very low after the large distance from the fiber end. Moreover, in the sensor interferometer, the reflectivity of silicon (30%) and glass (4%) are different, hence the peak intensity relative to average power of interference is not as high as in case of stray interferometer. The relative strength of the optical powers of stray and desired interferometers can be evaluated from Fig. 5.12, which shows screen shot of offline signals captured at suitable integration (exposure) time of CCD detector. The x-axis is wavelength (600-900 nm) and the y-axis is the 16-bit ADC counts (0-56,000) proportional to the optical power.

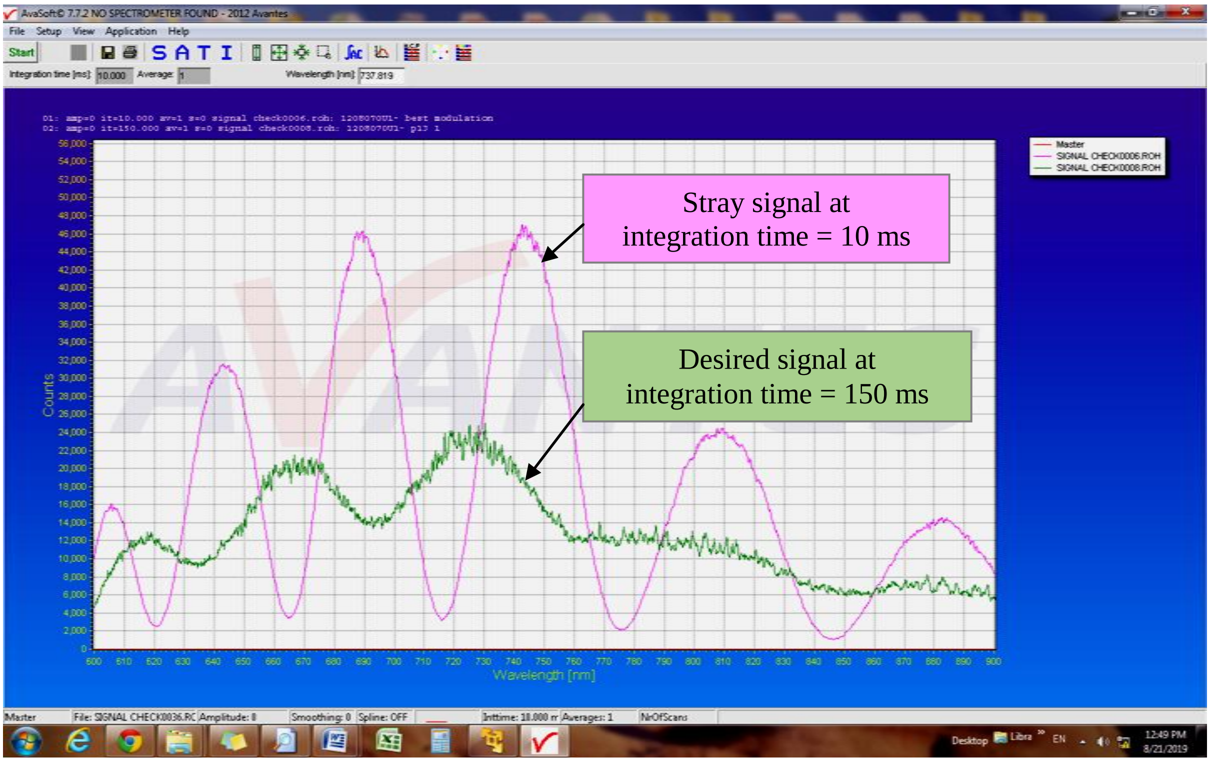

Fig. 5.12 Comparison of power levels of stray and desired optical signals

It can be seen that the power and contrast of the signal (or depth of modulation) is very high for stray interferometer compared to the desired interferometer. Here, the two signals are at different integration (exposure) times; 10 ms for stray interferometer and 150 ms for sensor interferometer. The ratio of integration times is 15 is considered to estimate the relative power of the two interferometers. The stray interferometer gives about 20 times stronger signal if the average powers (24000 counts vs. 18000 counts) of the two signals are compared. The stray interferometer gives about **30 times stronger** signal if the peak powers (47000 counts vs. 24000 counts) of the two signals are compared.

The optical detector (CCD linear array here) in the optical spectrometer gets saturated by the peak power in the interference (modulated) signal. Therefore, the desired signal cannot be acquired in the presence of the stray interferometer. The cavity length in sensor interferometer cannot be measured, if there is a gap between the fiber end face and glass. The signals are achieved with fair difficulty only after pushing the guided ferrule on to the glass wafer.

5.3.2.2 Scanning over the device area

In order to measure the **deflection shape** of in noncontact manner, the entire area of diaphragm needs to be scanned with the measuring optical fiber. The fabricated devices may have bow of up to 50 µm. Therefore, after the device is mounted on X-Y linear stages, it is difficult to bring the fiber (ferrule) axis exactly normal on the glass surface at all the points over the diaphragm area. Therefore, there **must be some non-contact scanning** on the glass surface over the entire area of diaphragm.

5.4. Novel technique for noncontact measurement

It is explained that the difficulty in measurement of the desired signal is arising from 1) weak signal from the desired interferometer, 2) unwanted reflections and 3) interferometric effect of unwanted reflections.

The unwanted reflections can be eliminated with antireflective coating on the surfaces. The desired signal can be strengthened by collimating the light using a microlens after the fiber. However, these techniques are expensive as well as assembly efforts are required with microlens. Therefore, after understanding the root of the problem, the novel technique is evolved.

The flat polished end of PC ferrule acts as a 'partial mirror' of the unwanted interferometer. It is understood if this back reflection could be eliminated then the problem would get solved. The reflection from upper surface of glass just adds to background level in the absence of first reflection (from fiber end) and interferometer effect is not created. The power density on the upper glass surface will reduce with increasing distance of the fiber. The developed technique is based on following logic:

The Angle Polished Connector (APC) [107-109] ferrules are used for termination of single mode fibers to circumvent the problem of back reflection found with PC ferrules. The Fresnel reflection arises from a sudden change of medium in the path of light such as glass to air or vice-versa. If the interface is well defined such as ‘polished’ surface of ferrule, the reflected component is directional. The back reflection is harmful to lasers in the optical circuits. The APC ferrule is cut and polished at 8° angle with respect to the normal to fiber axis.

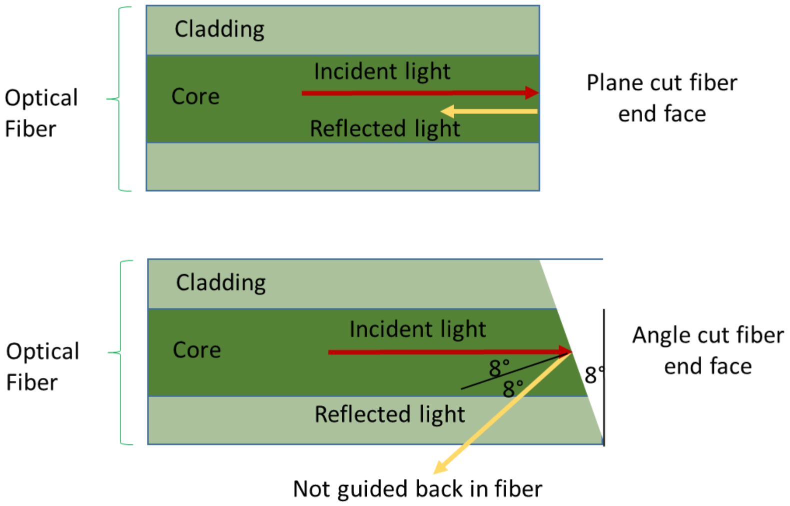

Fig. 5.13 Plane cut and angle cut ends of optical fiber

Therefore, the beam is back reflected at twice the angle (16°). The light at this much angle cannot be contained and guided by a single mode fiber (with numerical aperture, NA = 0.11) and eventually leaks out from the fiber after a short distance of propagation. This is how the back reflection does not reach the optoelectronic parts of the system. The emerging light from the APC end gets a tilt of less than 0.2° which is negligible, compared to the cone angle.

The APC ferrules are common with standard communication grade single mode fibers (SMF, 9 µm core) used in combination with lasers. The APCs are not common with standard multimode fibers (MMF), as they are deployed in conjunction with Light Emitting Diodes (LED), which are not susceptible to back reflections.

Custom made MMF cables are developed with APC ferrule. As the 62.5 µm MMF has higher numerical aperture (0.275) than 50 µm MMF (0.22). The half cone angle of the acceptance cone is given in Eq.5-5 and the values are given in Table 5.2

$$\boldsymbol{\theta} = \sin^{-1}(\boldsymbol{NA}) \qquad \textbf{Eq.5-5}$$

Table 5.2 Acceptance cone angle of standard communication grade multimode optical fibers

Sr. No.	Type of fiber	Core / Cladding diameter (µm)	Numerical aperture	Acceptance cone angle (°)
1	Multi mode fiber (MMF)	50/125	0.22	± 12.7
2	Multi mode fiber (MMF)	62.5/125	0.275	± 16

The direction of the reflected component is at 16°, therefore, the back reflection is better suppressed in the 50 µm APC terminated MMF than 62.5 µm APC terminated MMF, as latter has larger acceptance cone angle. The 50 µm MMF had better overall performance with higher contrast fringes and low background. The field-of-view of the fiber would be approximately equal to the core size of the fiber.

MMF with APC termination is used for the measurement of cavity lengths (CL) in thick glass sensors (Fig. 5.14) for pressure sensing. The developed technique is also used for post-fabrication characterization for etched depth of front cavity (by measuring near the edge). The technique is also used for scanning over the entire area of diaphragm to measure the deflection shape of latter.

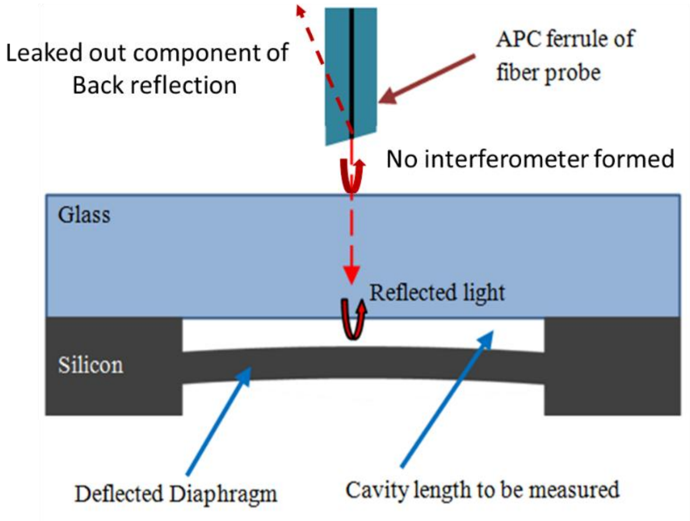

Fig. 5.14 Angle cut fiber to capture the interferometric signal

Signals are captured by the APC based fiber probe very easily. With increasing gap of APC probe from the glass surface, only the level of signal power changes, with no noticeable changes in the position of fringes. Thus, the use of angle cut fiber eliminates the need of intimate contact of fiber with the device. The APC fiber probe can scan over the entire device area in very simplified manner without any need of adjusting the Z value of the probe.

5.4.1. Packaging for thick glass devices for testing

In view of the difficulties faced in acquiring an optical signal from the sensor with thick (2 mm) glass, it emerges that the devices should be packaged using an APC terminated multimode fiber for functional testing and use. The details of prototype test packaging design are presented in Chapter 6.

5.5. Procedure of measurement of deflection shape

The device is cleaned and mounted on X-Y translation cum rotation stages (Fig. 5.15). The device is made to rest on three points. The sample is aligned with the X-Y directions with the help of rotation stage. The X-Y stage is driven manually using micro meter heads. The probe is mounted vertically above the sample.

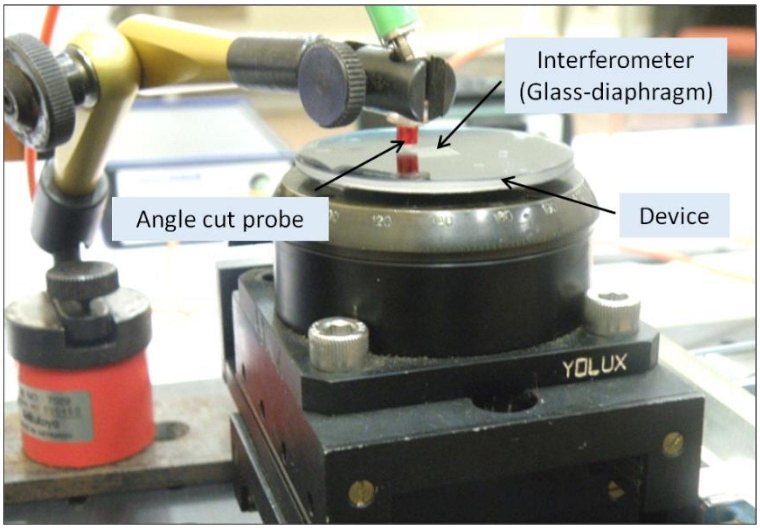

Fig. 5.15 Device mounted on the stage with APC fiber probe

5.5.1. The measurement set-up

The measurement is based on White Light Interferometry (WLI). In WLI there is no phase ambiguity and it gives the interferometric 'path length' in absolute terms. The WLI technique can be implemented in several fashions as described by Rao *et al.* [40]. Here, a broadband light source, the tungsten-halogen lamp and optical spectrometer have been used to implement WLI based measurement (Fig. 5.16).

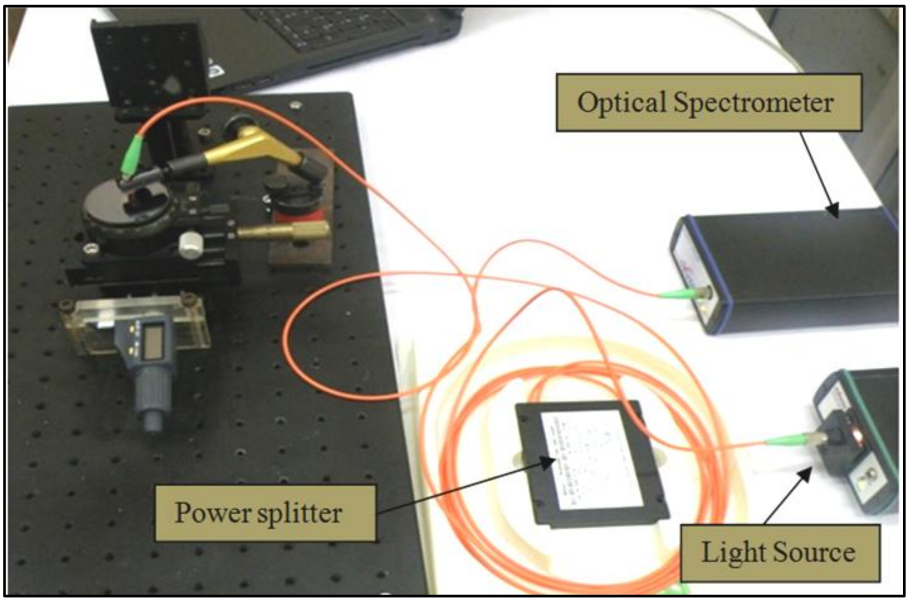

Fig. 5.16 Experimental set-up for the characterization of device

The spectrometer is based on diffraction grating and linear CCD array detector. The spectrometer used has 600-1100 nm wavelength range and less than 0.2 nm of wavelength resolution. It gives the spectral content of the signal to be analyzed in digitized format on a PC. The signal can be analyzed online by user developed software or offline. Signal corresponding to two values of the cavity length is given in Fig. 5.17. X-axis is wavelength in nanometres (600-800 nm) and Y-axis is optical power in 16-bit digital counts.

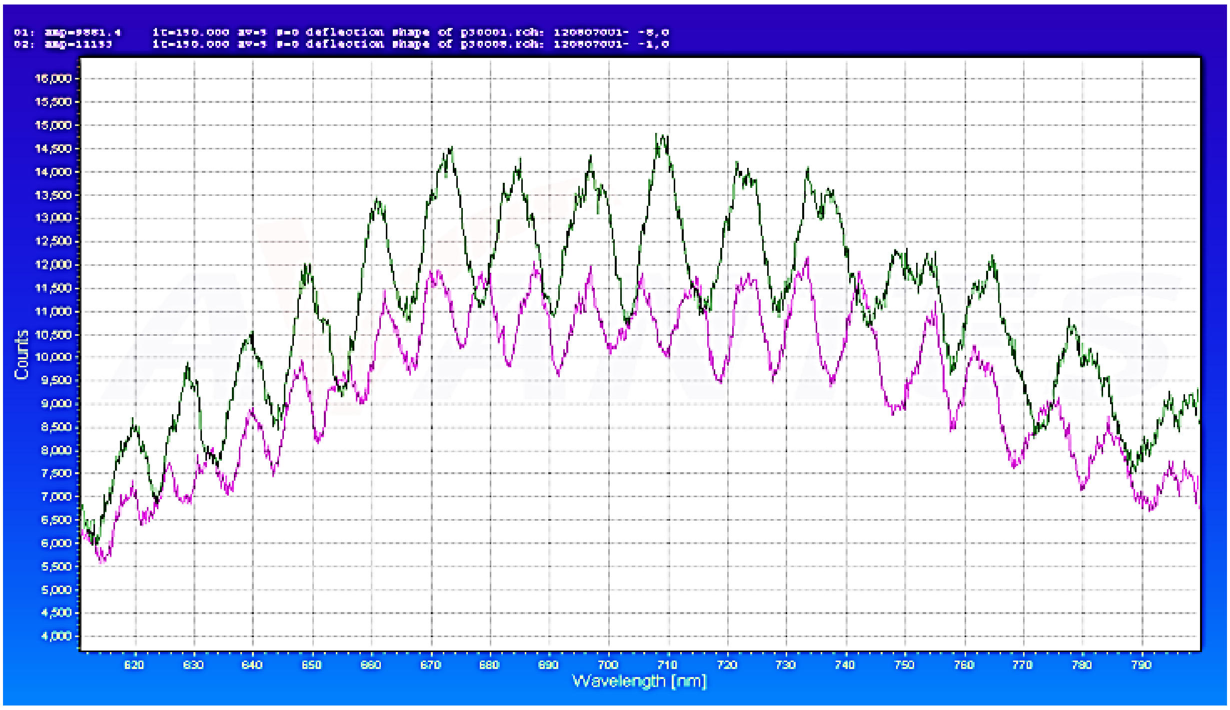

Fig. 5.17 Screen shot of saved signals corresponding to two different locations on the diaphragm

5.5.2. Online centring and scanning

The signals are first examined by moving the probe to different locations over the diaphragm. The increasing cavity length moves the fringes online in software towards right (larger wavelength) and decreasing cavity lengths toward left. It is because the maxima (peaks) wavelengths $\boldsymbol{\lambda_m}$ in the interferometric signal are proportional to the cavity length $\boldsymbol{l}$ as per Eq. 5-6, where $\boldsymbol{m}$ is the order of interference fringe.

$$\lambda_m = 2l/m \qquad \textbf{Eq.5-6}$$

At the centre, deflection is the maximum and cavity length is the minimum. Therefore, the cavity length decreases and accordingly the signal moves towards left side when the centre of the diaphragm is approached and vice-versa. When the sample is scanned in X-Y directions to locate the centre, the continuous video frames are monitored. The centre is located with accuracy of ± 50 µm.

The sample is then scanned in a grid of 17 x 17 points with pitch of 0.5 mm over 8 mm x 8 mm diaphragm. The scheme of scanning of diaphragm over the entire area is given in Fig. 5.18.The signals are captured for all these points. Each signal is a spectral frame of 3648 pixels, each pixel's y-value digitized in 16 bits. In each signal, only a portion of the spectrum is selected for further calculations of the FP cavity length. As the data is huge, alternate signals are analyzed first to find the deflection shape of the diaphragm.

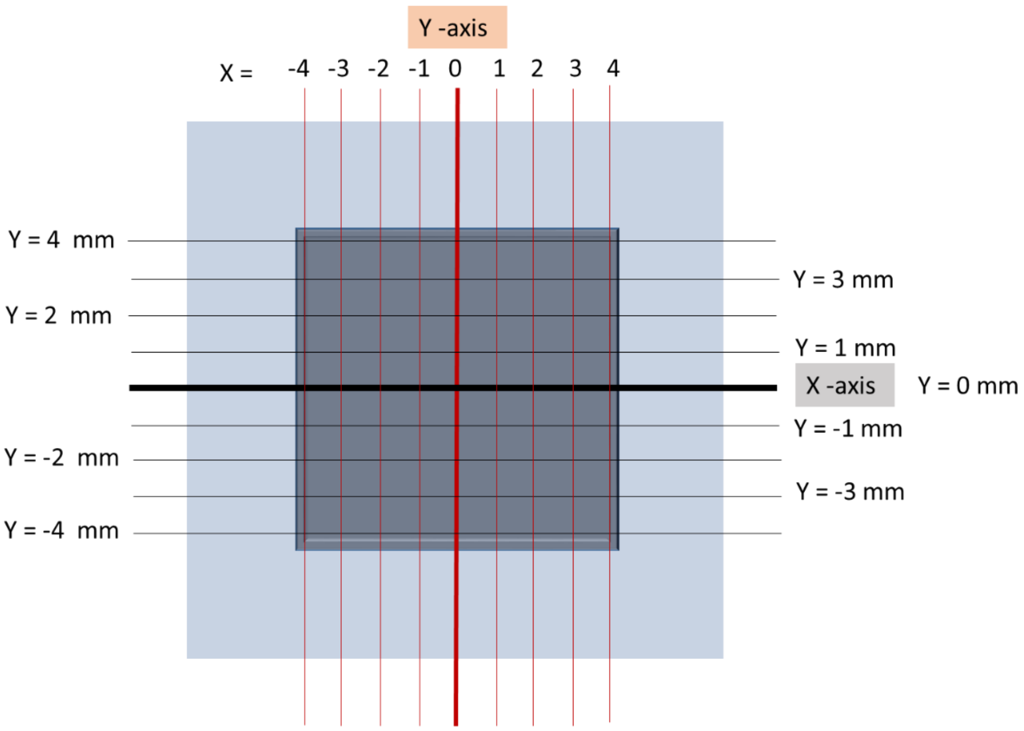

Fig. 5.18 Scheme for mapping the area of diaphragm

5.5.3. Cavity length calculation from signal

The modulation in the signal (Fig. 5.17) arises from interference. The peaks and valleys are uniquely positioned for a given optical path length in the cavity. The larger length has closer fringes and lesser optical power. Ideally any two peaks or valleys are sufficient to calculate the cavity length, in a very clean deep modulated signal. However, there are various electronic and optical noises present in the signal (Fig. 5.17). The signals are filtered to remove noise (Fig. 5.19) using a moving average low pass filter.

Multiple peaks and valleys are used to calculate the cavity length from each frame of spectral signal as per the procedure described in Suri *et al.* [64]. Sample calculations are presented in section 6.4.2 of next chapter. In this method, the peaks (or valleys) are taken from the modulated spectrum. The inverse of those values are taken which will follow a linear trend. Half of the inverse of slope gives the cavity length.

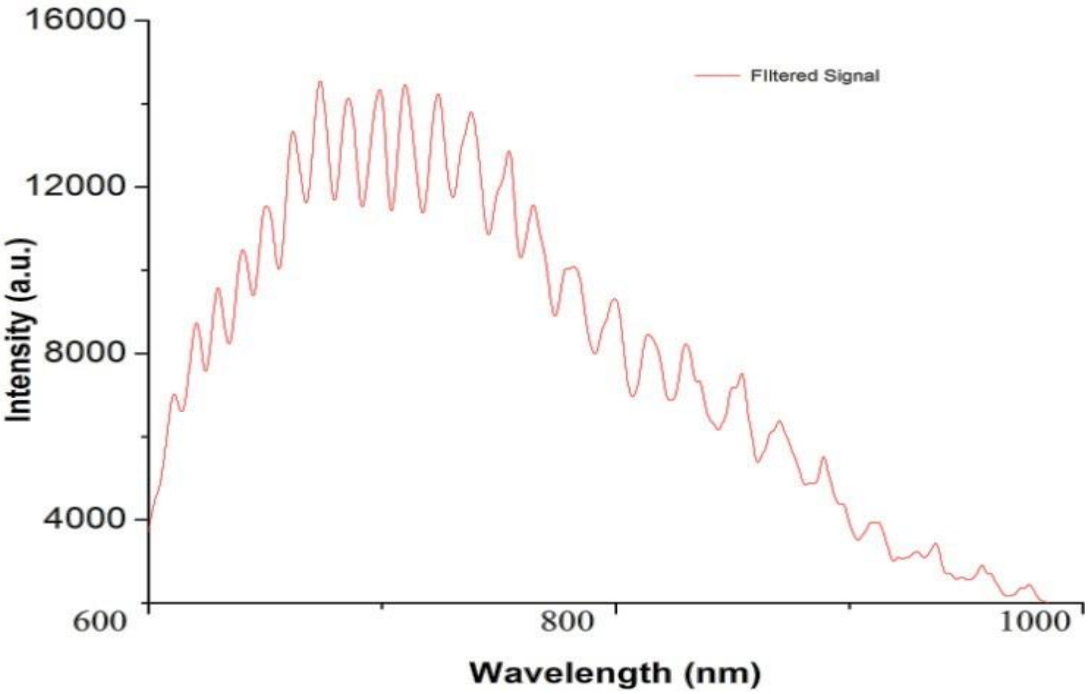

Fig. 5.19 Filtered spectral signal for calculation of cavity length value

5.5.4. Characterization of devices with the technique

The devices are checked with the APC based fiber probe to capture the signals near the edge as well as near the centre. The indicative values of measured cavity lengths are given in Table 5.3 for characterized 2.0 glass devices.

Table 5.3 Characterization results of the devices with 2 mm thick bonded glass

Sr. No.	Sensor ID	Designed Cavity length (µm)	Bonded glass thickness (mm)	Measured cavity length (µm) near edge or corner	Measured cavity length (µm) near center
1	P1	10	2.0	9.8	3.4
2	P5	15	2.0	13.5	12.3
3	P3	30	2.0	30.5	19.9
4	P13	55	2.0	50.9	46.1

It is found that the cavity depth is not uniform when the measurements are taken near the corners and near the edges of a cavity at different places. This may be because of non-uniform etching of the cavity. However, the developed method has been demonstrated for the characterization of the devices post-fabrication.

5.5.5. Measurement of deflection shape

The diaphragm is in deflected position inward to the cavity under the normal ambient pressure (Fig. 5.5). The deflected diaphragm has a convex shape towards the glass side. Therefore, the cavity length of the interferometer (formed between the glass and deflected silicon diaphragm) is minimum at the centre and increases towards the edges of the diaphragm. The Interferometric spectral signals at various points on the interferometer are captured using the novel probe. The cavity lengths at those points are calculated from the spectral signals. The experimentally found cavity lengths defining the shape of deflected diaphragm are plotted in Fig. 5.21 in 3D format.

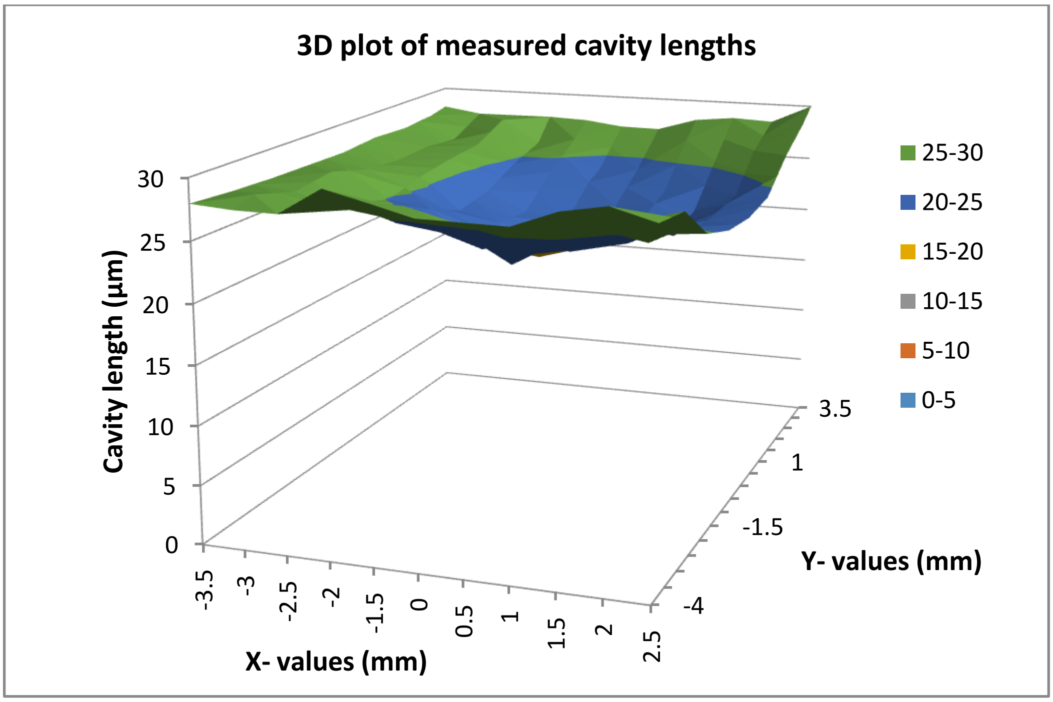

Fig. 5.20 3D plot of the measured cavity lengths over deflected diaphragm

In cavity length is higher at the periphery of diaphragm and decreases towards the centre. The plot looks little distorted. It is because the scale of Z-axis is 3 orders smaller than the scale of X and Y axes. The diaphragm area is 8000 µm x 8000 µm, whereas the deflection up to 12 µm. Nevertheless, existing undulations in the measured shape can be attributed to non-uniform etching of the front cavity.

Further, the measured cavity lengths along few lines of scan are given in Fig. 5.21. The deflection is maximum for the section taken through centre of diaphragm parallel to the edge (indicate by Y= 0 mm). The cavity length varies from about 28 µm to 19 µm, indicating a deflection of 9 µm at the centre. As the parallel sections are taken away from the centre of diaphragm the maximum deflection reduces accordingly. For a section taken at Y= 2.5 mm away from the centre, the maximum deflection for this section is about 7.3 µm.

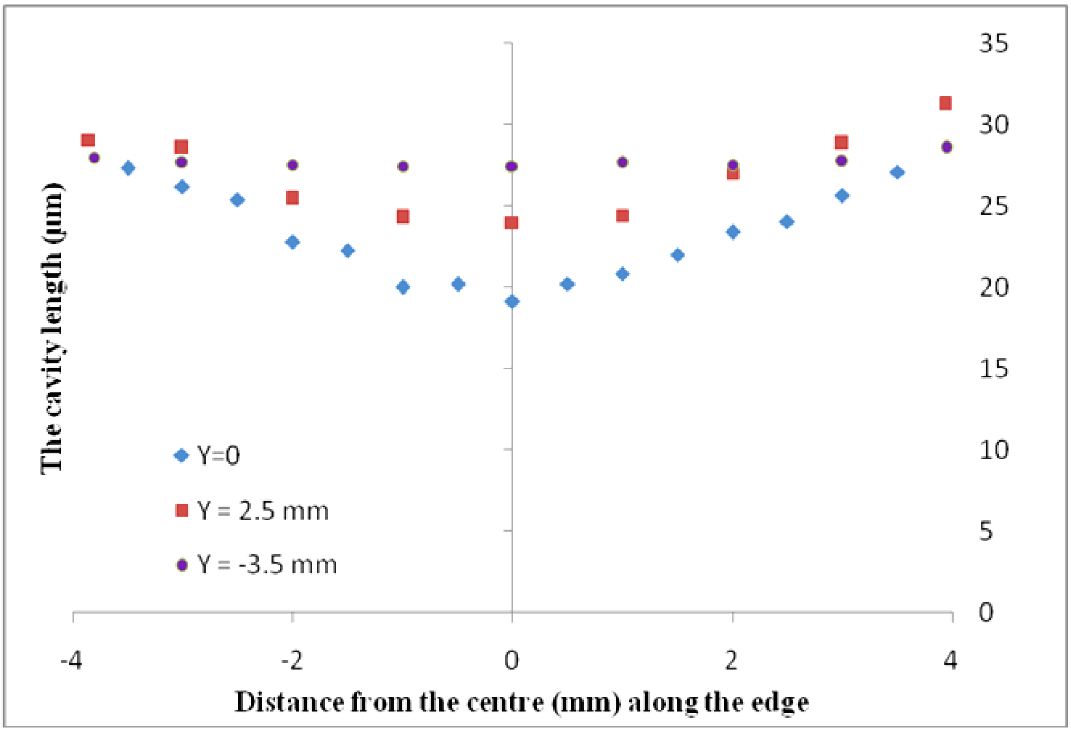

Fig. 5.21 Measured cavity lengths at various cross-sections of the diaphragm along the edge

For a section taken very close to edge of diaphragm, at Y = -3.5 mm distance from the centre of diaphragm, the cavity length is almost constant with total variation of 1.1 µm. This indicates that the developed technique is effective in measuring the cavity length correctly in noncontact manner.

5.5.6. Analysis of deflection shape of square silicon diaphragm

The deflection of diaphragm at various points is calculated from the values of measured cavity lengths by subtracting from the depth of the cavity near the edge. The deflection values at various cross-sections of diaphragm are calculated. A DSF described by La Cour [89] for anisotropic silicon square diaphragm in (100) plane with edges aligned to <110> directions is given in Eq.5.7 and fitted to experimental data. The left side is normalized deflection and '*L*' is half-side length of the diaphragm. The '*x*' and '*y*' are measured from centre of the diaphragm as origin. The fitted curves on two sections are shown in Fig. 5.22.

$$\left.\frac{w}{w_0}\right|_{\mathrm{Si}(001),\langle 110\rangle} = \left[1-(x/L)^2\right]^2\left[1-(y/L)^2\right]^2 \times \left[1+0.239207\left[(x/L)^2+(y/L)^2\right]\right] \qquad \text{Eq. 5-7}$$

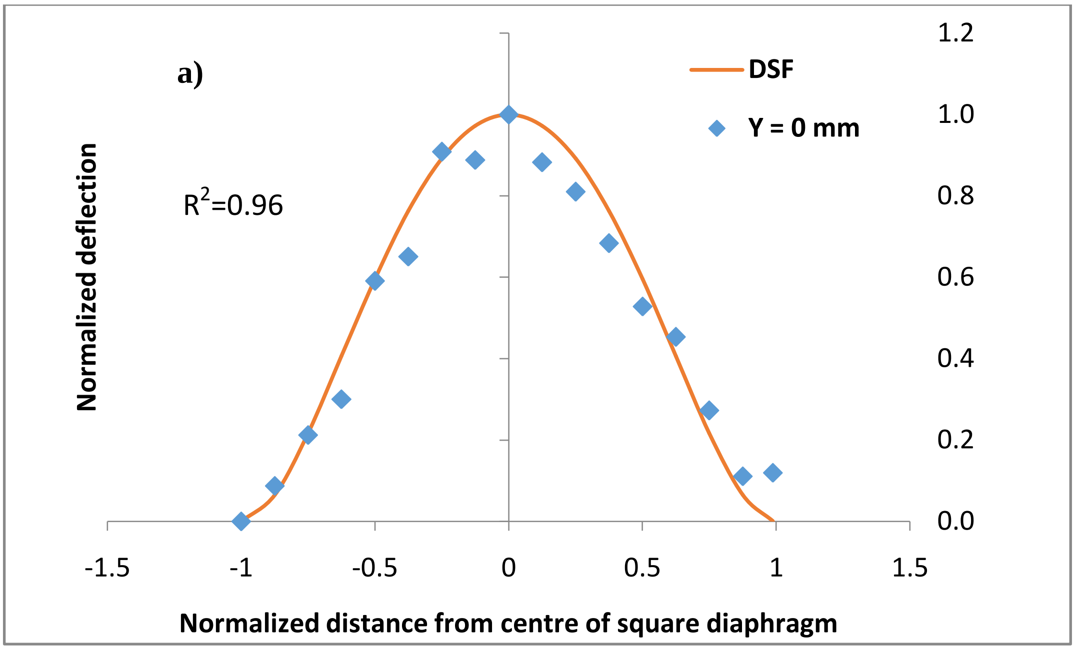

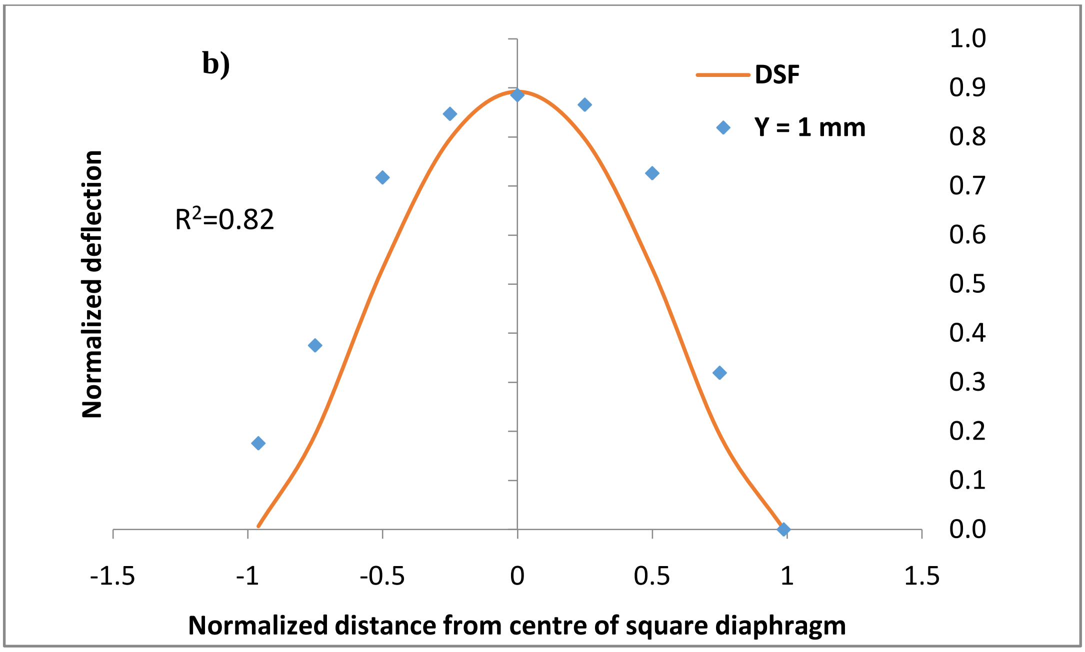

Fig. 5.22 Curve fitting of deflection shape function for section of diaphragm

5.5.7. Results and discussions

The deflection is maximum at the center (0,0) of diaphragm at Y=0 section along X-axis. The maximum deflection at any section is found decreasing with increasing Y distance from the center. The deflection decreases along any section from the value at the center of that section. The obtained data points are distributed away from theoretical curve which may be because of flaws in the fabrication process such as non-uniform etching, local variations in etch depths, pits and crater on diaphragm, scratches on glass, distortion of the device etc. Some significantly off points from a continuous trend may be eliminated and can be attributed to measurement errors. The signal of such points shall also be revisited closely to see for any anomaly as far as signal processing, setting of filters and right identification of peaks and valleys is concerned. The fitted curves (Fig. 5.22) have shown R-square value of 0.96 and 0.82 respectively for sections at 0 mm and 1 mm. The model fits satisfactorily for the section taken through the center (Y= 0 mm), however, for the Y= 1 mm section the model is not fitting well in the present study. It needs further investigation to confirm the validity of the deflection model in the present design space.

5.6. Summary

A novel technique of noncontact measurement and characterization of optical MEMS is proposed and demonstrated successfully. The technique is robust in probe alignment, positing over the sample and scanning. The technique is thus easy to implement. All the devices which were difficult to get the signal with PC ferrule could be measured with this technique. An APC terminated fiber can also be used in the assembly of optical pressure sensor for thick glass sensors and optionally for thin glass sensors.

Nonetheless, the methodology of scanning, device alignment and quality of fabrication can be improved to use the technique more effectively to establish the deflection shape in different design space of diaphragm. Additionally, more number of trials on different devices shall be taken in future for extended study.

As further future scope, detailed analysis of gap of the APC probe from device and its optimization can be studied. An application software can be developed to yield compiled results in comprehensive graphical and tabular formats. The scanning can be automated and controlled through the software. The systems can be made more sophisticated, accurate and user friendly.

Chapter 6

EXPERIMENTAL VALIDATION

6.1. Introduction

After the fabrication of devices, it is required to test them for basic functionality. The field of MEMS packaging involves several industrial standards and practices to produce robust and cost competitive sensors or actuators. In the present case, for academic interest, it is deemed acceptable to go for a prototype packaging to serve the purpose of basic functionality test. Also, in the present case the device is not diced, rather a full wafer is dedicated to one device each for experimental study. Initially, a very simple test packaging is developed for first batch of sensors. The initial testing of sensors is carried out using developed software based on wavelet and Hilbert transforms. However, later it is preferred to save the spectral signal and do the analysis offline. Later some minor modifications are introduced in packaging and sensors are tested. In this chapter, the packaging, testing, signal processing and results have been explained and discussed.

6.2. Prototype test packaging-1

The fabricated device has the shape of a disk. The pressure is to be applied from the silicon side of the disk and the optical interrogation is to be done from the glass side. A schematic of the prototype test packaging of type -1 is shown in Fig. 6.1. The design is based on a KF-50 vacuum flange. The blind flange made of stainless steel (SS316) is taken and a hole is drilled at the centre. A multimode fiber (62.5 μm core diameter) terminated with 2.5 mm diameter ceramic ferrule is used for optical read out.

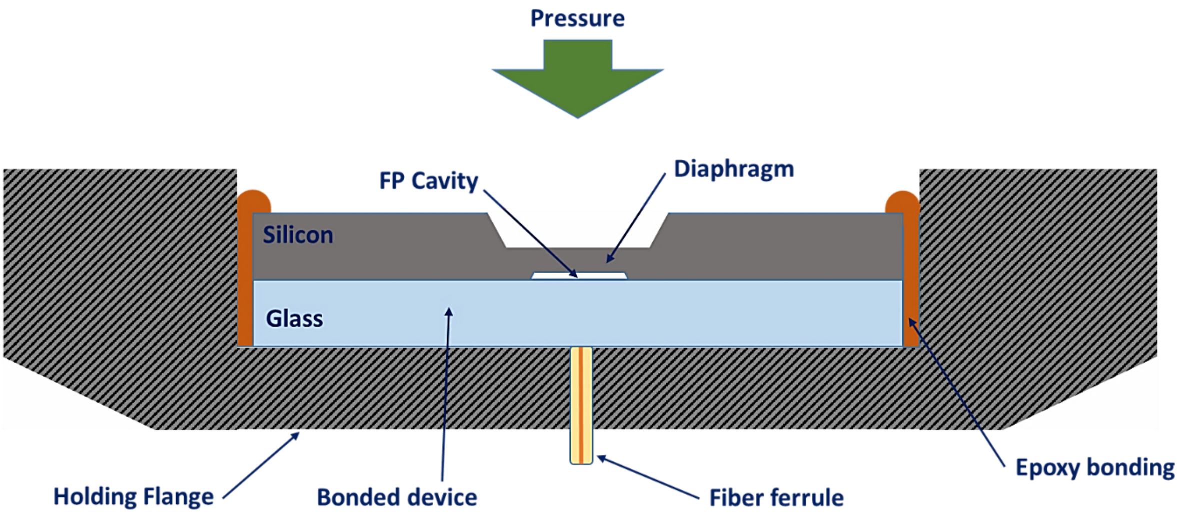

Fig. 6.1 Schematic of prototype test packaging of type-1

6.2.1. Assembly procedure for packaging-1

The fiber ferrule is inserted in the centre hole and the end face is levelled to base surface using a plane surface. The device is placed with glass side down. The optical measurement system is started to monitor the FP cavity length in real time. The interference spectral signal is very easily obtained from the devices of first batch due to thin glass (0.5 mm) used in fabrication. The flange cavity and the device had some play in diameter. The two wafers in the device were slightly off-centre in some cases and edges were somewhat chipped off. Thus, it is difficult to make the device concentric with the flange and fiber ferrule.

The diaphragm of the sensor is already in deflected position under the normal atmospheric pressure in the ambience. The cavity length would be minimum at the centre of diaphragm and would increase at away from the centre lateral direction. Therefore, the optical readout system is used to do the alignment of the fiber with the sensor diaphragm. The device is moved in lateral direction slightly while reading the cavity length of the interferometer online in the developed software. After the minimum of the measured lengths is achieved, the quick settling adhesive is dropped at the periphery to lock the position. Thereafter full periphery is sealed and the fiber ferrule is secured with the flange using adhesive.

Another KF flange is fabricated with ¼” NPT pressure port as lid of the assembly shown in Fig. 6.2. More photographs of packaged devices are given in Appendix A.9. The two flanges are tightened with standard O-ring and clamp for pressure testing of the device. A device packaged for testing in the type-1 packaging is shown in Fig. 6.2. The device has 0.5 mm thick bonded glass. A FC/PC terminated multimode optical fiber of core diameter 62.5 µm has been used. The fiber end face has been kept in contact with glass surface.

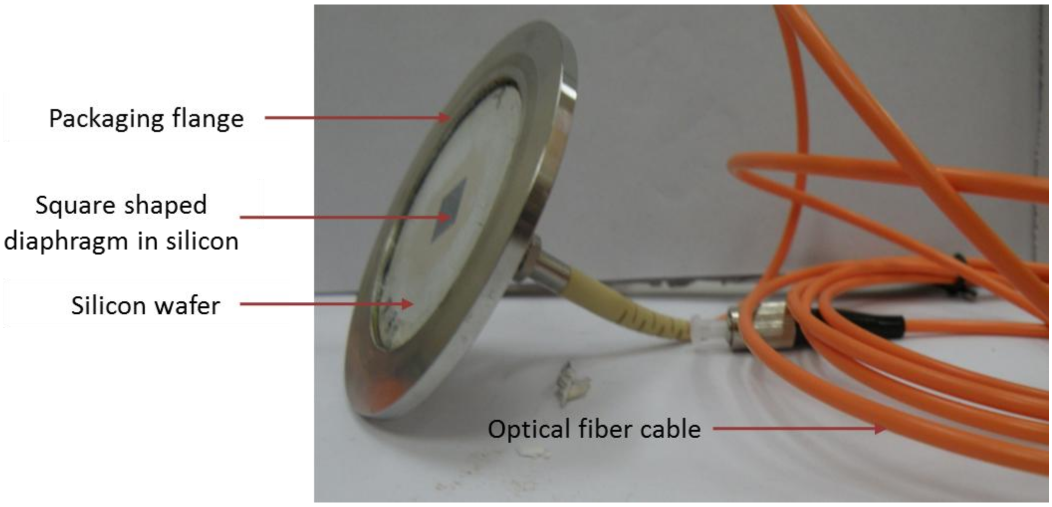

Fig. 6.2 Device packaged in test packaging of type-1

6.3. Prototype test packaging-2

The optical signal from a device of thin (0.5 mm) glass could be obtained easily while using a MMF with flat (PC) ferrule termination. However, it is found very difficult to obtain signals from thick (2.0 mm) glass devices. It is so due to two reasons. First reason is that the signal from the device is very weak due to the divergence of light coming out of the fiber and large thickness of glass. Second is the overwhelming of the desired signal due to extraneous reflections. The extraneous reflections arise from the glass-air interface (at fiber end) and air-glass interface (on the glass surface). These are Fresnel reflections due to abrupt change of media in the path of light propagation. In order to suppress these reflections, the fiber end face should sit flush on the glass surface. In case, there is a gap between fiber end and glass and both are parallel locally, then an unsought interferometer comes in existence, as shown in Fig. 6.3. This overwhelms the signal of intended interferometer.

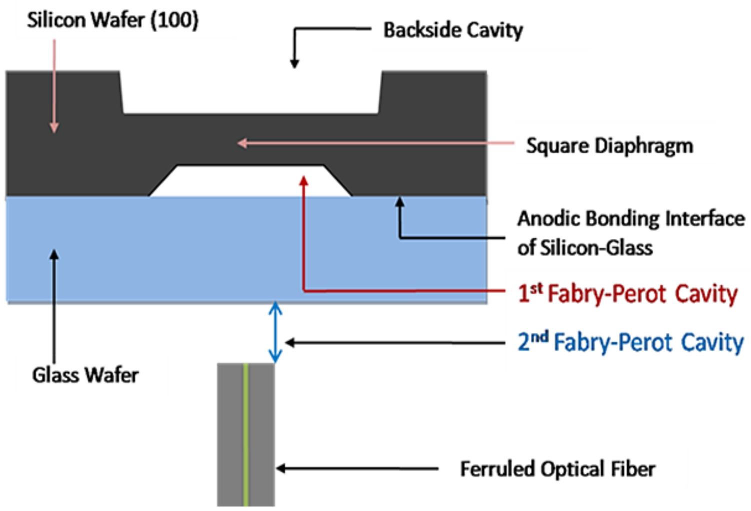

Fig. 6.3 A second interferometer may get formed in case of gap

Devices with thicker glass are likely to have greater distortions after the thermal bonding process of silicon and glass wafers. The device would not sit flush on the surface of flange of the package. The fiber and device are supposed to take relative perpendicular alignment through the flange. Though the fiber would be perpendicular to flange surface, the local area of the device could not be perpendicular to the fiber as shown in Fig. 6.4. The distortion is exaggerated for visualization.

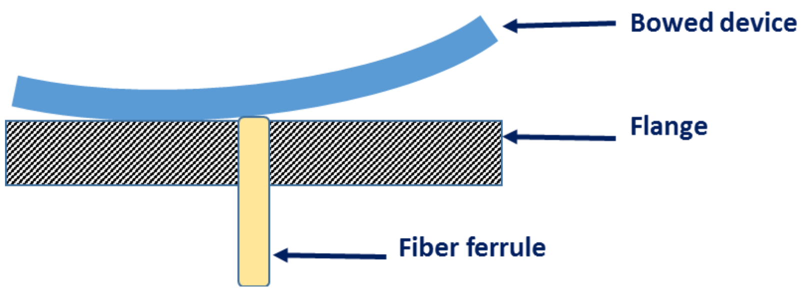

Fig. 6.4 Fiber end not in full contact with the glass surface of device

In order to overcome the problems due to distortion, the packaging is improved as shown in Fig. 6.5 and described hereunder.

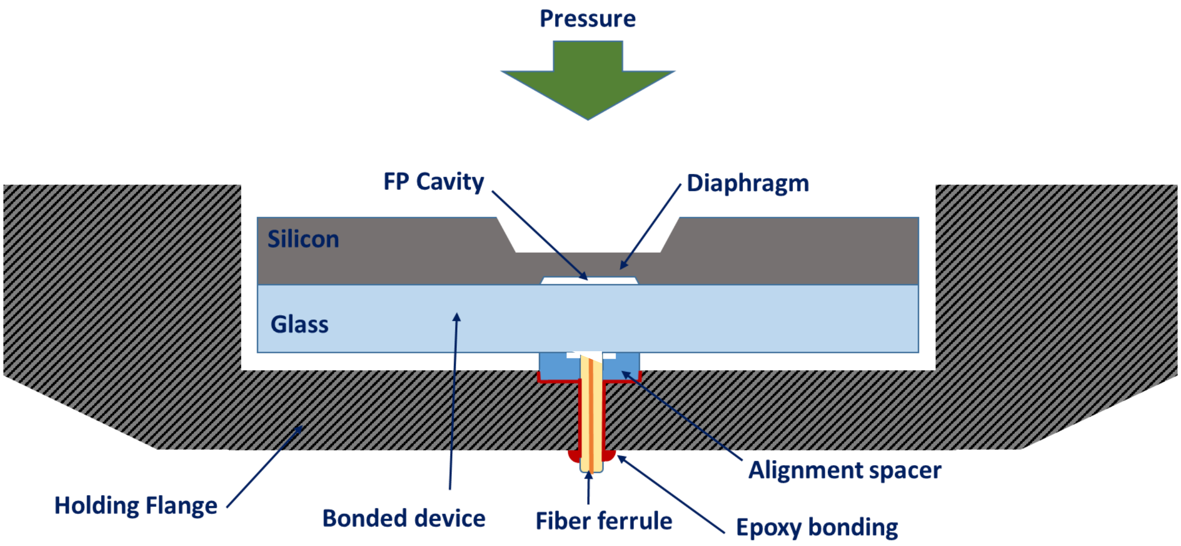

Fig. 6.5 Schematic of prototype test packaging of type-2 for thick glass sensor

This packaging has a flange to secure the device. There is a spacer ring used in this packaging. The spacer ring serves two purposes, a) providing alignment of fiber to diaphragm centre in lateral (horizontal) direction and b) keeping the fiber perpendicular to glass surface locally. The alignment spacer ring has a cavity in it which serves two purposes, a) the epoxy does not smear on the central optical part of the device and b) the air pocket ensures that the fiber ferrule gets entry into the ring till the glass without any back pressure.

6.4. Testing of the sensors

The test set-up for pressure testing of sensors and signal processing to calculate the FP cavity length are described in following subsections.

6.4.1. Test set up

The sensor is a pressure sensor based on optical principle. The basic test set up requires a pressure application module and the optoelectronic detection (or demodulation) system. The schematic of the test up used in this work is given in Fig. 6.6. The photograph of an actual set-up is shown in Fig. 6.7.

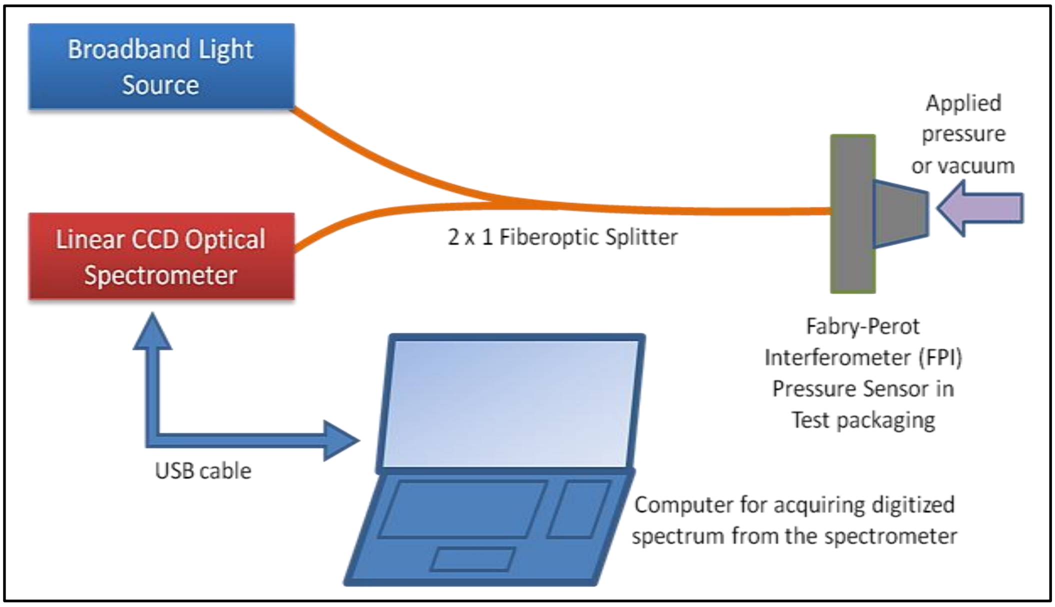

Fig. 6.6 Schematic of optical detection set-up for pressure testing of the sensors

The pressure range of the sensor is 1 bar (absolute). The sensor remains loaded with atmospheric pressure in normal conditions. Therefore, negative pressure shall be applied to test the sensor. A vacuum calibration hand pump (make: Beamex, model: PGV, range: 0 to −0.95 bar (g)) is used for this purpose.

The Fabry-Perot interferometer of the sensor is interrogated on the principle of white light interferometry (WLI). The WLI has advantage of absolute measurement of the cavity length and allows for larger deflection of diaphragm (explained in Chapter 2 Literature Survey).

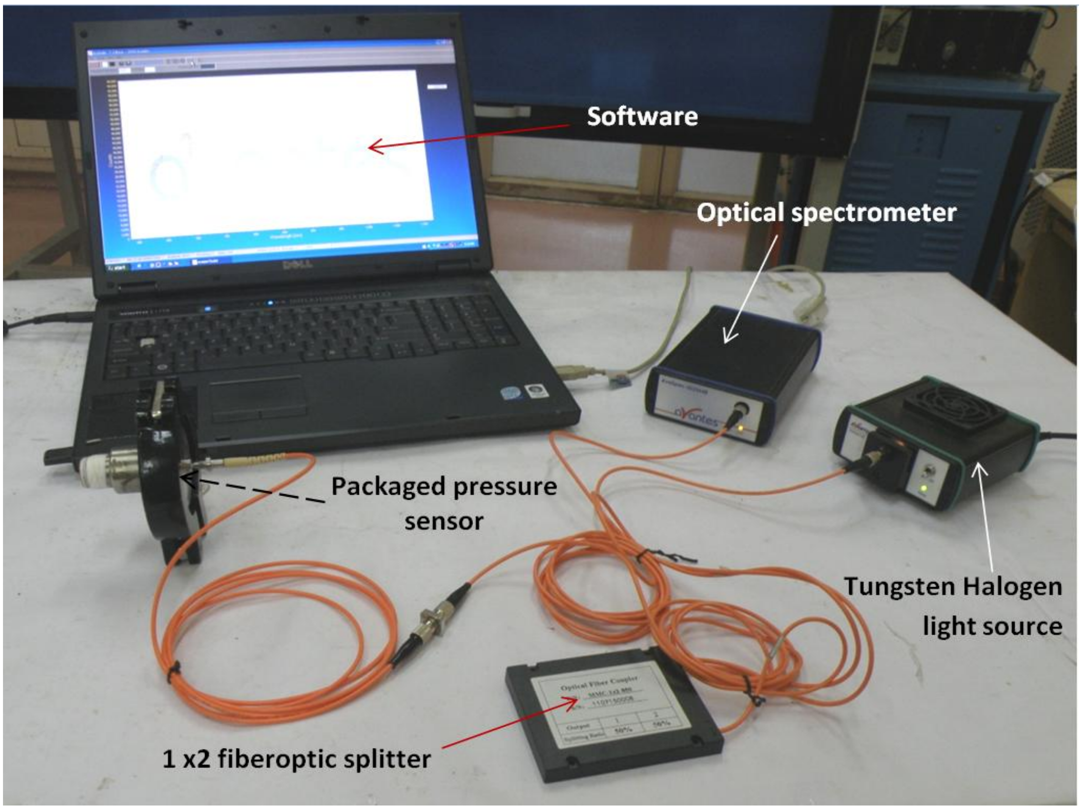

Fig. 6.7 The optical test set-up for FP sensors

A tungsten-halogen lamp (THL) is a 'broadband' light source with smooth continuous spectrum from 400 nm wavelength to more than 2000 nm. In this work, a subset of this range (600 – 900 nm) has been used. The light is launched from a THL light source (model: Avantes HAL) into a multimode optical fiber based circuit through a fiberoptic power splitter (also called coupler). It is a fiberoptic counterpart of the 'beam splitter' used in conventional interferometer set-ups. The broadband light reaches the FP cavity of the sensor. On interaction with FP cavity, different wavelength components undergo different phase retardation over the same physical length of cavity. Thus the light gets modulated in spectral domain. The peaks and valleys in the modulated spectrum are a unique signature of the cavity length of the measured interferometer.

The reflected spectral signal propagates back from the same optical fiber that carries the light to the FP cavity. This fiber is connected to a 1 x 2 optical power splitter that splits the signal power over the 2 fiber channels. As the first channel is connected to the light source, the other channel is used for detection of the signal.

An optical spectrometer is used to implement ‘channelled spectrum’ method of white light interferometry for signal detection. This is a high speed optical spectrometer based on diffraction grating and linear array photodetector. In the spectrometer, the incoming light is dispersed into different wavelength components by diffraction grating. The spectrum is captured by calibrated CCD linear array photodetector. This type of spectrometer has the advantage of high speed because the spectrum is being read electronically with any mechanical scanning. It is unlike typical monochromators which have mechanically tuneable optical filters or a rotating grating to scan and read the spectrum. A spectrometer based on silicon detector is chosen over an Indium Gallium Arsenide (InGaAs) based detector, as the former had larger number of pixels in the array. Accordingly, the wavelength range of operation is kept under 1100 nm window in which silicon based detector is responsive.

The optical spectrometer used in this work is from Avantes BV (model: AvaSpec ULS3648). It has a detector array of 3648 pixels of 8 µm width and 200 µm height. The diffraction grating is 600 lines/mm. The calibration wavelength range of spectrometer is about 600-1100 nm and resolution is less than 0.20 nm with 10 µm aperture. The digitized spectrum is sent by the spectrometer to the PC for further analysis. Screenshots of a stored spectral signals are shown in Fig. 6.8 and Fig. 6.9 respectively for two devices PS12 (design CL 60 µm) and PS10 (design CL 15 µm) under atmospheric pressure. The X-axis is wavelength (600-900 nm) and Y-axis is optical power in digital counts (0-70,000). The visibility or contrast of fringes in signal indicates the quality of interference. Calculations of visibility value of sensor signal are given in Appendix A.10.

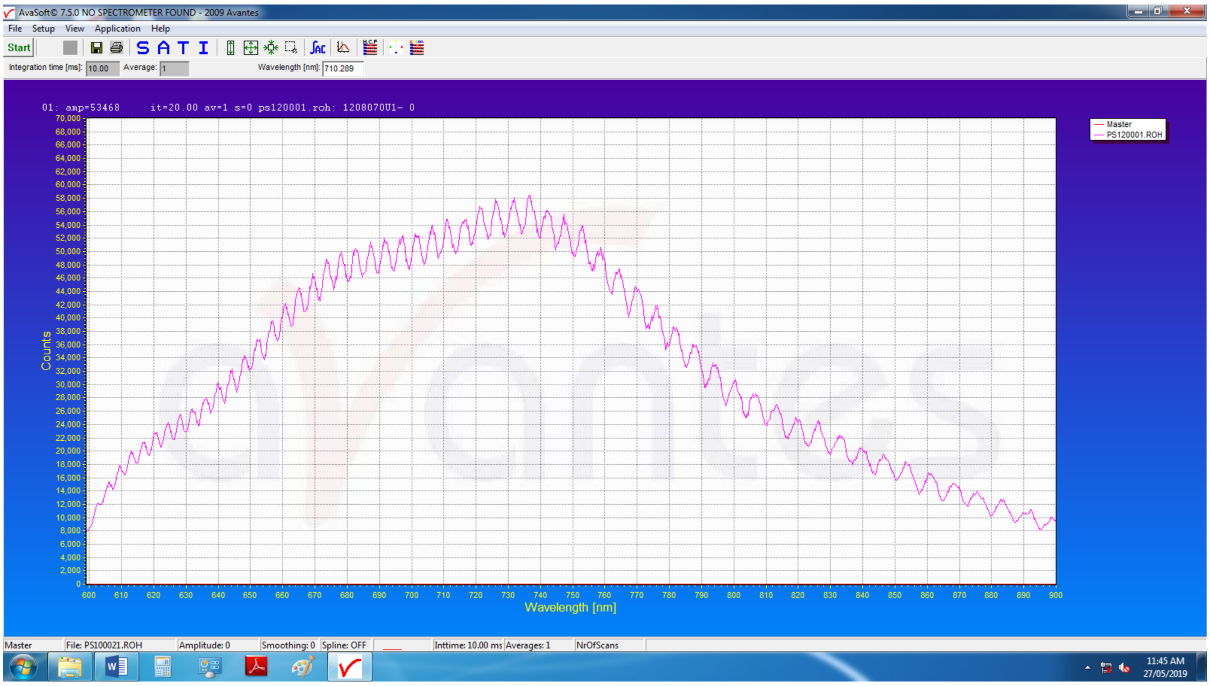

Fig. 6.8 Screenshot of spectral signal from device PS12

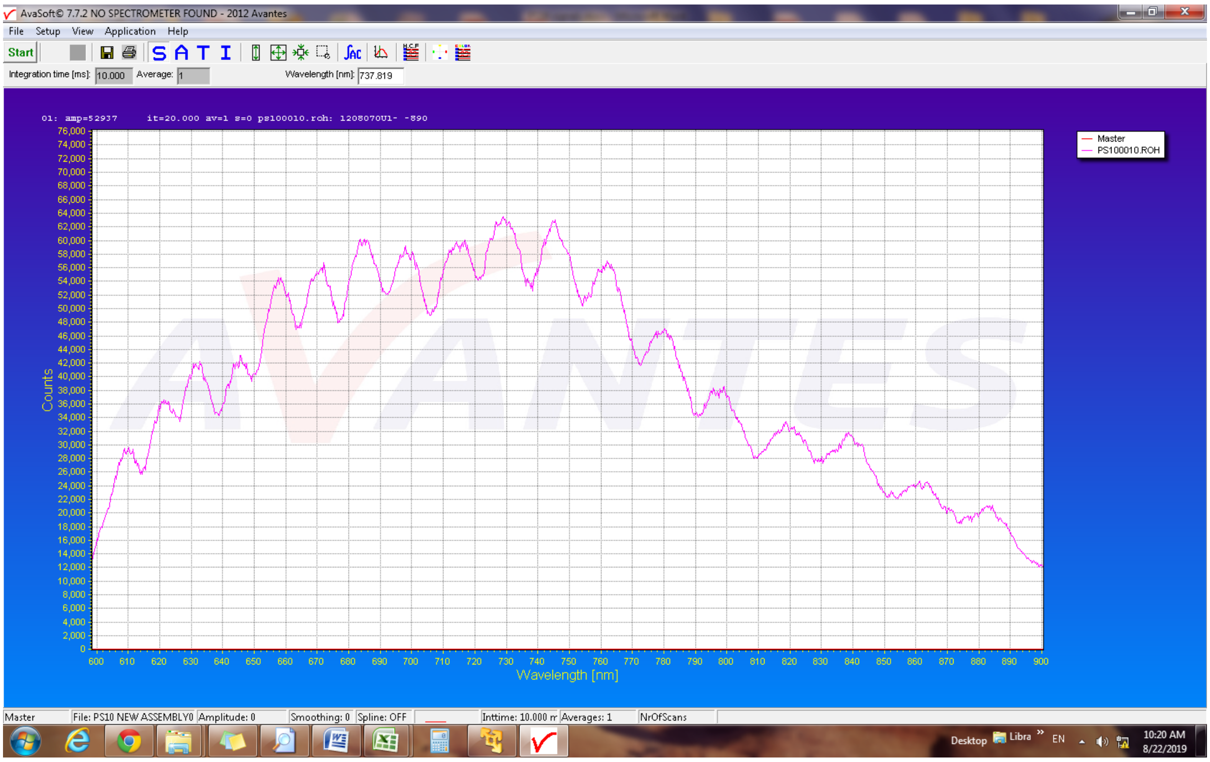

Fig. 6.9 Screenshot of spectral signal from device PS10

The sensor is already under atmospheric pressure. Therefore, the cavity lengths corresponding to Fig. 6.8 and Fig. 6.9 would be smaller than the nominal CL values of the sensors. Negative (vacuum) pressures are applied on sensors and the spectra are captured for each pressure value. In some cases, wherever possible, positive pressures are also applied for elaborate testing.

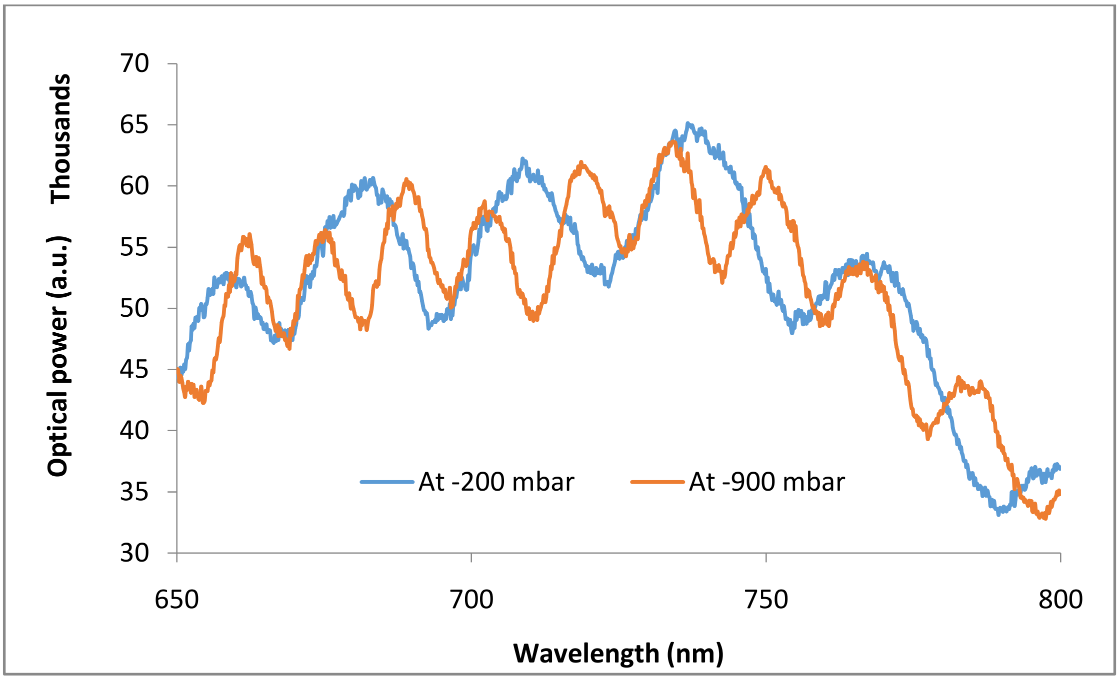

Fig. 6.10 Signals from device PS10 (15 µm) at two pressures

In Fig. 6.10, signals of a device PS10 (design CL 15 µm) are plotted. A clear fringe pattern emerged at -200 mbar vacuum pressure. On the other side of test pressure range, up to -900 mbar vacuum could be achieved with the hand pump used. Both the patterns are shown in Fig. 6.10. As the vacuum is increased, the cavity length also increased in response. The larger cavity gives more number of fringes in the same wavelength window; hence, the plot for -900 mbar pressure has more fringes than that for -200 mbar pressure. The fringe density on other pressures between -200 to -900 mbar would be in between these two plots and not plotted here for clarity.

Similarly, signals from device PS12 (design CL 60 µm) are plotted in Fig. 6.11 at two pressures, 0 mbar and -900 mbar. At -900 mbar, the cavity length is larger, hence so is the fringe density in the given wavelength window.

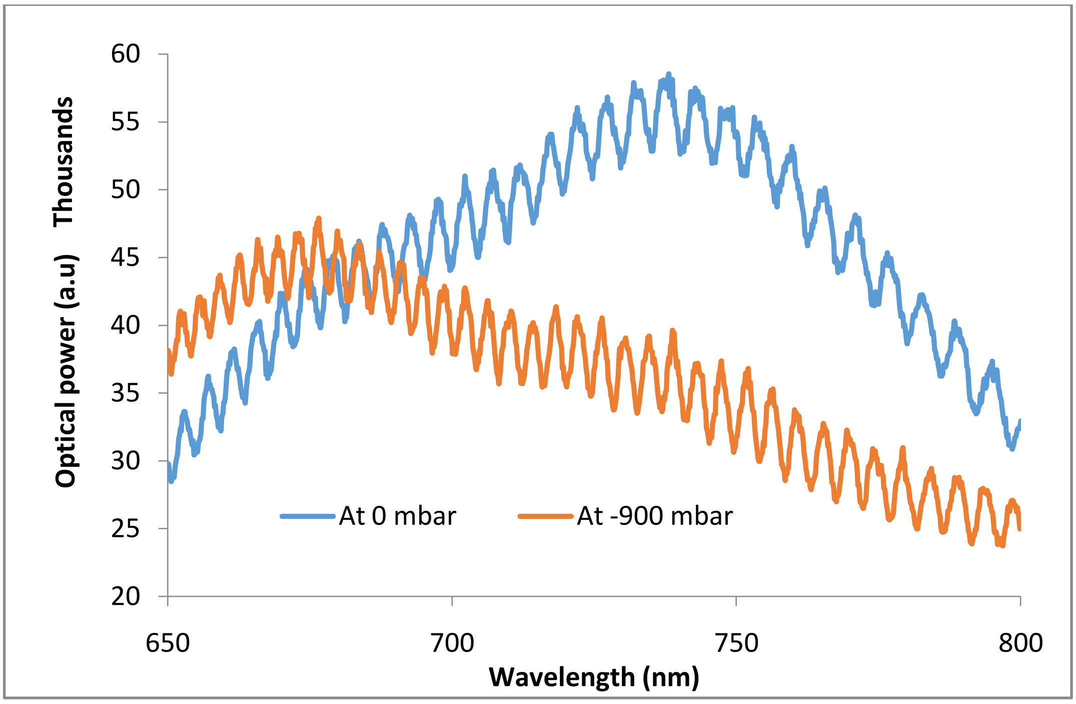

Fig. 6.11 Signals from device PS12 (60 µm) at two pressures

The digitized modulated spectrum acquired is analysed on a PC. The absolute value of cavity length is found for each applied pressure using multiple peaks or valleys of the spectrum as described next.

6.4.2. Signal processing for calculation of cavity length

The spectra are used for calculation of FP cavity lengths at different pressures. Ideally, two wavelength values of peaks or valleys in the spectrum are sufficient to calculate FP cavity length. However, this method is very much prone to errors unless extremely sharp peaks or valleys are formed in the signal. As per the physics of interference, all peaks and valleys are bound by a rule as explained further. It is therefore preferred to use multiple peaks and/or valleys for higher accuracy [64] of measured cavity lengths. The phase change (retardation) $\emptyset$ undergone by light of wavelength λ over path length $2l$ is given by

$$\emptyset = 4\pi l/\lambda \qquad \textbf{Eq. 6-1}$$

The peaks in the interference signal correspond to constructive interference, where the phase change ($\emptyset_m$) is an integral (m) multiple of 2π (Eq.12). The m is the order of fringe.

$$\boldsymbol{\emptyset_m = 4\pi l/\lambda_m = 2m\pi} \qquad \textbf{Eq. 6-2}$$

However, the absolute value of fringe order m is not necessarily required for further calculations. The wavelength values (λ_i) corresponding to peaks (or valleys) are noted with index (i)with increasing wavelength. The inverse of wavelengths ($1/\lambda_i$) is plotted against index (i)which shall ideally follow a straight line.

The slope (S)of this line is -($1/2l$) as per Eq. 6-3. The cavity length is calculated from the slope value using Eq. 6-4.

$$\boldsymbol{(1/\lambda_i) = -(1/2l).i = S.i} \qquad \textbf{Eq. 6-3}$$

$$\boldsymbol{l = -(1/2S)} \qquad \textbf{Eq. 6-4}$$

6.4.2.1 Sample calculations

As an example, data for sensor PS12 at is presented at 0 mbar and -900 mbar applied gauge pressures. For this large cavity length (> 50 µm), there are large number of peaks in the signal. Therefore, a middle portion of the signal in the wavelength window of 700 -760 nm has been selected for analysis. This window comprised of 12-14 peaks for 0 to -900 mbar pressure. The smaller cavity length would have lesser number of peaks. For positive pressure, the number of peaks is about 9 at +500 mbar pressure. The peaks have been picked directly in the Avantes Avasoft software using the cursor with sub-nanometre resolution (Fig. 6.12). The X-axis is wavelength (695-765 nm) and Y-axis is optical power in digital counts (27,000 -42,000).

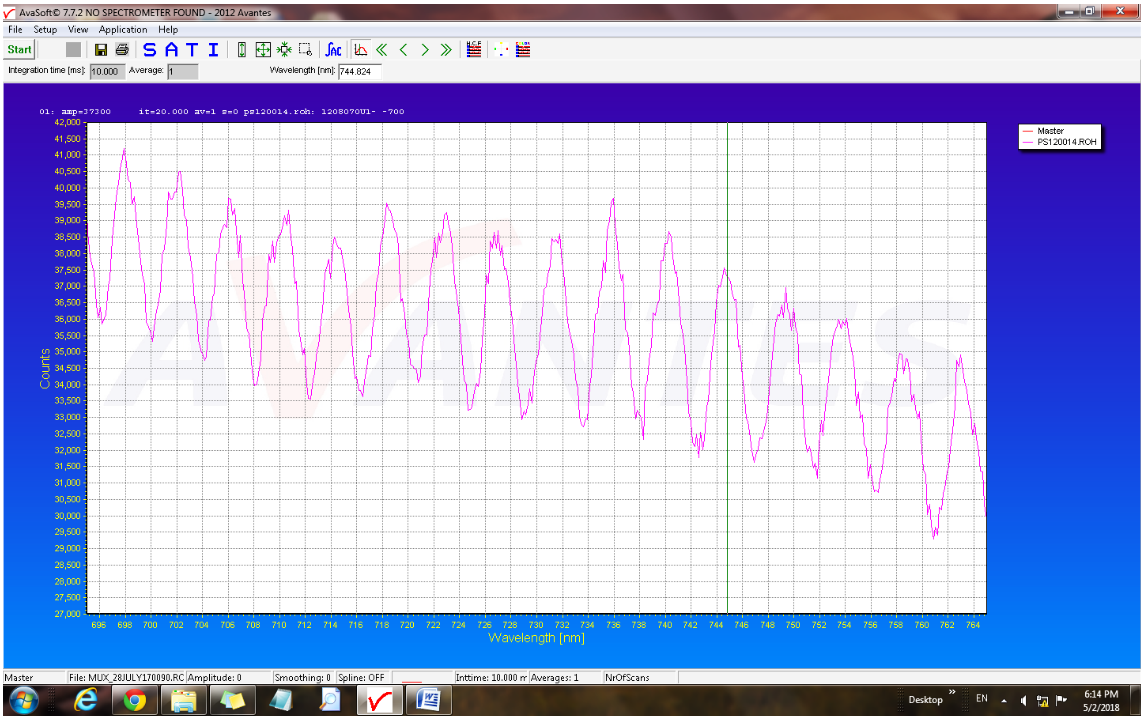

Fig. 6.12 Picking of peaks in the signal for PS12

In other cases, where the peaks are somewhat noisy, a moving average filter is used to remove the noise and find the peaks. The peaks are recorded in units of nanometres (nm) and the inverse is calculated in micrometer^{-1} (μm^{-1}), so that the cavity length comes in µm. The achievable resolution of cavity length or deflection is better than 10 nm by this technique. (For total deflection value of 15.6 µm, this would give a sensor resolution of better than 1:1500 or 0.67 mbar)

Table 6.1 Experimental data of sensor PS12 for cavity length calculations at two pressures

pressure		0 mbar			(-900 mbar)	
Index (i)		peaks (λi) (nm)	inverse (1/λi) (μm^{-1})		peaks (λi) (nm)	inverse (1/λi) (μm^{-1})
1		702.3	1.423892923		702.4	1.42369
2		707.3	1.41382723		706.3	1.41583
3		712.1	1.404297149		710.2	1.40805
4		717.3	1.394116827		714.2	1.40017
5		722.2	1.384657989		718.2	1.39237
6		727.3	1.374948439		722.2	1.38466
7		732.5	1.365187713		726.3	1.37684
8		737.6	1.355748373		730.5	1.36893
9		743.1	1.345713901		734.7	1.36110
10		748.4	1.336183859		738.9	1.35336
11		753.9	1.326435867		743.2	1.34553
12		759.3	1.317002502		747.5	1.33779
13		--------	----------		751.8	1.33014
14		--------	----------		756.3	1.32223
		Slope	Offset		Slope	Offset
		-0.0097119	1.43330		-0.007800	1.43140
		CL(um)	51.483		CL(um)	64.106

Slope of the best fit line is calculated in MS Excel spread sheet using Linest () function (Table 6.1). The data is also plotted for graphical representation in Fig. 6.13.

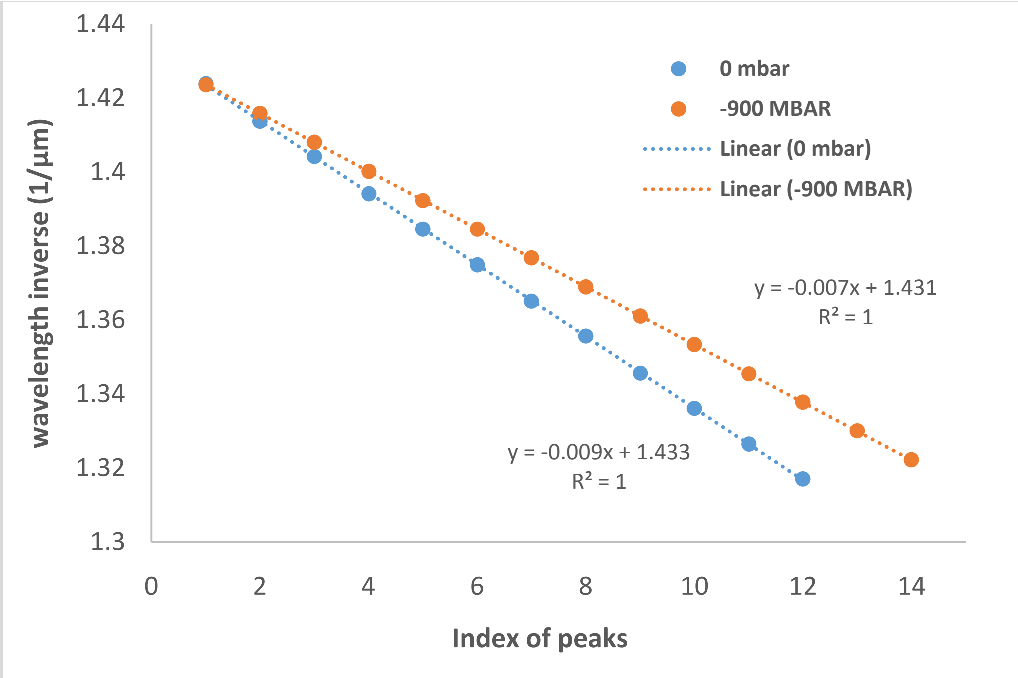

Fig. 6.13 Using multiple peaks from a spectral signal for finding the cavity length

The two lines have different slopes. The slope values of the trend line are same as those calculated in the table above. The smaller cavity length could have larger slope that is steeper line. The linear trend line fits very well on experimental data with R-square value 1, which certifies the appropriateness of data and physics behind the calculations.

6.5. Results and discussions

6.5.1. Cavity length vs. the applied gauge pressure

After having calculated the cavity length values at various pressures, the dependence of cavity length on applied pressure is plotted for the sensors of nominal cavity lengths of 10, 15, 30 and 60 µm. The applied pressure is negative pressure with respect to the atmospheric pressure. In the Fig. 6.14 to Fig. 6.18, the pressure is increasing from left to right on the x-axis. More negative pressure increases the cavity length and vice-versa. The cavity length is lesser when pressure is higher on the diaphragm. This is why the slope of the plots is negative.

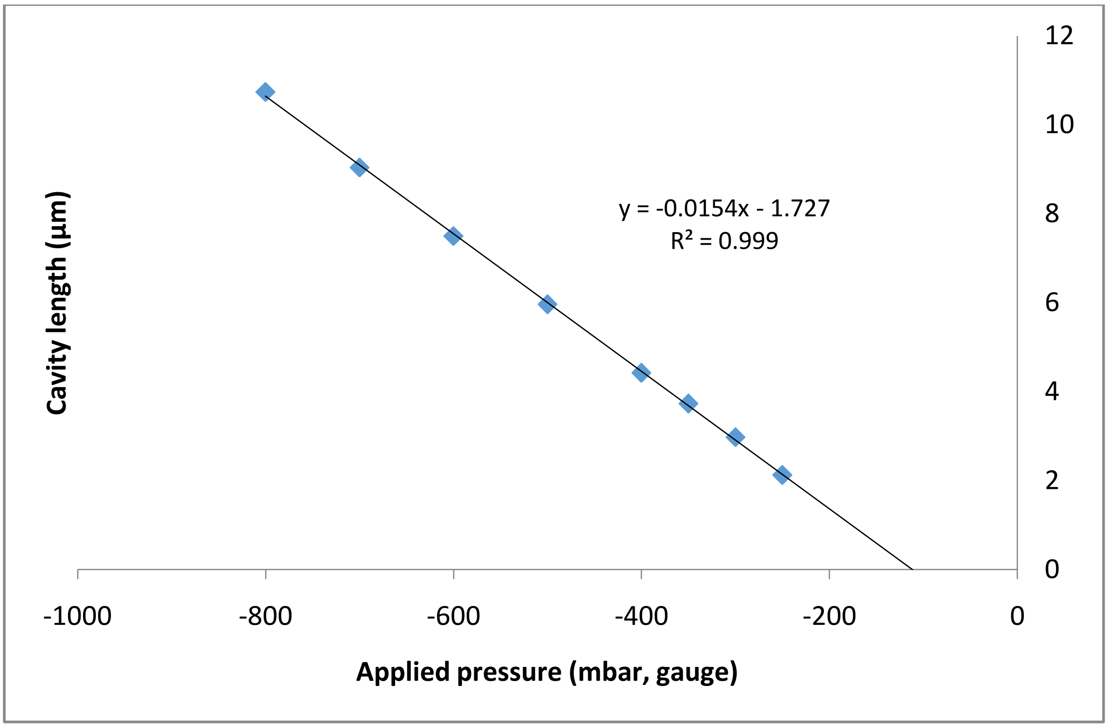

Fig. 6.14 Cavity length of sensor PS8 (10 µm) with applied pressure

The FP cavity of device PS8 (10 µm) is collapsed under atmospheric pressure (0 mbar, gauge). The fringes formed as negative pressure is applied and the FP cavity length increase to around 2 µm. The experimentally found 'apparent' pressure sensitivity is 15.4 µm/bar; as indicated by the slope of the best fit line in Fig. 6.14. It is named apparent sensitivity because it is likely to be a suppressed version of original sensitivity of diaphragm.

Similarly, the experimentally found pressure responses of various devices are given in Fig. 6.15 to Fig. 6.18. It is found that different device have different pressure sensitivities, ranging from 11.6 to 18.1 µm. The experimental results are summarized in the Table 6.2. This variation of sensitivity is primarily due to variations of diaphragm thicknesses from device to device. Secondly, there is some scaling of sensitivity due to the trapezoidal shape of the etched cavities in silicon. The deeper cavities have slightly smaller edge length of the diaphragm. The scaling corrections are considered during fitting of the analytical model on experimental data later in the chapter.

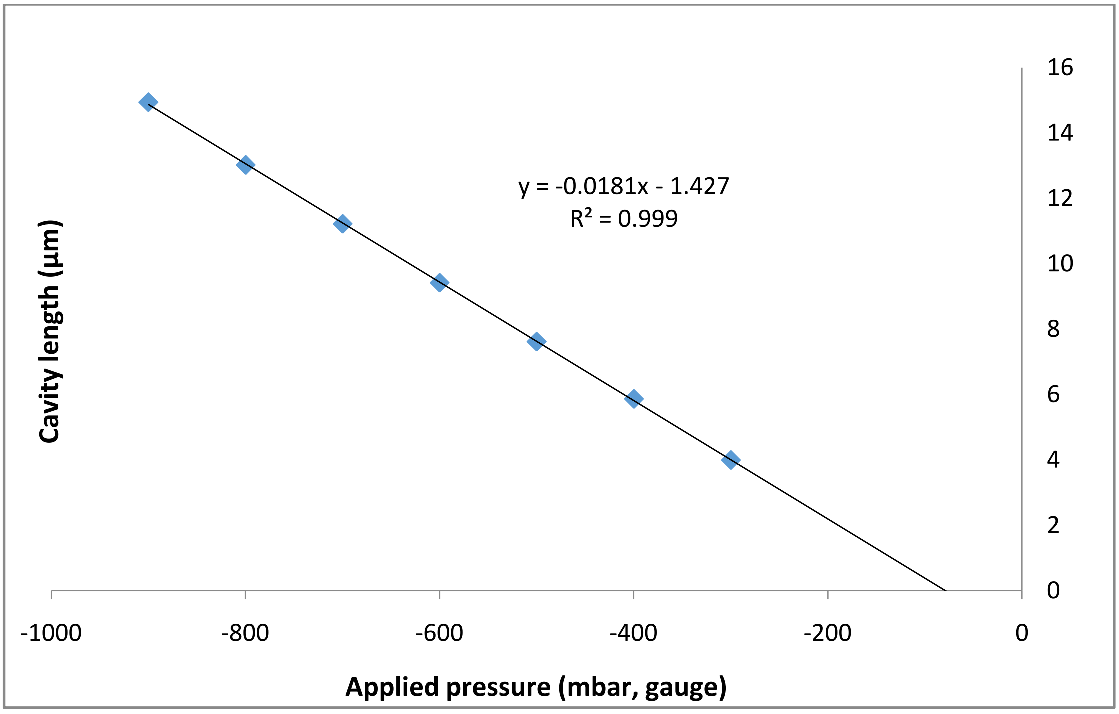

Fig. 6.15 Cavity length of sensor PS9 (15 µm) with applied pressure

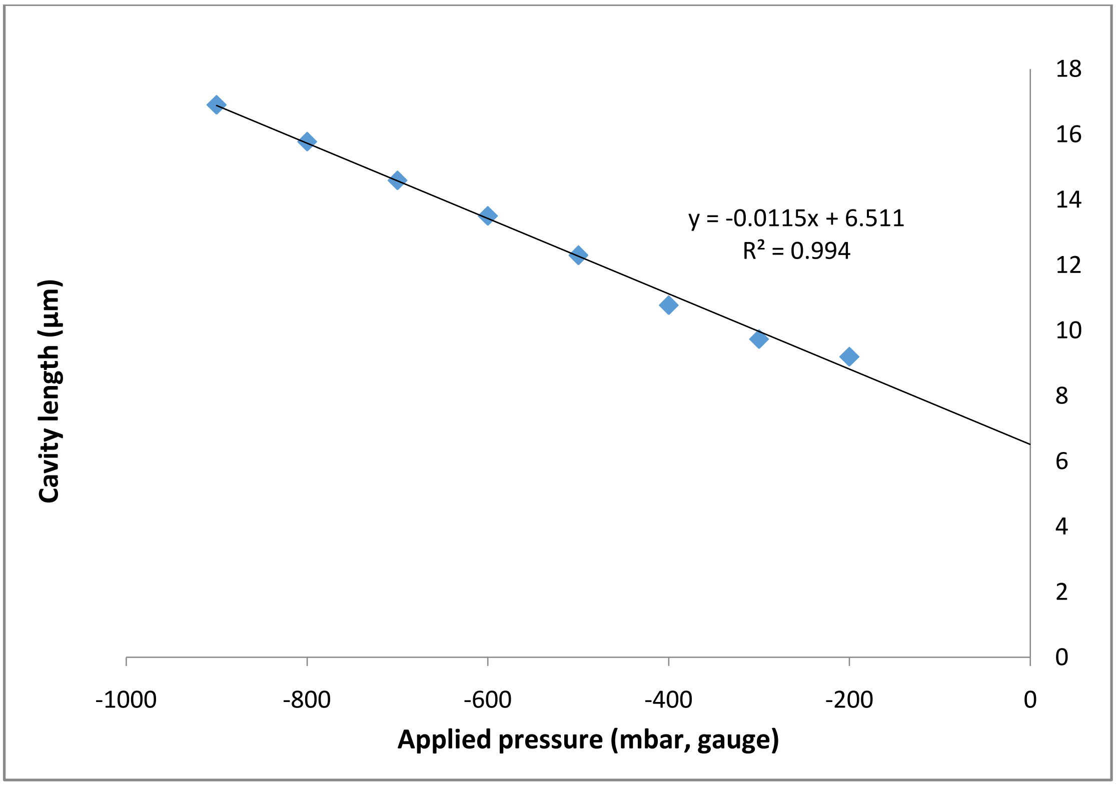

Fig. 6.16 Cavity length of sensor PS10 (15 µm) with applied pressure

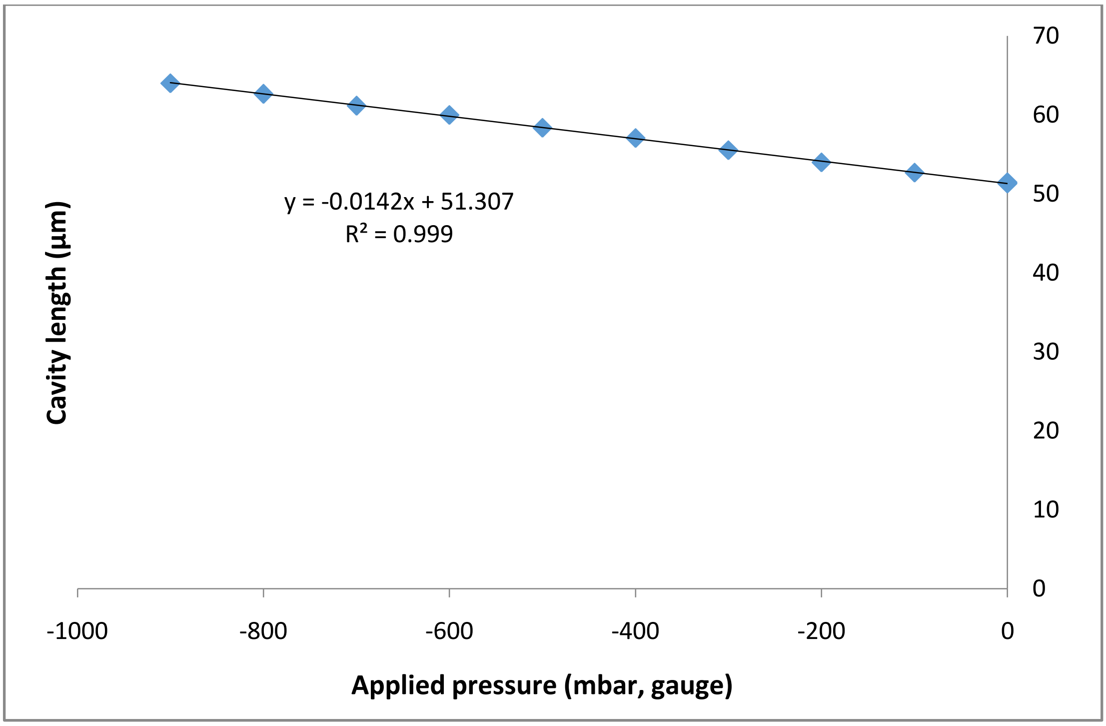

Fig. 6.17 Cavity length of sensor PS12 (60 µm) with applied pressure

6.5.1.1 Devices in packaging-2

A thick glass device P3 (designed CL 30 µm, measured 30.5 µm) is packaged in package type-2 as shown in Fig. 6.5. The test results of device are plotted in Fig. 6.18.

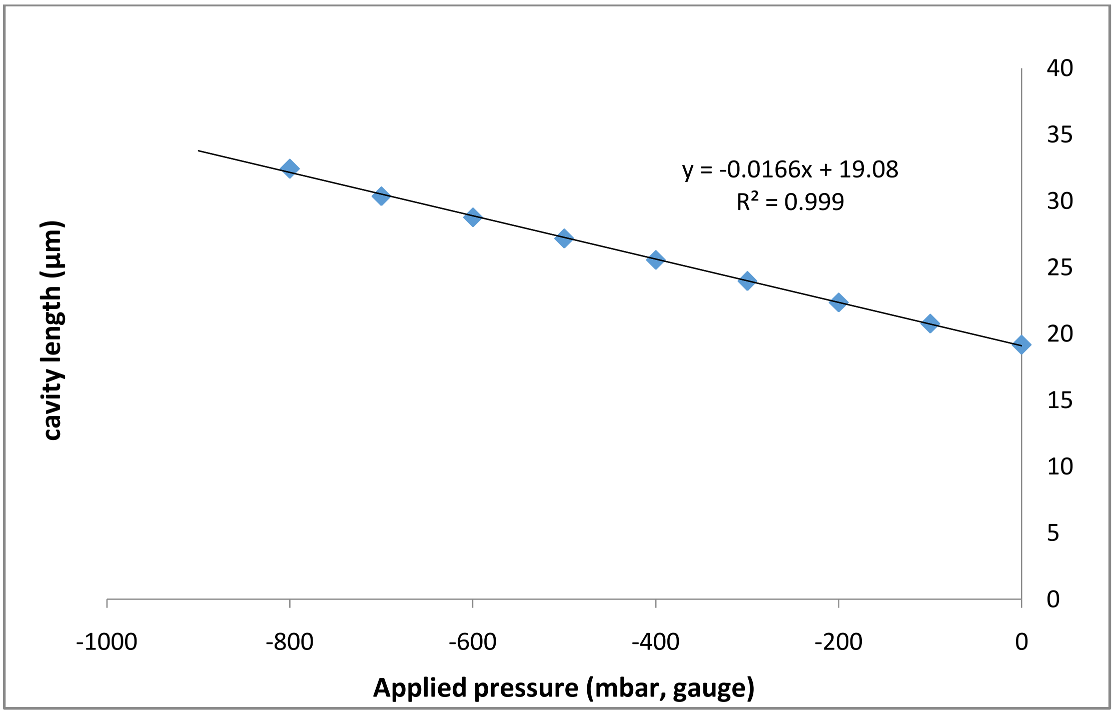

Fig. 6.18 Cavity length of thick glass sensor P3 (30 µm) with applied pressure

6.5.2. Deflection with applied pressure

The applied pressure in the experiment is in terms of gauge pressure, which is measured with respect to the atmospheric pressure. The atmospheric pressure is noted down during the experiment. When atmospheric pressure is added to the gauge pressure, it gives the absolute pressure value as per Eq.6-5.

$$\boldsymbol{Absolute\ pressure = gauge\ pressure + atmospheric\ pressure} \qquad \textbf{Eq. 6-5}$$

The initial cavity lengths (that is the front cavity depth without any deflection of diaphragm) were known from the characterizations carried out before anodic bonding of the wafers. Some of the devices (other than those already packaged) were also characterized for initial cavity length (CL) using the measurement technique developed in this work. The deflection of diaphragm is calculated by following relation (Eq.6-6).

$$\boldsymbol{Deflection\ of\ diaphragm = Intial\ CL - Measured\ CL} \qquad \textbf{Eq. 6-6}$$

The deflection characteristics of sensors PS10 (15 μm) and PS12 (60 μm) are shown in Fig. 6.19 and Fig. 6.20 for illustration. The pressure is presented in terms of absolute value, increasing from left to right on the x-axis. However, on y-axis instead of cavity length, deflection is plotted. As the cavity length decreases when the deflection increases, the deflection vs. pressure characteristics have positive slope.

A part of the deflection has negative sign which means that the diaphragm is deflected out of the cavity. The negative deflections are due to the presence of trapped gas in the sealed cavity. When the external pressure is less than the cavity pressure, the deflection is negative. When the external pressure is more than the cavity pressure, the deflection is inside the cavity. The deflection is zero, when the external pressure is exactly equal to the cavity pressure. This situation corresponds to initial conditions and the pressure in the cavity is the initial pressure of the trapped gas after the anodic bonding. Thus, from the following characteristics, the trapped gas pressure (initial cavity pressure) is the pressure at which the characteristic cuts the x-axis.

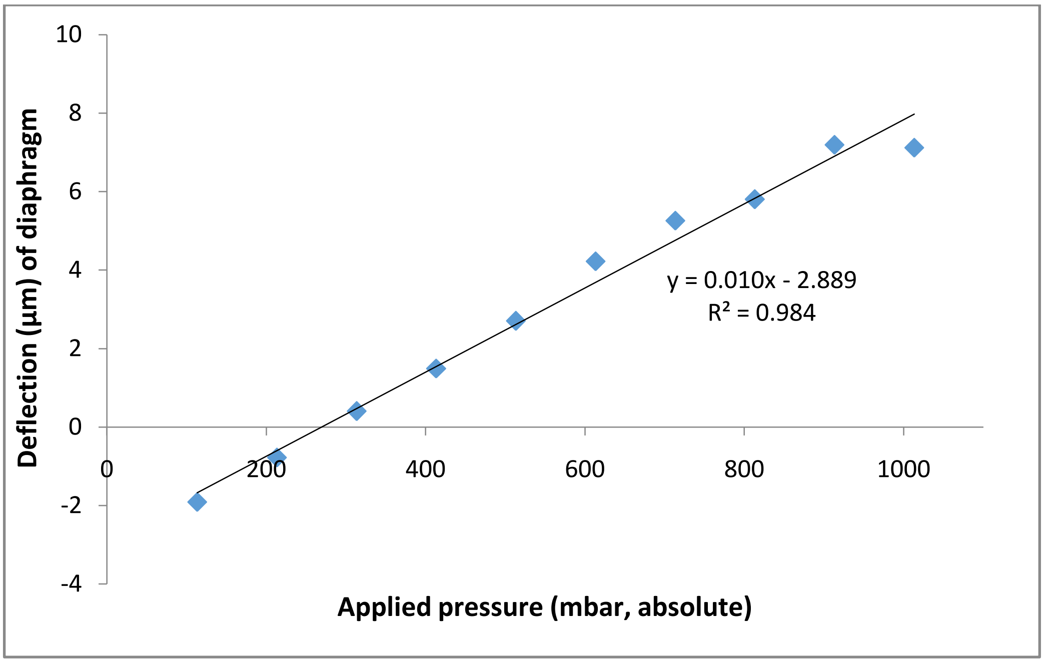

Fig. 6.19 Deflection characteristics of sensor PS10 (15 µm)

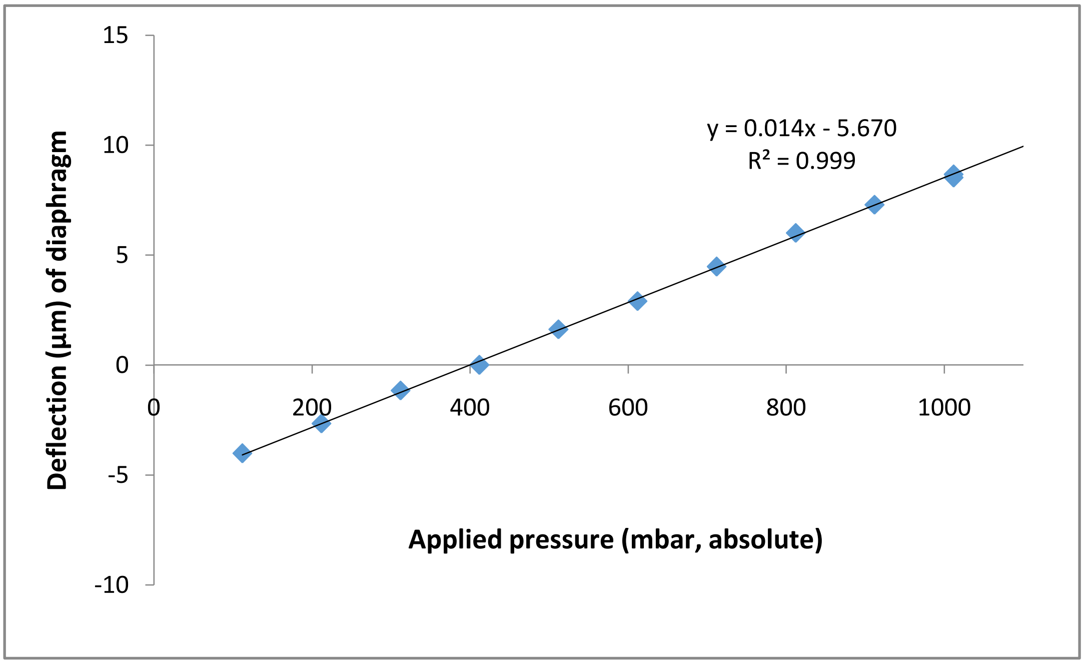

Fig. 6.20 Deflection characteristic of sensor PS12 (60 µm) with applied pressure

6.5.3. Estimation of initial cavity pressure

The tested sensors show negative (outward) deflection of the diaphragm when the applied pressure is below certain value. This indicates the presence of trapped gas in the sealed cavities. The pressure of the trapped gas can be estimated from the applied pressure that gives null-deflection of the diaphragm. As there are only discrete values of pressures applied during the experiments, best fit line is used to estimate the applied pressure that would have given null-deflection and same equals to the trapped gas pressure. The estimated pressure values for various sensors have been listed in Table 6.2 and plotted in Fig. 6.21Table 6.2 Estimated cavity pressures for various .

Table 6.2 Estimated cavity pressures for various sensors

Sr. No.	Sensor ID	Designed Cavity length (µm)	Cavity length value used (µm)	Experimental Slope (µm/bar)	Estimated cavity pressure (mbar) with CL ± 0.5 µm	R-square value of model fit	Estimated sensitivity of diaphragm B(µm/bar)	Suppression ratio
1	PS8	10	9.85	15.40	264 ± 32	0.999447	18.25	0.84
2	PS9	15	14.94	18.14	212 ± 28	0.999917	20.30	0.89
3	PS10	15	14.22	11.49	348 ± 49	0.999765	12.54	0.92
4	P3	30	30.5	16.58	336 ± 30	0.999988	17.70	0.94
5	PS12	60	59.64	14.13	425 ± 35	0.999477	14.61	0.97

The average estimated pressures of the trapped gas after anodic bonding fall in the range of 200 to 425 mbar. The trapped gas pressure estimated by the sensor characteristics show considerable variation, indicating that the anodic bonding process performed is not deterministic with respect to cavity pressure. Schematic of an anodic bonding setup and photograph of the lab instrument used in this work are shown in Appendix A.8 for further explanation.

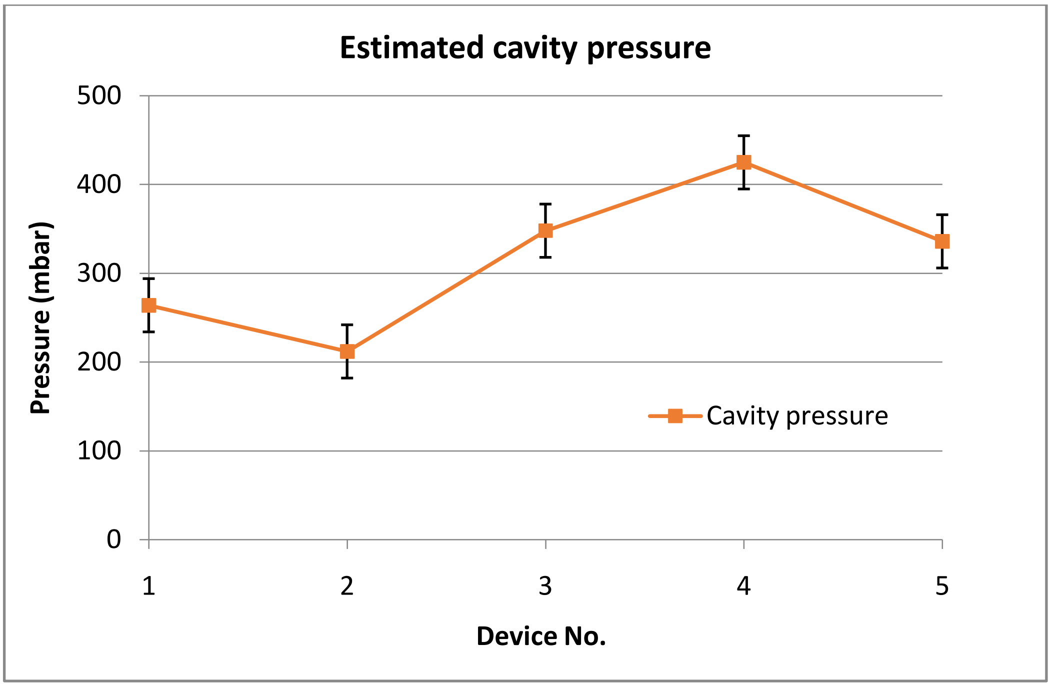

Fig. 6.21 Estimated cavity pressures after anodic bonding

The probable reasons for different pressures in the sealed cavity are as following:

a) The temperature control on the instrument is not precise. The temperature may vary by ± 50 °C. Therefore, as per Eq. 3-1, the trapped gas pressure may vary from 390 mbar to 450 mbar, if actual average bonding temperature is considered from 400 to 500 °C.

b) The electrode (cathode) contacts at the centre on the glass wafer. In general, the anodic bonding starts from the centre and expands outward. However, in the present case, there is cavity at the centre in the silicon wafer, so the bonding will start from some other point where the two wafers have intimate contact; and then the bonding expand to other areas. In few cases, extra pockets of trapped air can be noticed between the flat wafers (Appendix A.9). This may be due to residual stress [110] and bow in the silicon and glass wafers. The dynamics of bonding may sweep some amount of air in the cavity, thus increasing the cavity pressure. However, in the present testing any increase of pressure is not noticed.

c) The temperature variations over the area of wafers may cause some gas escape out of the cavity resulting in lower pressures than expected.

d) The cavity pressures have been calculated from the characterization values of the front cavity. However, due to probable non-uniform etching of the front cavity, they could be small variation in the cavity length. Therefore, a probable band of values of cavity pressure is also calculated giving allowance of ± 0.5 µm over the known or characterized CL value. The tolerance in the estimated cavity pressure is in the range of ± 28 mbar to ± 49 mbar for different devices listed in Table 6.2.

6.5.4. Fitting of analytical model on data

The cavity length (l_0) and trapped gas pressure (P_{c0}) are known respectively from characterization and experiments. These two inputs are used in the developed analytical model. The model is fitted to the experimentally found deflection characteristics of each sensor. The R-square value is calculated indicating the goodness of fit to the experimental data. The value of unsuppressed sensitivity (B) is adjusted to achieve the highest value of R-square. The ratio of experimental (apparent) deflection sensitivity to unsuppressed sensitivity is calculated to calculate the 'suppression ratio'. The data is presented in Table 6.2.

The estimated unsuppressed deflection sensitivities (B) of diaphragms in different sensors are found widely different than the designed value. The designed value is 15.63 µm/bar, whereas the estimated values are ranging from 12.54 µm/bar to 20.30 µm/bar. The upper value is about 30% more than the targeted value and the lower value is about 20% less. The reasons of such a variance are as following:

a) The major reason is variation in thickness of the diaphragms. As the deflection is inversely proportional to the cube of the thickness (Eq. 3-13), a 10% higher thickness will reduce the sensitivity by 25%. Similarly, a 10% lesser thickness will enhance the sensitivity by 37%.

b) The other important reason can be the "residual stress" in the bonded silicon-glass pair [111-112]. It is known that the after anodic bonding, the bonded pair gets some bowing and residual stress. Reference [87, 113] gives typical indicative values of the residual strain of 100 micro strains. Therefore, using the young modulus value for silicon, residual stress of about 17 MPa or more are possible in silicon in the bonded pair. In the present design, the stress in the diaphragm would be 75 MPa for deflection of 10 µm (Appendix A.11). However, it needs detailed study to model and characterize residual stress in the diaphragms of present design made with the present parameters of anodic bonding. The bonding parameters, wafers' thickness ratio, electrode type etc. shall be optimized for better control of residual stresses [114-116].

c) The third reason of scaling of the sensitivity is the trapezoidal shape of the etched front cavity in single crystal silicon wafer. The geometry of the trapezoid is well defined as the same is governed by the crystallographic structure and planes in the single crystal silicon. The diaphragm size is lesser by $\sqrt{2}l_0$ than the size of the square window. For a 60 µm deep etched cavity, the size will reduce by 85 µm. For other smaller cavity depths, this value will be smaller. The diaphragm side length will reduce from 8000 µm to 7915 µm. As the deflection proportional to power 4 of the side length, deflection will reduce to 95.8%. The reduction is about 4.2 % for 60 µm cavity, 2.1 % for 30 µm cavity and even lesser for smaller cavities. As a compensatory measure, the size of lithography window could be increased accordingly (such as 85 over 8000 µm) to end up with the diaphragm of same sizes;

however, the same is not feasible for practical reasons. As this is a systemic kind of error, the same is taken care while fitting developed analytical model on the experimental data.

As the sensitivities of different sensors are considerably different, it is appropriate to compare the experimental data after normalizing the curves with respect to unsuppressed sensitivity of diaphragms. In Fig. 6.22, the normalized spans have been plotted for two extreme values of the estimated sensitivities, 12 µm/bar and 20 µm/bar, to cover the entire range of tested devices. Moreover, it is experimentally found that the pressure of the trapped gas is ranging from 212 mbar to 425 mbar. Therefore, the two curves have been plotted at an average value of the gas pressure (320 mbar). In the fitted analytical model, care has been taken to modify the volume of the cavity for the trapezoidal shape made with lithography window of 8 mm x 8 mm size. The analytical model is plotted with average normalized deflection (ν) value of 0.3044, as taken originally.

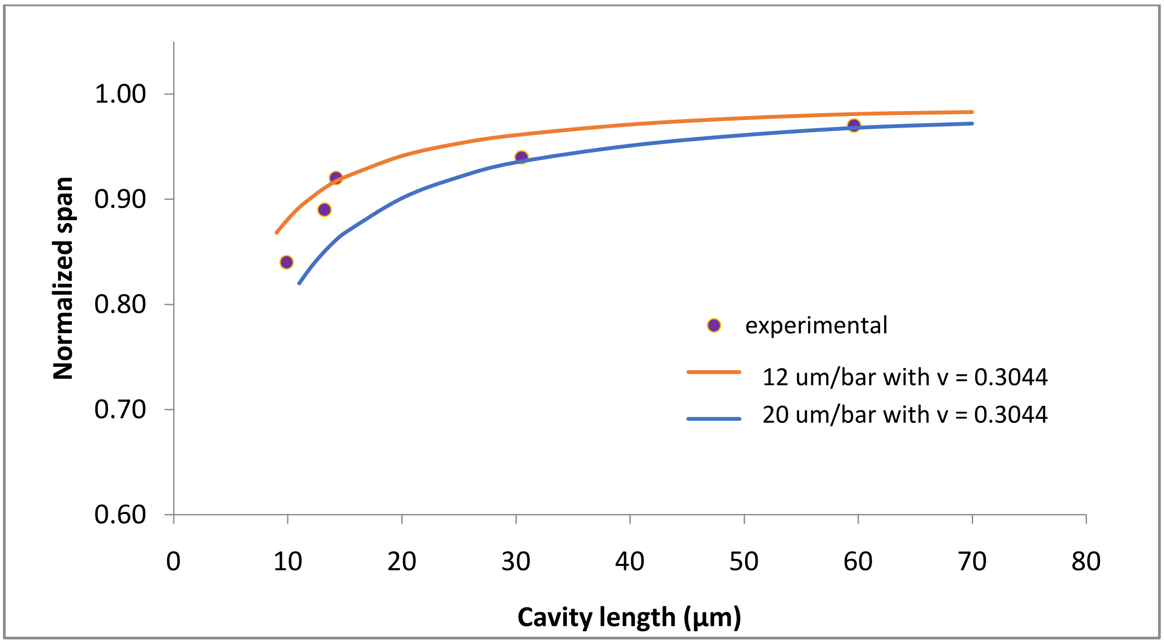

Fig. 6.22 Model fitting on experimental data

The experimental points fall fairly in the range covered by two sensitivity values. Thus, it is stated that the developed analytical model is fitting to the experimental data within the uncertainty band resulting from the fabrication process. It is to be clarified that taking 'ν' value of 0.32 does not change the curve considerably, as the cavity lengths here are somewhat above (9 µm onwards) the minimum possible (7 µm). Therefore, the models at two values of 'ν' are almost overlapping as shown in Fig. 6.23. As the difference at two values of 'ν' is not significant, the value 0.3044 is used in the fitting to experimental data.

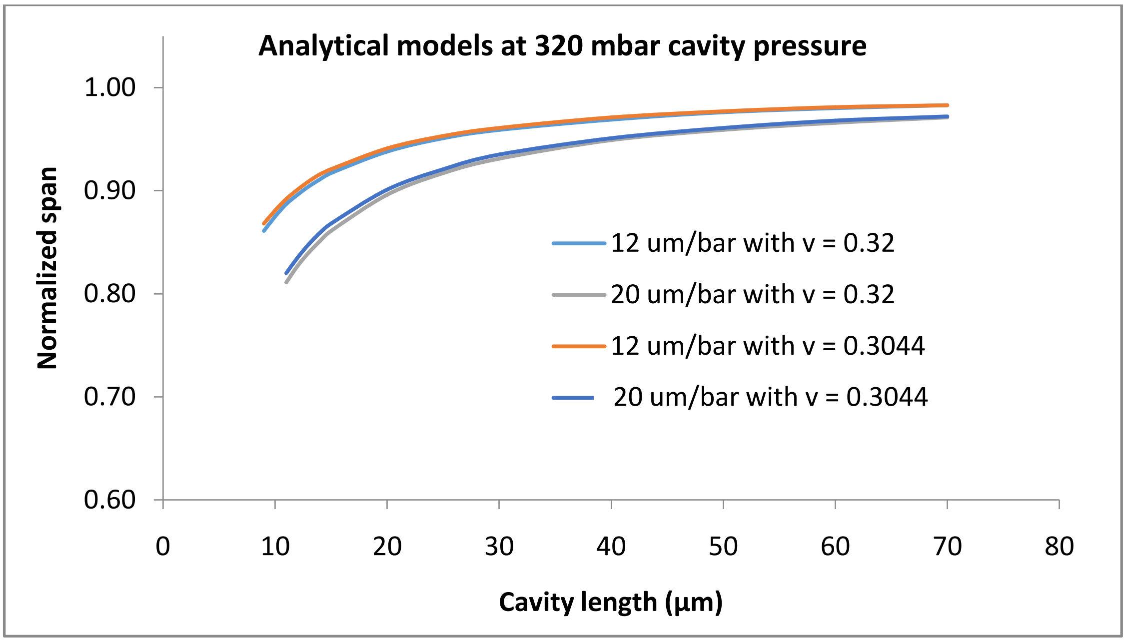

Fig. 6.23 Analytical model at two values of normalized average deflection

6.6. Summary

Devices of various cavity lengths have been fabricated using anodic bonding process between silicon and glass wafers. The devices of two batches had 0.5 mm and 2.0 mm thick glasses. The first batch of devices is tested for functionality as pressure sensor using a simple test packaging (type-1). The packaging is improved to obtain optical signals from devices made with thick glass. A spacer ring is introduced in the modified packaging (type-2). The spacer lifts the device and helps achieving higher orthogonality of device surface at centre with respect to fiber axis. The thick glass devices are tested using APC ferruled fibers for ease.

The experimental set-up for functional testing of these optical MEMS pressure sensors is described, followed by signal processing of spectra to calculate the CL at any applied pressure. The cavity length versus applied pressure characteristics for 5 sensors of various front cavity depths is presented. Thereafter, the 'deflection versus applied pressure' characteristics are found using the value of known or measured front cavity depth. From these characteristics, pressure of trapped gas in the cavity sealed through anodic bonding process is estimated. This pressure corresponds to null-deflection of diaphragm. Considerable variation is found in the pressure of trapped gas from device to device. This means the bonding procedure is not very deterministic in terms of the repeatability of the trapped gas pressure.

The developed analytical model is fitted to experimental data while taking the variations of trapped gas pressure and sensitivity of different tested sensors into account. The variations of the trapped gas pressure from device to device would affect the final deflection characteristics in a batch of sensors. The characteristics can be made more deterministic by going for larger volume of the cavity either directly or through a connected buffer cavity as explained in the next chapter.

The unsuppressed sensitivity of diaphragms is estimated from the knowledge of cavity pressure, cavity length and the apparent (experimental) sensitivity. The devices are found to have considerable variation in the pressure sensitivity primarily owing to the fabrication tolerances in achieving the desired thickness of diaphragm and secondly due to residual stresses after bonding.

Chapter 7

SENSORS WITH BUFFER CAVITY

7.1. Introduction

In the previous chapters it has been shown that large cavity lengths are beneficial for better performance of the sealed microcavity pressure sensors. It is already seen from the sensor characteristics that many parameters viz. span, offset and their temperature dependence are quite sensitive to the cavity length in the regime of smaller cavity lengths. Also, the pressure of trapped gas is likely to have variations from device to device. Therefore, a batch of sensors fabricated with small cavity lengths is likely to have large spread in sensors' characteristics. However, when the cavity lengths are on larger side, all these parameters attain their respective design values, thus minimizing any spread in sensor characteristics.

It is established through the present study that large cavity lengths are advantageous in terms of full and temperature-independent span and convergence of all other performance parameters to respective certain values. The similar goals could have been achieved if the pressure of the trapped gas would have been extremely low as compared to the pressure range of the sensor. However, the cavity pressure is not amenable for the chosen technology (such as anodic bonding under atmospheric pressure). Thus the other way left is to optimize the sensor characteristics through cavity length. In literature, the fiberoptic acoustic sensors have been provided with vent to atmosphere [117-119] or long cavity [120-121] for improving the frequency response of the diaphragm or cantilever.

Large cavity lengths such as 200 μm or more (or equivalent volume) are desirable from the perspective of achieving designed deflection characteristics. However, large cavity lengths for FPI sensors may not be desirable or possible by optical design and/or the fabrication process. For example, as observed in the wide literature on FPI pressure sensors, generally the FP cavity lengths are as low as submicron to as high as few tens of microns. The cavity lengths are much below 100 µm. The cavity lengths are generally short to have high contrast fringes in the interferometric signal. Sometimes the large cavity lengths may not be possible by the fabrication technology. For example, a standard 2” silicon wafer is around 280 µm thick, so it is not possible to fabricate a sensor with 500 µm length of cavity in that case. It is only possible if custom made silicon wafers with desired thickness are obtained. However, then the anodic bonding becomes difficult due to higher thickness of the silicon wafer.

Thus the short cavities are desired from the **optical design** and large cavity lengths are desired from the **mechanical design,** as explained. To overcome the **contradictory requirement**, the coupled **‘buffer cavity’** is proposed. Such a buffer volume cavity is supposed to connect to the Fabry-Perot cavity through micro-channels and provide ‘buffer’ volume to it (Fig. 7.1).

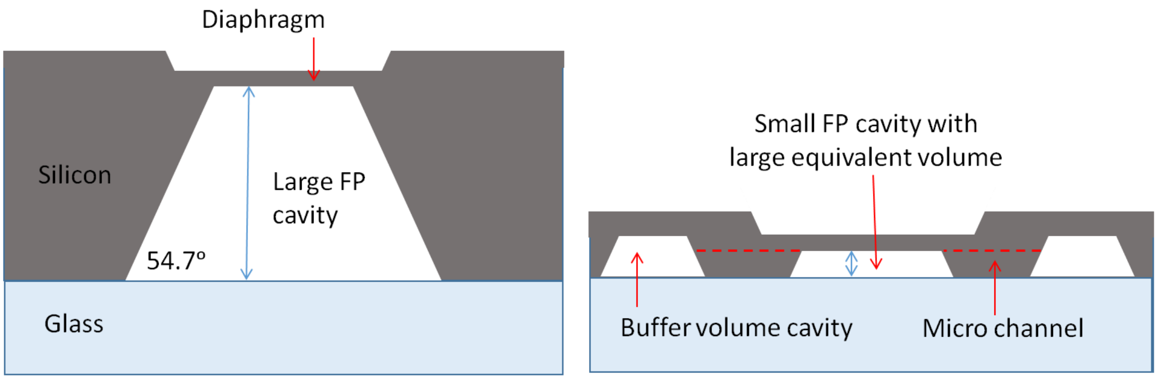

Fig. 7.1 Concept of buffer volume cavity to provide extra volume

In the Fig. 7.1, a large FP cavity sensor along with a short FP cavity sensor of equivalent volume is shown. In principle, the buffer cavity can be made in silicon or glass or as a combination of both depending on the fabrication technology and preferences. In the present design, the buffer cavity is made in silicon.

7.1.1. Methodology of calculations

The desired cavity length can be decided based on the sensor characteristic described so far and then the equivalent volume needed can be calculated. The volume of the coupled cavity can be chosen such that the total volume is **approximately** same as the desired equivalent volume. The approximate volume is acceptable because the span, offset and temperature coefficients become insensitive to the cavity length (or volume) once the latter is on larger side. The flow chart for design calculations of buffer cavity is given in Fig. 7.2.

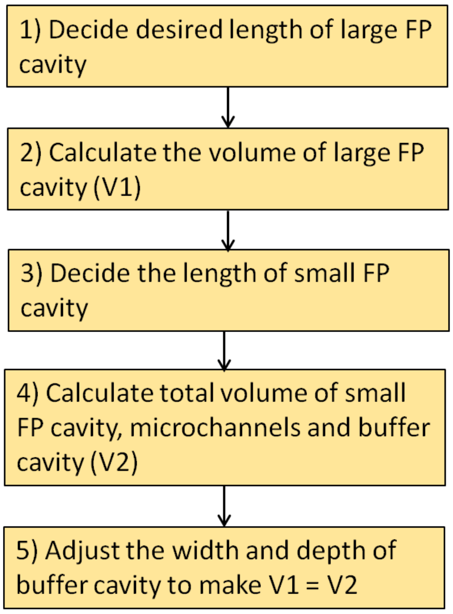

Fig. 7.2 Flowchart for designing the buffer cavity

7.2. Form and design of the buffer cavity

One simple implementation of the buffer cavity is shown in Fig. 7.3. In this design, the main cavity (FP cavity) is connected to the buffer volume through micro channels. The view is shown from the bonded glass side. The buffer cavity shall be able to bring the performance of small cavity FP pressure sensors (such as 7- 15 μm) at par with large cavity FP sensor, as far as suppression of span and other effects related to trapped gas are concerned.

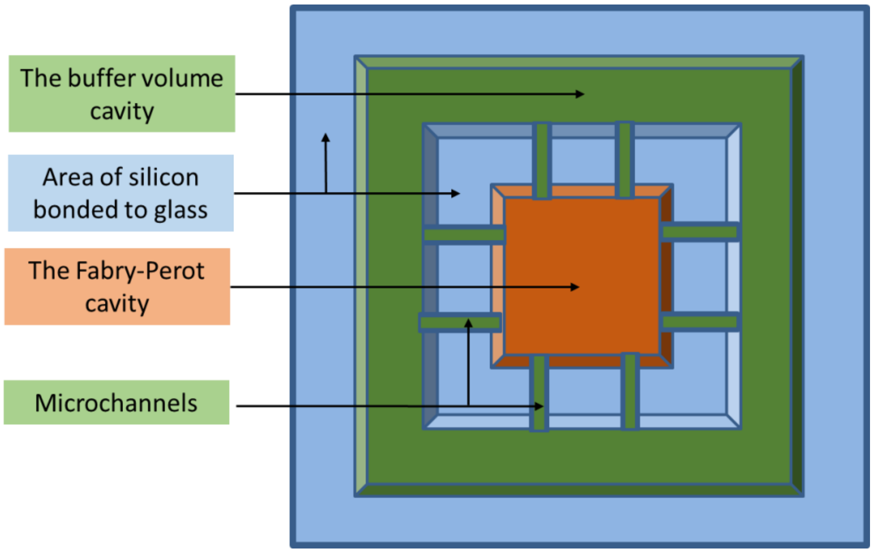

Fig. 7.3 Form and design of FP pressure sensor with buffer volume cavity

In the present design the following values of parameters given in Table 7.1are set and shown in Fig. 7.4.

Table 7.1 Design parameters for the buffer cavity

Sr.No.	Parameter	Value	Remark
1	Diaphragm side length (L)	8 mm	Fixed
2	FP cavity depth (l_0)	15 µm	Example for study
3	Width of first bonded after FP cavity = length of micro channels	4 mm	Chosen
4	Width of microchannel	1 mm	For fast flow of gas
5	Depth of microchannel	Depth of FP cavity	For ease of fabrication, common etching
6	Total number of microchannels	8	For symmetry and fast flow of gas
7	Width of buffer cavity	4 mm	Fixed for the design
8	Depth of buffer cavity (l_B)	To be calculated	To get equivalent volume

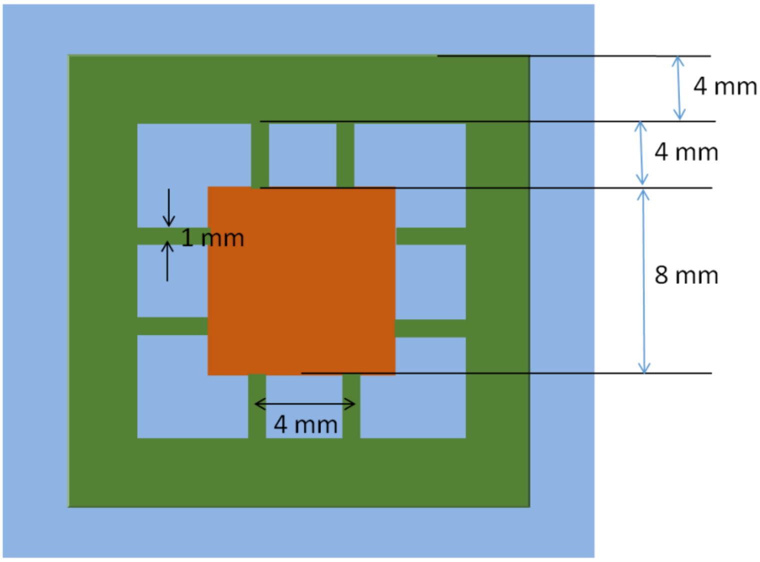

Fig. 7.4 Design parameters of sensor with buffer cavity

7.3. Volume calculations

The volumes of large FP cavity as well as that of small FP cavity along with total buffer volume are calculated.

7.3.1. Volume of large FP cavity

The cavity made in silicon using anisotropic bulk micromachining has a trapezoidal shape with fixed angle of 54.7° of taper wall (due to crystallographic planes) as shown in Fig. 7.5.

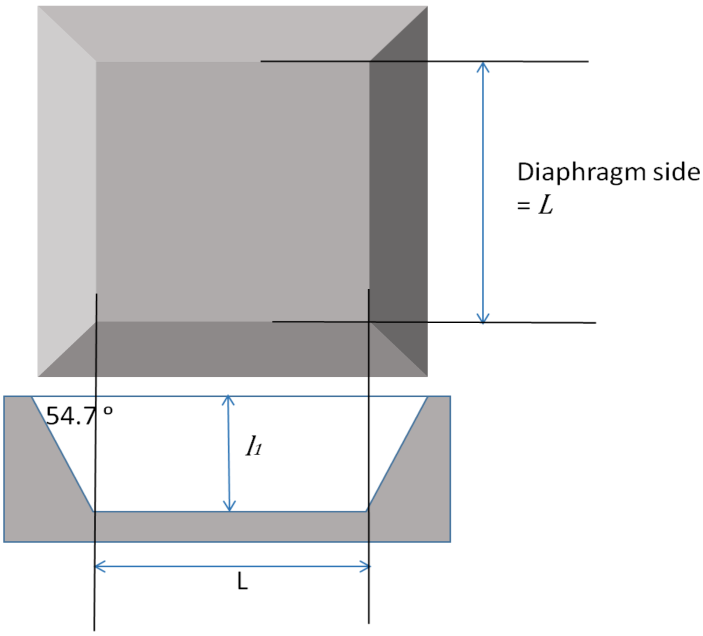

Fig. 7.5 Trapezoidal etched cavity in silicon wafer

The volume V_1 can be calculated from diaphragm side length L and cavity length l_1 as per Eq. 7-1. Here cross-section area at half the height of the trapezoidal cavity is taken and multiplied by cavity length.

$$V_1 = (L + 0.707\, l_1)^2 . l_1 \qquad \textbf{Eq. 7-1}$$

The calculated volume of large cavity of length 500 µm and diaphragm side length of 8 mm is given in Eq.7-2.

$$V_1 = 34.89 \text{ mm}^3 = 34.89 \text{ µl (micro litre)} \qquad \textbf{Eq. 7-2}$$

7.3.2. Volume of small FP cavity with buffer

For the small depths of FP cavity and microchannels, the effect of slanted walls can be neglected. The volume of FP cavity and channels can be found by multiplication of area and depth. The volume of buffer cavity is found by subtracting the volumes of two trapezoids. The simplified expression for the total volume V_2 is given by Eq 7-3, where the lengths (depths) are in millimetres.

$$V_2 = 96\, l_0 + \left(320 - 40\sqrt{2}. l_B\right). l_B \qquad \textbf{Eq. 7-3}$$

The volume V_2 for a 15 µm deep FP cavity and 100 µm deep buffer cavity is 32.87 mm^3. The depth of the buffer cavity can be adjusted to have volume of desired large cavity. It is important to note that the volume can be matched approximately, because both the volumes are high, and at large volume (equivalent large cavity length sensors) the span characteristics become insensitive to small difference of volume (Refer section 3.5.2).

7.4. Numerical simulation and validation of concept

In order to validate the concept of buffer cavity and to check the efficacy of the inclusion of buffer cavity, a numerical model is developed and finite element analysis has been carried out. The parameters of the FE simulations are same as given in Table 4.1. Three models are made with description as given in Table 7.2.

Table 7.2 Numerical models to study the effect of buffer cavity

Model No.	Length of FP cavity	Buffer included	Depth of the buffer cavity (μm)	Remark
Model 1	15 μm	No	Nil	Small FP cavity
Model 2	15 μm	**Yes**	90.5	Small FP cavity with buffer, Total volume same as Model 3
Model 3	500 μm	No	Nil	Large FP cavity

The quarter models of the device are used to minimize the computation efforts. The quarter model of single cavity and buffer cavity sensors are shown in Fig. 7.6 and Fig. 7.7.

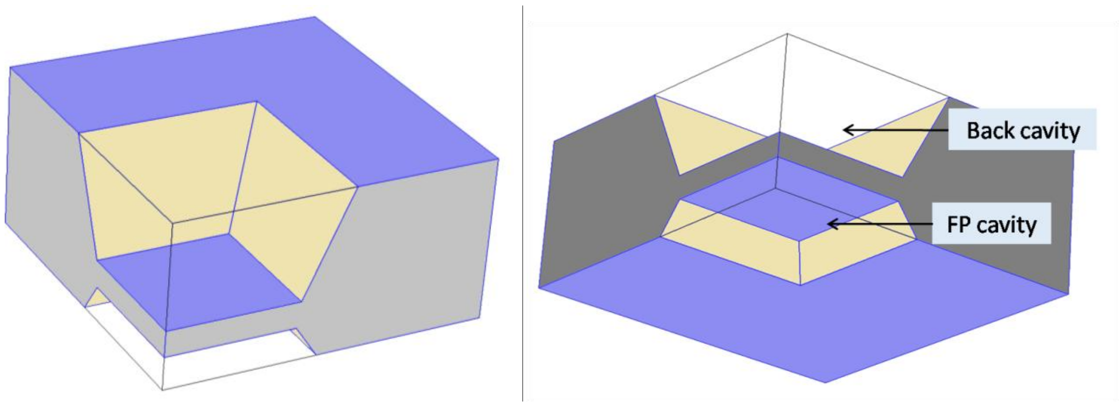

Fig. 7.6 Quarter model of silicon FP cavity without buffer cavity (model 1 and 3)

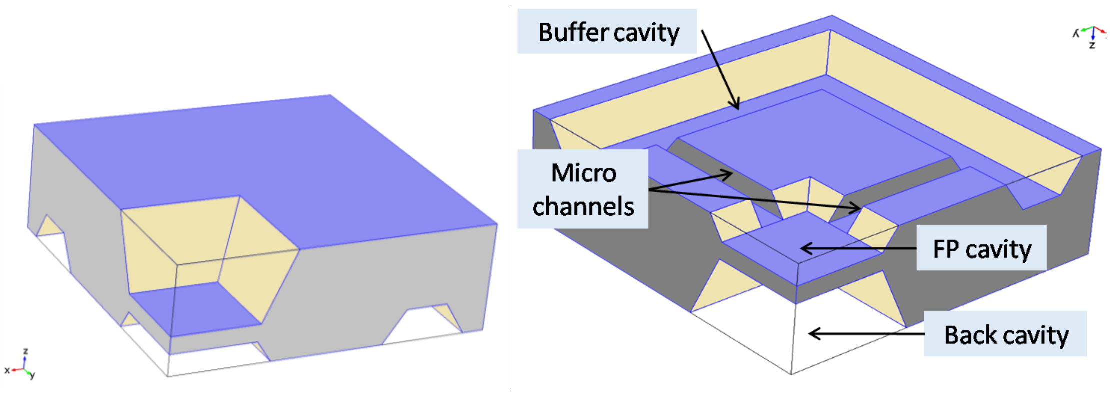

Fig. 7.7 Quarter model of silicon FP cavity with buffer cavity (model 2)

The pressure range to be covered is from 0 mbar (abs.) to 1000 mbar (abs.), whereas the pressure inside the cavity is 405 mbar (abs.) as per the initial condition. Therefore, the pressure is applied in two parts as a time based ramp function as given in Chapter 4. One is increasing ramp from 405 mbar to 1000 mbar over 1 second of time and then 1 second of dwell time. Similarly, second part of pressure is applied as decreasing ramp from 405 mbar to 0 mbar over 1 second of time and then 1 second of dwell time. The time resolution for applied pressure is 1 ms, hence the applied pressure is applied in 1000 steps for both the ramp functions.

In case of Model 2 (15 µm FP cavity with buffer) and Model 3 (500 µm long FP cavity), the volume of cavity is high compared to Model 1; hence the change in the cavity pressure is very small. The applied pressure as well as cavity pressure for buffer cavity sensor (BCS) is plotted in Fig. 7.8. In the Model 2, the static pressure in the FP cavity and in the buffer cavity buffer cavity will be same.

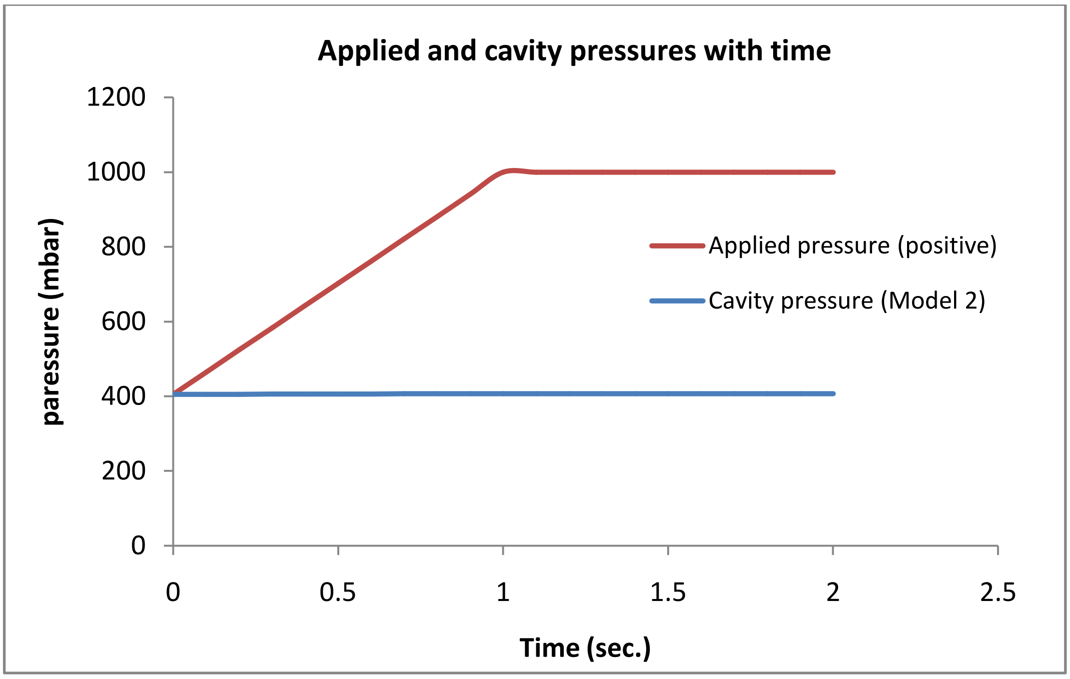

Fig. 7.8 Cavity pressure change with time in response to increasing applied pressure (model 2)

When the applied pressure changes from 405 to 1000 mbar, the diaphragm deflects inward the cavity and cavity pressure increase from 405 mbar to 407.2 mbar. The change in cavity pressure is **0.5 % only**, hence the 'reference' (the cavity) pressure gets more stabilized compared to that in small cavity length sensors (Refer section 4.3.1) after inclusion of buffer cavity. The change in volume of the buffer cavity sensor (BCS) is given in Fig. 7.9.

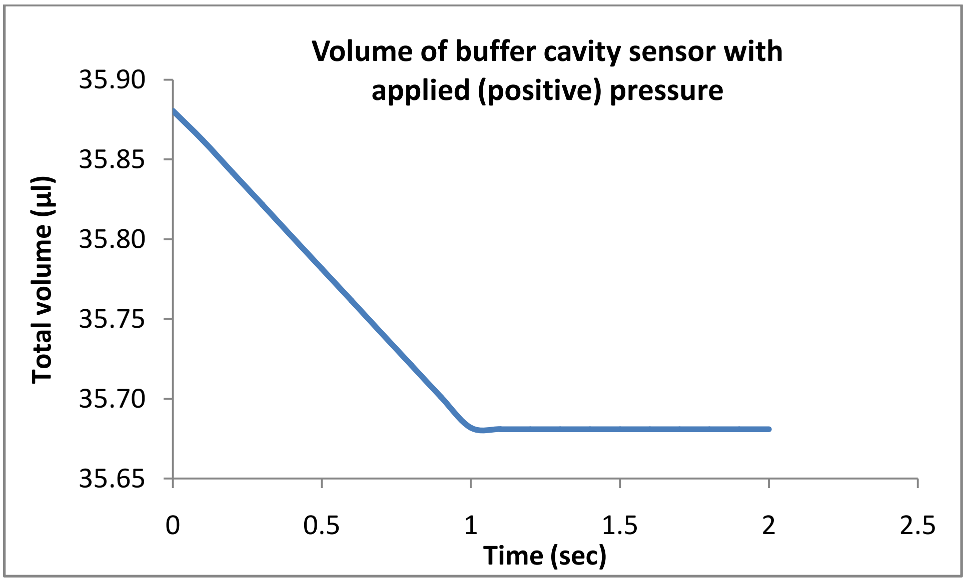

Fig. 7.9 Volume of buffer cavity sensor with pressure

The volume decreases when increasing ramp pressure is applied. The volume changes from 35.88 to 35.68 mm^3 (µl). The change of volume is 0.2 mm^3, which is small compared to the total volume of the cavity comprising the buffer. The change of volume is only **-0.56 %**, on changing the applied pressure from 405 mbar to 1000 mbar. On application of negative pressure (ramp from 405 to 0 mbar), the volume will increase by even lesser amount as the pressure change is lesser.

Similarly, for negative ramp applied pressure, the diaphragm moves outward the cavity and the cavity pressure decreases (Fig. 7.10). The cavity pressure reduces from 405 to 403.5 mbar, which is **-0.37 %** change.

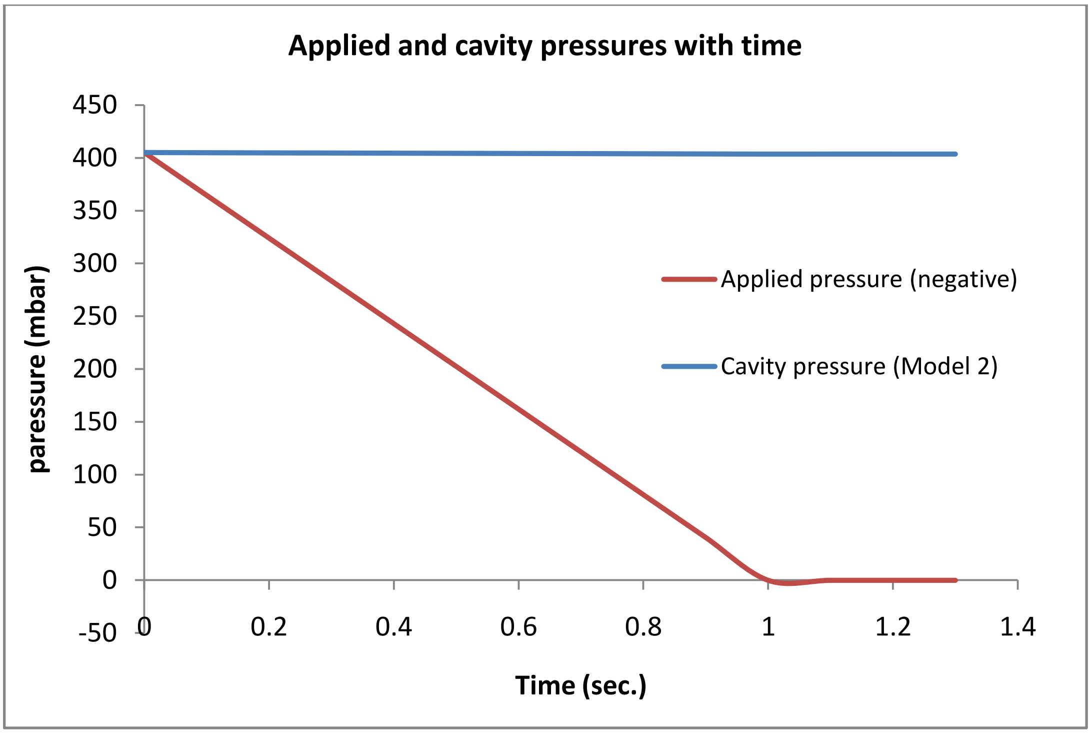

Fig. 7.10 Cavity pressure change with time in response to decreasing applied pressure (model 2)

The maximum deflection is about 9.63 µm at 1 bar applied pressure for model 2 (Fig. 7.11). The deflection is – 6.638 at 0 mbar applied pressure. The total deflection (span) is 15.733. The span is unsuppressed and the performance is at par with a large size cavity.

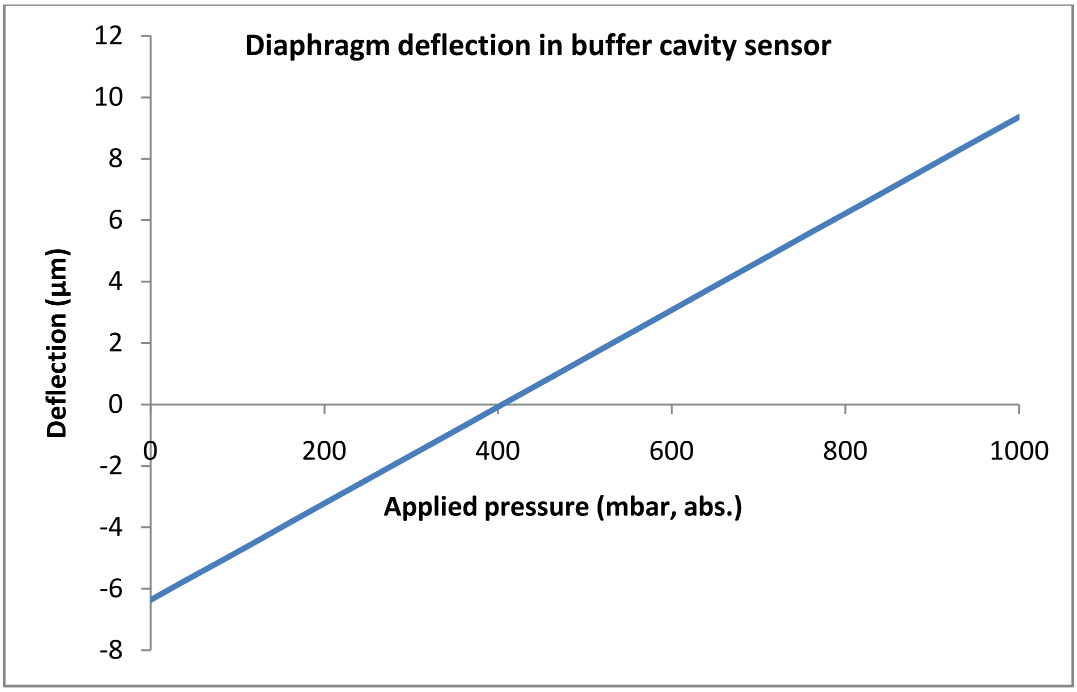

Fig. 7.11 Deflection characteristics of buffer cavity sensor (model 2)

7.4.1. Results and discussions of numerical simulation

It is found that the model 1 (small FP cavity) has lesser deflection at full pressure than that in model 2 (with buffer) and model 3 (large FP cavity). The deflections and cavity pressures of model 2 and model 3 have emerged same. The summary is given in Table 7.3.

Table 7.3 Results of FE simulations of models with and without buffer cavity

Model No.	**Length of FP cavity**	**Buffer**	**Cavity pressure increase (mbar) at 1 bar Pa**	**Deflection (µm) at 0 bar applied pressure**	**Deflection (µm) at 1 bar applied pressure**	**Achievable span (µm) over range 0-1 bar**
Model 1	15 µm	No	490.1	-5.645	7.975	13.62
Model 2	15 µm	**Yes**	407.3	-6.368	9.365	15.73
Model 3	500 µm	No	407.3	-6.330	9.310	15.64

The model 1 without buffer has a suppressed value of span. Also, the cavity pressure has changes from 405 to 490.1 mbar after on full positive pressure, 1 bar. The model 2 and 3 have large volume, so change in pressure is only 2.3 mbar over 405 mbar initial pressure. The span is almost full with buffer cavity.

The important points about the buffer cavity are:

i. A small area sensor would need small area of buffer cavity; therefore, the buffer cavity can be implemented without increasing the device size. Therefore, the buffer cavities can be implemented without sacrificing much area of the silicon wafer
ii. The main cavity with longer length would need smaller buffer cavity. It is applicable for FP cavities of medium lengths such as a 50 μm FP cavity.
iii. One design of buffer cavity will be applicable for all small FP cavity sensors. A buffer cavity giving a volume matching to a big cavity will relieve a 10 μm or a 20 μm FP cavity almost similarly. It is because the span is sensitive at small cavity lengths, but insensitive at large cavity lengths. Once a large volume buffer is included, all the small FP cavity sensors will get relieved to similar extent.

Following approaches can be considered to implement buffer cavity in alternative ways:

a) The diaphragm can be bossed one (planar projection at center), so that the desired FP cavity length and higher cavity volume can be achieved without additional coupled cavity
b) The additional cavity can be made on the glass in the main cavity around the leaving the optically function area with similar advantage as above and without affecting the mechanical behavior of diaphragm

7.5. Suggested fabrication method for buffer cavity devices

The fabrication of this device can be completed with 3 masks, as mentioned below:

1) Mask 1 is used to define aperture for 'buffer area'. This mask is used to pattern aluminium for RIE of the buffer cavity. The area of 'main cavity + microchannels' remains protected by aluminium layer during etching of buffer cavity. The etching is not done to the final desired depth of the buffer, because in the next step of wet etching buffer is also etched along with the main cavity and microchannels.

2) Mask 2 is used to define aperture for 'main cavity + microchannels + buffer'. Oxide layer is removed from this area. The wet etching is carried out to complete the micromachining of the front side of the device.

3) Mask 3 is used to define back cavity and pattern aluminium for Reactive Ion Etching (RIE) to form the back side cavity and realize the diaphragm.

7.6. Summary

The concept of buffer cavity has a solid theoretical foundation established through analytical as well as numerical modelling of the sealed cavity pressure sensors in the present work. The effectiveness of the buffer cavity is validated by developed numerical model of the buffer cavity sensor. The sensors with buffer cavity will have deterministic characteristics across the sensors in presence of fabrication tolerances of etch depths of the cavities as well as tolerances of residual pressure after anodic bonding.

Chapter 8

CONCLUSIONS AND FUTURE SCOPE

Conclusions

In this research work, fiberoptic pressure sensors working on the principle of a Fabry-Perot interferometer with MEMS based design have been investigated. Important conclusions of the present research work are summarized below:

1) An **analytical model** is developed for “deflection” of diaphragm as a function of applied pressure and other design parameters in a sealed microcavity pressure sensor.
2) Deflection characteristics are studied based on developed analytical model for pressure sensors of range 0-1 bar and 0-10 bar, for trapped gas pressure of 405 mbar and designed span of 15.63 µm.
3) The study indicates that the span gets reduced to a lower value than the designed span. For example, the span achieved for a 1 bar pressure sensor of 7 µm cavity length is 11.87 µm while the designed span value is 15.63 µm. The phenomenon is named as “suppression of span”.
4) The suppression of span is there when the trapped gas pressure changes in response to movement of diaphragm.
5) The achievable span for 10 bar sensor is 15.36 µm (at cavity length 15 µm, trapped gas pressure 405 mbar). The achievable span is very close (98.25 %) to the designed span value 15.63 µm. The suppression of span is 1.75 % at the most in this case.

6) It is found from analytical model that a 1 bar pressure sensor is affected more than a 10 bar sensor, because the diaphragm is more sensitive for 1 bar sensor. Therefore, 1 bar sensors have been studied in greater detail.
7) The suppression of span is more for smaller cavity lengths when all other parameters are fixed. For example, achievable spans for a 1 bar sensor at 405 mbar trapped gas pressure are 76 %, 90.9 % and 93.86 % for cavity lengths of 7, 20 and 30 μm respectively.
8) The minimum possible cavity length is found from the developed analytical model. The minimum possible cavity length is about 7 μm and 15 μm respectively for 1 bar and 10 bar sensors, at trapped gas pressure of 405 mbar.
9) The minimum possible cavity length is smaller for higher pressures of trapped gas. For example, for 600 mbar pressure of trapped gas, minimum possible cavity length is 2 μm.
10) The suppression of span is more for sensors having higher trapped gas pressure. For example, for 1 bar sensor of 7 μm cavity length and 600 mbar pressure of the trapped gas, the achievable span is 11.33 μm. It is 72.48 % to the designed span value 15.63 μm. The suppression of span is 27.52 %.
11) The span, offset, and temperature coefficients of those are very sensitive to cavity length of the sensor in the regime of small values.
12) At large cavity lengths such as > 200 μm; the span and offset becomes almost independent of cavity length. Hence, large cavity lengths are beneficial for achieving more deterministic characteristics in a batch of sensors.
13) The temperature dependence of span vanishes at large cavity lengths, whereas that of offset becomes constant. Hence, large cavity lengths are beneficial with respect to temperature behaviour of the gas.

14) **Numerical model** of sealed cavity pressure sensors of 1 bar range is developed. The values of trapped gas pressure (405.3 mbar) and designed span (15.63 μm) are taken same as those in analytical model. Finite element analysis is carried out to find deflection characteristics of sensors of different cavity lengths. It is found that the achievable span is smaller for smaller cavity length. The span is 11.59 μm for sensor of 7 μm cavity length. The span is 74.13 % of designed span, which is in good agreement with the results of analytical model.

15) The pressure in the cavity is also studied with respect to applied pressure for sensors of different cavity lengths. For sensor of 7 μm cavity length, the cavity pressure changes from 329.4 mbar to 584.7 mbar over the applied pressure range of 0 to 1 bar. The change in cavity pressure is large for small cavity length sensors. For example, the total change of cavity pressure is 255.3 mbar and 9.8 mbar respectively for sensors of cavity length 7 μm and 200 μm.

16) The analytical and numerical models are compared in Section 4.4. Both the models are in close agreement, thus the developed analytical model is **validated** by FE simulations.

17) The sensors are designed and then fabricated at IIT Delhi.

18) The sensors are packaged and tested for pressure response. The pressure of trapped gas is estimated experimentally for all the sensors. The estimated pressures are in the range of 212 - 424 mbar**,** against the ideal pressure of 405 mbar estimated by the theory.

19) The analytical model is fitted on the experimental data using measured cavity length and estimated pressure of trapped gas. The deflection sensitivity of diaphragms of fabricated sensors is estimated. The suppression ratio is calculated. It is found that

suppression is lesser for sensors of larger cavity. Thus the analytical model is **validated** by experiments.

20) It is found that the peak value of signal from a thick (2 mm) glass device is almost **30 times weaker** than the signal of stray interferometer. The fringe modulation of the stray interferometer is quite high (84%) than that of sensing interferometer (17%). Therefore, it is difficult to capture the signal.

21) A novel **technique** is developed to measure the cavity length of thick glass sensors by using an angle-cut multimode optical fiber. The technique is used for sensor characterization as well as for **noncontact measurement** of entire area of glass-silicon interferometer. The deflection shape of square silicon diaphragm is characterized from the results of non-contact scanning. The technique is **validated** by fitting the theoretical model to experimental data.

22) Concept of "**buffer cavity**" is introduced to provide extra volume to improve the sensor characteristics for sensors of small cavity lengths. The concept is **validated** with FE based simulations.

Future scope

In any research work, there is always some scope for further and deeper explorations. From the present work, following are the areas which shall be explored in future.

1) The sensors with buffer cavity should be fabricated and validated experimentally. The physical form of buffer cavity (in silicon or glass or any other) shall be decided to suit feasibility or ease of fabrication.

2) The sensor should be fabricated with thin (0.5 mm or lesser) glass for higher signal-to-noise. In order to have high optical quality reflective surface of silicon diaphragm as well as better control on depth of FP cavity, Silicon-on-Insulator (SoI) wafers can be used.

3) In case of thick (2.0 mm) glass, a collimating lens (such as graded index lens) should be used to acquire the optical signal without any effect of glass thickness on signal power.
4) The bonding related bending of silicon-glass pair and residual stresses in the diaphragm should be investigated.
5) The sensor shall be diced and packaged using advance MEMS packaging techniques. Snubber can be included for safety of silicon diaphragm from pressure surges which could be a mode of failure. Oil filled media isolated packaging can be used against reactive fluids. The optical surfaces should be duly ingress protected.
6) The temperature effects of the gas alone have been analyzed theoretically. However, there are multiple ways through which temperature may affect the pressure measurement. These include temperature dependence of packaging stress, residual stress in bonded device, linear thermal expansion, change of material properties etc. These effects can be studied or compensated directly.
7) For thin glass sensors, the stray interferometer can be used to advantage. In the packaging, the second interferometer can be formed deliberately which will respond to temperature only. The composite signal of two interferometers can be demodulated and temperature compensation can be implemented. This may require enhancing the reflectivity of the pressure sensing interferometer
8) Alternatively, the bonded glass can be optimized for use as a temperature sensing Fabry-Perot etalon and designing the temperature compensated pressure sensor.
9) The effect of gap of APC based fiberoptic probe (over the sample) on signal-to-background ratio shall be studied.
10) The elimination of back reflection from multimode fiber of different NA values can be studied and the fibers can be terminated at greater cut angle to completely eliminate the back reflection.

REFERENCES

[1] C. S. Rangan, G. R. Sarma, and V. S. V Mani, *Instrumentation Devices and Systems*, New Delhi: Tata McGraw Hill, 1983, pp. 1–232.

[2] A. S. Morris and L. Reza, “Sensor Technologies,” in *Measurement and Instrumentation: Theory and Application*, 2nd ed., Academic Press, 2015, pp. 375–631.

[3] A. K. Ghosh, *Introduction to Measurements and Instrumentation*, 5th ed. New Delhi: PHI Learning, 2012, pp. 113-521.

[4] P. Rai-Choudhury, *MEMS and MOEMS Technology and Applications*. Washington: SPIE Press, 2000, pp.169-208, 302-330.

[5] M. E. Motamedi, *MOEMS Micro-Opto-Electro-Mechanical Systems*. Washington: SPIE Press, 2005, pp. 1-17.

[6] SensorTechnics, “Pressure sensors and pressure transmitters from Sensortechnics.” [Online]. Available: https://www.first-sensor.com/en/products/pressure-sensors/pressure-sensors-and-transmitters/. [Accessed: 29-Aug-2019].

[7] S. Beeby, G. Ensell, M. Kraft, and N. White, *MEMS Mechanical Sensors*. Boston, London: Artech House, Inc., 2004.

[8] J. Fraden, *Handbook of Modern Sensors: Physics, Designs, and Applications*, 5th ed. Switzerland: Springer International Publishing, 2016, pp. 429-451.

[9] P. A. Alvi, *MEMS Pressure Sensors: Fabrication and Process Optimization*. IFSA Publishing, 2014.

[10] S. Meti, K. B. Balavald, and B. G. Sheeparmatti, “MEMS Piezoresistive Pressure Sensor: A Survey,” *Int. J. Eng. Res. Appl.*, vol. 6, no. 4, pp. 23–31, 2016.

[11] S. S. Kumar and B. D. Pant, “Design principles and considerations for the ‘ideal’ silicon piezoresistive pressure sensor: A focused review,” *Microsyst. Technol.*, vol. 20,

no. 7, pp. 1213–1247, May 2014.

[12] B. G. BALAVALAD, Kirankumar B. SHEEPARAMATTI, “A Critical Review of MEMS Capacitive Pressure Sensors,” *Sensors & Transducers*, vol. 187, no. 4, pp. 120–128, 2015.

[13] P. Eswaran and S. Malarvizhi, “MEMS capacitive pressure sensors: A review on recent development and prospective,” *Int. J. Eng. Technol.*, vol. 5, no. 3, pp. 2734–2746, 2013.

[14] J. S. Wilson, “Pressure Sensors page,” in *Sensor Technology Handbook*, Elsevier, 2005, pp. 411–456.

[15] E. Udd, “An overview of fiber-optic sensors,” *Review of Scientific Instruments*, vol. 66, no. 8. pp. 4015–4030, 1995.

[16] A. Ghatak and K. Thyagarajan, *Introduction to Fiber Optics*. Cambridge University Press, 1998.

[17] I. E. Omega, “Examples of Pressure Sensor Applications – Omega Engineering,” 2020. [Online]. Available: https://www.omega.com/en-us/resources/pressure-transducers-applications. [Accessed: 16-Jun-2020].

[18] B. G. Liptak, “Volume One: Process Measurement and Analysis,” in *Instrument Engineers’ Handbook,* 4th ed., CRC press, p. 760.

[19] P. Hariharan, *Basics of interferometry*. Academic Press, 1992.

[20] M. Born and E. Wolf, “Elements of the theory of interference and interferometer,” in *Principles of Optics*, 7th ed., Cambridge University Press, 1999, pp. 286–409.

[21] A. Ghatak and K. Thyagarajan, *Optical electronics*. Cambridge University Press, 1989.

[22] A. R. Bahrampour, S. Tofighi, M. Bathaee, and F. Farnaz, “Optical Fiber Interferometers and their Applications,” in *Interferometry – Research and Applications in Science and Technology*, Intechopen, 2012.

[23] B. H. Lee *et al.*, “Interferometric fiber optic sensors,” *Sensors*, vol. 12, no. 3, pp. 2467–2486, 2012.

[24] L. Wang and N. Fang, “Applications of Fiber-Optic Interferometry Technology in Sensor Fields,” in *Optical Interferometry*, B. A. Alexandr, B. Mithun, and W. Jue, Eds. Intechopen, 2017.

[25] M. Rajibul Islam, M. Mahmood Ali, M. H. Lai, K. S. Lim, and H. Ahmad, “Chronology of fabry-perot interferometer fiber-optic sensors and their applications: A review,” *Sensors (Switzerland)*, vol. 14, no. 4, pp. 7451–7488, 2014.

[26] T. Jiao *et al.*, “Simultaneous measurement of refractive index and temperature using a Mach-Zehnder interferometer with forward core-cladding-core recoupling,” *Opt. Laser Technol.*, vol. 111, pp. 612–615, Apr. 2019.

[27] H. C. Lefèvre, “The fiber-optic gyroscope: Achievement and perspective,” *Gyroscopy Navig.*, vol. 3, no. 4, pp. 223–226, 2012.

[28] B. Culshaw, “The optical fibre Sagnac interferometer: An overview of its principles and applications,” in *Measurement Science and Technology*, 2006, vol. 17, no. 1.

[29] Y. Xin, X. Dong, Q. Meng, F. Qi, and C. L. Zhao, “Alcohol-filled side-hole fiber Sagnac interferometer for temperature measurement,” *Sensors Actuators, A Phys.*, vol. 193, pp. 182–185, Apr. 2013.

[30] L. Liu *et al.*, “Fiber-Optic Michelson Interferometric Acoustic Sensor Based on a PP/PET Diaphragm,” *IEEE Sens. J.*, vol. 16, no. 9, pp. 3054–3058, May 2016.

[31] T. Gang *et al.*, “Fiber-optic Michelson interferometer fixed in a tilted tube for direction-dependent ultrasonic detection,” *Opt. Lasers Eng.*, vol. 88, pp. 60–64, Jan. 2017.

[32] A. D. Kersey, “A review of recent developments in fiber optic sensor technology,” *Optical Fiber Technology*, vol. 2, no. 3. Academic Press Inc., pp. 291–317, 01-Jul-

1996.

[33] C. K. Kirkendall and A. Dandridge, "Overview of high performance fibre-optic sensing," *Journal of Physics D: Applied Physics*, vol. 37, no. 18. IOP Publishing, p. R197, 21-Sep-2004.

[34] P. Roriz, O. Frazão, A. B. Lobo-Ribeiro, J. L. Santos, and J. A. Simões, "Review of fiber-optic pressure sensors for biomedical and biomechanical applications," *J. Biomed. Opt.*, vol. 18, no. 5, p. 050903, May 2013.

[35] B. Tucker, Ed., *Fiber Optic Sensors Sourcebook*. NY Research Press, 2015.

[36] G. Wild and S. Hinckley, "Acousto-ultrasonic optical fiber sensors: Overview and state-of-the-art," in *IEEE Sensors Journal*, 2008, vol. 8, no. 7, pp. 1184–1193.

[37] Y. J. Rao, "Recent progress in fiber-optic extrinsic Fabry-Perot interferometric sensors," *Opt. Fiber Technol.*, vol. 12, no. 3, pp. 227–237, Jul. 2006.

[38] Q. Yu and X. Zhou, "Pressure sensor based on the fiber-optic extrinsic fabry-perot interferometer," *Photonic Sensors*, vol. 1, no. 1. pp. 72–83, 2011.

[39] J. Wang, H. Xiao, J. Deng, R. G. May, and A. Wang, "Self-calibrated interferometric/intensity-based (SCIIB) optical fiber pressure sensor," in *Process Monitoring with Optical Fibers and Harsh Environment Sensors*, 1999, vol. 3538, p. 21.

[40] Y. J. Rao and D. A. Jackson, "Recent progress in fibre optic low-coherence interferometry," *Measurement Science and Technology*, vol. 7, no. 7. Institute of Physics Publishing, pp. 981–999, 1996.

[41] B. Yu, A. Wang, and G. R. Pickrell, "Analysis of fiber Fabry-Pérot interferometric sensors using low-coherence light sources," *J. Light. Technol.*, 2006.

[42] C. E. Lee and H. F. Taylor, "Fiber-Optic Fabry-Perot Temperature Sensor Using a Low-Coherence Light Source," *J. Light. Technol.*, vol. 9, no. 1, pp. 129–134, 1991.

[43] Y. N. Ning, K. T. V. Grattan, and A. W. Palmer, "Fibre-optic interferometric systems using low-coherence light sources," *Sensors Actuators A. Phys.*, vol. 30, no. 3, pp. 181–192, Feb. 1992.

[44] C. Belleville and G. Duplain, "White-light interferometric multimode fiber-optic strain sensor," *Opt. Lett.*, vol. 18, no. 1, p. 78, Jan. 1993.

[45] Z. Guo *et al.*, "Absolute Single Cavity Length Interrogation of Fiber-Optic Compound Fabry–Perot Pressure Sensors Through a White Light Non-Scanning Correlation Method," *Sensors*, vol. 19, no. 7, p. 1628, Apr. 2019.

[46] K. Chen, Z. Wang, M. Guo, B. Liu, and Q. Yu, "Single-mode fiber-optic Fabry–Perot interferometry sensor based on optical cross-correlation demodulation," *Opt. Eng.*, vol. 58, no. 02, p. 1, Feb. 2019.

[47] Y. Wang, X. Ni, M. Wang, Y. Cui, and Q. Shi, "Demodulation of an optical fiber MEMS pressure sensor based on single bandpass microwave photonic filter," *Opt. Express*, vol. 25, no. 2, p. 644, Jan. 2017.

[48] S. Pevec and D. Donlagic, "Miniature all-fiber Fabry–Perot sensor for simultaneous measurement of pressure and temperature," *Appl. Opt.*, vol. 51, no. 19, pp. 4536–4541, 2012.

[49] Z. Zhang *et al.*, "Diaphragm-free gas-pressure sensor probe based on hollow-core photonic bandgap fiber," *Opt. Lett.*, vol. 43, no. 13, pp. 3017–3020, 2018.

[50] Shrinkhla Ghildiyal ; Prabhat Ranjan ; Shivam Mishra ; R. Balasubramaniam ; Joseph John, "Fabry–Perot Interferometer-Based Absolute Pressure Sensor With Stainless Steel Diaphragm," *IEEE Sens. J.*, vol. 19, no. 15, pp. 6093–6101, 2019.

[51] A. Rathod, S. Mishra, S. Ghildiyal, and S. Mukhopadhyay, "Transform domain methods for performance enhancement of EFPI sensor," *Sensors Actuators, A Phys.*, vol. 189, pp. 1–7, 2013.

[52] C. Ma, B. Dong, J. Gong, and A. Wang, “Decoding the spectra of low-finesse extrinsic optical fiber Fabry-Perot interferometers,” *Opt. Express,* 2011.

[53] H. Zhang *et al.*, “Miniature all-silica microbubble-based fiber optic Fabry-Perot pressure sensor with pressure leading-in tube,” *J. Sensors*, vol. 2019, 2019.

[54] S. Liu *et al.*, “Nano silica diaphragm in-fiber cavity for gas pressure measurement,” *Sci. Rep.*, vol. 7, no. 1, 2017.

[55] D. Donlagic and E. Cibula, “All-fiber high-sensitivity pressure sensor with SiO_2 diaphragm,” *Opt. Lett.*, vol. 30, no. 16, p. 2071, Aug. 2005.

[56] X. Wang, J. Xu, Y. Zhu, K. L. Cooper, and A. Wang, “All-fused-silica miniature optical fiber tip pressure sensor,” *Opt. Lett.*, vol. 31, no. 7, p. 885, Apr. 2006.

[57] J. Wang, B. Dong, E. Lally, J. Gong, M. Han, and A. Wang, “Multiplexed high temperature sensing with sapphire fiber air gap-based extrinsic Fabry--Perot interferometers,” *Opt. Lett.*, vol. 35, no. 5, pp. 619–621, Mar. 2010.

[58] W. Li *et al.*, “Fiber-optic Fabry–Perot pressure sensor based on sapphire direct bonding for high-temperature applications,” *Appl. Opt.*, vol. 58, no. 7, p. 1662, Mar. 2019.

[59] J. Wu *et al.*, “In situ M-printed optical fiber-tip CO2 sensor using a photocrosslinkable poly(ionic liquid),” *Sensors Actuators, B Chem.*, vol. 259, pp. 833–839, Apr. 2018.

[60] J. Eom, C. J. Park, B. H. Lee, J. H. Lee, I. B. Kwon, and E. Chung, “Fiber optic Fabry-Perot pressure sensor based on lensed fiber and polymeric diaphragm,” *Sensors Actuators, A Phys.*, vol. 225, pp. 25–32, Apr. 2015.

[61] A. P. Zhang, F. Xiong, H.-Y. Tam, J. Wu, M. Yao, and P. K. A. Wai, “Optical Fiber-Tip Fabry–Pérot Interferometric Pressure Sensor Based on an In Situ μ-Printed Air Cavity,” *J. Light. Technol. Vol. 36, Issue 17, pp. 3618-3623*, vol. 36, no. 17, pp. 3618–3623, Sep. 2018.

[62] G. C. Hill *et al.*, “SU-8 MEMS Fabry-Perot pressure sensor,” *Sensors Actuators, A Phys.*, vol. 138, no. 1, pp. 52–62, 2007.

[63] Jun Ma, W. Jin, H. L. Ho, and J. Y. Dai, “High-sensitivity fiber-tip pressure sensor with graphene diaphragm,” *Opt. Lett.*, vol. 37, no. 13, pp. 2493–2495, 2012.

[64] V. K. Suri, S. Mishra, R. Balasubramaniam, and S. Ghildiyal, “US20140168659A1 - Micromachined metal diaphragm based fabry-perot fiberoptic sensor system and data processing involving the same - Google Patents,” *US20140168659A1*, 2010. [Online]. Available: https://patents.google.com/patent/US20140168659. [Accessed: 05-Nov-2019].

[65] B. Liu, J. Lin, H. Liu, A. Jin, and P. Jin, “Extrinsic Fabry-Perot fiber acoustic pressure sensor based on large-area silver diaphragm,” *Microelectron. Eng.*, vol. 166, pp. 50–54, Dec. 2016.

[66] F. Xu *et al.*, “High-sensitivity Fabry–Perot interferometric pressure sensor based on a nanothick silver diaphragm,” *Opt. Lett.*, vol. 37, no. 2, pp. 133–135, 2012.

[67] S. Nesson, M. Yu, X. Zhang, and A. H. Hsieh, “Miniature fiber optic pressure sensor with composite polymer-metal diaphragm for intradiscal pressure measurements,” *J. Biomed. Opt.*, vol. 13, no. 4, p. 044040, 2008.

[68] P. Jia *et al.*, “Batch-producible MEMS fiber-optic Fabry–Perot pressure sensor for high-temperature application,” *Appl. Opt.*, vol. 57, no. 23, p. 6687, Aug. 2018.

[69] J. Yin *et al.*, “Batch-producible fiber-optic fabry-pérot sensor for simultaneous pressure and temperature sensing,” *IEEE Photonics Technol. Lett.*, vol. 26, no. 20, pp. 2070–2073, 2014.

[70] W. Wang, X. Jiang, and Q. Yu, “Temperature self-compensation fiber-optic pressure sensor based on fiber Bragg grating and Fabry-Perot interference multiplexing,” *Opt. Commun.*, vol. 285, no. 26, pp. 3466–3470, 2012.

[71] Y. Zhang, L. Yuan, X. Lan, A. Kaur, J. Huang, and H. Xiao, "High-temperature fiber-optic Fabry–Perot interferometric pressure sensor," *Opt. Lett.*, vol. 38, no. 22, pp. 4609–4612, 2013.

[72] H. Bae and M. Yu, "Miniature Fabry-Perot pressure sensor created by using UV-molding process with an optical fiber based mold," *Opt. Express*, vol. 20, no. 13, p. 14573, Jun. 2012.

[73] W. Yuan, F. Wang, A. Savenko, D. H. Petersen, and O. Bang, "Optical fiber milled by focused ion beam and its application for Fabry-Pérot refractive index sensor," *Rev. Sci. Instrum.*, 2011.

[74] S. Ghildiyal, R. Balasubramaniam, and J. John, "Diamond turned micro machined metal diaphragm based Fabry Perot pressure sensor," *Opt. Laser Technol.*, vol. 128, p. 106243, 2020.

[75] K. Totsu, Y. Haga, and M. Esashi, "Ultra-miniature fiber-optic pressure sensor using white light interferometry," *J. Micromechanics Microengineering*, vol. 15, no. 1, pp. 71–75, Jan. 2005.

[76] S. Dasgupta, "Optically interrogated MEMS pressure sensors for propulsion applications," *Opt. Eng.*, vol. 40, no. 4, p. 598, Apr. 2001.

[77] M. Li, M. Wang, and H. Li, "Optical MEMS pressure sensor based on Fabry-Perot interferometry," *Opt. Express*, vol. 14, no. 4, pp. 1497–1504, 2006.

[78] D. C. Abeysinghe, S. Dasgupta, J. T. Boyd, and H. E. Jackson, "A novel MEMS pressure sensor fabricated on an optical fiber," *IEEE Photonics Technol. Lett.*, vol. 13, no. 9, pp. 993–995, Sep. 2001.

[79] X. Wang *et al.*, "An ultra-sensitive optical MEMS sensor for partial discharge detection," *J. Micromechanics Microengineering*, vol. 15, no. 3, pp. 521–527, 2005.

[80] X. Q. Ni, M. Wang, X. X. Chen, Y. X. Ge, and H. Rong, "A novel optical fibers

MEMS pressure sensor," *J. Phys. Conf. Ser.*, vol. 34, no. 1, pp. 996–1001, Apr. 2006.

[81] J. Yin *et al.*, "Investigation of temperature characteristic of MEMS-based optical fiber pressure sensor," in *2013 International Conference on Optical Instruments and Technology: Optical Sensors and Applications*, 2013, vol. 9044, p. 90440B.

[82] J. Yin *et al.*, "Self-referenced residual pressure measurement method for fiber-optic pressure sensor chip," *IEEE Photonics Technol. Lett.*, vol. 26, no. 10, pp. 957–960, May 2014.

[83] "Heating Ventilating and Air Conditioning (HVAC)." [Online]. Available: https://allsensors.com/applications/hvac-pressure-sensor-applications. [Accessed: 15-Jun-2018].

[84] "Industrial Pressure Sensor Applications." [Online]. Available: https://allsensors.com/applications/industrial-pressure-sensor-applications. [Accessed: 15-Jun-2018].

[85] O. Engineering, "Where Are Pressure Transducers Used? – Omega Engineering." [Online]. Available: https://www.omega.com/en-us/resources/pressure-transducers-applications. [Accessed: 02-May-2020].

[86] X. Wang, B. Li, O. L. Russo, H. T. Roman, K. K. Chin, and K. R. Farmer, "Diaphragm design guidelines and an optical pressure sensor based on MEMS technique," *Microelectronics J.*, vol. 37, no. 1, pp. 50–56, 2006.

[87] A. Cozma and B. Puers, "Characterization of the electrostatic bonding of silicon and Pyrex glass," *J. Micromechanics Microengineering*, vol. 5, no. 2, pp. 98–102, 1995.

[88] M. Rahman and S. Chowdhury, "Square Diaphragm CMUT Capacitance Calculation Using a New Deflection Shape Function," *J. Sensors*, vol. 2011, p. 12, 2011.

[89] M. F. La Cour *et al.*, "Modeling and measurements of CMUTs with square anisotropic plates," in *IEEE International Ultrasonics Symposium, IUS*, 2013, pp. 2187–2190.

[90] M. Di Giovanni, *Flat and corrugated diaphragm design handbook*, 1st ed. NewYork Basel: Marcel Dekker, 1982.

[91] M. Bao, *Analysis and Design Principles of MEMS Devices*, 1st ed. Elsevier, 2005.

[92] A. Nallathambi and T. Shanmuganantham, “Design of Diaphragm Based MEMS Pressure Sensor with Sensitivity Analysis for Environmental Applications,” *Sensors & Transducers*, vol. 188, no. 5, pp. 48–54, 2015.

[93] T. Corman, “Vacuum-Sealed and Gas-Filled Micromachined Devices,” Royal Institute of Technology, 1999.

[94] S. Mack, H. Baumann, U. Gösele, H. Werner, and R. Schlögl, “Analysis of Bonding- Related Gas Enclosure in Micromachined Cavities Sealed by Silicon Wafer Bonding,” *J. Electrochem. Soc.*, vol. 144, no. 3, pp. 1106–1111, Dec. 2019.

[95] K. M. Tenny and J. S. Cooper, *Ideal Gas Behavior*. StatPearls Publishing, 2018.

[96] T. Helmenstine, “Ideal Gas vs. Non-Ideal Gas Example Problem,” 2020. [Online]. Available: https://www.thoughtco.com/ideal-vs-non-ideal-gas-example-problem-609507. [Accessed: 29-Feb-2020].

[97] S. M. Sze, *VLSI Technology*, 2nd ed. McGraw-Hill Series in Electrical Engineering, 1999.

[98] S. Turek and J. Hron, “Proposal for numerical benchmarking of fluid-structure interaction between an elastic object and laminar incompressible flow,” *Lecture Notes in Computational Science and Engineering*, vol. 53. Springer Verlag, pp. 371–385, 2006.

[99] M. Nazem, J. P. Carter, and D. W. Airey, “Arbitrary Lagrangian-Eulerian method for non-linear problems of geomechanics,” in *IOP Conference Series: Materials Science and Engineering*, 2014, vol. 10, no. 1, p. 012074.

[100] M. Souli and J. P. Zolesio, “Arbitrary Lagrangian-Eulerian and free surface methods in

fluid mechanics," *Comput. Methods Appl. Mech. Eng.*, vol. 191, no. 3–5, pp. 451–466, Nov. 2001.

[101] M. M. Noor, B. Bais, and B. Y. Majlis, "The effects of temperature and KOH concentration on silicon etching rate and membrane surface roughness," in *IEEE International Conference on Semiconductor Electronics, Proceedings, ICSE*, 2002, pp. 524–528.

[102] E. Haimi, V. Eikko, and K. Lindroos, "Evolution of Surface Roughness in KOH Etching of Silicon Caused by Material Defects," 2003.

[103] P. Pal, S. Tuli, and S. Chandra, "A new technique of front-to-back alignment for MEMS," *Sens. Lett.*, vol. 2, no. 1, pp. 78–81, Mar. 2004.

[104] S. Dhanekar, S. Chandra, and R. Balasubramaniam, "Micro-mixer device with deep channels in silicon using modified RIE process: fabrication, packaging and characterization," *Microsyst. Technol.*, vol. 22, no. 3, pp. 515–522, Mar. 2016.

[105] C. R. Nave, "Inverse Square Law," 1998. [Online]. Available: http://hyperphysics.phy-astr.gsu.edu/hbase/Forces/isq.html#isq. [Accessed: 29-Jul-2020].

[106] M. Han and A. Wang, "Exact analysis of low-finesse multimode fiber extrinsic Fabry-Perot interferometers.," *Appl. Opt.*, 2004.

[107] R. M. Bunch and J. P. Caughey, "Angularly-polished optical fiber tips," in *Applications of Optical Engineering: Proceedings of OE/Midwest '90*, 1991, vol. 1396, pp. 411–416.

[108] J. M. Senior, *Optical Fiber Communications: Principles and Practice*, 3rd ed. England: Pearson Education India, 2010.

[109] J. J. Davenport, M. Hickey, J. P. Phillips, and P. A. Kyriacou, "Method for producing angled optical fiber tips in the laboratory," *Opt. Eng.*, vol. 55, no. 2, p. 026120, Feb. 2016.

[110] I. D. Vrinceanu and S. Danyluk, "Measurement of residual stress in single crystal silicon wafers," in *8th International Advanced Packaging Materials Symposium*, 2002, pp. 297–301.

[111] I. Sadaba, C. H. J. Fox, and S. McWilliam, "An investigation of residual stress effects due to the anodic bonding of glass and silicon in MEMS fabrication," in *Applied Mechanics and Materials*, 2006, vol. 5–6, pp. 501–508.

[112] T. K. Shing, "Analysis of anodic bonding and packaging effects in micro sensors," in *2000 International Conference on Modeling and Simulation of Microsystems - MSM 2000*, 2000, pp. 613–616.

[113] R. Inzinga, T. Lin, M. Yadav, H. T. Johnson, and G. P. Horn, "Control and quantification of residual stresses in anodically bonded MEMS structures," in *Conference Proceedings of the Society for Experimental Mechanics Series*, 2011, vol. 2, pp. 269–273.

[114] R. A. Inzinga, T. W. Lin, M. Yadav, H. T. Johnson, and G. P. Horn, "Characterization and Control of Residual Stress and Curvature in Anodically Bonded Devices and Substrates with Etched Features," *Exp. Mech.*, vol. 52, no. 6, pp. 637–648, Aug. 2012.

[115] M. Harz and H. Engelke, "Curvature changing or flattening of anodically bonded silicon and borosilicate glass," *Sensors Actuators, A Phys.*, vol. 55, no. 2–3, pp. 201–209, Jul. 1996.

[116] H. M. and W. Bruckner, "Stress Reduction in Anodically Bonded Silicon and Borosilicate Glass by Thermal Treatment," *J. Electrochem. Soc.*, vol. 143, no. 4, pp. 1409–1414, 1996.

[117] J. Jiang *et al.*, "Noncontact Ultrasonic Detection in Low-Pressure Carbon Dioxide Medium Using High Sensitivity Fiber-Optic Fabry-Perot Sensor System," *J. Light. Technol.*, vol. 35, no. 23, pp. 5079–5085, Dec. 2017.

[118] H. Liao *et al.*, “Phase Demodulation of Short-Cavity Fabry–Perot Interferometric Acoustic Sensors with Two Wavelengths.,” *IEEE Photonics J.*, vol. 9, no. 2, 2017.

[119] K. Chen *et al.*, “Fast demodulated white-light interferometry based fiber-optic Fabry–Perot cantilever microphone,” *Opt. Lett.*, vol. 43, no. 14, p. 3417, 2018.

[120] B. Liu, J. Lin, H. Liu, Y. Ma, L. Yan, and P. Jin, “Diaphragm based long cavity Fabry–Perot fiber acoustic sensor using phase generated carrier,” *Opt. Commun.*, vol. 382, pp. 514–518, 2017.

[121] Q. Dong *et al.*, “Miniature fiber optic acoustic pressure sensors with air-backed graphene diaphragms,” *ASME. J. Vib. Acoust*, vol. 141, no. 4, 2019.

APPENDIX

A.1 Calculation of pressure value after anodic bonding

The residual cavity pressure after bonding under atmospheric pressure is given by Eq.A.1 as following

$$\boldsymbol{P_c = P_{atm}\ (T/T_{bonding}).(V_0\ /V_c\ )} \qquad \textbf{Eq. A.1}$$

Where $\boldsymbol{P_c\ , P_{atm}, V_0, V_c, T, T_{bonding}}$ denote pressure inside the sealed cavity, ambient (atmospheric) pressure, initial (no-deflection) cavity volume, cavity volume in general, cavity air temperature and bonding temperature respectively.

$$\boldsymbol{P_{atm}} = 1013.25\ mbar, \qquad \boldsymbol{T} = 300\ K, \qquad \boldsymbol{T_{bonding}} = 750\ K$$

To estimate the initial cavity pressure after sealing, initial cavity volume (when diaphragm is not deflected) volume is considered, hence $\boldsymbol{V_c = V_0}$. Using the above values and equation,

$$P_c = (1013.25\ mbar)\ (300K/750K).(V_0\ /V_0\ ) = \ 405.3\ mbar$$

A.2 Calculations of deflection of square diaphragm

The deflection of an edge-clamped square diaphragm at the centre is given by

$$x = 0.01384\ \frac{PL^4}{Eh^3} \qquad \textbf{Eq. A.2}$$

Where P, L, E and h are applied pressure, edge (side) length, Young modulus and thickness of diaphragm. The widely excepted value of young modulus for (100) single crystal silicon is

169 GPa. This is the effective value as if the material is isotropic. After putting the value of Young modulus, the deflection formula is simplified to

$$x = 8.189 \times 10^{-8} \frac{PL^4}{h^3} \qquad \textbf{Eq. A.3}$$

However, in the present work, the coefficient is **8.386 x 10^{-8}**, which is very close to the value in the above equation. The diaphragm thickness for 15.63 μm deflection is 129 μm.

$$x = 8.386 \times 10^{-8} \frac{PL^4}{h^3} \qquad \textbf{Eq. A.4}$$

The value is arrived at by solving the anisotropic formulation for silicon diaphragm as explained below. The effective elastic coefficient value C_{11} = 194.25 GPa has been used. The diaphragm thickness for 15.63 μm deflection is 130 μm. However, in the present work, deflection sensitivity value is considered in modelling and the exact thickness of diaphragm is not directly related.

A.3 Deflection model of anisotropic silicon diaphragm

The values are calculated step-by-step as per the reference La Cour *et al.* and presented in Table A. 1. The description is given in the first column and formula and calculated values are shown in further columns.

Table A. 1 Derivation of deflection formula

Silicon stiffness constants (Gpa) at 300K in crystal co-ordinate system	**c_{11}**	**c_{12}**	**c_{44}**
	165.6	63.9	79.5
Effective stiffness constants (GPa) in the coordinate system of diaphragm in (100) plane, edges aligned to <110> directions	**C_{11}** $= (c_{11} + c_{12} + 2\ c_{44})/2$	**C_{12}** $= (c_{11} + c_{12} - 2\ c_{44})/2$	**C_{66}** $= (c_{11} - c_{12})/2$
	194.25	35.25	50.85
Constant (k_2)	$k_2 = 2\ (C_{12} + 2\ C_{66})\ /\ C_{11} = 1.41003861$		
Constant (β) defines the shape	$\beta = (182 + 143\ k_2)\ /\ (1432 + 91\ k_2) = 0.245871$		
Anisotropic flexural rigidity (D_a)	$D_a = h^3 C_{11}/12$		
Maximum deflection (w_0) at centre of diaphragm	$w_0 = \frac{77(1432 + 91\ k_2)}{256(16220 + 11\ k_2\ (329 + 13\ k_2))} \cdot P(L/2)^4/D_a$ $= (0.021720172)\ P(L/2)^4/D_a$ $= (0.021720172)\ P(L^4/16)\ (12/h^3 C_{11})$ $= \mathbf{8.386 \times 10^{-8}}\ \boldsymbol{PL^4/h^3}$ ($C_{11} = 194250$ MPa)		

A.4 Steps of simplification of equation Eq. 3-16

The equation Eq.

$$\boldsymbol{x = B.(P - \frac{C.T}{(V_0 - A.x)})} \quad \textbf{Eq. A.5}$$

Multiplying by denominator $\boldsymbol{(V_0 - A.x)}$ **;**

$$\boldsymbol{x\ (V_0 - A.x) = B.(P(V_0 - A.x) - C.T\ )} \quad \textbf{Eq. A.6}$$

Opening first bracket;

$$x\,(V_0 - A.x) = BP(V_0 - A.x) - BCT\ ) \qquad \textbf{Eq. A.7}$$

Opening second bracket and multiplication by -1;

$$V_0 x - A.x^2 = BPV_0 - ABP.x - BCT \qquad \textbf{Eq. A.8}$$

$$-V_0 x + A.x^2 = -BPV_0 + ABP.x + BCT \qquad \textbf{Eq. A.9}$$

Adjusting in the form of a quadratic equation;

$$A.x^2 - (V_0 + ABP)x - B(PV_0 - CT) = 0 \qquad \textbf{Eq. A.10}$$

Finding the roots quadratic equation;

$$x = \left(\frac{V_0}{2A} + \frac{BP}{2}\right) \pm \sqrt{\left(\frac{V_0}{2A} - \frac{BP}{2}\right)^2 + \frac{BCT}{A}} \qquad \textbf{Eq. A.11}$$

The quadratic equation has two roots (that is two solutions for ***x***). As the quantity under the square-root is always positive here, the roots will be ‘real’ (not complex numbers).

The validity of equation should be first checked when there is no entrapped gas by putting the term $\frac{BCT}{A} = 0$. The equation in that case should reduce to the one for normal pressure sensor.

$$x = \left(\frac{V_0}{2A} + \frac{BP}{2}\right) \pm \left(\frac{V_0}{2A} - \frac{BP}{2}\right) \qquad \textbf{Eq. A.12}$$

When the root with positive sign is taken, the pressure dependent term cancels out, and it suggests that the deflection is not a function of applied pressure. Therefore, that solution does not have any physical significance. When the solution with negative sign is considered, the equation reduces to following form, which suggests that the deflection is the product of applied pressure and the sensitivity of diaphragm; and the same has a physical significance.

$$\boldsymbol{x} = \boldsymbol{BP} \qquad \textbf{Eq. A.13}$$

Therefore, the solution with negative sign is appropriate and used in the analytical modelling. The derived characteristic equation is as following;

$$\boldsymbol{x} = \left(\frac{\boldsymbol{V_0}}{\boldsymbol{2A}} + \frac{\boldsymbol{BP}}{\boldsymbol{2}}\right) - \sqrt{\left(\frac{\boldsymbol{V_0}}{\boldsymbol{2A}} - \frac{\boldsymbol{BP}}{\boldsymbol{2}}\right)^{\boldsymbol{2}} + \frac{\boldsymbol{BCT}}{\boldsymbol{A}}} \qquad \textbf{Eq. A.14}$$

A.5 Calculations of constants for analytical model

As per Eq.3-7, for β = 0.24587

$$\nu = \frac{64\,(147+42\,\beta)}{33075} = 0.30442626 \qquad \textbf{Eq. A.15}$$

For diaphragm of edge length of 8 mm (8000 µm),

$$A = \nu . L^2 = 0.30442626 \times (8000 \times 8000) = 19483281 \qquad \textbf{Eq. A.16}$$

For atmospheric pressure $\boldsymbol{P_{atm}} = 1013.25$ mbar (0.101325 MPa) and bonding temperature $\boldsymbol{T_{bonding}} = 750$ K, the constant C' is

$$C' = \frac{P_{atm}}{T_{bonding}} = 0.101325/750 = 0.0001351 \text{ MPa/K} \qquad \textbf{Eq. A.17}$$

A.6 Minimum cavity length

There is a designed full scale deflection (span) of diaphragm in a pressure sensor. The present sensor is based on the principle of a Fabry-Perot (FP) interferometer. The deflection of diaphragm is measured by measuring the cavity length between the centre of diaphragm and a fixed reference surface (Fig. A. 1).

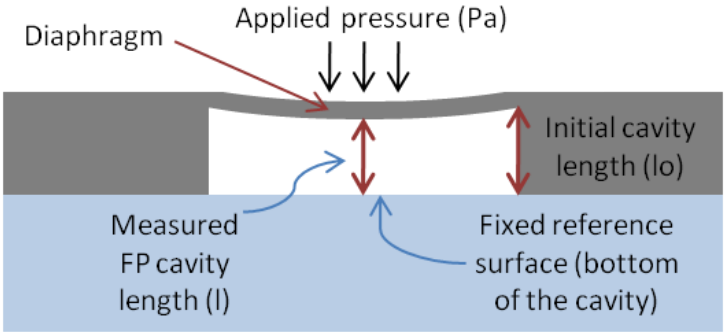

Fig. A. 1 Initial and measured cavity lengths in the FP pressure sensor

In the present case, the reference surface is the surface of a glass wafer which is also the bottom of the cavity. The bottom of the cavity must not physically stop the diaphragm in its normal operation (though, the same may be useful for over range protection of diaphragm).

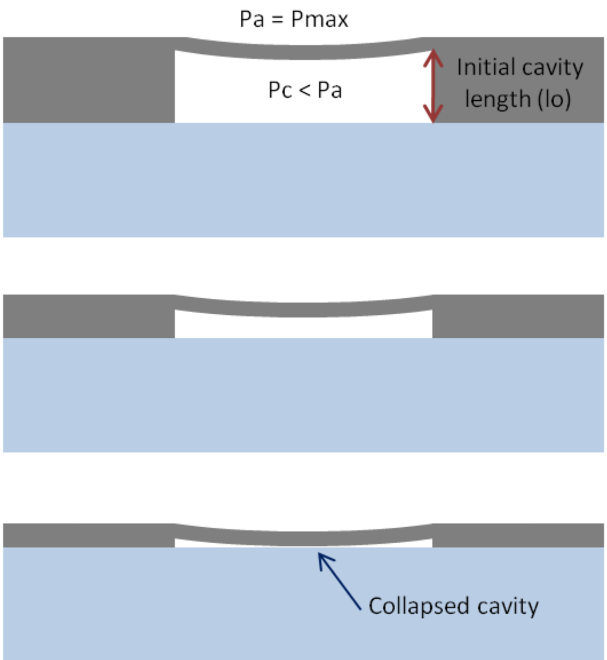

Fig. A. 2 Collapse condition of the FP cavity under full applied pressure

If the (initial) cavity length is more than the design span value, the movement of diaphragm will not be hindered in normal operation. However, when the cavity length is smaller than the span, the cavity will collapse under full applied pressure (Fig. A. 2).

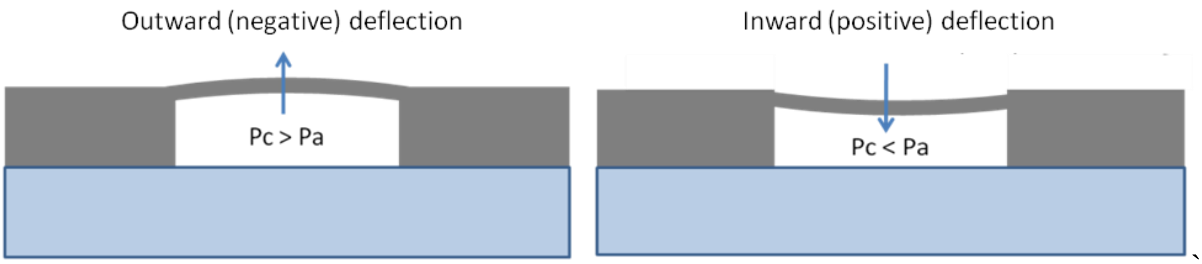

Fig. A. 3 Outward and inward deflections in an absolute pressure sensor

However, in case of absolute pressure sensors having residual pressure in sealed cavity, part of the deflection is outward of the cavity and remaining is inward (Fig. A. 3). As the inward deflection is lesser than the span, the minimum possible cavity length (for no-collapse condition) is also lesser. Further, if there is 'suppression of span', the achievable span as well as inward (positive) part of it, get smaller. Therefore, the minimum cavity length can be even smaller.

In order to find the minimum cavity length, a value of cavity length just above the designed span is taken to start with. For example, in the present case, the designed span value is 15.63 µm, hence cavity length of 16 µm is taken. Then, the full inward (positive) deflection of the diaphragm is found using the developed characteristic equation. If it is found that there is certain gap still there between the diaphragm and the bottom of the cavity, a lower value of the cavity length is taken. In a few iterations, the approximate value of minimum cavity length for the given sensor parameters can be found. A plot for 1 bar pressure sensor with trapped gas pressure of 405 mbar is shown in Fig. A. 4 for illustration.

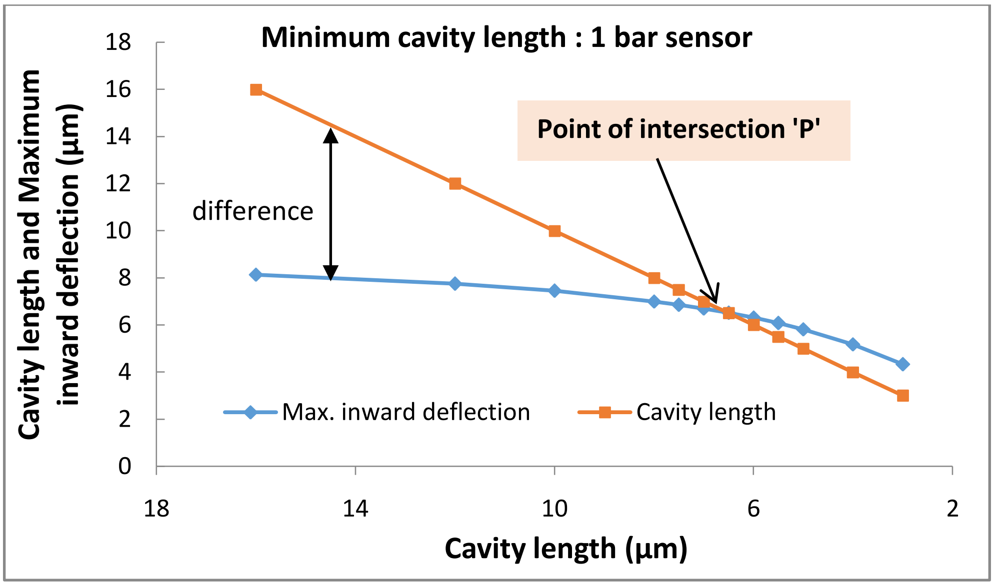

Fig. A. 4 Minimum cavity length for 1 bar pressure sensor

In Fig. A. 4, the x-axis is cavity length in decreasing order. On the y-axis, the same cavity length as well as the positive (inward) part of deflection is plotted. At 16 µm cavity length, the positive deflection is about 8.1 µm. The difference between the two quantities is evident from the y-axis values. This means that the diaphragm's movement ends much above the bottom of the cavity and there is scope to further reduce the cavity length. The inward deflection also reduces with decreasing cavity length, but at slower rate. At certain cavity length, the diaphragm just touches the bottom of cavity. This is the minimum cavity length is based on the criterion of no-collapse. The cavity gets collapsed on increasing the pressure beyond the full scale. This condition corresponds to intersection of two curves at point 'P' given in Fig. A. 4. Thus the minimum cavity length for 1 bar pressure sensor with trapped gas pressure is around 7 µm. There is no physical significance of the part of the curve on right of the point 'P'. Similar graph is shown for a pressure sensor of 10 bar range, 15.63 µm designed span and 405 mbar pressure of the trapped gas in Fig. A. 5. The minimum cavity length is approximately 14.75 µm.

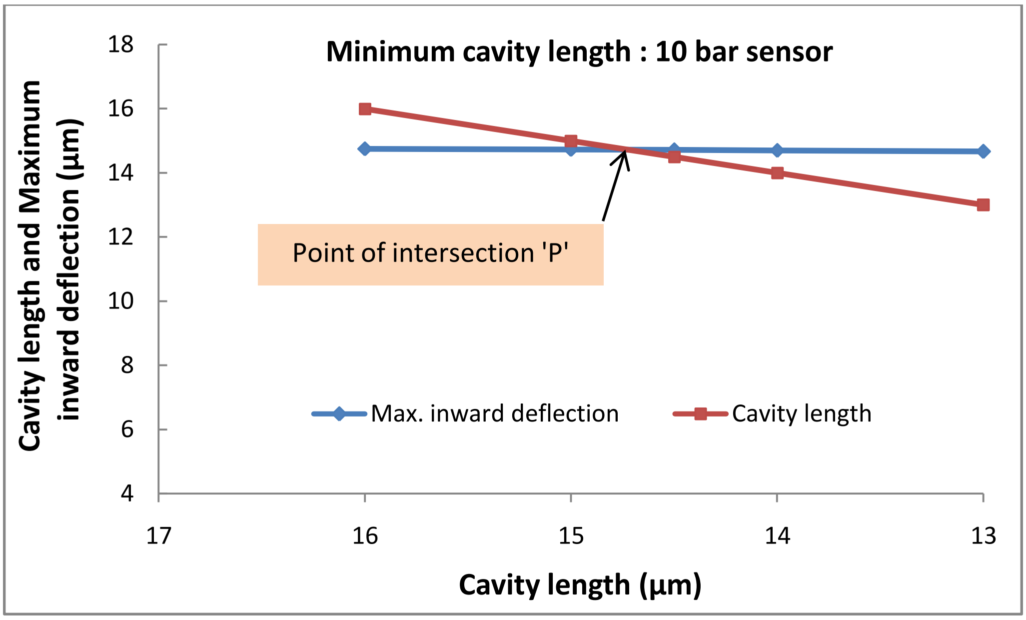

Fig. A. 5 Minimum cavity length for 10 bar pressure sensor

A.7 Silicon wafer specifications

The specifications of the silicon wafer used in the fabrication of devices are given in Table A. 2.

Table A. 2 Specifications of silicon wafer

Sr	Specification	Value
1	Make	Siltronix
2	Type	n-type, (100)
3	Diameter	2"
4	Thickness (µm)	275
5	Single side polished (SSP) or double side polished (DSP)	Single side polished (SSP)
6	Thickness tolerance (± µm)	15
7	Total thickness variation (TTV) standard (µm)	< 10
8	TTV minimum on SSP (µm)	5
9	Bow (µm)	< 30
10	Flatness on polished surface (µm)	< 1
11	Roughness on polished surface (nm)	< 1 nm

A.8 The anodic bonding set-up and process

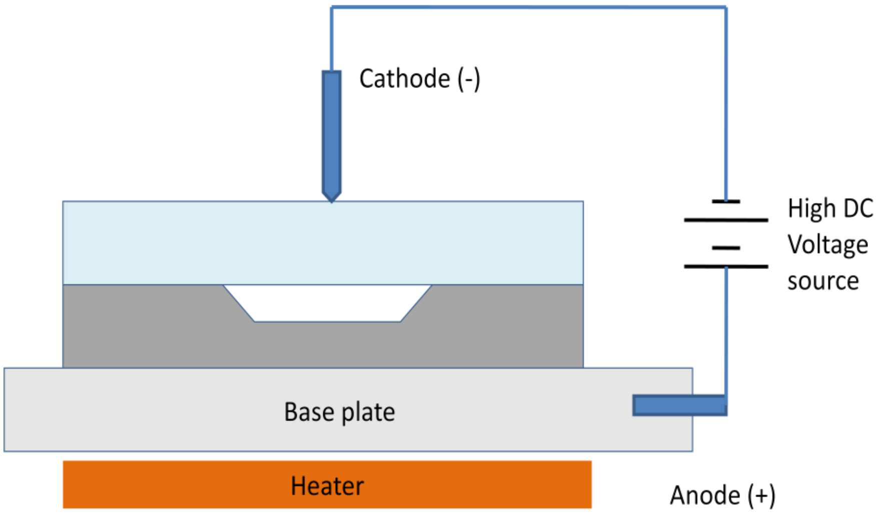

Fig. A. 6 Schematic of anodic bonding set -up

The schematic and photograph of the anodic bonding set-up are given in Fig. A. 6. In the anodic bonding of silicon and glass, the latter should have alkali ions. The pair is first heated at high temperature (such as 450 °C) to enhance the mobility of ions and electrons. The silicon is connected to positive terminal (anode) of high voltage DC power supply and glass to negative terminal (cathode). When the high voltage (e.g. 1200 VDC) is applied, the two wafers are pulled by each other and come in intimate contact. The current starts flowing and fusion at the surface takes place. In general, the bonding starts from the interface location below contact point of cathode; and spreads radially outward. In the present case, there is a cavity in silicon below the cathode, so the bonding starts from some other point. The bonding time depends on the parameters of bonding and on the specification of the two wafers. Photograph of the bonding set-up used in the lab is given in Fig. A. 7.

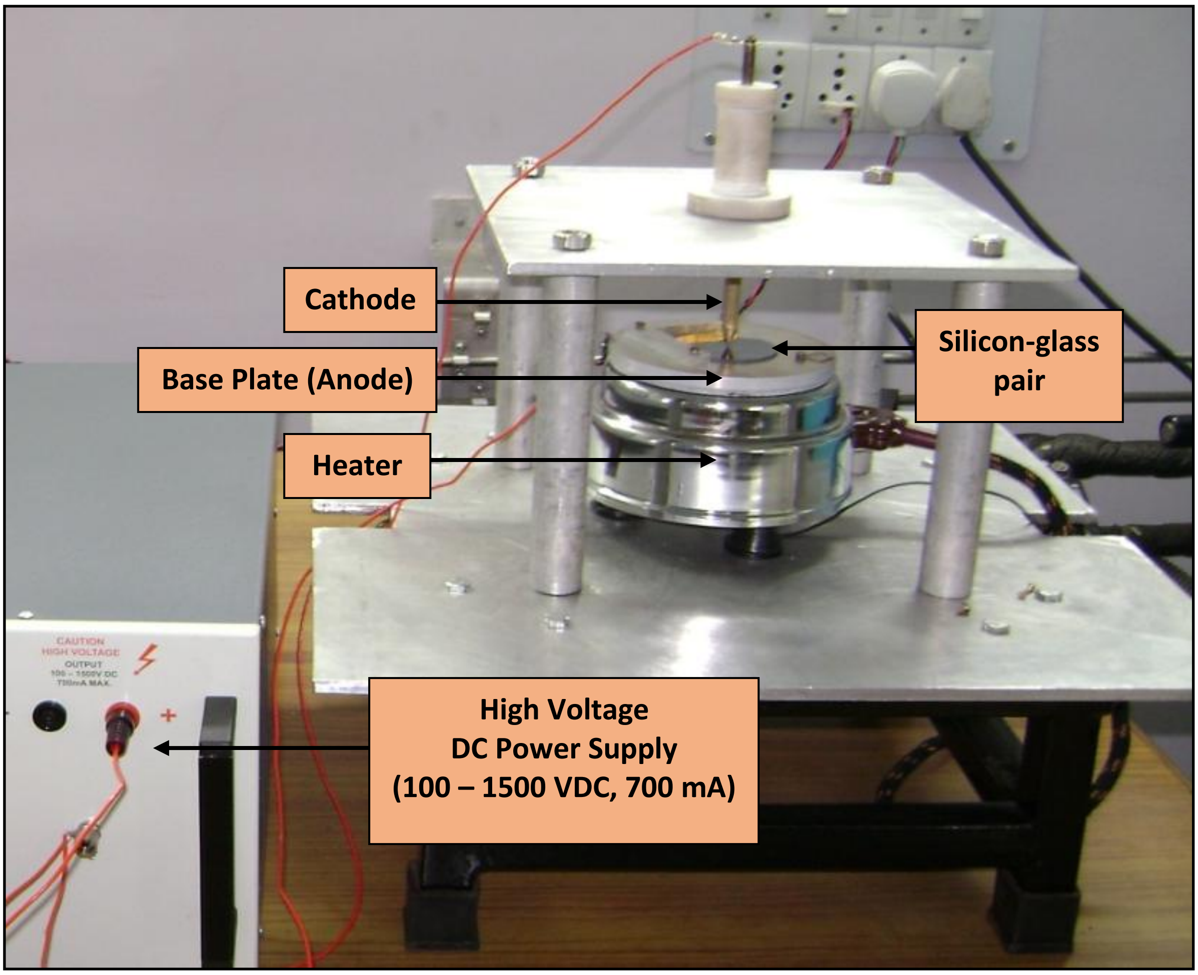

Fig. A. 7 Photograph of anodic bonding set-up used

The sub-atmospheric pressure is captured in the sealed cavity as the density of the gas reduces after heating at high temperature and the molecules escape from the cavity before the voltage is actually applied and the sealing takes place.

A.9 Fabricated devices and packaging

Some of the fabricated devices are shown in Fig. A. 8. The upper side is glass. In Fig. A. 9, a device is shown with extra pocket of air after anodic bonding. This may be due to bow and flatness issues in the silicon and glass wafers. In the Fig. A. 10, dimensional measurements of a device are shown. In Fig. A. 11, a device package in modified KF-50 vacuum flange is shown. An O-ring and another flange comprising pressure port caps the device for functional testing.

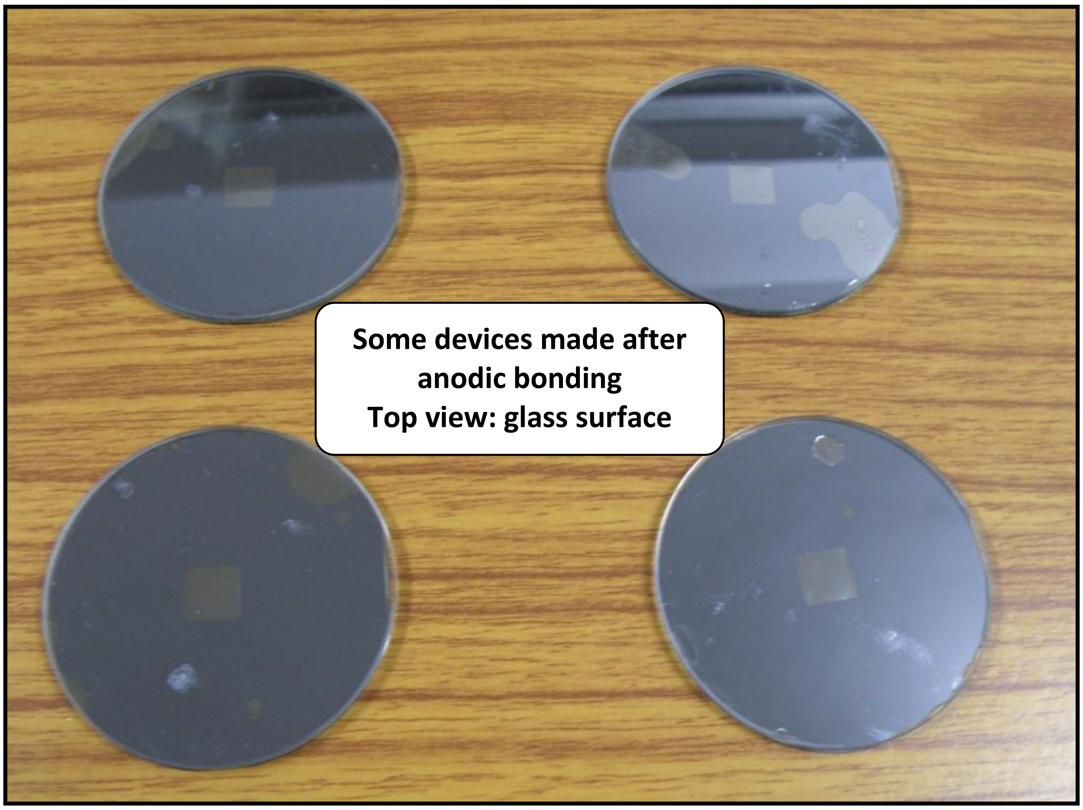

Fig. A. 8 Photograph of a batch of devices

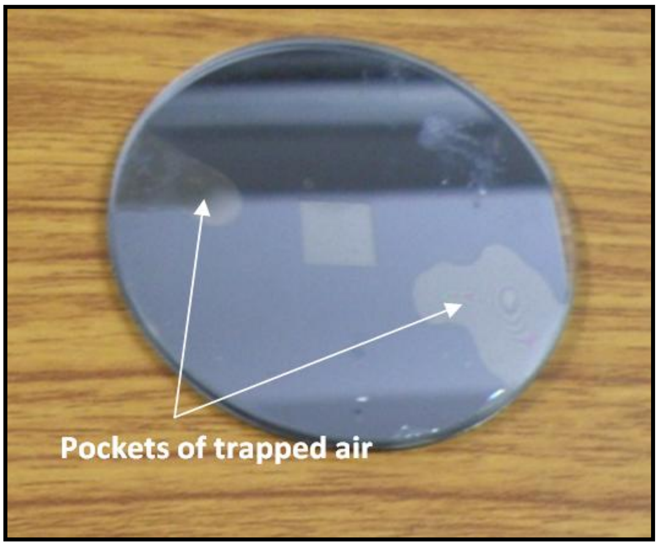

Fig. A. 9 Photograph showing extra air pockets in device

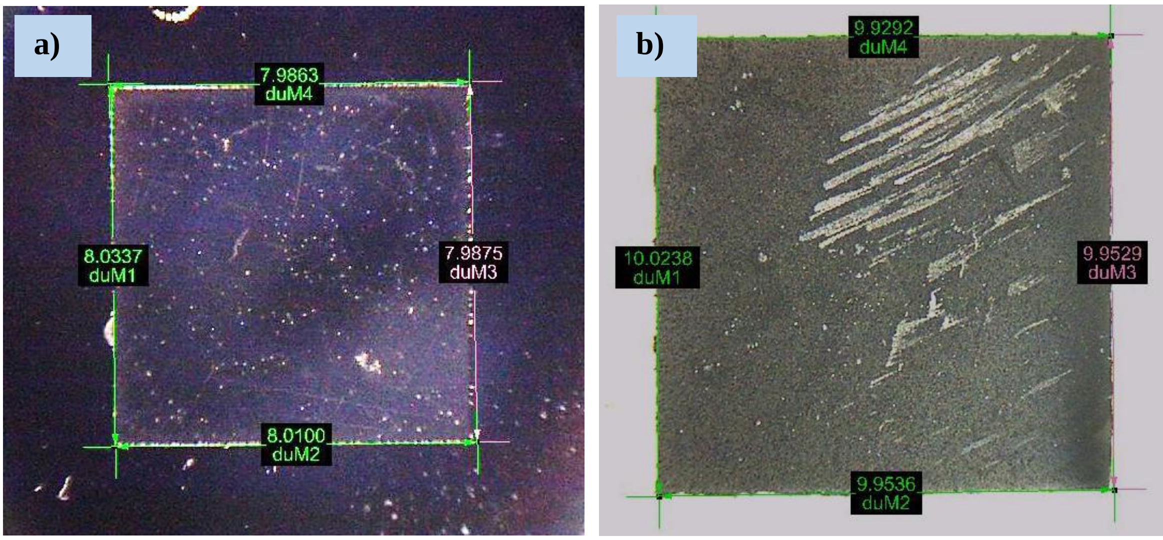

Fig. A. 10 The dimensions of the sensor window a) front and b) back

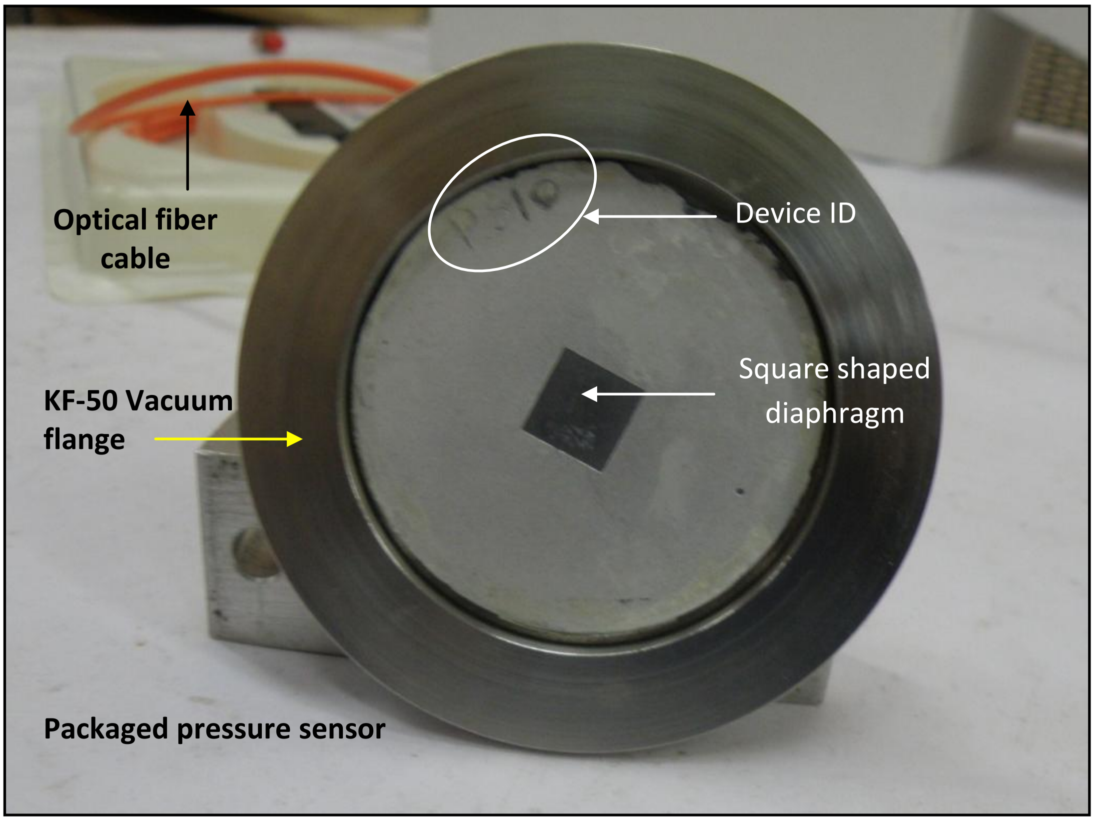

Fig. A. 11 A packaged device

A.10 Visibility of interference signal

The quality of interference signal is assessed based on the visibility or contrast of the fringes. It is basically the amplitude of fringe modulation over the average power. The visibility V can be calculated by following formula for a given signal.

$$V = \left(\frac{Y_{max} - Y_{min}}{Y_{max} + Y_{min}}\right) \qquad \textbf{Eq. A.18}$$

Where, Y_{max} and Y_{min} are the maximum and minimum intensity (y-axis value) in a fringe. Visibility for two sensors is calculated here for example.

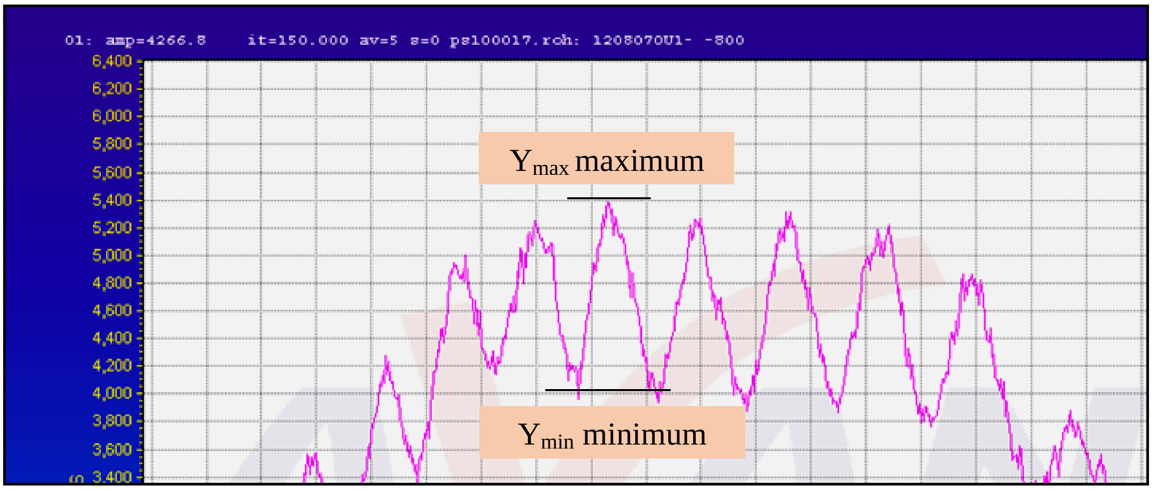

Fig. A. 12 Signal from device PS10 (15 µm)

Using the maximum and minimum values 5400 and 4000, as indicated by horizontal lines in the Fig. A. 12, the **visibility is 14.9 %** for sensor PS10 of design cavity length 15 µm (13 µm for this signal). Similarly, in Fig. A. 13, the maximum and minimum values for a fringe are 58,000 and 52,000, thus the visibility is about 5.5 %. The power level of first signal is low even at high integration time, because the signal is acquired with an APC based probe.

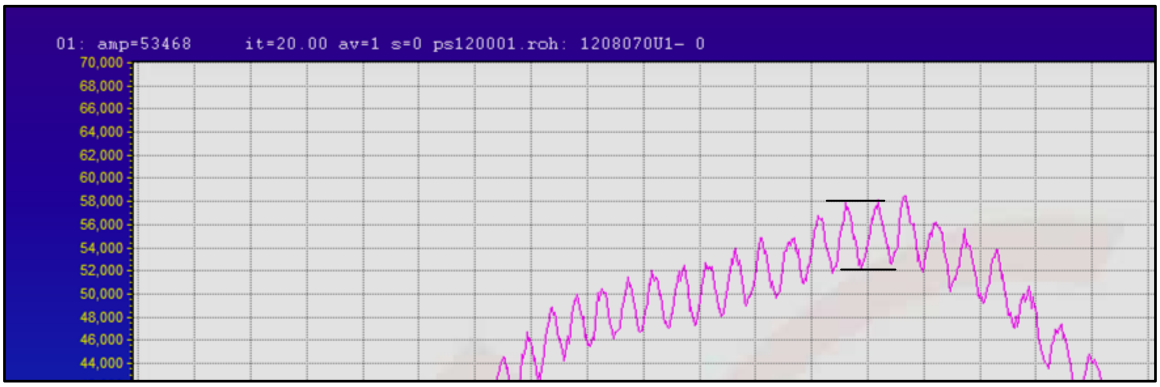

Fig. A. 13 Signal from device PS12 (60 μm)

The visibility for sensor PS12 is less compared to other sensor, because the cavity length is high (about 51.5 μm for this signal), and the beam reflected from diaphragm is weaker due to beam divergence and longer distance of travel.

A.11 Stress in diaphragm

The designed full scale deflection of diaphragm is 15.63 μm. However, due to presence of trapped gas in the cavity, the positive deflection is limited to < 10 μm. The negative deflective is even lesser in magnitude, so the maximum stress is in case of positive deflection in the present study. In this case, though the applied pressure is full (1000 mbar), it is the differential (net applied) pressure which is responsible for deflection. As the diaphragm is working in the linear regime, the net applied pressure can be estimated in the ratio of deflection. The net pressure for 10 μm deflection will be 640 mbar (0.064 MPa). The maximum stress in square diaphragm occurred at the centre of the edges and is given by

$$\sigma_{max} = 0.308\, P \left(\frac{L}{h}\right)^2 = 0.308 \times 0.064 \times \left(\frac{8000}{130}\right)^2 = 75.7 \text{ MPa} \qquad \textbf{Eq. A.19}$$

Thus, the maximum stress in the diaphragm is about 75 MPa, which is much under the 7000 MPa.

****